NASA/TM–2015-104606 / Vol. 43

Technical Report Series on Global Modeling and Data Assimilation, Volume 43

Randal D. Koster, Editor

MERRA-2: Initial Evaluation of the Climate

Michael G. Bosilovich, Santha Akella, Lawrence Coy, Richard Cullather, Clara Draper, Ronald Gelaro, Robin Kovach, Qing Liu, Andrea Molod, Peter Norris, Krzysztof Wargan, Winston Chao, Rolf Reichle, Lawrence Takacs, Yury Vikhliaev, Steve Bloom, Allison Collow, Stacey Firth, Gordon Labow, Gary Partyka, Steven Pawson, Oreste Reale, Siegfried D. Schubert, and Max Suarez

National Aeronautics and
Space Administration

Goddard Space Flight Center
Greenbelt, Maryland 20771

November 2015

NASA STI Program ... in Profile

Since its founding, NASA has been dedicated to the advancement of aeronautics and space science. The NASA scientific and technical information (STI) program plays a key part in helping NASA maintain this important role.

The NASA STI program operates under the auspices of the Agency Chief Information Officer. It collects, organizes, provides for archiving, and disseminates NASA's STI. The NASA STI program provides access to the NASA Aeronautics and Space Database and its public interface, the NASA Technical Report Server, thus providing one of the largest collections of aeronautical and space science STI in the world. Results are published in both non-NASA channels and by NASA in the NASA STI Report Series, which includes the following report types:

- TECHNICAL PUBLICATION. Reports of completed research or a major significant phase of research that present the results of NASA Programs and include extensive data or theoretical analysis. Includes compilations of significant scientific and technical data and information deemed to be of continuing reference value. NASA counterpart of peer-reviewed formal professional papers but has less stringent limitations on manuscript length and extent of graphic presentations.
- TECHNICAL MEMORANDUM. Scientific and technical findings that are preliminary or of specialized interest, e.g., quick release reports, working papers, and bibliographies that contain minimal annotation. Does not contain extensive analysis.
- CONTRACTOR REPORT. Scientific and technical findings by NASA-sponsored contractors and grantees.
- CONFERENCE PUBLICATION. Collected papers from scientific and technical conferences, symposia, seminars, or other meetings sponsored or co-sponsored by NASA.
- SPECIAL PUBLICATION. Scientific, technical, or historical information from NASA programs, projects, and missions, often concerned with subjects having substantial public interest.
- TECHNICAL TRANSLATION. English-language translations of foreign scientific and technical material pertinent to NASA's mission.

Specialized services also include organizing and publishing research results, distributing specialized research announcements and feeds, providing help desk and personal search support, and enabling data exchange services. For more information about the NASA STI program, see the following:

- Access the NASA STI program home page at http://www.sti.nasa.gov
- E-mail your question via the Internet to help@sti.nasa.gov
- Fax your question to the NASA STI Help Desk at 443-757-5803
- Phone the NASA STI Help Desk at 443-757-5802

NASA/TM–2015-104606/Vol. 43

Technical Report Series on Global Modeling and Data Assimilation, Volume 43

Randal D. Koster, Editor

MERRA-2: Initial Evaluation of the Climate

Michael G. Bosilovich
Goddard Space Flight Center, Greenbelt, MD
Santha Akella
Science Systems Applications Inc., Lanham, MD
Lawrence Coy
Science Systems Applications Inc., Lanham, MD
Richard Cullather
Earth System Science Interdisciplinary Center, College Park, MD
Clara Draper
Universities Space Research Association, Columbia, MD
Ronald Gelaro
Goddard Space Flight Center, Greenbelt, MD
Robin Kovach
Science Systems Applications Inc., Lanham, MD
Qing Liu
Science Systems Applications Inc., Lanham, MD
Andrea Molod
Earth System Science Interdisciplinary Center, College Park, MD
Peter Norris
Universities Space Research Association, Columbia, MD
Krzysztof Wargan
Science Systems Applications Inc., Lanham, MD
Winston Chao
Goddard Space Flight Center, Greenbelt, MD
Rolf Reichle
Goddard Space Flight Center, Greenbelt, MD
Lawrence Takacs
Science Systems Applications Inc., Lanham, MD
Ricardo Todling
Goddard Space Flight Center, Greenbelt, MD
Yury Vikhliaev
Universities Space Research Association, Columbia, MD
Steve Bloom
Science Systems Applications Inc., Lanham, MD
Allison Collow
Universities Space Research Association, Columbia, MD
Gary Partyka
Science Systems Applications Inc., Lanham, MD
Stacey Firth
Science Systems Applications Inc., Lanham, MD
Gordon Labow
Science Systems Applications Inc., Lanham, MD
Steven Pawson
Goddard Space Flight Center, Greenbelt, MD
Oreste Reale
Universities Space Research Association, Columbia, MD
Siegfried Schubert
Goddard Space Flight Center, Greenbelt, MD
Max Suarez
Goddard Space Flight Center, Greenbelt, MD

National Aeronautics and
Space Administration

Goddard Space Flight Center
Greenbelt, Maryland 20771

November 2015

Level of Review: This material has been technically reviewed by technical management

Abstract

The years since the introduction of MERRA have seen numerous advances in the GEOS-5 Data Assimilation System as well as a substantial decrease in the number of observations that can be assimilated into the MERRA system. To allow continued data processing into the future, and to take advantage of several important innovations that could improve system performance, a decision was made to produce MERRA-2, an updated retrospective analysis of the full modern satellite era. One of the many advances in MERRA-2 is a constraint on the global dry mass balance; this allows the global changes in water by the analysis increment to be near zero, thereby minimizing abrupt global interannual variations due to changes in the observing system. In addition, MERRA-2 includes the assimilation of interactive aerosols into the system, a feature of the Earth system absent from previous reanalyses. Also, in an effort to improve land surface hydrology, observations-corrected precipitation forcing is used instead of model-generated precipitation. Overall, MERRA-2 takes advantage of numerous updates to the global modeling and data assimilation system.

In this document, we summarize an initial evaluation of the climate in MERRA-2, from the surface to the stratosphere and from the tropics to the poles. Strengths and weaknesses of the MERRA-2 climate are accordingly emphasized.

TABLE OF CONTENTS

1. Introduction

Retrospective analyses (or reanalyses) integrate satellite-based data and conventional weather observations into a modeling framework to provide Earth system (e.g., atmospheric) datasets that are continuous in space and time. The concept of reanalysis was put forward more than 30 years ago, and NASA has since been involved at many levels. The first publicly available reanalysis from NASA was performed at 2°×2.5° resolution for 15 years with the GEOS-1 data assimilation system (Schubert et al., 1993; Pfaendtner et al. 1995). The results of that reanalysis helped guide system development for the GEOS-2 system. While there was no retrospective analysis performed with GEOS-2, both GEOS-3 and GEOS-4 provided customized reanalysis data products for NASA instrument teams and missions, such as CERES and EOS Aqua and Terra (see, for example, Figure 1-1).

With GEOS-5, a renewed effort was put forth to make a broadly disseminated reanalysis to support many of NASA's strategic elements. This reanalysis was called the Modern Era Retrospective analysis for Research and Applications, or MERRA (Rienecker et al. 2011). MERRA included a number of output variables unique among reanalyses, for example, complete vertically integrated budgets and 50m winds (for wind power generation). MERRA data have been widely used in the community; high quality reanalysis datasets are always in great demand. However, without a major effort to update the data assimilation, MERRA would not be able to assimilate the most recent instruments, meaning that the analysis would eventually degrade.

Analyses of MERRA data taught us much about the strengths and weaknesses of the GEOS-5 modeling and data assimilation system and suggested several key innovations for the system (discussed in Section 2) that could lead to an updated and improved reanalysis product: MERRA-2. MERRA-2 is envisioned to be a bridge toward a more fully coupled Earth system analysis. Not only does it take advantage of these innovations to provide better quality near real time data, it also allows us to evaluate them in preparation for future systems. Just as important, the development of MERRA-2 allows us to continue providing a near real-time product, given that the system underlying MERRA is becoming obsolete – it can no longer ingest many critical satellite radiances.

This technical memorandum is one of a series that provides a first look at MERRA-2's depiction of the Earth's climate and weather. Further information is provided by Molod et al. (2015) and Takacs et al. (2015a&b), who discuss some of the key changes imposed on the MERRA system to produce MERRA-2. Also, McCarty et al. (2015) describe the MERRA-2 analyzed observations, and Randles et al. (2015) evaluate the assimilated and interactive aerosol fields. The subjects in the present document's evaluation sections are diverse, ranging from the surface to the stratosphere and from the tropics to the poles. Nevertheless, this document represents only an initial evaluation – more time and effort is needed to fully expose the strengths and weaknesses of the MERRA-2 products. More complete evaluations are being prepared and submitted for peer-reviewed publication. This document is not intended to be the final word on the MERRA-2 climate, but rather, a starting point for further research.

Clouds, SLP and Surface Wind from Several NASA Reanalyses
00Z 14 MAR 1993

GEOS-1 (c. 1993)

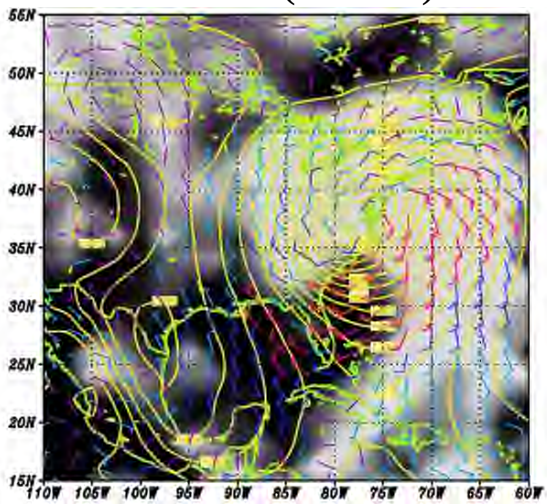

GEOS-4 (c. 2002)

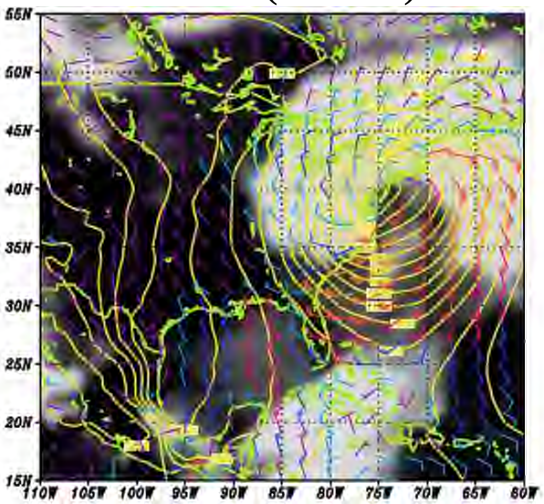

MERRA (GEOS-5.2, c. 2008)

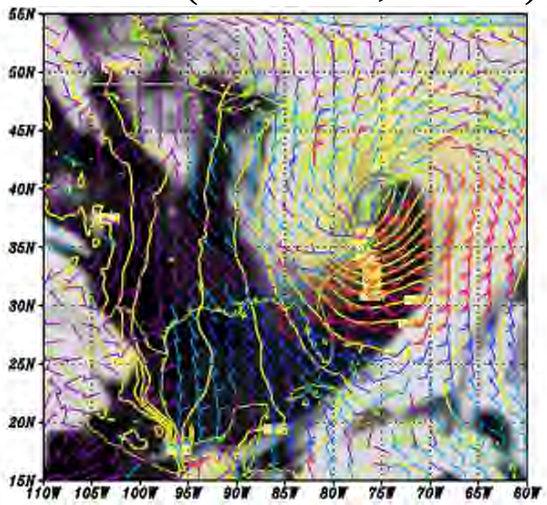

MERRA-2 (GEOS-5.12, c. 2014)

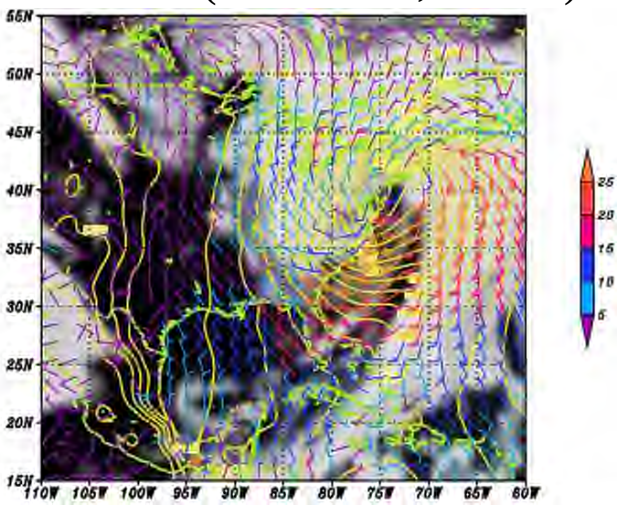

GOES-IR

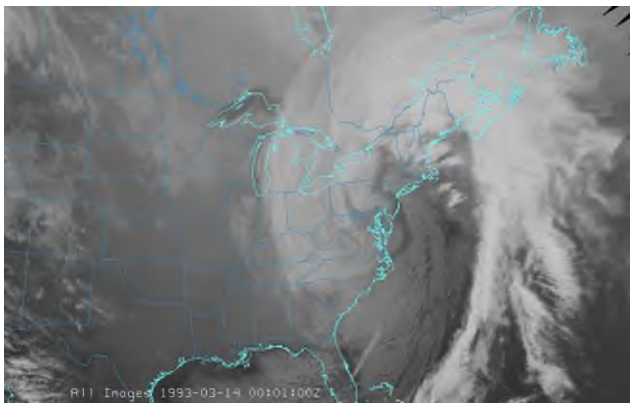

Figure 1-1 Examples of NASA reanalysis data for a significant winter storm, with GOES-IR for comparison.

2. MERRA-2 System Description

MERRA-2 is produced with version 5.12.4 of the Goddard Earth Observing System (GEOS-5.12.4) atmospheric data assimilation system. The key components of the system are the GEOS-5 atmospheric model (Reinecker et al. 2008; Molod et al. 2015) and the Gridpoint Statistical Interpolation (GSI) analysis scheme (Wu et al. 2002; Kleist et al. 2009b). The model uses the finite-volume dynamical core of Lin (2004) at a horizontal resolution of 0.5° × 0.625° in latitude and longitude, respectively, and 72 hybrid-eta levels from the surface to 0.01 hPa. The analysis is computed at the same spatial resolution as the atmospheric model using a three-dimensional variational (3DVar) algorithm based on the GSI with a 6-h update cycle and the so-called first-guess-at-appropriate-time (FGAT) procedure for computing temporally accurate observation-minus-background departures. The analysis is applied as a correction to the background state using an incremental analysis update (IAU) procedure (Bloom et al. 1996). The MERRA-2 system has many of the same basic features as the MERRA system (GEOS-5.2.0) described in Rienecker at al. (2011) but includes a number of important updates. These updates are summarized here for convenience, with most described in greater detail either later in this document or in the companion publications cited below.

a. Updates to the GEOS-5 model and GSI

Since MERRA, the GEOS-5 model has undergone substantial changes to both its dynamical core and its physical parameterizations. Whereas in MERRA the horizontal discretization of the model is computed on a latitude-longitude grid, MERRA-2 uses a cubed sphere grid (Putman and Lin 2007). This allows relatively uniform grid spacing at all latitudes and mitigates the more severe grid spacing singularities that occur on a latitude-longitude grid. Upgrades to the model's physical parameterizations include increased re-evaporation of frozen precipitation and cloud condensate, changes to the background gravity wave drag, and an improved relationship between the ocean surface roughness and ocean surface stress (Molod et al. 2015). The MERRA-2 model also includes a Tokioka-type trigger on deep convection as part of the Relaxed Arakawa-Schubert (RAS, Moorthi and Suarez 1992) convective parameterization scheme, which governs the lower limit on the allowable entrainment plumes (Bacmeister and Stephens 2011). A new glaciated land representation and a seasonally-varying sea ice albedo have been implemented, leading to improved air temperatures and reduced biases in the net energy flux over these surfaces (Cullather et al. 2014)..

The boundary conditions for sea surface temperature (SST) and sea ice concentration (SIC) in MERRA-2 differ from the 1° weekly (or monthly) product of Reynolds et al. (2002) used in MERRA. SST and SIC in MERRA-2 are derived from three sources: monthly 1° data as in Taylor et al. (2000) for the period prior to 1982, daily 1/4° data as in Reynolds et al. (2007) from 1982 thru March 2006, and daily 1/20° data from the Operational Sea Surface Temperature and Sea Ice Analysis (OSTIA) as in Donlon et al. (2012) from April 2006 onwards. The processing of these data into a unified and physically consistent gridded set of SST and SIC boundary conditions for MERRA-2 is described in Section 8a of this document.

Within the GSI there have been numerous updates since MERRA, including updates to the Community Radiative Transfer Model (CRTM, Chen et al. 2008) used for the assimilation of satellite radiances. MERRA-2 uses version 2.1.3 of the CRTM for assimilation of all satellite radiances, whereas MERRA uses a prototype version in combination with the Goddard Laboratory for Atmospheres TOVS forward model (GLATOVS, Susskind et al. 1983). Differences between the prototype and version 2.1.3 of the CRTM are too numerous to mention here, but a detailed description of the latter can be found in Liu and Boukabara (2014). Other updates to the GSI for MERRA-2 include the implementation of a new moisture control variable. The new variable is based on a normalization of the pseudo-relative humidity by the background error standard deviation; it has a more Gaussian error distribution than the non-normalized pseudo-relative humidity used in MERRA. Also within the GSI, a tangent linear normal mode constraint (TLNMC, Kleist et al. 2009a) is applied during the minimization procedure to control noise and improve the overall use of observations. The background error covariances in the GSI have undergone significant retuning since MERRA, in accordance with the various system upgrades during this interval.

Studies have documented the difficulty of maintaining realistic balances between variations in total mass and total water content in previous reanalyses (e.g., Trenberth and Smith 2005; Bosilovich et al. 2011; Robertson et al. 2011; Berrisford et al. 2011). In particular, analysis adjustments to moisture are often large (when, ideally they should be small), highly sensitive to changes in the observing system, and mostly balanced by unphysical changes in precipitation. Reconsideration of these issues during the development of MERRA-2 prompted modifications to GEOS-5 to conserve atmospheric dry mass and to guarantee that the net source of water from precipitation and surface evaporation equals the change in total atmospheric water. As described by Takacs et al. (2015), these changes include (i) the addition of sources and sinks of atmospheric water in the model continuity equation so that changes in total mass are driven purely by changes in total water, (ii) addition of a constraint to GSI that penalizes analysis increments of dry air, and (iii) a rescaling of the tendencies in the IAU so that the global mean is removed from the analysis increment of water. As shown in Section 6b, these changes indeed result in the dry mass being conserved in MERRA-2, as well as a significant reduction (relative to MERRA) in spurious changes in global precipitation associated with changes in the observing system.

b. Updates to the observing system

MERRA included no new satellite observation sources after the introduction of NOAA-18 in 2005. MERRA-2, in contrast, includes numerous additional satellite observations. The entirety of the input observations for MERRA-2 is described in McCarty et al. (2015). Notable additions compared with MERRA include: local bending angle observations from Global Positioning System radio occultation (GPSRO), polar orbiting microwave and infrared sounder radiances from NOAA-19, data from MetOp-A and -B including the hyperspectral Infrared Atmospheric Sounding Interferometer (IASI), and data from the Suomi National Polar-orbiting Partnership (NPP) including the Advanced Technology Microwave Sounder (ATMS) and hyperspectral Cross-track Infrared Sounder (CrIS). In addition, geostationary radiances from the Meteosat Second Generation (MSG) Spinning Enhanced Visible Infrared Imager (SEVIRI) are assimilated, as are retrieved temperature and ozone profiles from the Aura Microwave Limb Sounder (MLS) and retrieved total column ozone from the Aura Ozone Monitoring Instrument (OMI). As shown in

Figure 2-1, the number of assimilated observations in MERRA-2 grows from approximately 3 million in 2010 to almost 5 million per 6-h cycle in 2015, while MERRA assimilates approximately 1.5 million observations from 2002 onward. The GSI in MERRA-2 is also capable of assimilating microwave and hyperspectral infrared radiances from planned future satellites including MetOp-C and the Joint Polar Satellite System (JPSS).

MERRA-2 assimilates recalibrated versions of some of the satellite observation types used in MERRA. In MERRA-2, Remote Sensing Systems version 7 (RSS v7) recalibrated radiances and retrieved surface wind speeds from the DMSP Special Sensor Microwave Imager (SSM/I) are used, whereas MERRA uses RSS v6. The use of retrieved ozone from the Solar Backscatter Ultraviolet Radiometer (SBUV) also differs, with MERRA-2 assimilating version 8.6 on 21 layers from 1980 thru 2004 before switching to OMI and MLS in October 2004. In contrast, MERRA uses SBUV version 8 throughout, in a form degraded from its original 21 layers to 12.

c. Additional components

In addition to a standard meteorological analysis, MERRA-2 includes an aerosol analysis, as described in Randles et al. (2015). The (inline) MERRA-2 aerosol analysis represents a significant step toward a future integrated Earth system reanalysis and is a natural advancement from MERRAero, a previous offline aerosol analysis driven by MERRA meteorological forcing. The current system uses the GEOS-5 Goddard Aerosol Assimilation System (GAAS, Buchard et al. 2015) with the Goddard Chemistry, Aerosol, Radiation, and Transport (GOCART, Chin et al. 2002) model to analyze five aerosol species (15 total tracers) including black and organic carbon, dust, sea salt and sulfates. The analysis is produced at 3-h intervals, with assimilation of bias-corrected aerosol optical depth (AOD) from several ground- and satellite-based sensors including the Advanced Very High Resolution Radiometer (AVHRR), Moderate Resolution Imaging Spectroradiometer (MODIS), Multi-angle Imaging Spectroradiometer (MISR) over bright surfaces, and the Aerosol Robotic Network (AERONET). The aerosol lifetimes are driven by prescribed sea-surface temperature and sea-ice, daily volcanic and biomass burning emissions, and high-resolution inventories of anthropogenic emission sources. The analyzed aerosols affect the meteorology of MERRA-2 through direct radiative coupling with the GEOS-5 model dynamics.

As in MERRA, MERRA-2 land surface estimates utilize no directly assimilated land surface observations, reflecting instead the time integration of surface meteorological conditions by the GEOS-5 land model. Precipitation is generated by the atmospheric model during the IAU segment of the assimilation procedure and, over land especially, is subject to considerable errors that can propagate into land surface hydrological fields and beyond (Reichle et al. 2011). To mitigate these effects in MERRA-2, observation-corrected precipitation estimates are applied as part of the land surface forcing and to modulate the wet deposition of aerosols over land and ocean. The generation and use of the observation-corrected precipitation estimates are described in Reichle and Liu (2014). Generally speaking, the estimates are derived from publicly available, observationally based global precipitation products disaggregated from daily or pentad totals to hourly

accumulations using precipitation estimates from MERRA[1]. The land surface in MERRA-2 sees a combination of corrected and model-generated precipitation depending on latitude, with the land surface forced primarily by the corrected estimates at low to mid-latitudes, by its own, model-generated precipitation at high latitudes, and by a weighted mixture in between to prevent spatial discontinuities in climatological means. It should be noted that the atmospheric water and energy prognostic variables associated with the creation of precipitation in MERRA-2 are not directly modified by the corrected estimates although they can be indirectly modified through subsequent feedback with the land surface. MERRA-2 is one of several recent applications of GEOS-5 that uses observation-corrected precipitation estimates, including the GMAO's seasonal forecasting system (Ham et al. 2014), the MERRA-Land data product (Reichle et al. 2011), and MERRAero.

Finally, a bias correction scheme for aircraft temperature observations has been implemented in MERRA-2, motivated by the known warm bias of these measurements compared with other data sources (Cardinali et al. 2003, Dee and Uppala 2009; Rienecker et al. 2011). The scheme uses the mean observed-minus-background departures to estimate the bias for temperature reports from individual aircraft, identified by their tail number. The bias estimates are updated after each analysis. The scheme is used to correct Aircraft Meteorological DAta Relay (AMDAR) and Aircraft Communications Addressing and Reporting System (ACARS) reports only, since other sources of aircraft observations in MERRA-2 do not have unique identifiers by which they can be tracked. As of 2015, bias corrections for approximately 3700 separate aircraft are tracked in MERRA-2. The performance of the scheme is discussed in McCarty et al (2015). In general, it is found that the corrections tend to be relatively stable for long periods and across the different MERRA-2 processing streams but can show large changes when the bias characteristics of the observations suddenly change. The scheme is, however, designed to adjust to such changes in bias.

[1] In the event that MERRA were no longer available, estimates from an alternate source would be used, such as the GMAO's near real time forecast system.

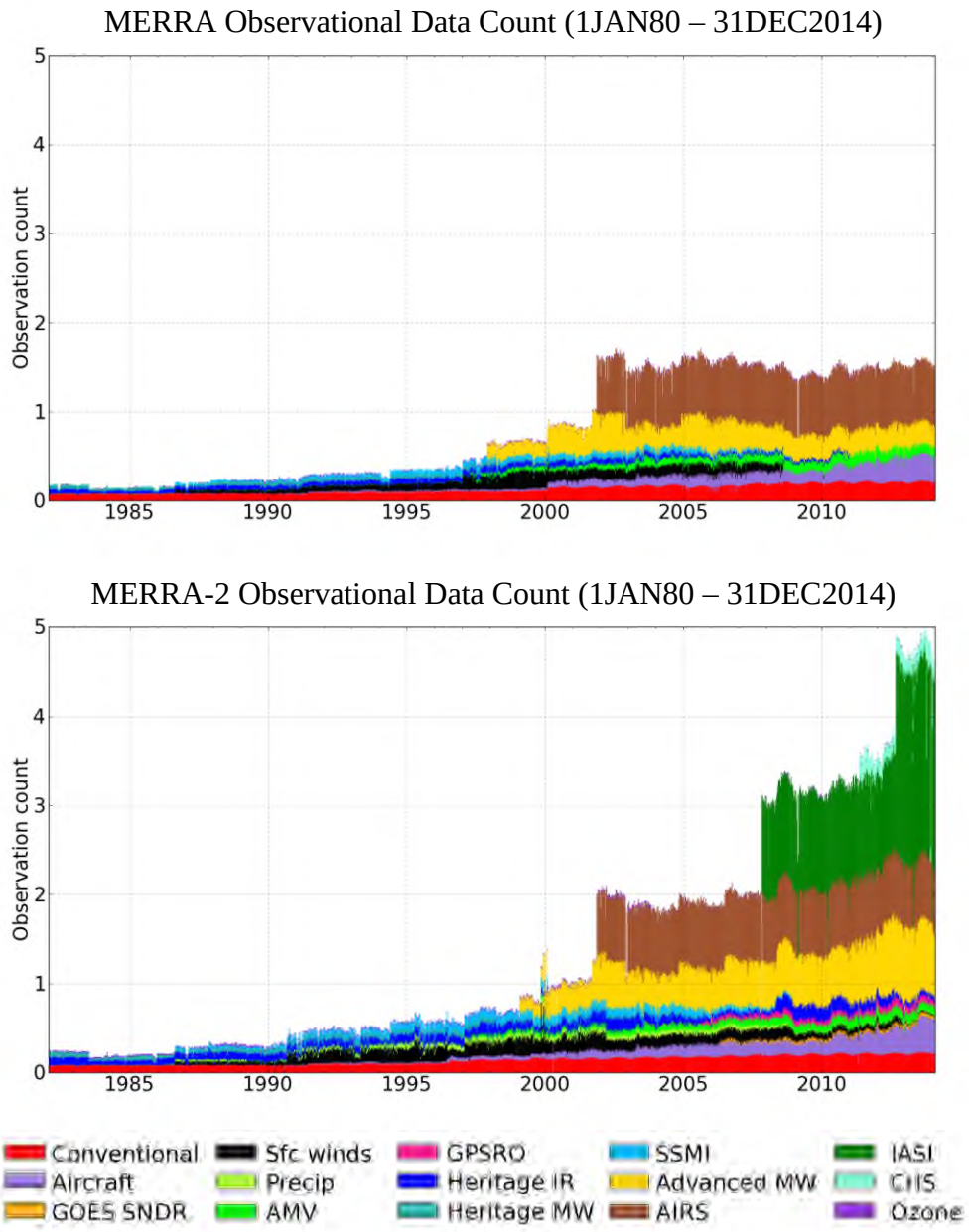

Figure 2-1 Time series of assimilated observations in MERRA (top) and MERRA-2 (bottom) for the period 1 January 1980 thru 31 December 2014. Units are millions per 6 hours.

3. Climate State (T, U, V and Q)

The seasonal behavior of the MERRA-2 mean state is presented and compared to the corresponding fields from MERRA (Rienecker et al., 2011) and ERA-Interim (Dee et al., 2011). The comparisons generally entail examination of annual means from the three reanalyses. The examination of the mean seasonal state includes the zonal and meridional wind fields, mass streamfunction, temperature and relative humidity. The velocity potential at 200 hPa is shown as an indicator of the divergence aloft associated with diabatic heating, and the eddy height at 300 hPa is shown to assess the characterization of the stationary waves.

a. Zonal Wind and Temperature

The annual average of the zonal mean zonal wind field is shown in Figure 3-1 and Figure 3-2. In each figure, the top panel shows the MERRA-2 result, the middle panel shows either the MERRA (Figure 3-1) or the ERA-Interim result (Figure 3-2), and the bottom panel shows the difference. The MERRA-2 zonal wind field is well constrained by observations outside of the tropics, just as in other reanalyses (Rienecker et al. 2008), and differences there among the different reanalyses are generally quite small, as can be seen by the resemblance between the MERRA-2 (top) and other reanalysis (middle) fields in both figures. The largest extratropical differences between the MERRA-2 zonal wind and either reanalysis are up to 20% of the wind speed poleward of 60S throughout the troposphere. In the tropics, where the wind is not as well constrained by observations, there are larger differences among the three reanalyses, in particular near the tropical tropopause, on the order of the magnitude of the zonal winds there.

The MERRA-2 zonal winds poleward of 60S and near 150 mb in the tropics both exhibit temporal trends that necessitate a closer examination of the differences among the three reanalyses. Figure 3-3a shows the time series of the zonal mean zonal wind at 72S and 400 mb (the region of maximum difference between MERRA-2 and MERRA) along with the linear trend line for MERRA-2 and MERRA, wind fields. There is an abrupt change in behavior in 1997, bringing the MERRA-2 winds into closer agreement with MERRA (and the other reanalyses, not shown here) in the latter part of the time period. This abrupt change may reflect the influence of the surface wind observing system used in the early part of MERRA-2. At 150 mb at the equator (Figure 3-3b-d) there is also an abrupt change in the character of the MERRA-2 zonal wind in the year 2000 bringing the MERRA-2 zonal wind into closer agreement with both MERRA and ERA-Interim.

The annual mean zonal mean temperature fields are shown in Figure 3-4 and Figure 3-5. In general the MERRA-2 temperatures are within 1K of MERRA and ERA-Interim temperatures, as seen in the bottom panels of the figures. There are differences of up to 0.6 K between MERRA-2 (MERRA-2 is warmer) and either MERRA or ERA-Interim in the middle to upper troposphere in the tropics. Unlike the differences seen in the zonal wind field, this temperature difference is more systematic and constant in time. This excessive warming in MERRA-2 is consistent with additional radiative heating related to excessive tropical cloud cover (see Section 5), or it might result from the choice of observational error estimates that are smaller than those in MERRA. There are larger differences between MERRA-2 (and MERRA) and ERA-Interim near the tropical

tropopause, but the MERRA-2 values are more in line with other estimates (see the middle panel of Figure 3-6), suggesting that perhaps the MERRA-2 tropical tropopause is well placed relative to ERA-Interim.

b. Meridional Wind and Mass Streamfunction

Figure 3-7 and Figure 3-8 compare the annual mean meridional wind fields from each of the three reanalyses. The annual mean field shows a signature of the boreal winter positive meridional wind aloft in the northern hemisphere as well as the signature of the boreal summer negative meridional wind aloft in the southern hemisphere. There is good general agreement among the reanalysis estimates in terms of magnitude and location of wind maxima (the top and middle panels in both figures look similar). Relative to MERRA, the MERRA-2 northern hemisphere meridional winds in both the diverging and converging branches of the Hadley cell are displaced equatorward. This brings MERRA-2 into closer agreement with ERA-Interim (Figure 3-8) with respect to the latitude of the maximum wind. In general the MERRA-2 meridional wind is stronger than that in ERA-Interim, as shown in the bottom panel of Figure 3-8, where the sign of the difference is opposite to the sign of the wind field itself. Figure 3-9a,b show the annual mean zonally integrated mass streamfunction, a measure of the strength of the Hadley circulation, from MERRA-2 and MERRA, respectively. The Hadley cell is stronger and displaced equatorward in MERRA-2 in the northern hemisphere, associated with the equatorward position of the maximum meridional wind field.

c. Eddy Height

The northern hemisphere wintertime stationary wave pattern of MERRA-2 is evaluated with the December-January-February (DJF) eddy geopotential height field at 300 hPa, shown in comparison to the MERRA field in Figure 3-10. A dominant feature is the Pacific-North-America (PNA) pattern, the series of troughs and ridges spanning the north Pacific basin. The PNA pattern, along with the other features of the stationary wave pattern in DJF, is indistinguishable between MERRA-2 and MERRA, and the pattern also matches that in the ERA-Interim eddy height field (not shown).

d. Velocity Potential

The annual mean 200 hPa velocity potential (χ) field for MERRA-2 is shown in Figure 3-11 as compared to MERRA. The gradients of χ represent the divergent part of the flow and reflect the response to diabatic heating aloft due primarily to convection and radiative cloud forcing. The velocity potential pattern in MERRA-2 (top panel of Figure 3-11) is dominated by the outflow in the western Pacific associated with the Australian and Asian monsoons and the warm pool convection, and there is good agreement with the MERRA field.

e. Humidity

The annual relative humidity (RH) fields from MERRA-2, MERRA and ERA-Interim are shown in Figure 3-12 and Figure 3-13. The differences in relative humidity between MERRA-2 and MERRA (Figure 3-12, bottom panel) are dominated by the general behavior of MERRA-2 to show

higher relative humidity, almost everywhere at every level in the troposphere. This is also the case for the specific humidity (not shown), so the differences are not primarily temperature-related. This difference is associated with the behavior of the underlying version of the GEOS-5 AGCM; the increased moisture in the AGCM version used for MERRA-2 was shown by Molod et al (2015) to result from the increased re-evaporation of snowfall. As shown in Figure 3-13, the MERRA-2 relative humidity is closer to ERA-Interim estimates than to MERRA, although MERRA-2 is still more humid than ERA-Interim in the upper troposphere.

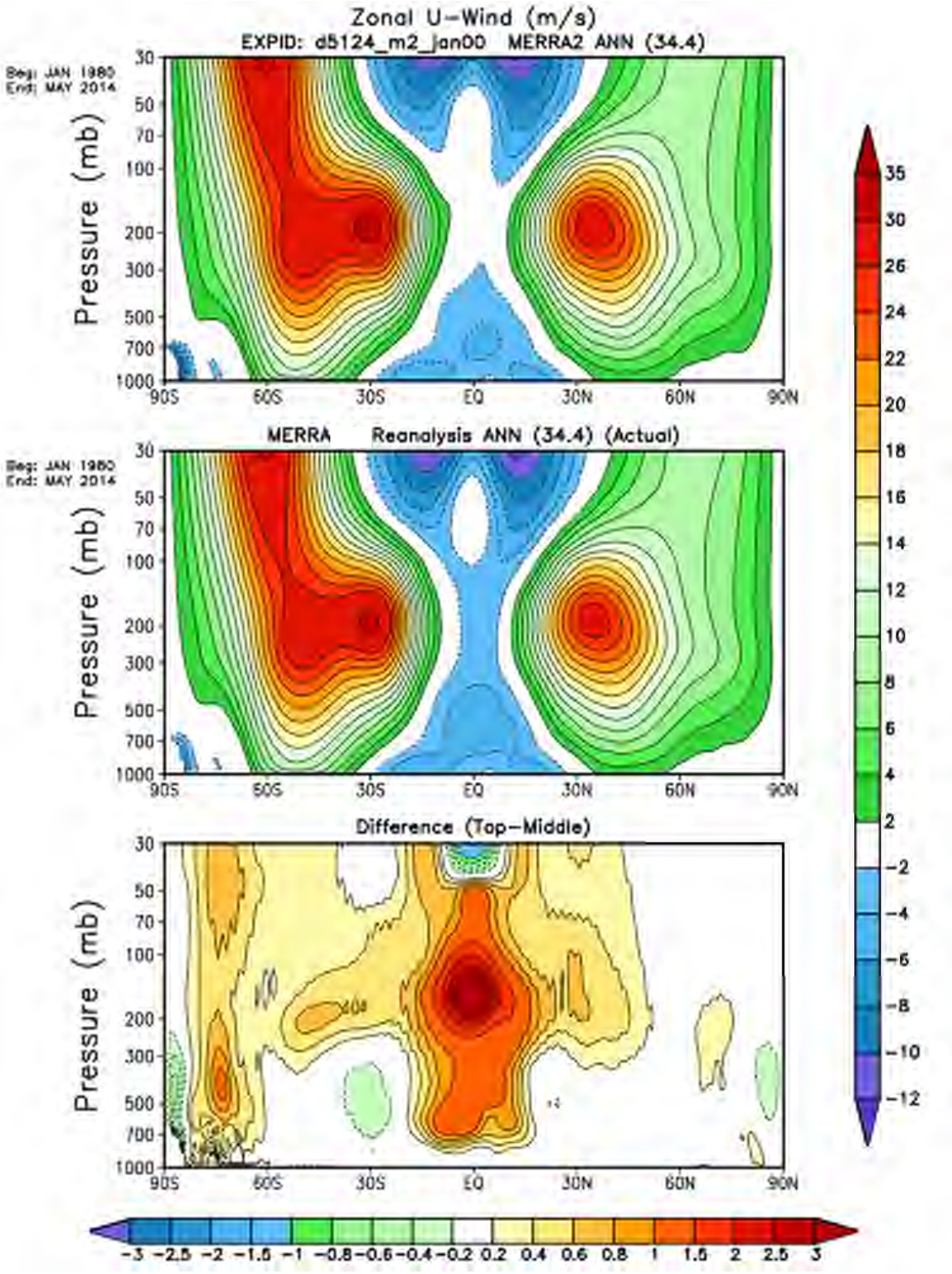

Figure 3-1 Climate mean zonal average of the zonal wind for MERRA-2 (top), MERRA (middle) and their difference (bottom). The means have a contour interval of 2ms^{-1}, while the difference has a contour interval of 0.2ms^{-1}.

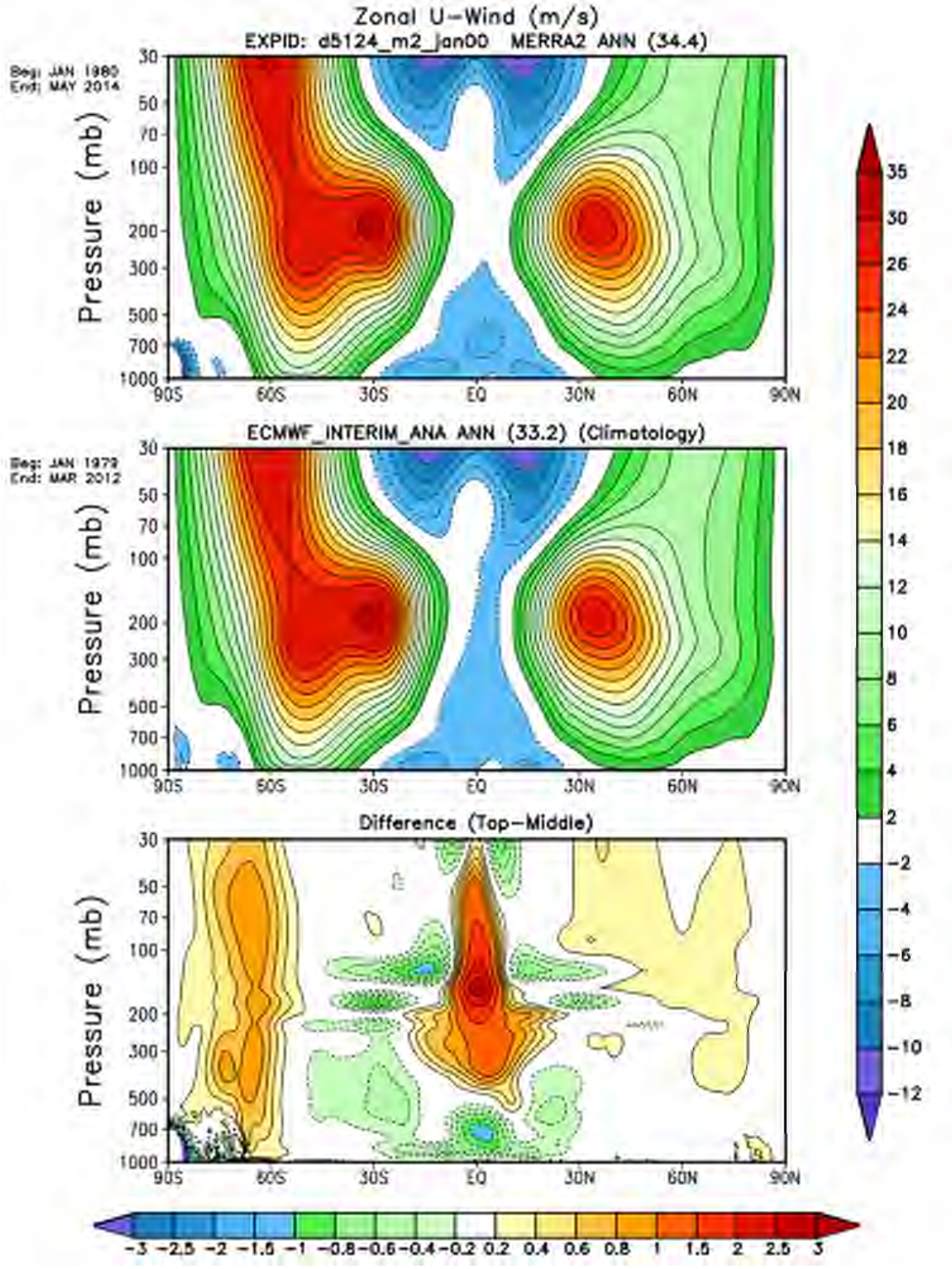

Figure 3-2 As in Figure 3-1, except for comparing MERRA-2 to ERA-Interim.

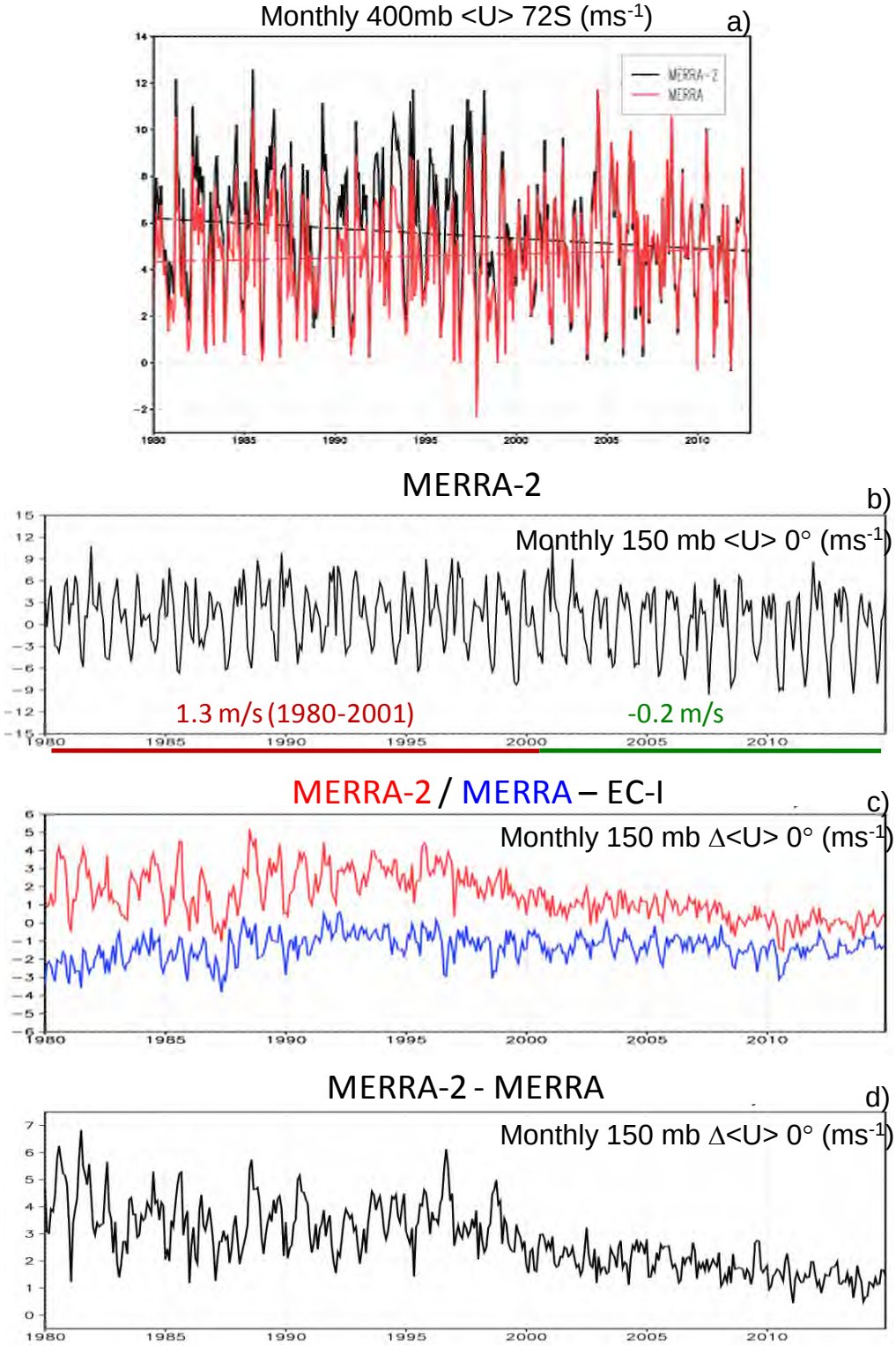

Figure 3-3 Monthly mean zonal average of the zonal winds at (a) 400mb 72S, (b) 150 mb equator, (c) differences of MERRA-2 and MERRA from ERA-Interim at 150mb equator and (d) the differences between MERRA-2 and MERRA at 150mb equator. Units are ms^{-1}.

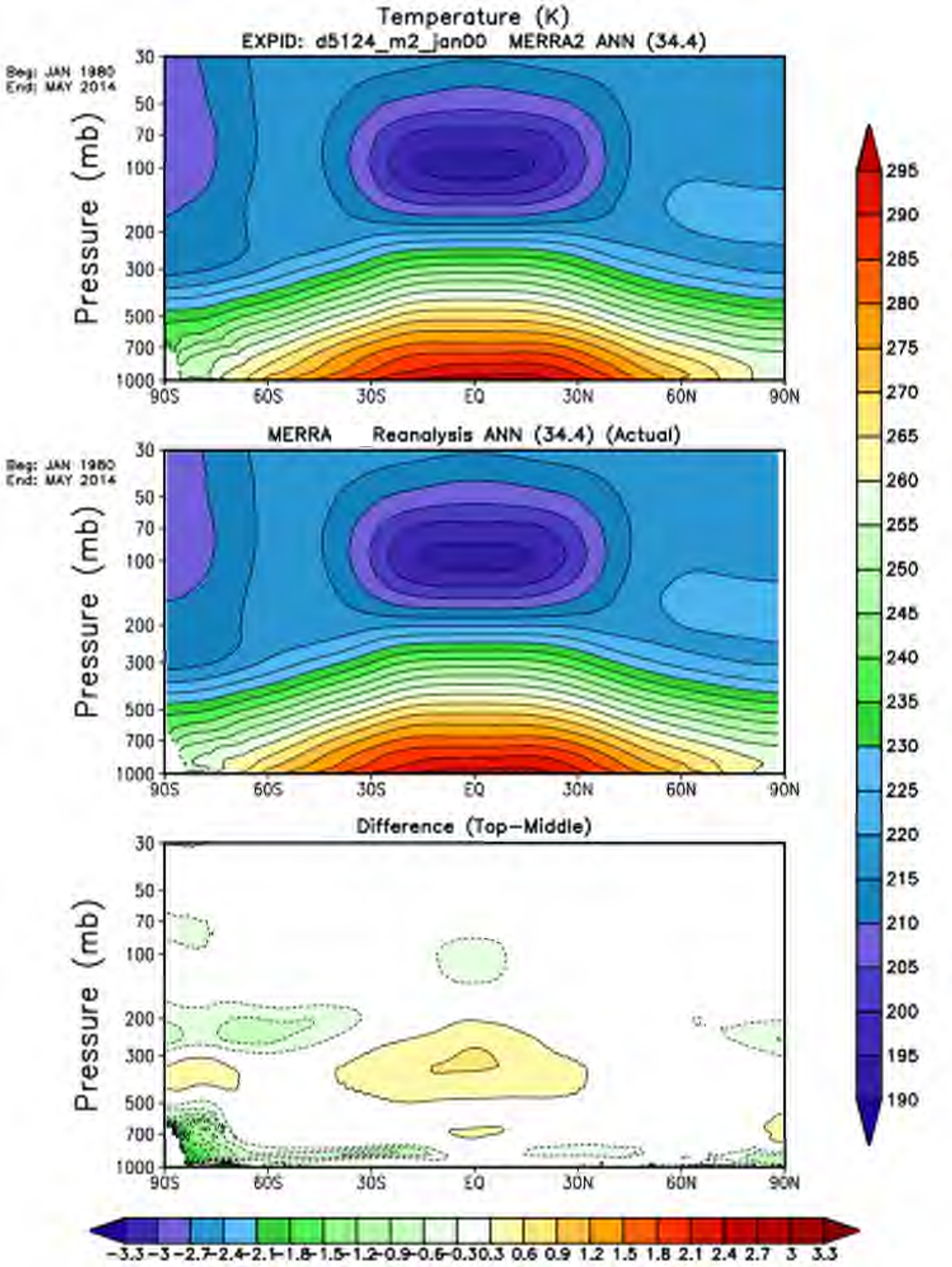

Figure 3-4 Climate mean zonal average of the temperature for MERRA-2 (top), MERRA (middle) and their difference (bottom). The mean plots have a contour interval of 5K, while the difference plot has a contour interval of 0.3K.

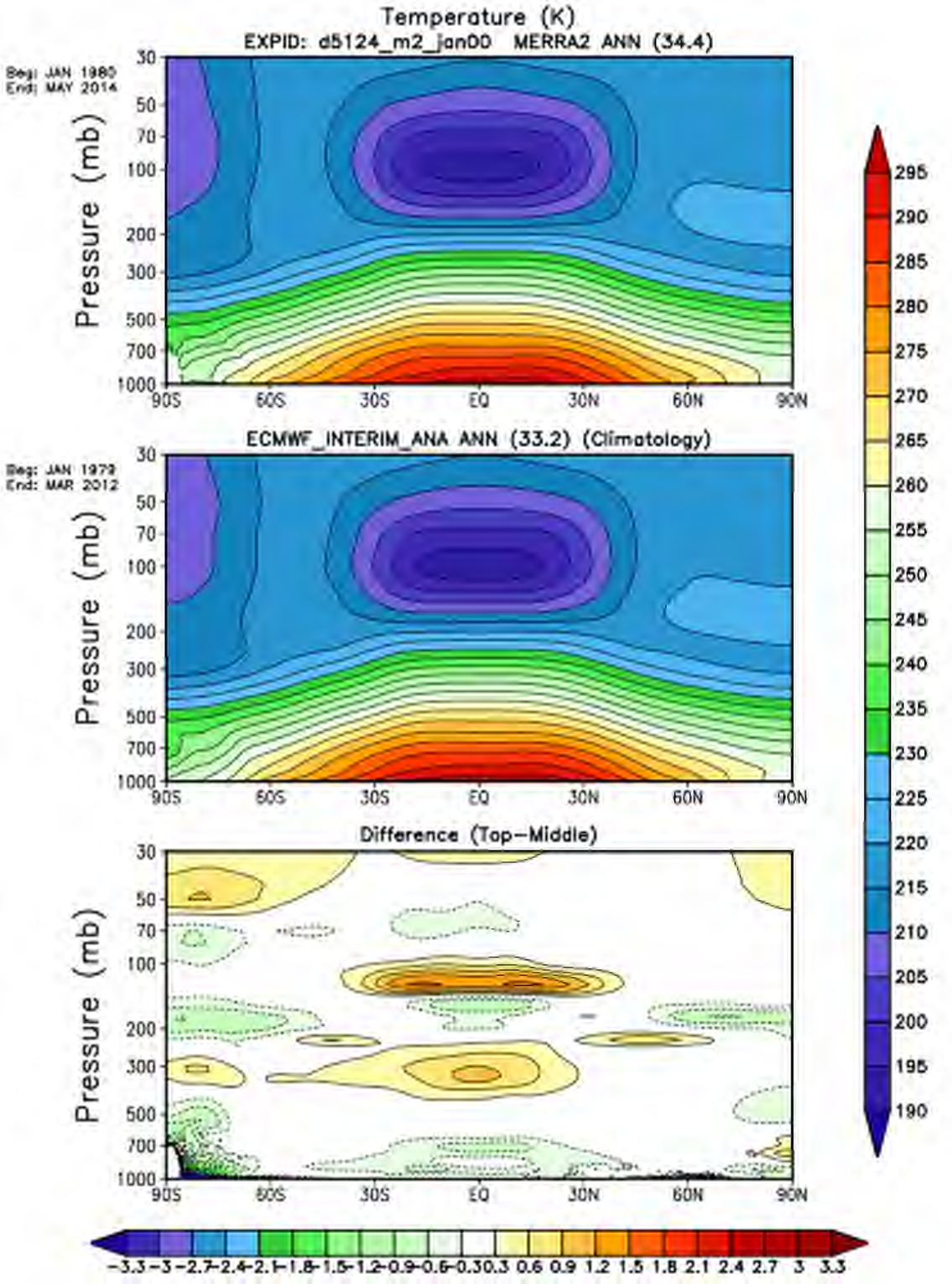

Figure 3-5 As in Figure 3-4, except for comparing MERRA-2 to ERA-Interim.

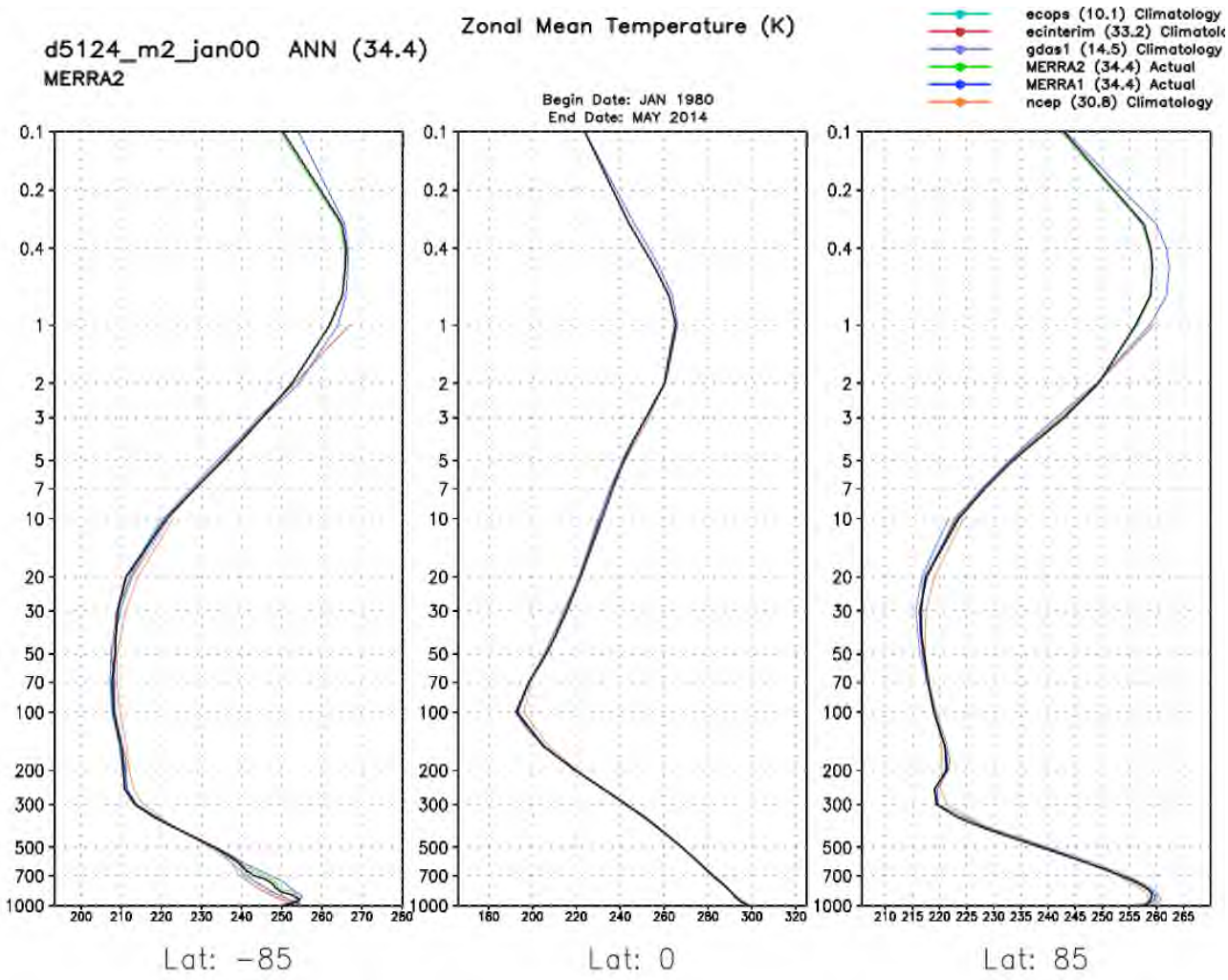

Figure 3-6 Zonal mean temperature profiles at the labeled latitude for each of the analysis climatologies listed in the legend. The number in parentheses in the legend shows the number of years that make up that climatology.

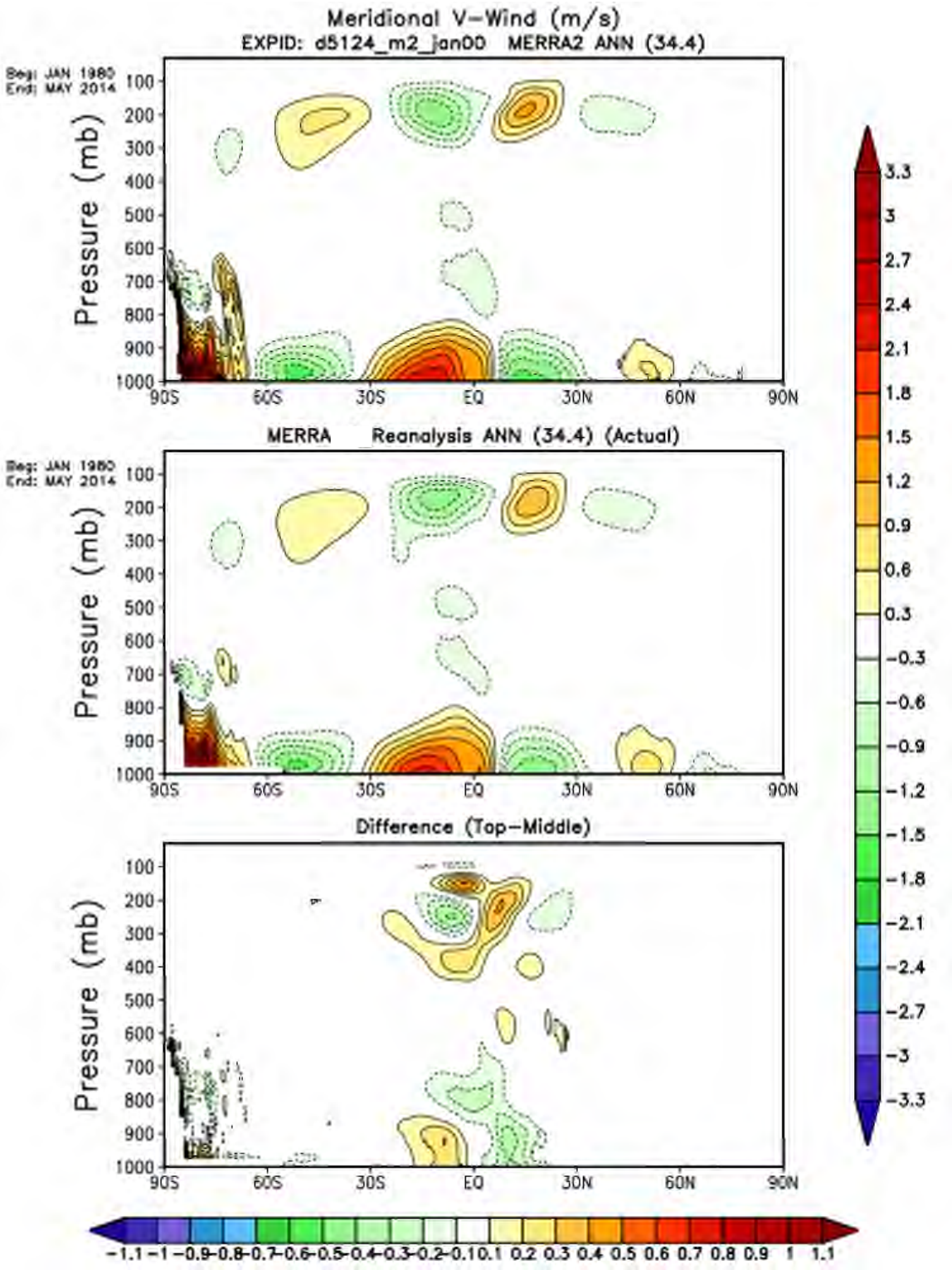

Figure 3-7 Climate mean zonal average of the Meridional wind for MERRA-2 (top), MERRA (middle) and their difference (bottom). The mean plots have a contour interval of 0.3ms^{-1}, while the difference plot has a contour interval of 0.1ms^{-1}.

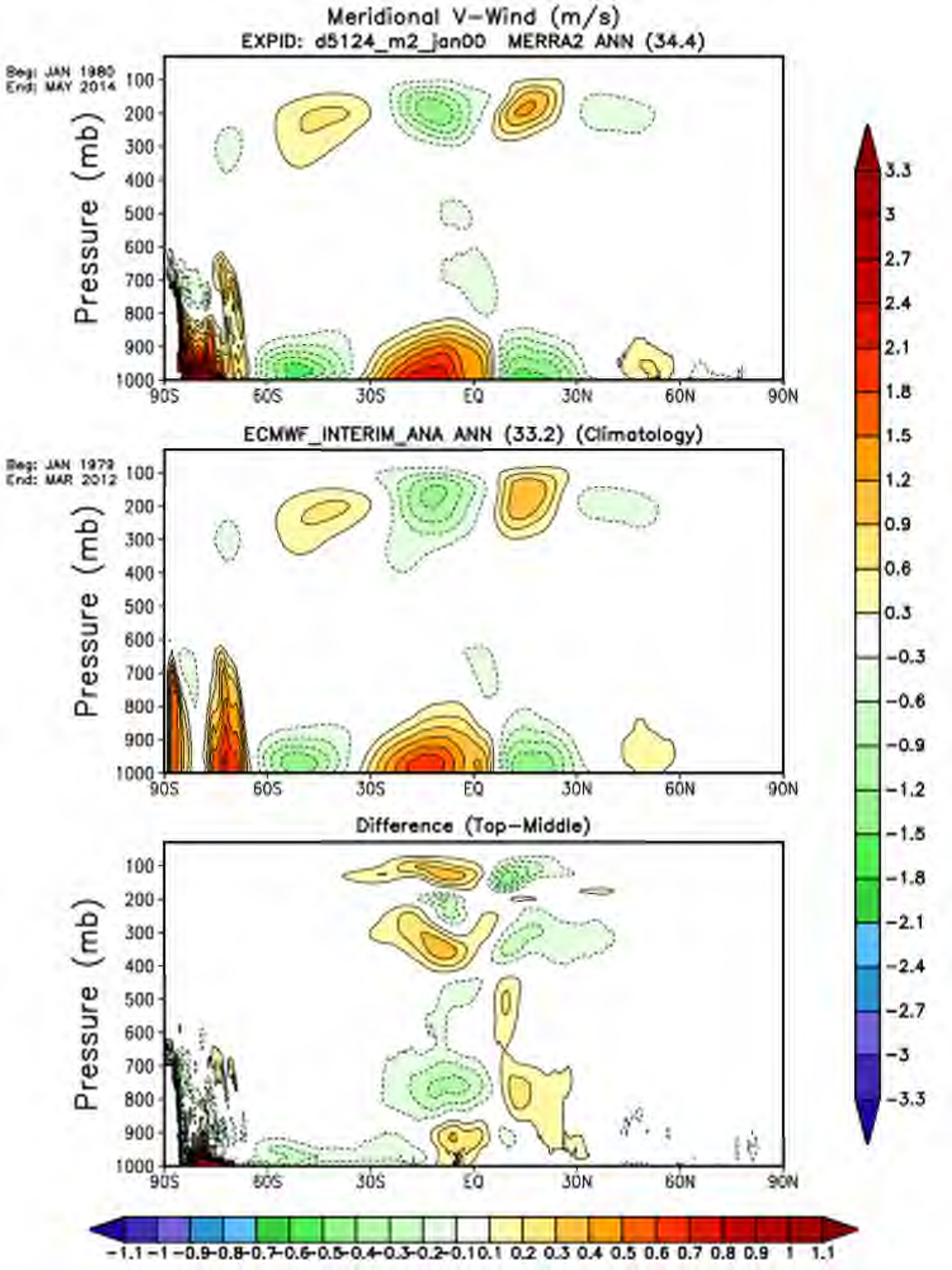

Figure 3-8 As in Figure 3-7, except for comparing MERRA-2 to ERA-Interim.

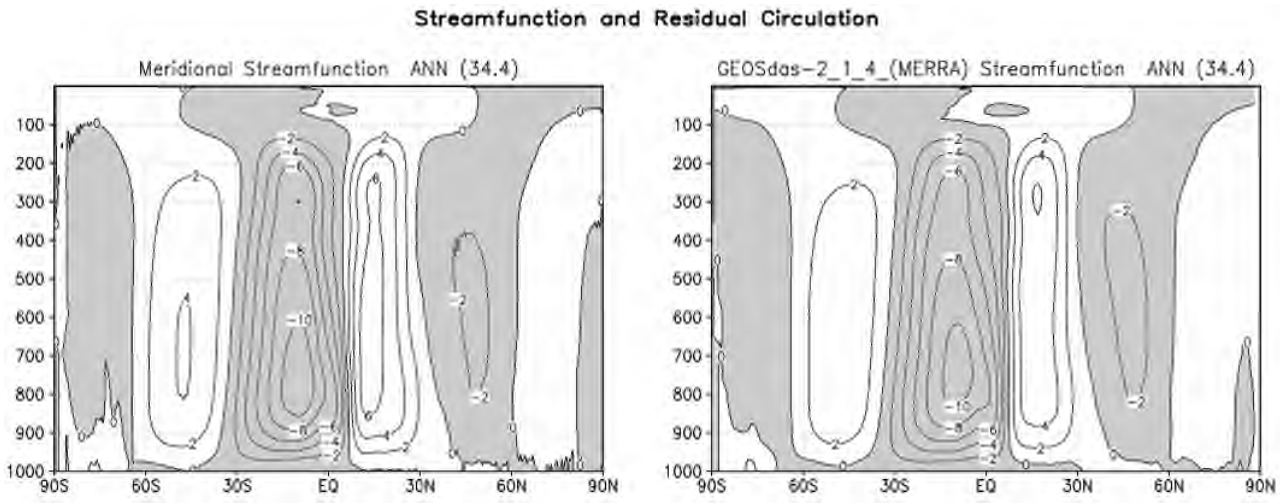

Figure 3-9 Zonal average meridional streamfunction for MERRA-2 (top left) and MERRA (top right).

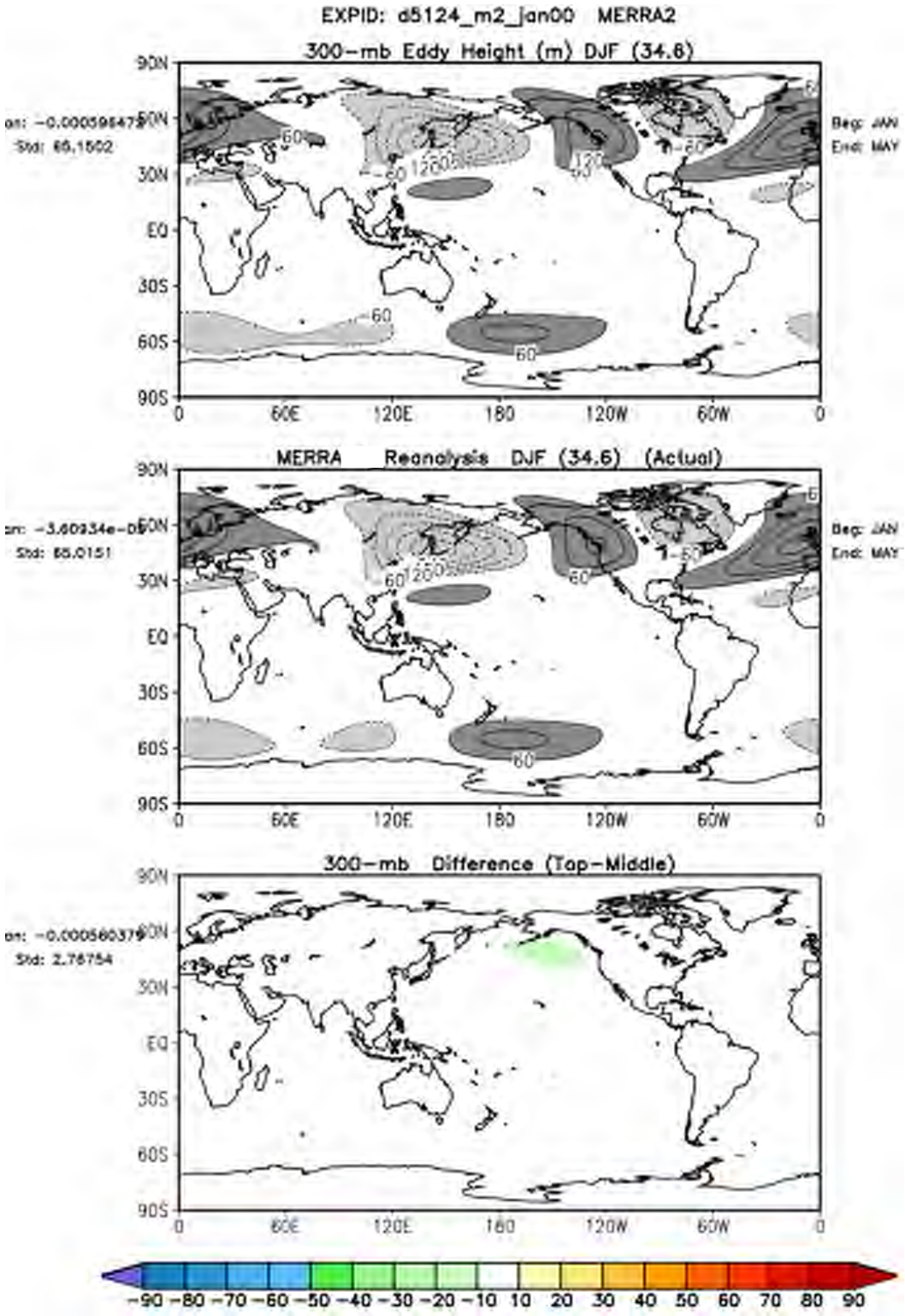

Figure 3-10 Climate mean of the 300mb Eddy height (geopotential height field with the zonal mean removed) for MERRA-2 (top), MERRA (middle) and their difference (bottom). The mean plots have a contour interval of 60m, while the difference plot has a contour interval of 10ms^{-1}.

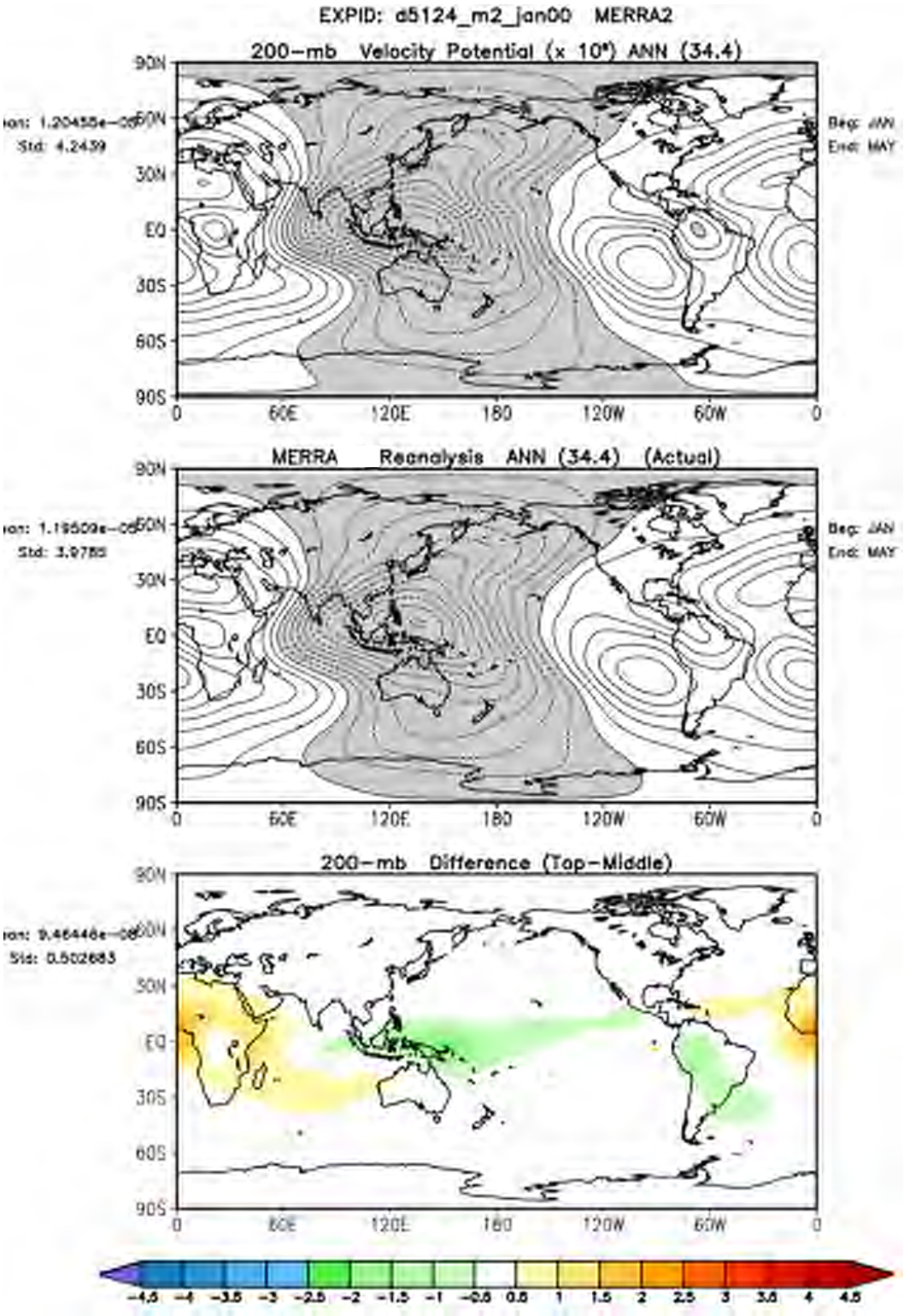

Figure 3-11 Climate mean of the 200mb Velocity Potential (m^2s^{-1}) for MERRA-2 (top), MERRA (middle) and their difference (bottom).

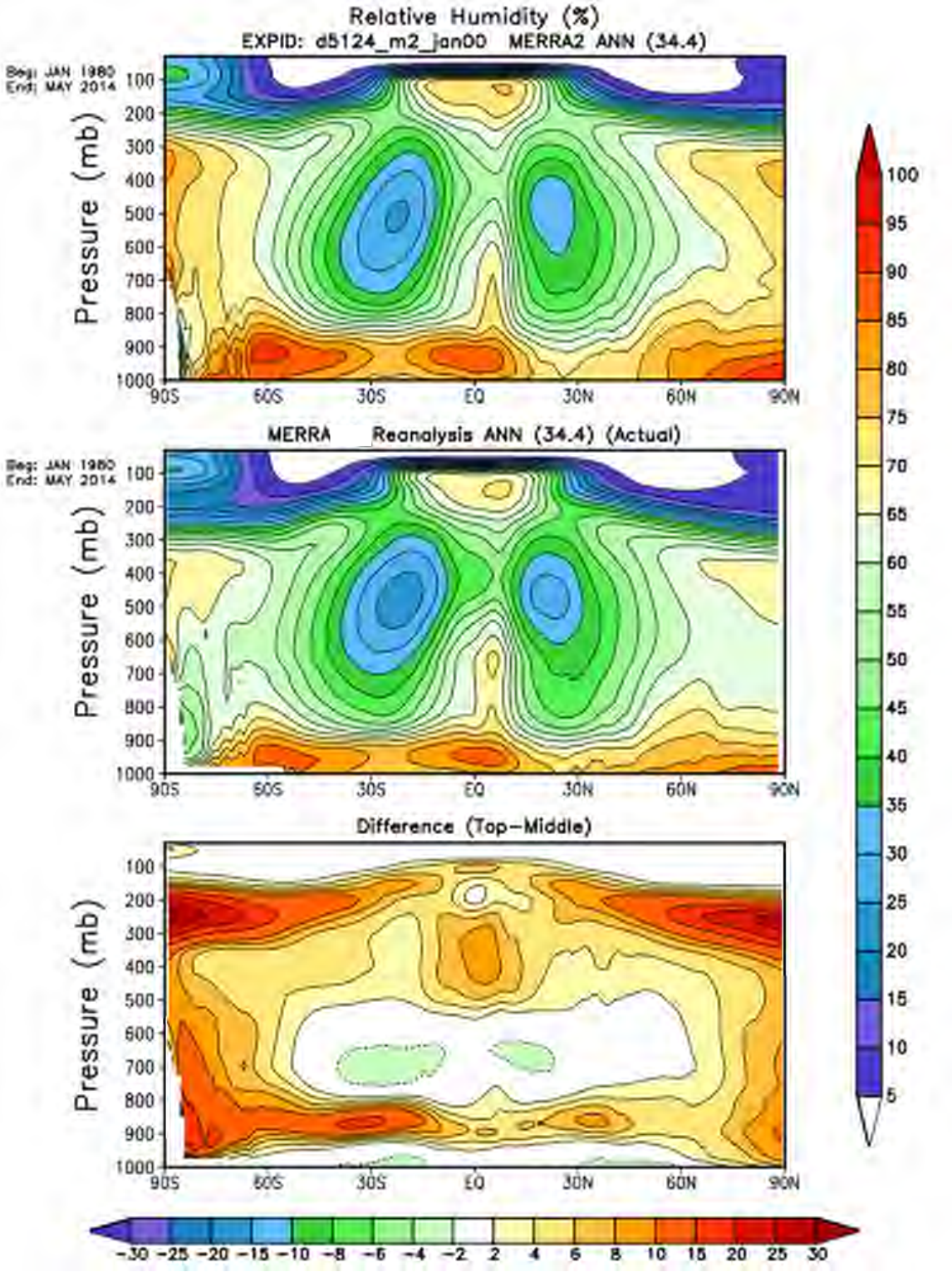

Figure 3-12 Climate mean zonal average of the relative humidity for MERRA-2 (top), MERRA (middle) and their difference (bottom). The mean plots have a contour interval of 5%, while the difference plot has a contour interval of 2%.

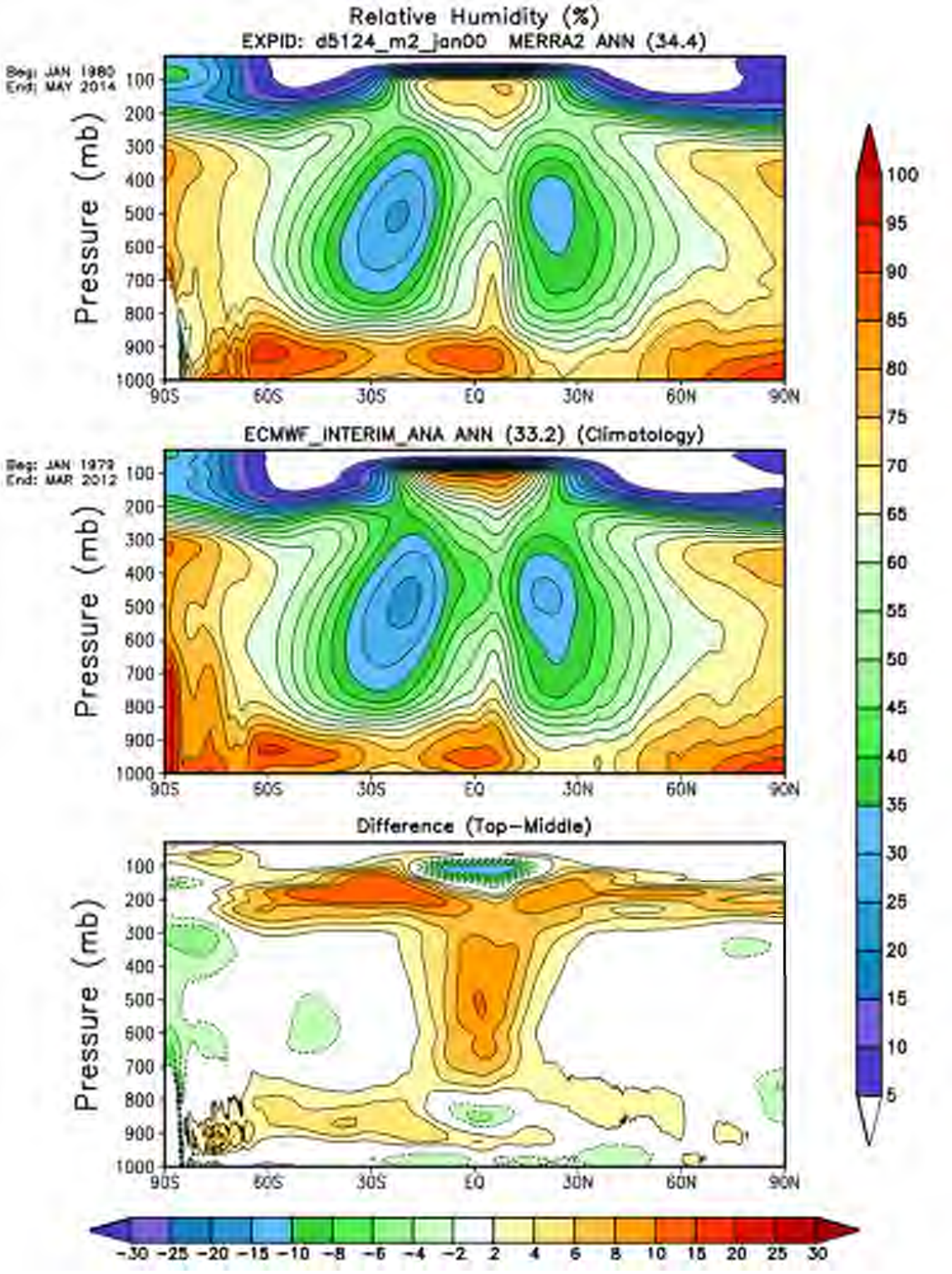

Figure 3-13 As in Figure 3-12, except for comparing MERRA-2 to ERA-Interim.

4. Global Energy Budget

a. Global Area Average Energy Flows

The net heating and cooling of the Earth is a primary contributor to the climate and how it changes (Trenberth et al. 2015; Loeb et al. 2009). The energy balance for models can be complicated by the prescribed SSTs that do not change with the surface fluxes, and even more so in reanalyses where the atmospheric analysis also adds or removes heat, based on the forecast departure from observations. Here, we provide a global average MERRA-2 energy budget compared to a recent assessment developed by the NASA Energy and Water Cycle Studies (NEWS) program. The NEWS energy budget (L'Ecuyer et al. 2015) was developed with input from a vast array of NASA observations (2000-2010) and analyses (analyses were used minimally and only out of necessity). However, these data were combined with uncertainty estimates, which were then used to aid in closing the energy budget and the water budget together. We also compare these fluxes with those of MERRA, as a benchmark.

Table 4-1 Energy budget terms from the NEWS integrative project (L'Ecuyer et al. 2015), which includes the original collected data and a balanced budget with uncertainties (e), alongside MERRA-2 and MERRA for the period of 2000-2010. Not included in the table are the atmospheric heating rates from MERRA and MERRA-2 analysis increments, which are 6.8 and -2.4 Wm^{-2}, respectively. Units are Wm^{-2}.

Budget Term		Original	e	Constrained	e	MERRA-2	MERRA
Incoming Solar	F	340	± 0.5	340	± 0.5	340	341
Outgoing Shortwave	OSR	100	± 5.0	98	± 2.0	106	100
Outgoing Longwave	OLR	238	± 2.0	239	± 2.0	238	242
Downwelling LW at SFC	LW↓sfc	344	± 7.0	339	± 4.0	332	331
Downwelling SW at SFC	SW↓sfc	190	± 6.0	187	± 3.0	186	193
Surface Emitted	LW↑sfc	398	± 6.0	400	± 4.0	394	394
Surface Reflected	SW↑sfc	22	± 2.0	22	± 1.0	23	24
Sensible Heating	SH	21	± 5.0	23	± 3.0	19	18
Precipitation LH	LvP	77	± 7.0	80	± 4.0	87	81
Evaporation LH	LvE	75	± 7.0	80	± 4.0	86	76
Surface Heat Storage	Net Abs.	0.6	± 0.4	0.91		-4.5	11.4

Table 4-1 shows the energy budget terms with uncertainties from NEWS (before and after uncertainty constraints are introduced), MERRA-2 and MERRA. The first, and perhaps most noticeable, bias in the MERRA-2 fluxes is reflected top-of-atmosphere (TOA) shortwave radiation. This leads to too much energy leaving the Earth at the top of atmosphere, about -4-5Wm^{-2} during the 2000s. This will be discussed further in the cloud radiative effects section. In both MERRA systems, the downwelling radiation at the surface is underestimated while the net surface shortwave radiation matches the constrained values well. In MERRA-2, there are regions of increased precipitation where MERRA was biased low. There are some regions where excessive precipitation occurs. The regional evaluation of MERRA-2 precipitation and evaporation is in

Section 6. The global surface imbalance in MERRA-2 is improved over that in MERRA, and also the mean heating from the analysis is smaller in MERRA-2 than in MERRA (a positive result). These points will be discussed further in this section.

b. Temporal Variability

Figure 4-1 shows the time variation of the global mean top of atmosphere energy terms, comparing MERRA-2 with MERRA, other reanalyses and the Allan et al. (2014) Natural Environment Research Council (NERC) reconstructed TOA Fluxes. All of the reanalyses have some variations that do not agree with these observations. While there may be some slight improvement in MERRA-2 compared to MERRA, the decreasing absorbed shortwave trend, around the time of the 1991 eruption of Mt. Pinatubo, leads to an excessive heat loss to space. Figure 4-2 shows the radiative effects from clouds and aerosols separately, indicating that the decreasing trend in absorbed shortwave is more related to cloud effects. The next section will discuss further the effects of clouds on MERRA-2 radiation. The aerosol effects of the major volcanic eruptions on the TOA radiation are obvious and agree with the radiation observations. CFSR also includes interactive aerosols, but not the aerosol assimilation (Saha et al. 2010). Randles et al (2015) provide the details of the aerosol assimilation in MERRA-2. MERRA-2's OLR variability compares well with the observations having one of the smallest global mean biases.

At the surface, a signal similar to MERRA-2's TOA reflected shortwave is apparent in the incoming surface shortwave (Figure 4-3a). MERRA-2's global surface reflected shortwave is lowest of all the reanalyses, but perhaps more comparable to the available observations (Figure 4-3b). As noted earlier, MERRA and MERRA-2 both underestimate the surface longwave radiation components in the global average. Note that the interannual variability seems to be quite similar among all the reanalyses (Figure 4-3c-d). Surface evaporation exhibits temporal variations related to the SST variability but also to some relevant observing systems (Figure 4-3e); this will be expanded on in Section 6. Likely, some of the issues that influence evaporation are also influencing the sensible heat variability.

c. Spatial Variability

While the global averages and time series provide a mean sense of the radiative fluxes, these means often reflect the large biases of specific regions. For example, biases can differ significantly over the tropical oceans, land and cryosphere. Figure 4-4 to Figure 4-6 show the mean radiation (2000-2014) for MERRA-2, CERES EBAF and their difference for TOA and surface longwave and shortwave components of the radiative fluxes.

MERRA-2 underestimates the outgoing longwave radiation in the warm pool, a common problem among reanalyses. Underestimated OLR occurs in the Inter-America Seas (Figure 4-4), though it is noted that precipitation here has improved substantially from MERRA (Figure 6-3). As mentioned previously, not enough of the incoming shortwave radiation is absorbed globally, but here we see the TOA reflected shortwave radiation is overestimated in the warm pool. Reflected energy from clouds seems to be a factor here. Interestingly, over the midlatitude continents, reflected shortwave is underestimated. Cloud radiative effects will be discussed in Section 5. The

large negative bias in global surface downwelling longwave radiation is mainly related to Northern Africa across the Middle East and into Asia (Figure 4-5). In addition, significant deficits in Antarctica and broad smaller underestimates across the oceanic midlatitude storm track regions contribute to the global underestimate of the downwelling longwave radiation. The upwelling longwave radiation biases are related to the downward radiation mainly from Northern Africa east through Asia. The reflected shortwave radiation at the surface is generally reasonable (Figure 4-6), but the occurrence of sea ice seems to disagree between MERRA-2 and CERES.

Overall, MERRA-2's radiation fields have the spatial patterns that characterize the observed climate, as represented by CERES. The difference maps call out the regional biases that lead to the global average differences; in some places, these regional biases can be significant.

d. Implied Ocean Heat Transport

In the Earth climate system, the non-uniform meridional distribution of net heating through the ocean-atmosphere interface must be balanced by meridional heat transport in the ocean. Northward ocean heat transport, implied from the net surface heat flux, is a metric that can help us evaluate the realism of a spatial distribution of surface heat flux in MERRA-2 compared to observations and other reanalysis products. The zonal and vertically integrated heat balance in the ocean is expressed by the following equation:

$$\frac{\partial \theta}{\partial t} + \frac{1}{a\cos(\phi)} \frac{\partial}{\partial \phi} (F_\theta) = Q, \tag{4-1}$$

where θ is the zonal integral of ocean heat content, F_θ is the meridional heat transport, and Q is the zonal integral of net surface heating. We ignore the diffusion term here since the contribution of diffusivity to the meridional ocean heat transport is small. If there is no long term drift in the ocean heat content, the time mean of the first term on the left hand side of equation (4-1) vanishes, and the time mean of F_θ can be found by integrating the time mean of Q from the latitude where F_θ is known (e.g. one of the poles) to the given latitude. However, a non-zero global mean of the net surface heating is seen in MERRA-2; this indicates a net input of heat into the ocean, which would result in long term drift in the ocean heat content. For simplicity of analysis we assume that this drift is spatially uniform and take it into account by subtracting from the net surface heating its global mean. Therefore, our estimate of meridional heat transport is:

$$\bar{F_\theta} = \int_{\phi_0}^{\phi} a\cos(\phi) \bar{Q}' d\phi, \tag{4-2}$$

where the overbar denotes a time average and Q' is the net surface heating with the global mean removed and integrated zonally.

Figure 4-7a-d shows zonally integrated time mean net surface shortwave, net surface longwave, latent heat, and sensible heat fluxes in giga-watts per meter for MERRA, MERRA-2 and ECMWF ERA-Interim reanalysis products and for the WHOI OAFlux objective analysis (used here instead of the CERES EBAF because it includes sensible and latent heating needed to compute the total

surface energy flux). WHOI OAFlux estimates for all four fluxes are significantly weaker than reanalysis estimates. Figure 4-7e shows the zonal integral time mean net surface heat flux with global mean subtracted to account for non-zero net surface heating. (1.6 Wm^{-2} was added to MERRA-2 surface heating, and 18 Wm^{-2}, 10 Wm^{-2}, and 30 Wm^{-2} were subtracted from MERRA, ERA-Interim and WHOI OAFlux surface heating, respectively.) Figure 4-7f shows the ocean northward heat transport implied from quantities in Figure 4-7e according to equation (4-2). Estimates of ocean heat transport from Ganachaud and Wuncsh (2000) and Trenberth and Caron (2001) are displayed for comparison. There is a large discrepancy between different estimates of heat transport. There is a clear improvement in MERRA-2 heat transport compared to MERRA in the southern hemisphere and northern high latitudes, but in the northern subtropics MERRA-2 underestimates transport compared to all other estimates.

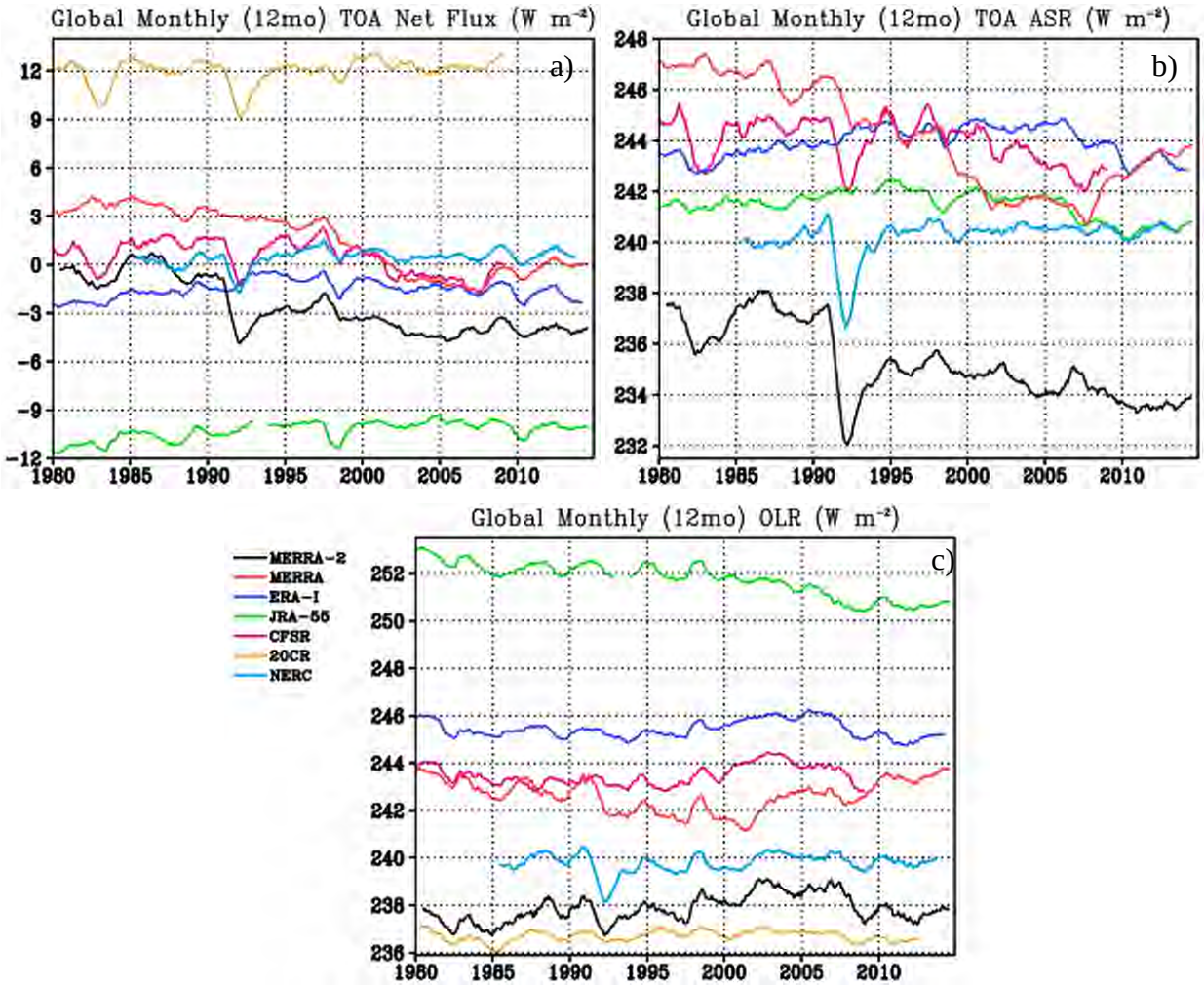

Figure 4-1 Comparison of TOA radiative fluxes for the listed reanalyses and the NERC-CERES reconstructed data (Allan et al. 2014) for (a) TOA Net Flux, (b) TOA Net Absorbed Shortwave Radiative Flux and (c) Outgoing Longwave Radiation. The data are globally averaged and then filtered with a 12 month centered running mean.

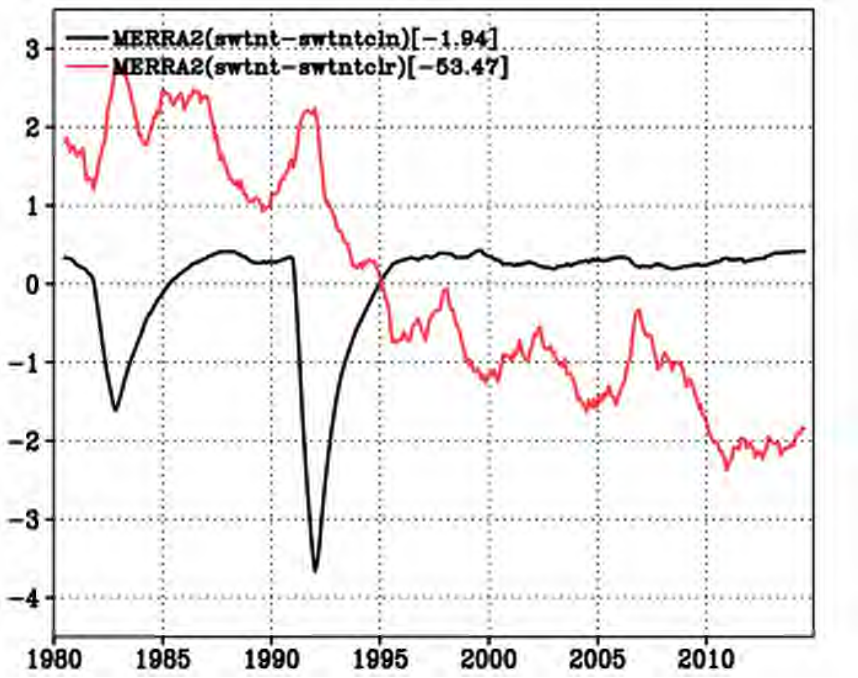

Figure 4-2 Anomalies of aerosol radiative effect (black) and cloud radiative effect (red) with the time mean values shown in the legend. These are global averages with a 12 month running mean. Units are W m^{-2}.

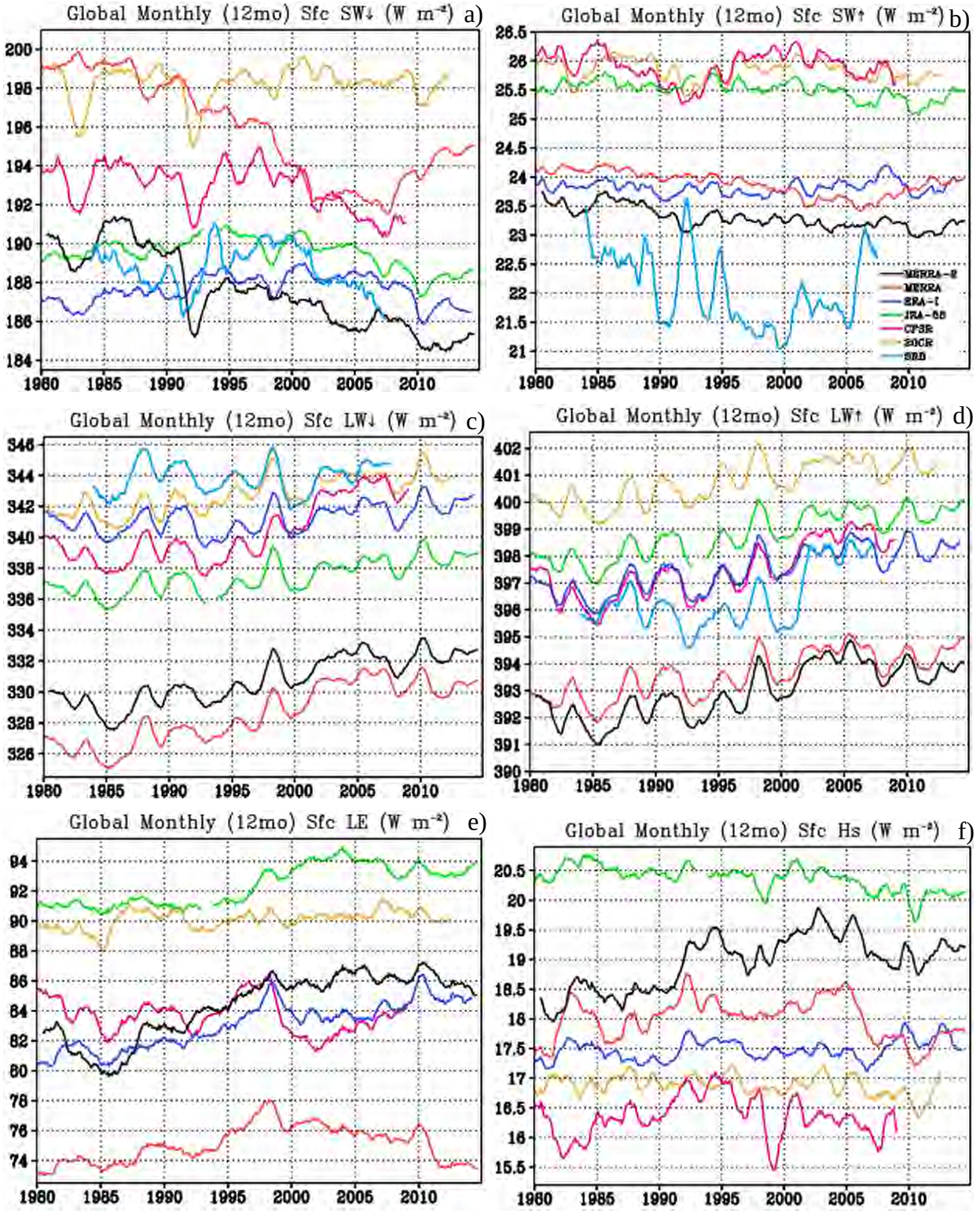

Figure 4-3 As in Figure 4-1, except for the surface fluxes: (a) downward shortwave, (b) reflected shortwave, (c) downward longwave, (d) upward longwave, (e) latent heat and (f) sensible heat.

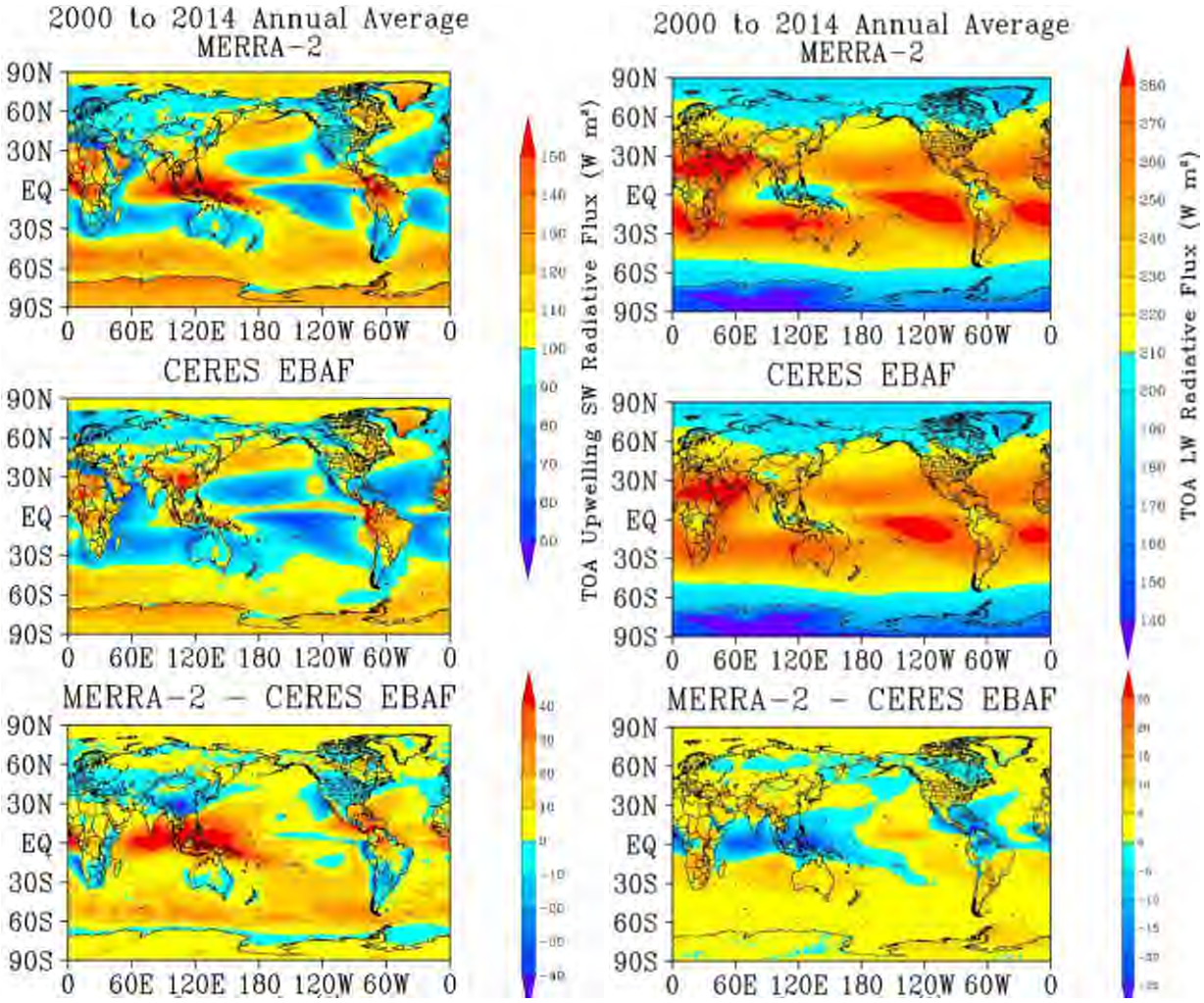

Figure 4-4 Comparing MERRA-2 (top row) to CERES EBAF (middle row) and their difference field (bottom row) for TOA outgoing longwave radiation (right) and TOA reflected shortwave radiation (left). Units are Wm^{-2}.

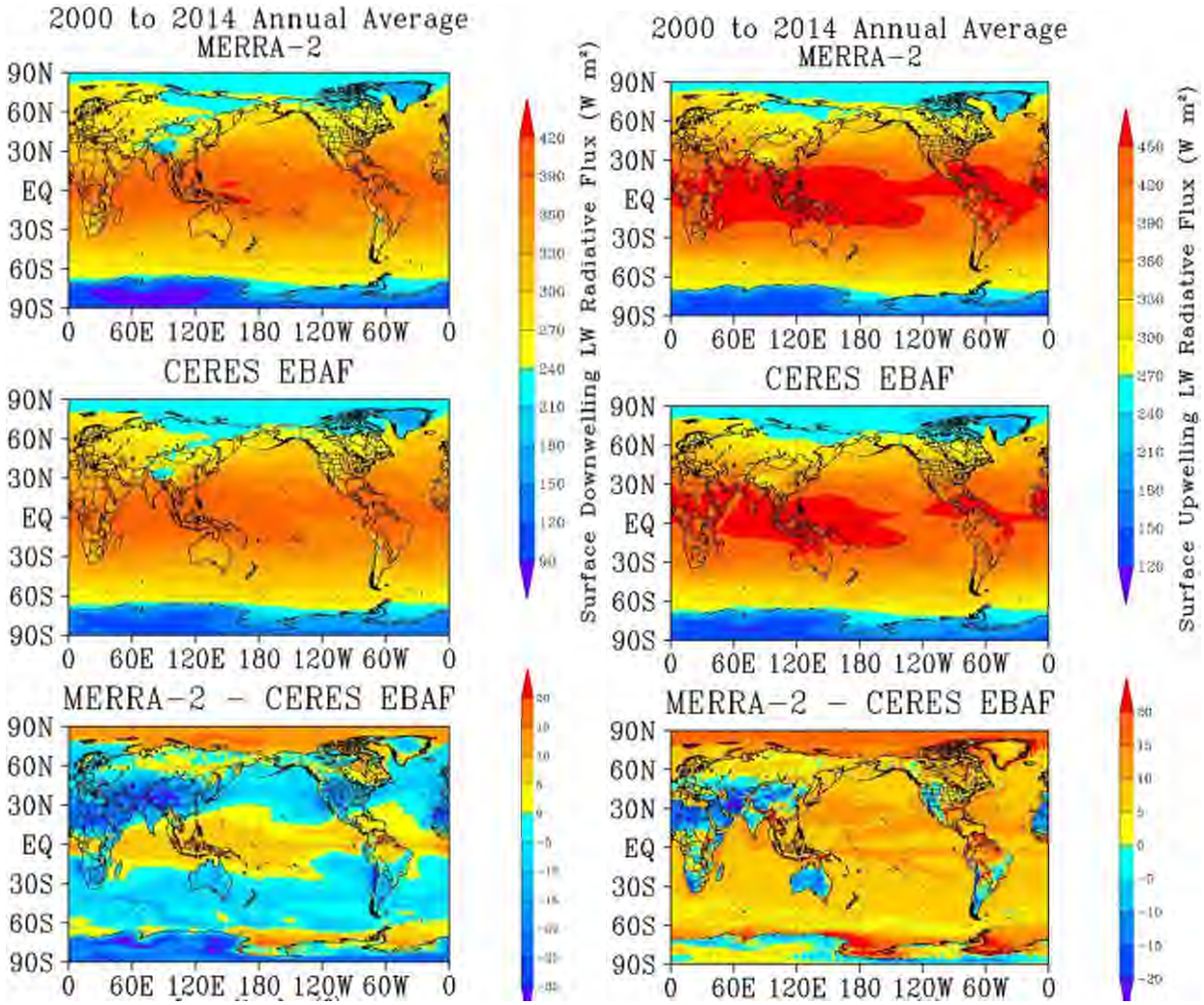

Figure 4-5 As in Figure 4-4, except for surface downwelling longwave radiation (left) and surface upwelling longwave radiation. Units are Wm^{-2}.

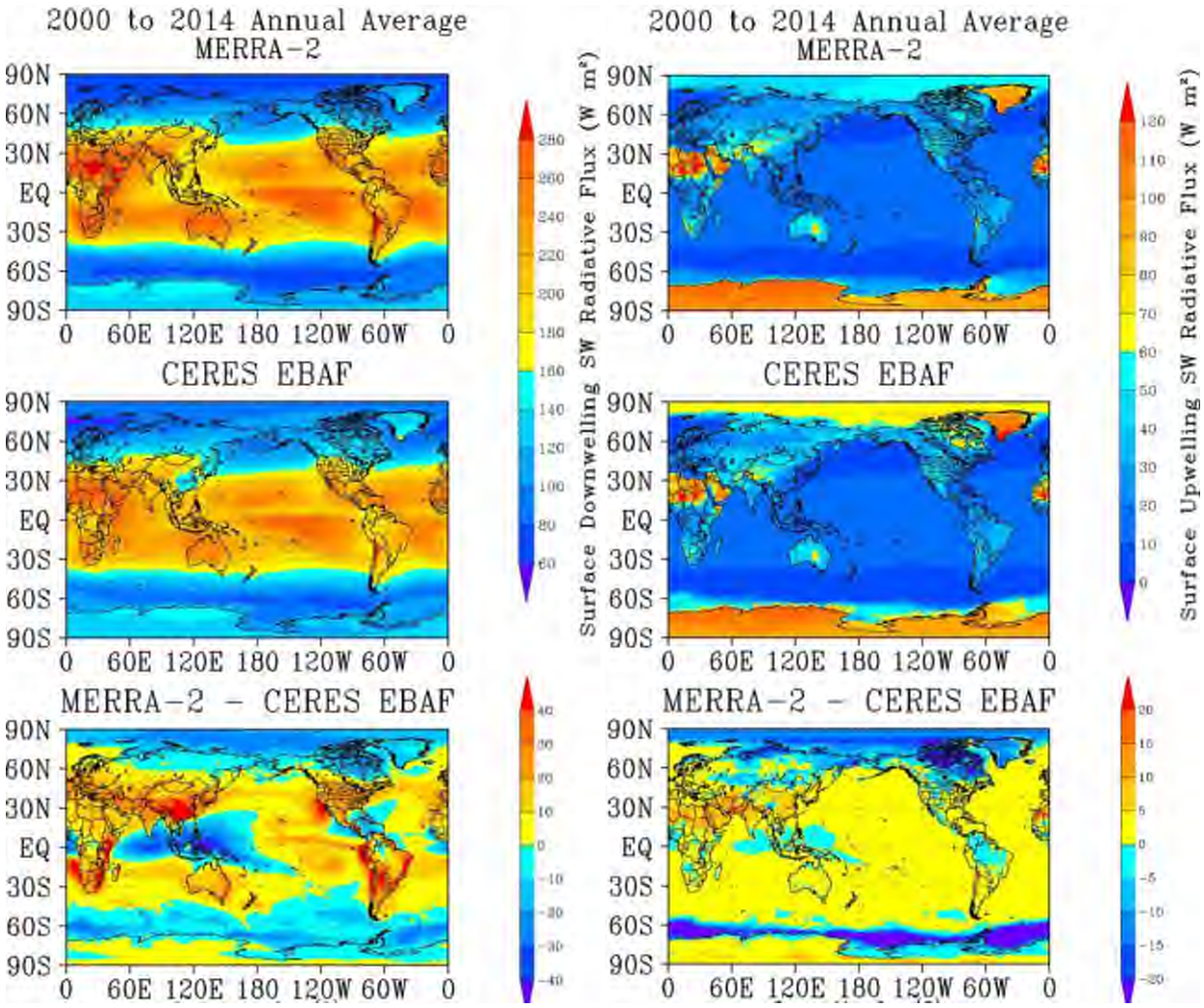

Figure 4-6 As in Figure 4-4, except for surface downwelling SW (left) and surface upwelling radiation (right). Units are Wm^{-2}.

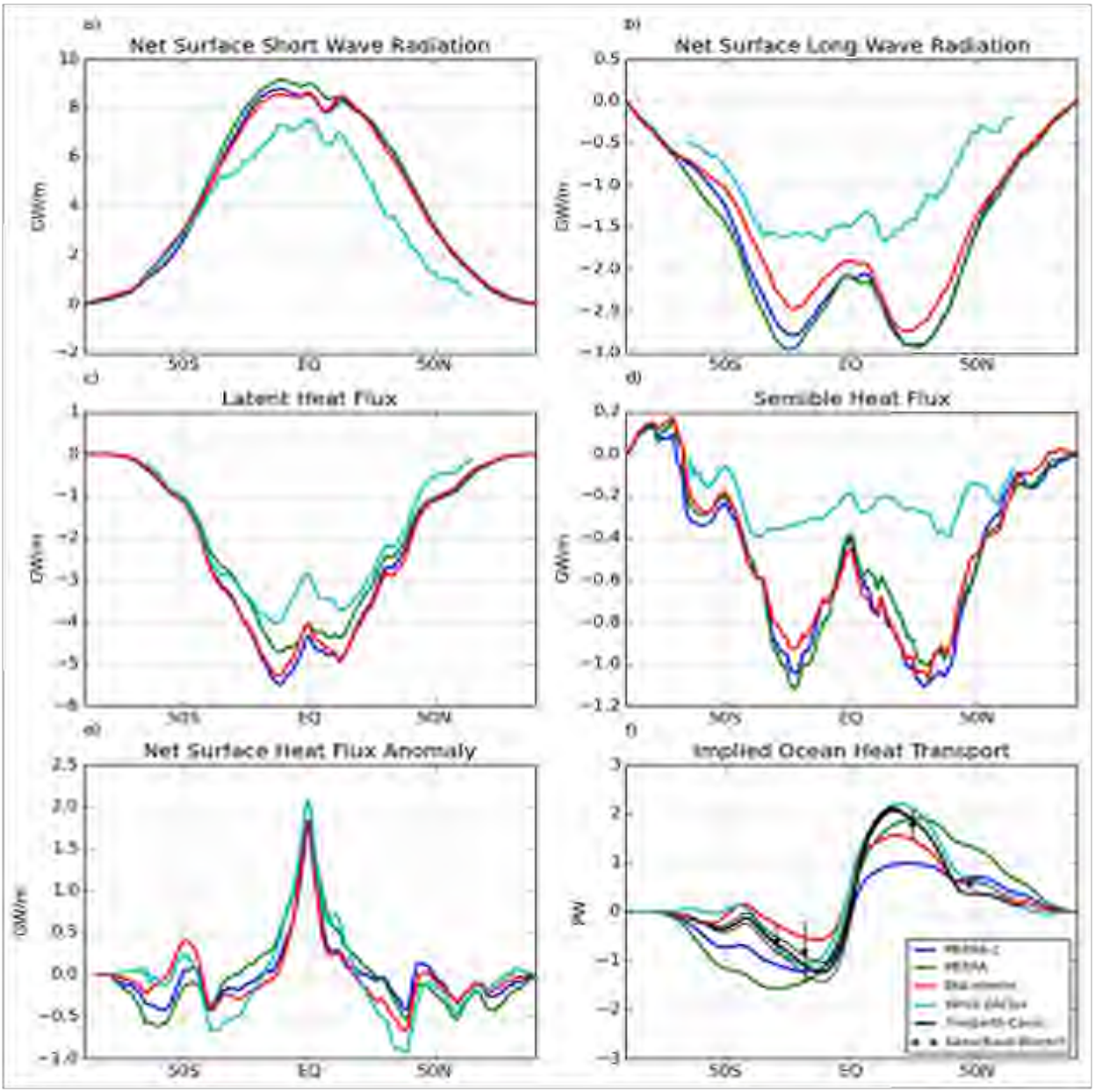

Figure 4-7 Zonally integrated time mean ocean surface fluxes (a-e) in giga-watts per meter for MERRA, MERRA-2, ECMWF ERA-Interim reanalyses and WHOI OAFlux objective analysis. (a) Net surface shortwave radiation; (b) net surface long wave radiation; (c) latent heat flux; (d) sensible heat flux; (e) net surface heat flux anomaly (global mean removed). (f) Implied northward ocean heat transport in peta-watts for MERRA, MERRA-2, ECMWF ERA-Interim, and WHOI OAFlux along with estimations from Trenberth and Caron (2001) and Ganachaud and Wunsch (2000).

5. Cloud Radiative Forcing

Clouds are the perhaps the most important (and difficult to model) modulator of the Earth's radiative energy balance. It is therefore very important for any reanalysis product to have realistic cloud radiative forcing (CRF). In view of this, the current study will compare MERRA-2 Top-of-Atmosphere (TOA) CRF against the CERES (Clouds and the Earth's Radiant Energy System) EBAF (Energy Balanced and Filled) satellite-based observational dataset and against the earlier MERRA reanalysis.

The EBAF dataset is a Level III CERES product that has "CERES net balanced [TOA] fluxes, where the global net is constrained to the ocean heat storage term. [It] spatially interpolates (fills) clear-sky fluxes in non-observed regions. EBAF is for climate model evaluation, estimating the Earth's global mean energy budget and to infer meridional heat transport (CERES WWW, retrieved Nov 6, 2015, http://ceres.larc.nasa.gov/products.php?product=EBAF-TOA) The EBAF dataset employs a diurnal temporal model provided by CERES to produce full diurnal average estimates from the Aqua and Terra observations.

All results in this chapter use monthly means, aggregated into 14 year averages, for the period Mar 2000 – Feb 2014 (CERES EBAF is available March 2000 onwards). We will look at Dec-Jan-Feb (DJF), Jun-Jul-Aug (JJA), and annual (ANN) averages.

a. TOA Cloud Forcing – Annual Average

Figure 5-1 and Figure 5-2 show a comparison of the MERRA-2 and MERRA TOA shortwave cloud forcing (SCF) against CERES EBAF. MERRA and MERRA-2 are realistic, showing tropical convection, high-latitude stratus, and subtropical subsidence zones (cloud minima). In general, MERRA-2 does better than MERRA over continents (e.g., Eurasia and North America) in its representation of Inter-Tropical Convergence Zone (ITCZ) cloudiness and, correspondingly, in its clear delineation of the subtropical subsidence zone cloud minima. On the negative side, MERRA-2 has excessive Western Pacific and Southern Ocean cloud cooling (i.e., albedo). The impact of this can be seen in MERRA-2's TOA energy balance (Figure 4-1). In terms of the global mean, the latter two problems dominate, leading to an excessive cloud cooling of 7.7 Wm^{-2} for MERRA-2 (with respect to EBAF), compared with only a 0.3 Wm^{-2} difference for MERRA. The zonal averages generally bear out these conclusions (Figure 5-3 and Figure 5-4), showing that MERRA-2 has excessive SCF in the tropics and Southern Ocean, although the Northern mid-latitudes are somewhat better for MERRA-2.

Figure 5-5 to Figure 5-8 show the corresponding comparisons for TOA longwave cloud forcing (LCF). Note the positive LCF, showing how clouds warm the planet in the longwave by thermal trapping. Both MERRA and MERRA-2 have realistic global patterns, showing tropical convection, mid-/high-latitude cloud, and subtropical subsidence zones (cloud minima). MERRA-2 seems to do better over continents and in the ITCZ and subsidence zones, but it has excessive

Western Pacific convection. The zonal difference plots show that MERRA-2 clearly does better in southern mid-latitudes and in the subtropical subsidence zones, but again has excessive tropical cloudiness. The latter excess tends to dominate the global averages, with MERRA-2 having an excess over EBAF of 3.0 Wm^{-2} (not large), compared with a MERRA deficit of only -0.5 Wm^{-2}. In general, MERRA-2 fares better in LCF than in SCF.

Figure 5-9 to

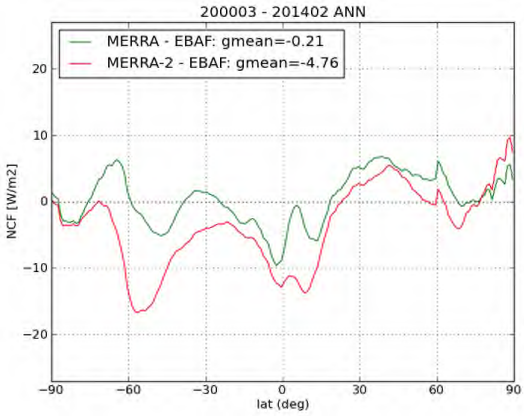

Figure 5-12 show the corresponding situation for TOA net cloud forcing (NCF), i.e., SCF + LCF. Note the widespread negative values (especially in stratus regions), indicating a net planetary cooling due to clouds. In general, MERRA-2 does better over Eurasia and North America, but it has excessive cloud cooling over the Western Pacific, the Southern Ocean, and in Central Africa. The zonal plots again show this excessive MERRA-2 cooling in the Tropics and Southern Ocean, but otherwise show similar features to MERRA. The global average net TOA cloud forcing is -0.2 Wm^{-2} for MERRA and -4.8 Wm^{-2} for MERRA-2, both with respect to CERES EBAF.

b. TOA Solar Cloud Forcing – Seasonal Variation

For Figure 5-13 to Figure 5-16, we compare the 14 year seasonal (JJA and DJF) averages of solar cloud forcing (SCF), normalized by the incoming TOA solar flux. Results are shown for the two seasons because of their strong seasonal variation. It appears to us that the MERRA-2 global patterns are somewhat more realistic than those of MERRA, for example in their representations of the ITCZ and the subsidence zones, although there are certainly issues with the magnitudes. Note that both analyses (MERRA and MERRA-2) and CERES EBAF show the strengthening of Southern Ocean cloud in the austral summer (DJF), and the greater southward extent of the northern hemisphere storm track cloud (but slight weakening of the mean SCF) during the same period (the boreal winter). This gives rise to the greater "lopsidedness" of the DJF normalized zonal SCF as compared with JJA (see Figure 5-15 and Figure 5-16). Also noted is the weakening, general bifurcation, and southern movement of tropical cloud forcing during DJF. In terms of a comparison of zonal means with MERRA, MERRA-2 has excessive Southern ocean solar cloud forcing in both seasons, whereas MERRA is quite close to CERES. MERRA-2 also has excessive tropical SCF, even more than MERRA. MERRA-2 definitely has a better southern edge to the boreal winter storm track and a better estimate of its intensity.

c. Normalized-SCF vs. LCF joint probability density plots

Next we look at contour plots of the joint probability density of normalized SCF vs. LCF for different regions. These are shown in Figure 5-17 to Figure 5-19. On the x-axis is –SCF / ISR, basically the cloud solar albedo. (ISR is the incoming TOA solar radiation.) On the y-axis is LCF, the longwave cloud forcing. Larger values of LCF represent greater thermal trapping by clouds. For thick clouds this is a rough proxy for cloud height. The purple, orange, and olive contours contain, respectively, the 10, 50, and 90% of the total. All densities outside each contour are smaller than those inside. Filled contours show CERES EBAF as an observational reference. Thick and thin lines show MERRA-2 and MERRA, respectively. Each sample used to form the probability density is a monthly average. Note that dilution by cloud fraction / occurrence will move a cloud-type linearly towards the origin.

Figure 5-17 shows the joint probability density contours for the tropics. The stratiform branch (lower left area of density in the figure) of MERRA-2 looks very good (cf., MERRA a bit too bright). The convective branch (upper rightmost area of density in the figure) of MERRA-2 looks to have a bright and high bias that cannot be explained by linear dilution by cloud fraction / occurrence. Figure 5-18 shows similar plots for the southern and northern mid-latitudes. In the south, MERRA-2 has a bit of a bright bias. In the north, both MERRA and MERRA-2 look good, but MERRA-2 is a little better. Finally, Figure 5-19 shows similar plots for the southern and northern high-latitudes. In the south, MERRA-2 has a strong bright bias, worse than MERRA. In the north, both look good but the most common 10% is diluted.

We have provided a brief summary of the behavior of MERRA-2 top-of-atmosphere cloud radiative forcing as compared to the CERES EBAF observations and against the earlier MERRA reanalysis. On the positive side, MERRA-2 has a better overall global cloud forcing pattern. In particular, the tropical ITCZ, the subtropical cloud minima, and the transition to mid/high-latitude cloud have a more realistic pattern. Continental cloud, especially in the northern hemisphere, is also improved. On the negative side, tropical Western Pacific cloud is too bright in MERRA-2, as is Southern Ocean cloud.

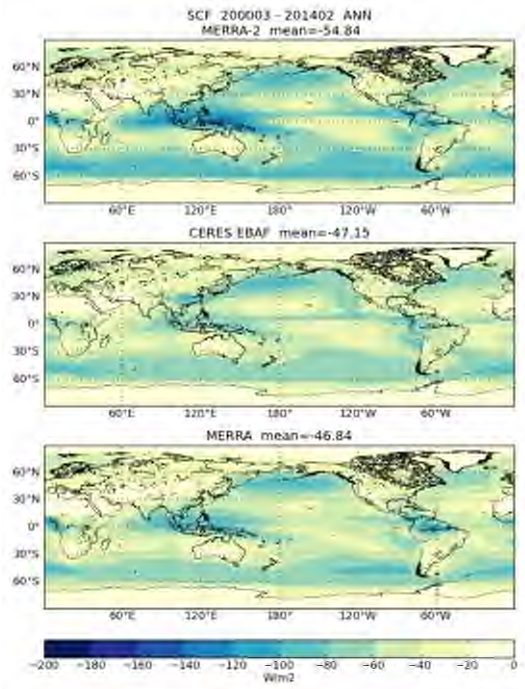

Figure 5-1 TOA Shortwave Cloud Forcing (SCF) averaged over Mar 2000 – Feb 2014 for MERRA-2 (top), CERES EBAF (middle), and MERRA (bottom). The negative values indicate that clouds cool the planet in solar wavelengths by reflection of radiation.

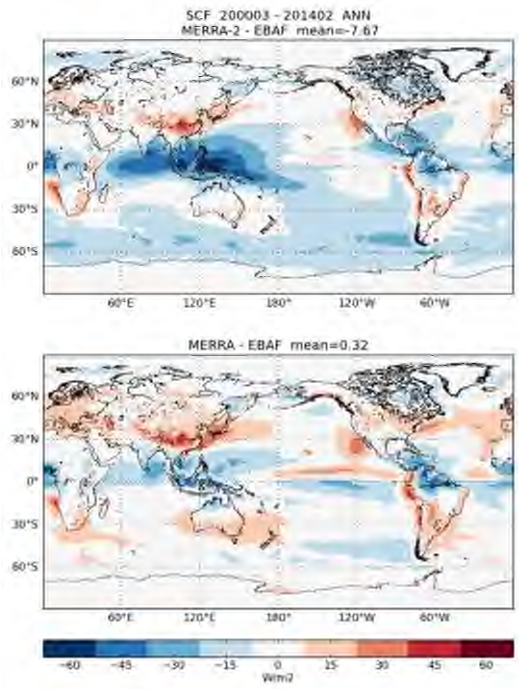

Figure 5-2 The corresponding differences: MERRA-2 minus EBAF (top) and MERRA minus EBAF (bottom).

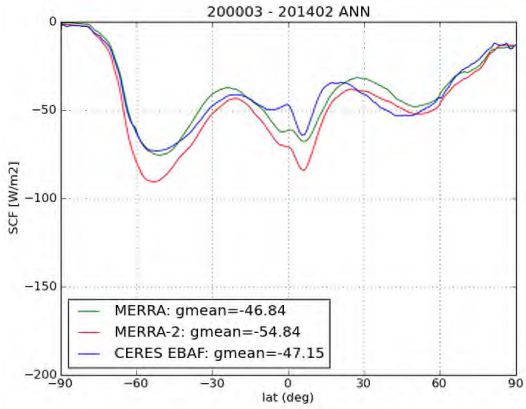

Figure 5-3 Zonal Averages of Figure 5-1.

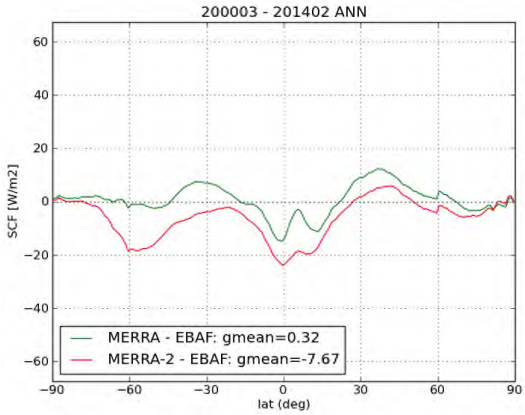

Figure 5-4 Zonal averages of Figure 5-2.

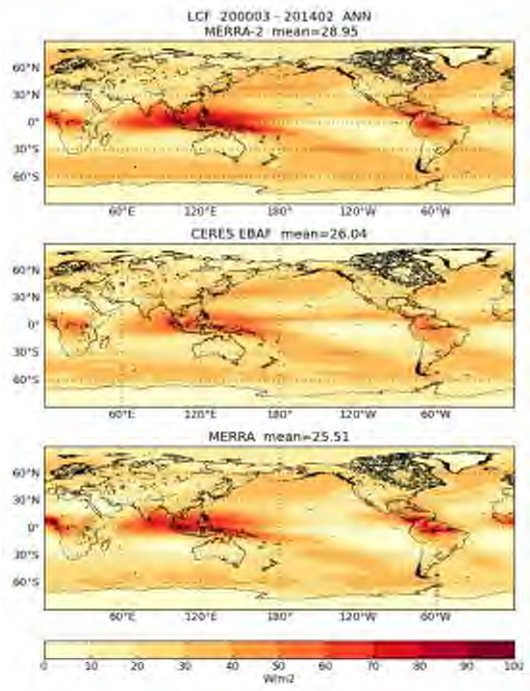

Figure 5-5 TOA Longwave Cloud Forcing (LCF) averaged over Mar 2000 – Feb 2014 for MERRA-2 (top), CERES EBAF (middle), and MERRA (bottom). The positive values indicate that clouds warm the planet in the longwave by thermal trapping.

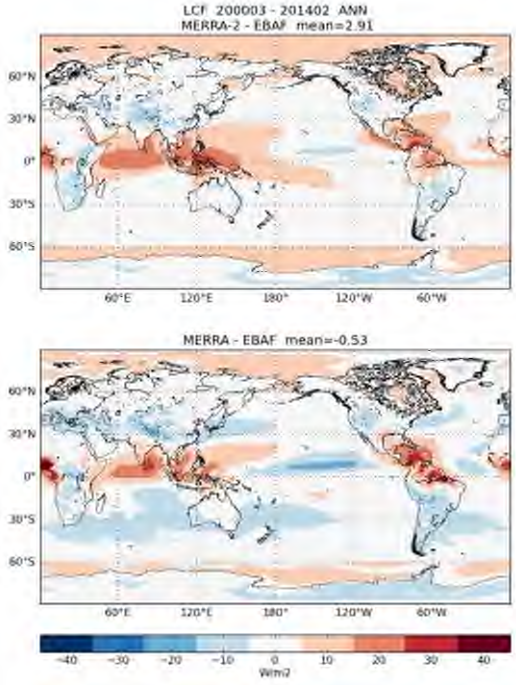

Figure 5-6 The corresponding (to Figure 5-5) differences: MERRA-2 minus EBAF (top) and MERRA minus EBAF (bottom).

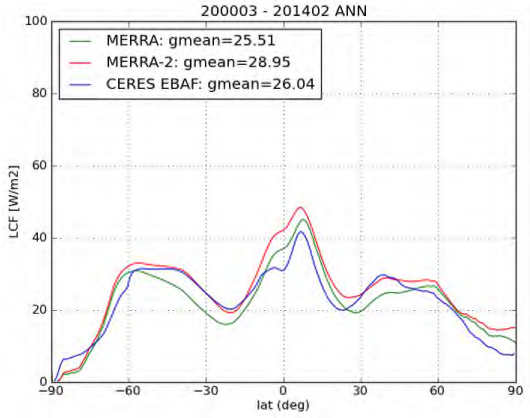

Figure 5-7 Zonal average of Figure 5-5.

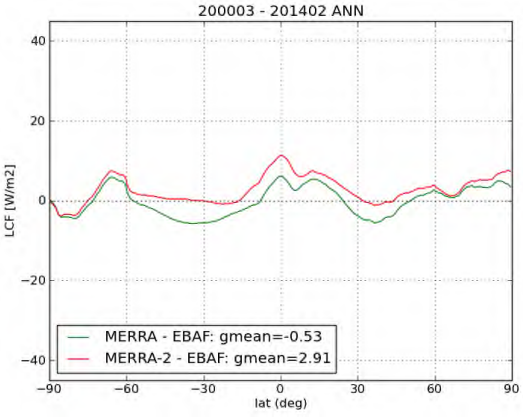

Figure 5-8 Zonal average of Figure 5-6.

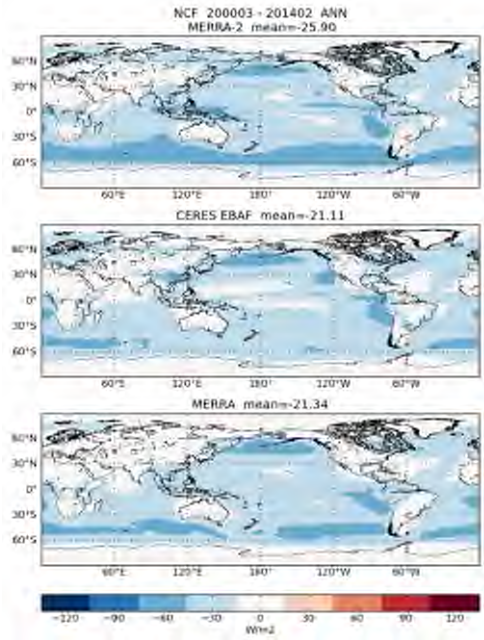

Figure 5-9 TOA Net Cloud Forcing (NCF=SCF+LCF) averaged over Mar 2000 – Feb 2014 for MERRA-2 (top), CERES EBAF (middle), and MERRA (bottom). The widespread negative values show net planetary cooling due to clouds.

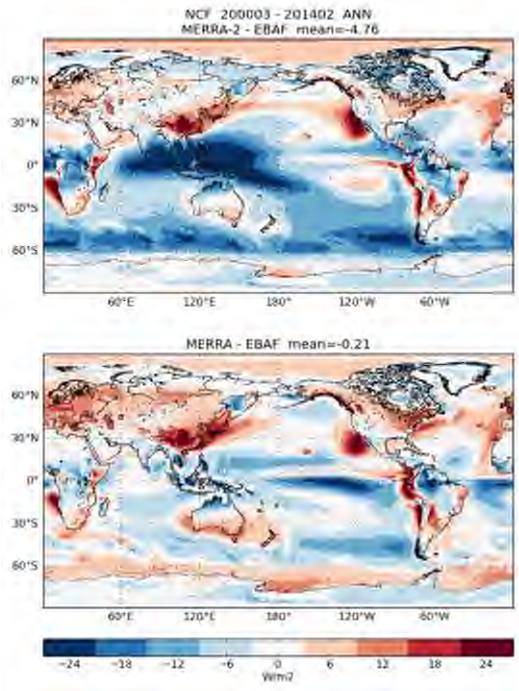

Figure 5-10 The corresponding differences: MERRA-2 minus EBAF (top) and MERRA minus EBAF (bottom).

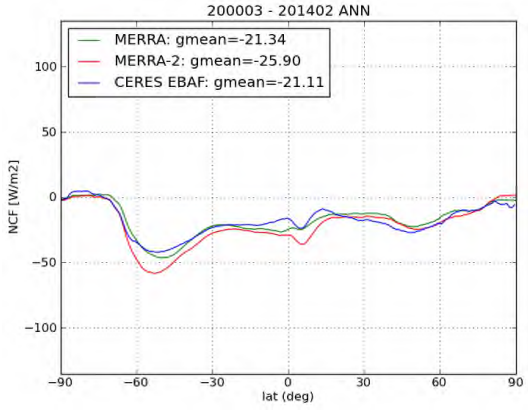

Figure 5-11 Zonal average of Figure 5-9.

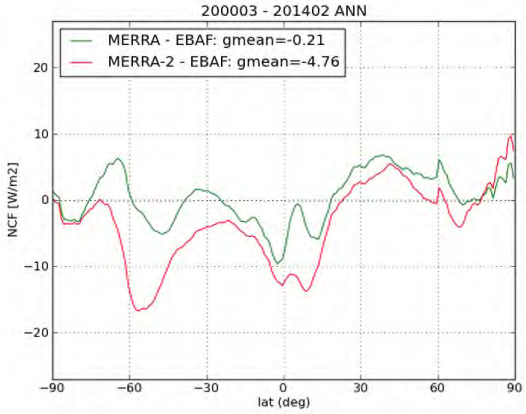

Figure 5-12 Zonal average of Figure 5-10.

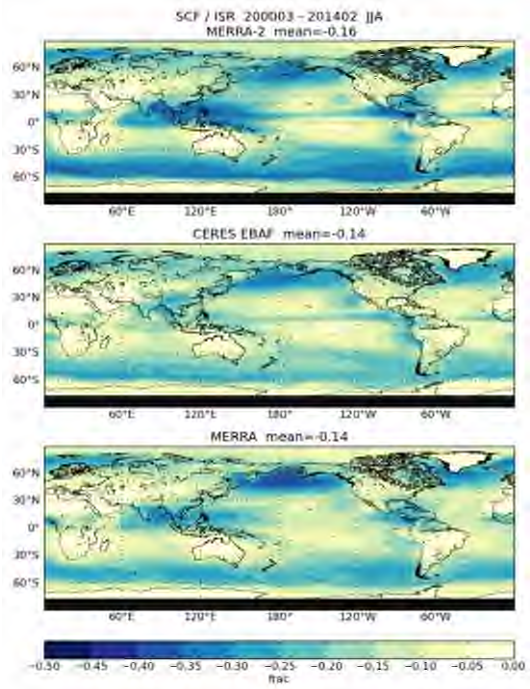

Figure 5-13 TOA Shortwave Cloud Forcing (SCF) averaged over JJA for Mar 2000 – Feb 2014, normalized by the average of the incoming TOA solar radiation (ISR) for the same period, for MERRA-2 (top), CERES EBAF (middle), and MERRA (bottom).

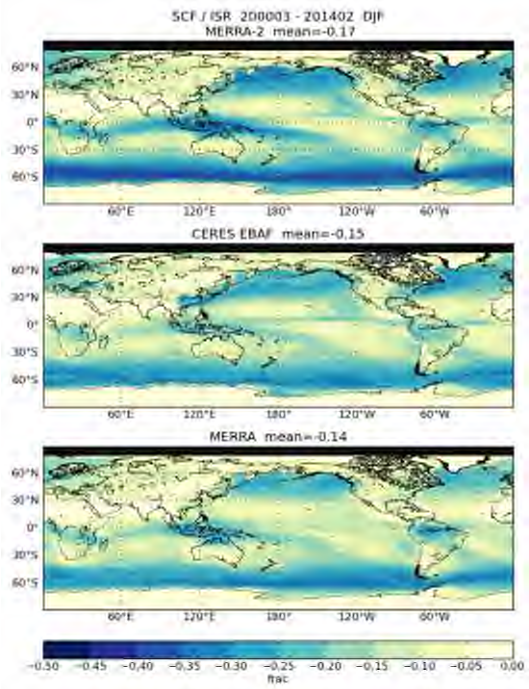

Figure 5-14 As in Figure 5-13 except for DJF.

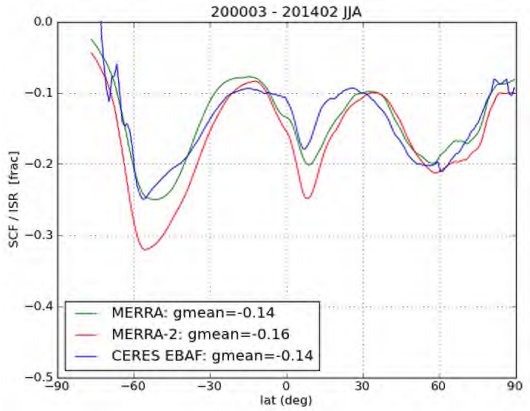

Figure 5-15 Zonal average of Figure 5-13.

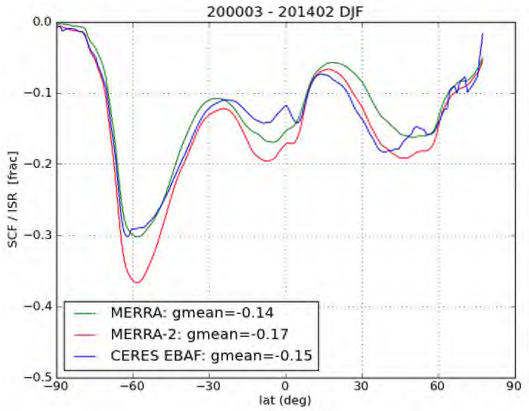

Figure 5-16 Zonal average of Figure 5-14.

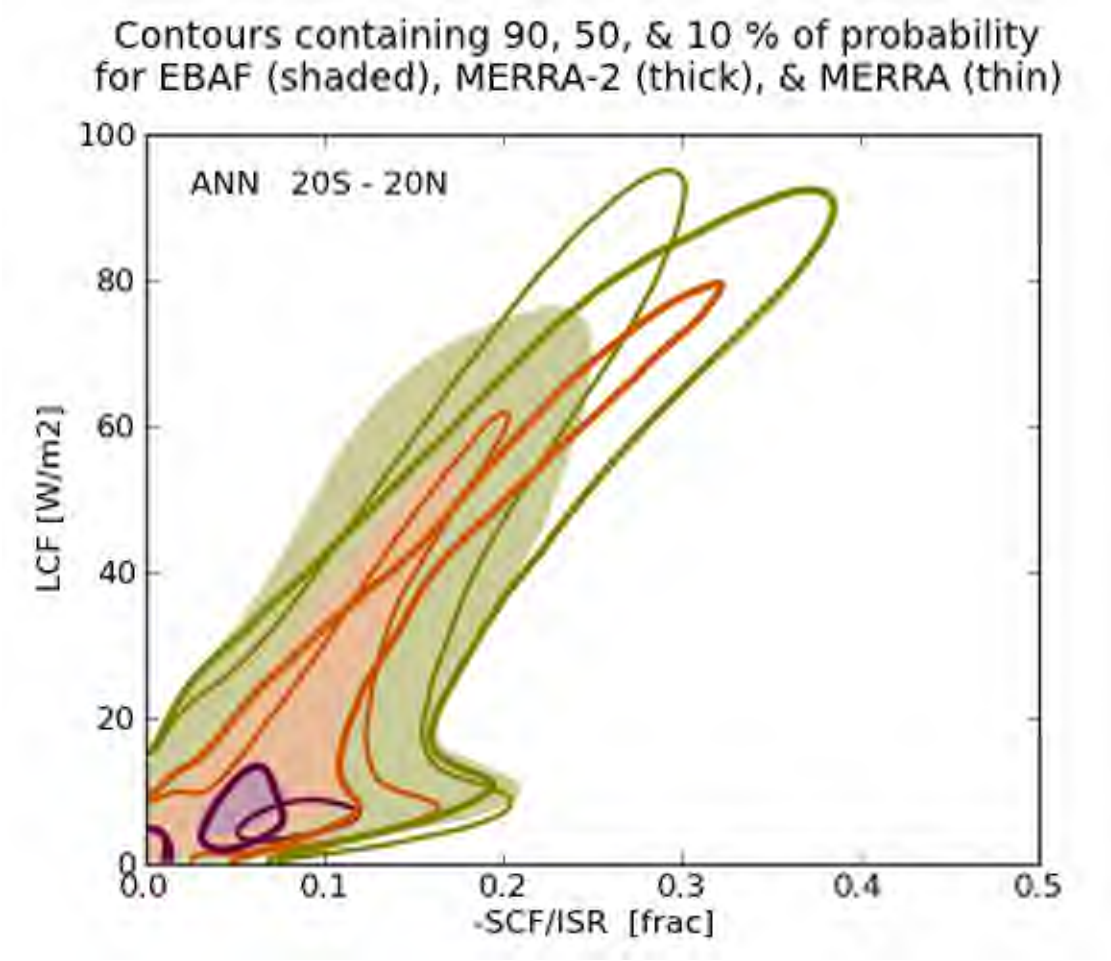

Figure 5-17 A contour plot of the joint probability density of normalized SCF vs. LCF, as described in the text, for the tropics and the full fourteen year period March 2000 - Feb 2014. The purple, orange, and olive contours contain, respectively, 10, 50, and 90% of the total probability with the highest probability densities. All densities outside each contour are smaller than those inside. Filled contours show CERES EBAF as an observational reference. Thick and thin lines show MERRA-2 and MERRA, respectively. The stratiform (lower) branch of MERRA-2 looks very good (cf. MERRA, a bit too bright). The convective (upper) branch of MERRA-2 looks to have a bright bias that cannot be explained by linear dilution (see text).

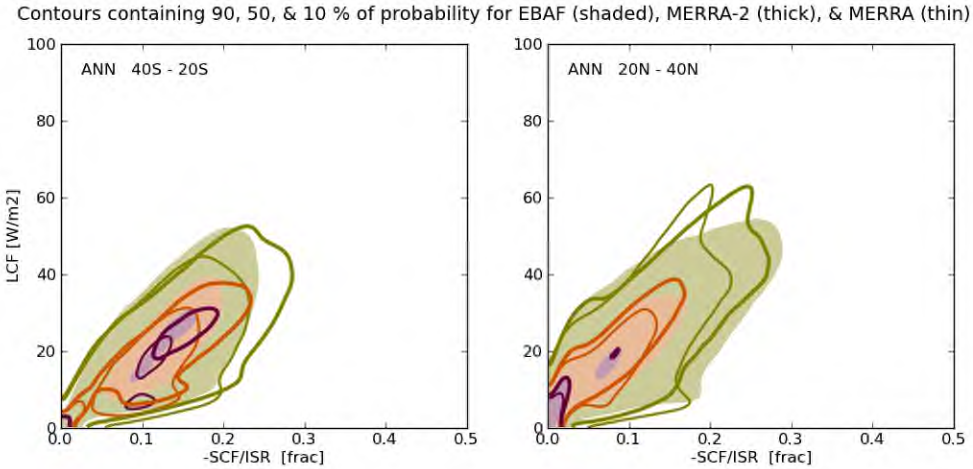

Figure 5-18 As for Figure 5-17, but for the southern and northern mid-latitudes. In the south, MERRA-2 has a bit of a bright bias. In the north, both MERRA and MERRA-2 show favorable comparisons, with MERRA-2 only just slightly more favorable.

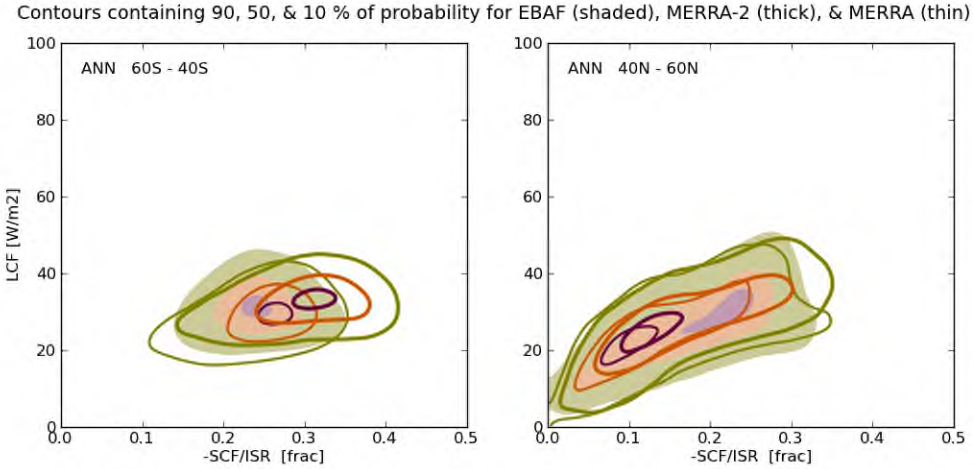

Figure 5-19 As for Figure 5-17, but for southern and northern high-latitudes. In the south, MERRA-2 has a strong bright bias, more than MERRA. In the north, both look good but the most common 10% is diluted.

6. Precipitation and Global Water Cycle

a. Precipitation Climatology

The precipitation produced by the atmospheric model in the reanalysis system is a useful diagnostic, considering that it is a component of both the water cycle and the energy cycle (through latent heating), and also that there are some reasonable and well-known merged gauge-satellite precipitation data products available (e.g. GPCP, Adler et al. 2003) for reanalysis evaluation. However, biases in model precipitation can have detrimental effects on regional hydrology in reanalyses (e.g. Reichle et al. 2011; Bosilovich et al 2011). Consequently, within MERRA-2 the model-generated precipitation is corrected with satellite and/or gauge-based observations before reaching the surface. For further details, refer to Section 7a and to Reichle et al. (2014).

While the observation-corrected precipitation forcing should improve the representation of MERRA-2's land hydrology and surface meteorology, the difference between the precipitation generated by the model and the observation-corrected fields seen by the surface will need to be considered for water budgets that encompass both the surface and atmosphere. The model-generated precipitation (variable **PRECTOT** in the MERRA-2 data collection) will be the sink of water from the atmospheric water budget, but the observation-corrected precipitation (variable **PRECTOTCORR** in the MERRA-2 data collection) will be the source of water for land budgets (and for wet deposition for the aerosol tendencies). In this section, we first compare the MERRA-2 model-generated precipitation to the observation-corrected precipitation, however; this section primarily focuses on the evaluation of the model-generated precipitation.

Figure 6-1 compares the long term mean of the MERRA-2 modeled precipitation to that of the observation-corrected precipitation for DJF and JJA. MERRA-2 suffers from some typical errors seen in all reanalyses (Bosilovich et al. 2011), such as an overestimate of the precipitation in the tropical west Pacific Ocean, the eastern tropical ITCZ, and the SPCZ. As described in Section 7a, the precipitation corrections start tapering off at 42.5 degrees N/S and are no longer present poleward of 62.5 degrees. The tapering reverts the observation-corrected data to the model precipitation, so that the minimal differences seen at high latitudes occur by design (Reichle et al. 2014). This means that the observation-corrected precipitation should not be considered a validation data set for model-generated precipitation, especially at the higher latitudes.

One of the most noticeable differences between the modeled and observation-corrected precipitation is the presence, in the modeled fields, of extreme values in the vicinity of high topography in the tropics (Figure 6-1), particularly along the Andes and the maritime continent. Figure 6-2 explores this feature closer, comparing MERRA-2 modeled precipitation to GPCC gauge data where gauges are found. While the biases are systematic along the Andes gauge locations, there does not seem to be a 1:1 correlation between bias and terrain height, so that certain regional effects (such as the extreme rainfall totals in Colombia) may also be related to local

features. Because some of these precipitation rates are unnaturally large, model-generated precipitation in such areas should be used with caution. These large values, while only covering a small area, can nevertheless sway global or large-scale statistics.

As mentioned above, the observation-corrected precipitation data does not allow a proper evaluation of model precipitation in high latitudes (poleward of 42.5 degrees). Figure 6-3 thus compares MERRA-2 and MERRA to GPCP. During boreal summer MERRA-2 overestimates precipitation in high latitude land regions. (Further discussion of the MERRA-2 high latitude precipitation can be found in Section 9 of this document.) Despite the tropical land positive bias, the warm pool positive bias in MERRA-2 is slightly improved. Comparisons with the GPCP data also indicate that the high precipitation bias in MERRA over the Intra-America Sea has been reduced greatly with MERRA-2, and precipitation in the Indian Ocean has also improved. Subsequent sections will evaluate temporal variability. For the remainder of Section 6, we focus only on the model-generated precipitation, unless noted otherwise.

b. Precipitation and Water Vapor Increments Interannual Variability

Side effects associated with changes in the observing system are a known issue in reanalyses (Kalnay et al, 1996). During the development of MERRA, an experiment conducted before executing the reanalysis focused on the effects of including data from the SSMI instrument, given that SSMI provides a large influx of new water vapor observations. Results showed that MERRA precipitation changed by less than 10% with the addition of SSMI (Bosilovich et al. 2008). However, on running the full system, AMSU-A radiances introduced a much larger change to the water cycle than expected (Figure 6-4 and Bosilovich et al. 2011). MERRA-2, on the other hand, presently exhibits smaller precipitation changes, at the global scale, than MERRA, but still has somewhat more temporal variability than the observations. (Figure 6-4 shows GPCP data, but this is comparable to CMAP and the observation-corrected precipitation input to MERRA-2.) In the global mean sense, MERRA-2 precipitation is higher than GPCP, but it leans toward the lower end of the contemporary reanalyses. While the serious perturbations present in MERRA have been ameliorated, some significant changes occur in MERRA-2 in the early years. These will be discussed in subsequent sections.

Figure 6-5 shows the global monthly mean time series of precipitation (P), evaporation (E), and the analysis increment (ANA), as well as of the combinations E-P and E-P+ANA. Aside from MERRA's strong shifts in the time series, the most noticeable feature is that MERRA's E-P changes sign over the course of the time series, directly related to variations in the analysis increment. Of course, this is a non-physical result; we expect that globally, E=P over the long term. In MERRA-2, E is very close to P, but this is by design through the implementation of a constraint that penalizes the analysis increment for large global values (Takacs et al. 2015a&b). This constraint prevents the analysis increment from having a large global average. In any given region, however, the water vapor analysis increment can still have a significant magnitude. Figure 6-6 shows the global spatial variance of the water vapor increment for MERRA and MERRA-2, which represents the variations that can occur within the domain being averaged. The plot shows that there are variations within the global domain in MERRA-2 that are comparable to what occurred in MERRA, and that these can change over time with the observing system. The two time series

resemble each other, despite MERRA-2 not having a global mean analysis increment much different from zero.

The effect of this constraint on the water vapor increments also influences the total column water (TCW, Figure 6-7). MERRA TCW experiences several distinct jumps, especially with SSMI and AMSU-A (NOAA15), while MERRA-2 variations are much more stable in time (meaning fewer spurious jumps in the data). The trend in the MERRA-2 time series compares well with most of the contemporary reanalyses (aside from MERRA and CFSR, which exhibit spurious jumps due to observing system changes). However, the trend in RSS TCW (version 7, Wentz and Schabel, 2000) is somewhat larger than in these reanalyses.

c. Precipitation Diurnal Cycle

Figure 6-8 shows the amplitude (mm day^{-1}) and phase (local solar time of the peak) of the precipitation diurnal cycle (PDC) in the JJA season averaged over 2011-2012 from the MERRA-2 dataset. Plots for the same period based on TRMM data are shown in Figure 6-9. The grid cells for which the computation of the PDC did not pass a significance test are left blank; the significance test was conducted using the method of Lee et al. (2007). Over the eastern part of the Pacific and the Atlantic oceans, MERRA-2 has more grid cells that pass the significance test than TRMM. Aside from the high mountain areas of the Ethiopian Highland, the Himalayas, southwest of China, New Guinea, the Andes, and Mexico, MERRA-2 has smaller PDC amplitude over land than TRMM. The larger PDC amplitude over the high mountains in MERRA-2 is the result of excessive precipitation with a strong diurnal variation in the GEOS-5 GCM in these areas (Chao, 2012).

In terms of the phase of PDC, MERRA-2 reflects the biased behavior of the GEOS-5 GCM, which produces a peak around noon over relatively flat land. Also, the observed propagation of convective systems over the U.S. Great Plains is not reproduced well in MERRA-2. Due to the large grid size used in MERRA-2, the diurnal propagation of convection out to sea along the southwest coasts of Mexico and Sumatra, seen in the TRMM data, is not reproduced in MERRA-2 (Chao, 2013).

d. MJO Precipitation

The Madden Julian Oscillation is a special mode of variability in the climate system that bears evaluation. Here, MERRA-2 precipitation is used to produce a Wheeler-Kiladis (1999) diagram using data from Jan 2011 to Dec 2012. Figure 6-10a,b shows the logarithm of the spectral power of MERRA-2 precipitation (mm day^{-1}) for the symmetric (with respect to the equator) and anti-symmetric components. Figure 6-10 can be compared with Figure 6-11, which shows the same calculations based on GPCP gauge/satellite merged observations. MERRA-2 has a stronger MJO signal than GPCP, an outcome supported by plots of the time sequence of precipitation averaged between 15S and 15N using MERRA-2 and GPCP datasets (Figure 6-12). However, the reason for this outcome is an open question. Also evident in Figure 6-10 and Figure 6-11 are stationary features over several longitudinal locations that exist in MERRA-2 but not in GPCP. These are likely related to the excessive precipitation over topography, noted earlier.

Also, note that the results in Figure 6-10a have a larger magnitude than those produced by Lin et al. (2005, see their Figure 5), although the general patterns in the two figures are the same. This discrepancy, which is likely due to a units conversion problem in either our computation or in Lin's, remains unresolved. However, this does not affect the conclusion that MERRA-2 has a stronger MJO signal than GPCP. It also does not affect the outcome revealed in Figure 6-13, which shows the ratio between the logarithm of the spectral power of the precipitation and that of the "background" (see Wheeler and Kiladis 1999 for explanation) for symmetric and antisymmetric components. As expected, the MJO and Kelvin waves are clearly seen in the symmetric component figure and the mixed-Rossby-gravity waves are in the antisymmetric component figure.

e. Global Water Cycle

Since fluxes are rarely directly measured and there are wide gaps in the available observations, reanalyses play a significant role in understanding the global water cycle (e.g. Trenberth et al., 2011). As shown earlier in this document, the global precipitation and evaporation in MERRA-2 are in very close balance, owing to the mass conservation constraint applied to the water vapor increments (Takacs et al., 2015a&b). Regionally, water vapor increments still have non-negligible mean values, and so they must still be considered in the atmospheric water cycle. Here, we evaluate the oceanic source of atmospheric water and the cycling of the water from the ocean to the continents.

In a recent assessment of the early 21st century water and energy budget, Rodell et al. (2015) developed a 10-year climatology of the water cycle from NASA satellite observations (with MERRA data minimally used to fill gaps). Uncertainties were included from the data providers, and a balanced budget was derived within the range of the uncertainties. In addition, the water and energy budgets were solved for together. Figure 6-14 shows how the global water cycle depiction resulting from the Rodell et al. (2015) analysis compares to the MERRA-2 data. All data are for the 2000-2010 period used by Rodell et al (2015). This is a strong test for a reanalysis system. Physically, the land budget should be equal but opposite to the ocean budget and the amount of water transport between them. That is,

$$-(E\text{-}P\text{+}ANA)_{land} = (E\text{-}P\text{+}ANA)_{ocean} = \text{Transport of water vapor}$$

Trenberth et al. (2011) compares global averages of E-P for ocean, P-E for land, and transport for each of the contemporary reanalyses (their figure 9). In some cases the differences between the land and ocean E-P magnitudes can be twice the dynamical moisture transport, indicating very large increments. MERRA-2 and MERRA each write out the analysis increment component of the water vapor budget, so it is presented for MERRA-2 as a separate value in Figure 6-14. The interesting feature in MERRA-2 is that because the global increments are constrained, the complementary land and ocean increments integrate to being equal and opposite.

Over the ocean, the evaporation in MERRA-2 is larger than the NEWS-corrected estimate, while the increments in MERRA-2 take away from the atmospheric water vapor. Even so, there is more water vapor moving from the ocean to the land in MERRA-2 compared to NEWS estimates. The continental interpretation is more complicated. While the global land estimate of precipitation exceeds that of the observations, this feature is primarily in the tropics (Figure 6-1, connected to the topography precipitation bias). In general, the water vapor must be low over land as the analysis increment is positive. Also, the land evaporation is higher than the NEWS estimate even though it is a function of the observation-corrected precipitation rather than the model-generated precipitation. Note that the corrected precipitation forcing and evaporation are diagnosed at the full grid space over land areas, while the value for runoff is determined from the data collection containing the land fraction only, and thus a proper land balance is not expected in Figure 6-14. In general, the water cycle terms are more active than the corrected budget developed by the NEWS team but are not outside the range of previous reanalyses, except for the model generated land precipitation and the ocean-land transport.

The discussion so far has focused on the 2000-2010 average water cycle. An important question regarding reanalyses is whether new or changing observing platforms affect the representation of the water cycle. Figure 6-4 to Figure 6-7 presented time series of precipitation, the variance of the analysis increments and the total column water. In Figure 6-15 we plot the time series of the yearly values of the ocean- and land-specific components examined in Figure 6-14. Over land, the analysis increment seems to be steadily increasing over time. However, on closer inspection, the land water vapor increments jump at 2003, near the beginning of Aqua, which included the AIRS, MHS and AMSU-A instruments. A sensitivity experiment was thus performed in which the MERRA-2 system was run for 3 years without AIRS (short dotted lines in the figure). The AIRS-withholding experiment shows the impact that AIRS has on the system, increasing the water vapor increments and precipitation over land. Land evaporation is not significantly affected owing to the observation-corrected precipitation forcing for the land surface. Despite the changes in analysis increment and precipitation, the moisture transport remains steady throughout the period. This is in stark contrast to the previous reanalysis, which showed an increasing trend of water vapor transport over time, but it is similar to reduced observation reanalyses such as 20CR and model AMIP simulations (Robertson et al. 2014, their Figure 5).

The ocean time series of Figure 6-15 shows a strong relationship between MERRA-2 precipitation and evaporation. In this case, we assume that the evaporation is leading the precipitation. There is a sharp increase in the evaporation near 1987 when SSMI winds are first assimilated, and a decreasing trend in evaporation from 1980-1985, concurrent with a decreasing trend in sea surface temperature. Deconstructing the ocean evaporation will be undertaken at a later time. It appears, though, that observations that affect the ocean evaporation have an influence on the MERRA-2 global water cycle (e.g. global E and P in Figure 6-5). As in Figure 6-14, both the moisture transport and the analysis increment are nearly equal and of opposite sign when comparing land and ocean. This feature of MERRA-2 is not present in other reanalyses (or MERRA, Bosilovich et al. 2011) and is likely a result of the water vapor mass conservation constraint.

f. US Summertime Precipitation Variability

Reanalyses aim to produce a depiction of the weather at each analysis time. Precipitation is a key social and scientific aspect of the weather, and it is particularly difficult for weather forecasts to reproduce it accurately, especially in the summer when rainfall is derived from physical processes rather than from the dynamics of synoptic weather systems. Bosilovich (2013) evaluated MERRA against gauge observations and other reanalyses to test its ability to reproduce the summer seasonal precipitation over the United States. MERRA was able to reproduce certain aspects of the summer seasonal precipitation but had some deficiencies in others. In particular, MERRA was not able to produce seasonal highs and lows in regional precipitation that were similar to observations. For example, droughts and floods were only weakly reproduced.

Figure 6-16 shows the time series of JJA seasonal precipitation anomalies in the Midwest US as derived from CPC gauge observations and from MERRA and MERRA-2 model-generated precipitation. MERRA's limitations are apparent, especially when comparing 1988 (regional drought) and 1993 (large-scale flooding) values with the observations. MERRA-2, on the other hand, is able to reproduce the 1988 and 1993 anomalies and is generally much better at tracking the overall variability of the observed anomalies.

For precipitation, MERRA-2 indeed shows improved statistical comparison to observations relative to MERRA in all parts of the US. Figure 6-17 presents summary statistics for several regions of the continental United States (as defined by Bosilovich 2013). In general, precipitation means are better across the US for MERRA-2 than for MERRA, and in many regions the MERRA-2 values improve over those of other reanalyses as well. There is also a marked increase in the standard deviation of the MERRA-2 time series relative to MERRA. As discussed above, for example, MERRA-2 more realistically reproduces the seasonal extremes in Midwestern precipitation. Note, however, that MERRA-2 overestimates the standard deviation in some regions. Improvements in MERRA-2 are most evident in the anomaly correlation (versus observations) of the seasonal time series. Not only does MERRA-2 produce the highest values, these values are generally substantially higher than those of all of the other reanalyses (Figure 6-17c). As for linear trend, we recognize that 30 seasons is not sufficient for an estimate that accurately reflects climate change; still, we did make the calculation as a sanity check on the reanalyses. MERRA's trends were very small, except for a strong decreasing trend in the Midwest. MERRA-2's trends seem to be tracking the observations a little better (though similar to MERRA, it shows too strong of a positive trend in the southeast US).

Figure 6-18 shows the spatial distributions of the JJA precipitation bias in MERRA and MERRA-2. MERRA exhibits large-scale biases, with underestimates in the Midwest and overestimates in the Southeast. These biases are generally reduced in MERRA-2. However, MERRA-2 features a significant underestimate of Gulf coastal precipitation along with an excess of precipitation in the Northeastern (NE) states (Figure 6-18d,f). The increase (relative to MERRA) in MERRA-2 precipitation over the Rocky Mountains in Colorado may be related to the same physics issues that cause excessive precipitation over topography in the tropics (discussed earlier), but then it would not be clear why this increase does not occur elsewhere in the Rockies.

Figure 6-19 shows the number of wet days* for which the precipitation exceeds the 99th percentile in JJA for MERRA, MERRA-2 and CPC gauge observations. MERRA clearly overestimates the days when extreme precipitation falls, whereas MERRA-2 agrees much better with the gauge data. This is because the MERRA 99th percentile precipitation is generally smaller than the observations, and because MERRA has many more wet days (days with precipitation > 1mm) from which to count days of exceedance. MERRA-2 on the other hand, has generated high values of extreme precipitation, much closer to what the gauge observations show (Figure 6-20). In addition, the patterns of extreme precipitation in MERRA-2 are much more comparable to the observations than MERRA. Keep in mind that Figure 6-18 through Figure 6-20 are showing the model-generated precipitation as opposed to the observation-corrected precipitation used to force the land.

In the global water budget, we see that there can be land/ocean signatures of the changing observing system (Figure 6-15). Figure 6-21 aims to test this over the US, using the area-averaged monthly mean time series of the water cycle terms. Any mean trend averaged over the US seems small for precipitation and evaporation, relative to their variability. However, there is a notable separation between P-E and MFC that develops over time, and this is reflected also in the analysis increment term. In other words, there appears to be an increasing trend over the US in the water vapor increment in time. We note here only the occurrence of this trend. A further evaluation of the assimilated observations, exploring all the conventional and satellite observations, will be done in time (e.g. Bosilovich et al. 2015).

* Wet days are defined as days with precipitation >1mm. This threshold affects the number of days from which a grid point's percentile is determined. The number of days above the threshold may therefore be different in different regions, and also different for the reanalyses and observation data sets; thus the number of days above the 99th percentile can also differ.

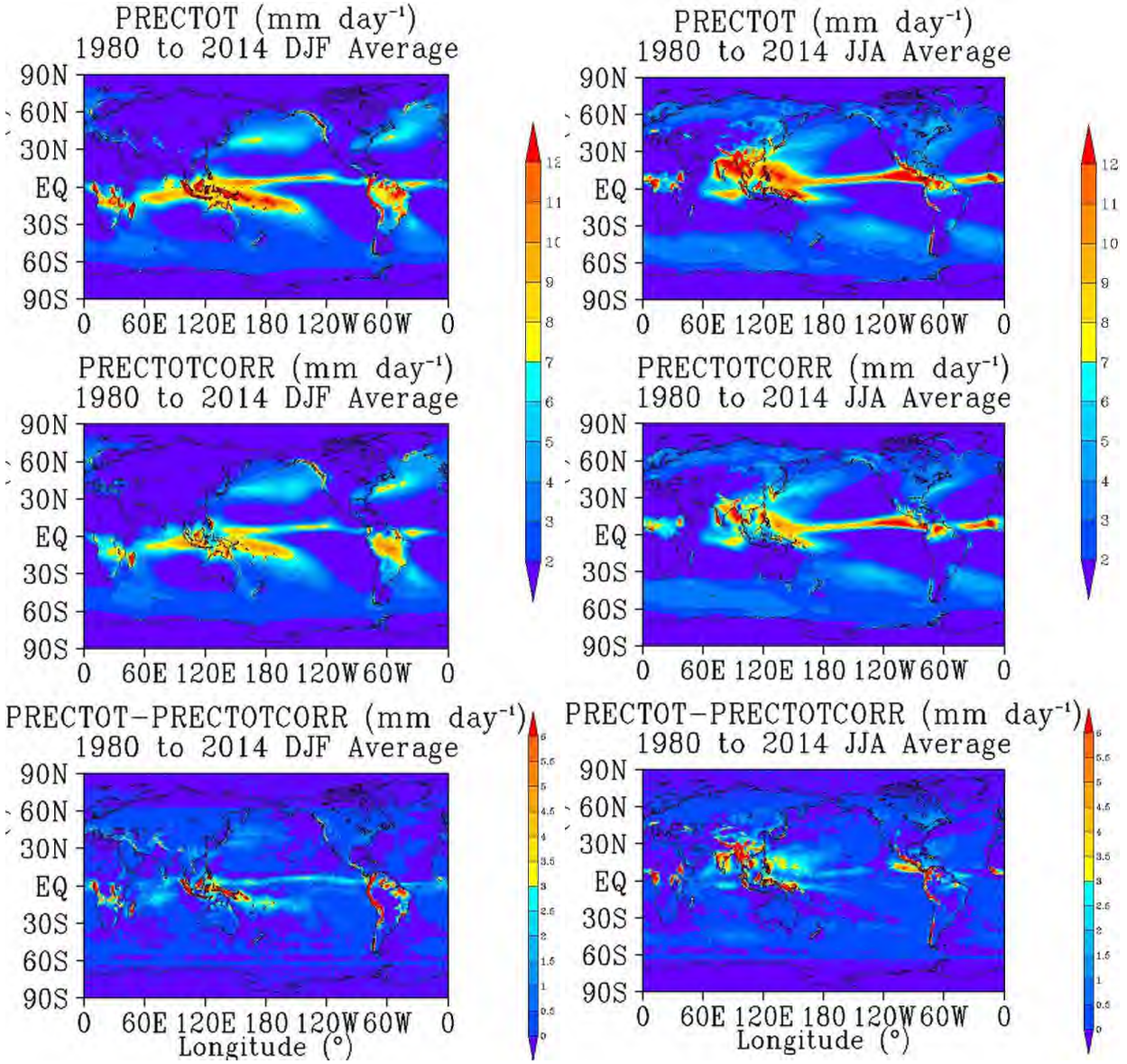

Figure 6-1 Long term mean of precipitation produced by the MERRA-2 model (PRECTOT), the observation corrected precipitation used by the land model (PRECTOTCORR) and their difference for DJF (left) and JJA (right).

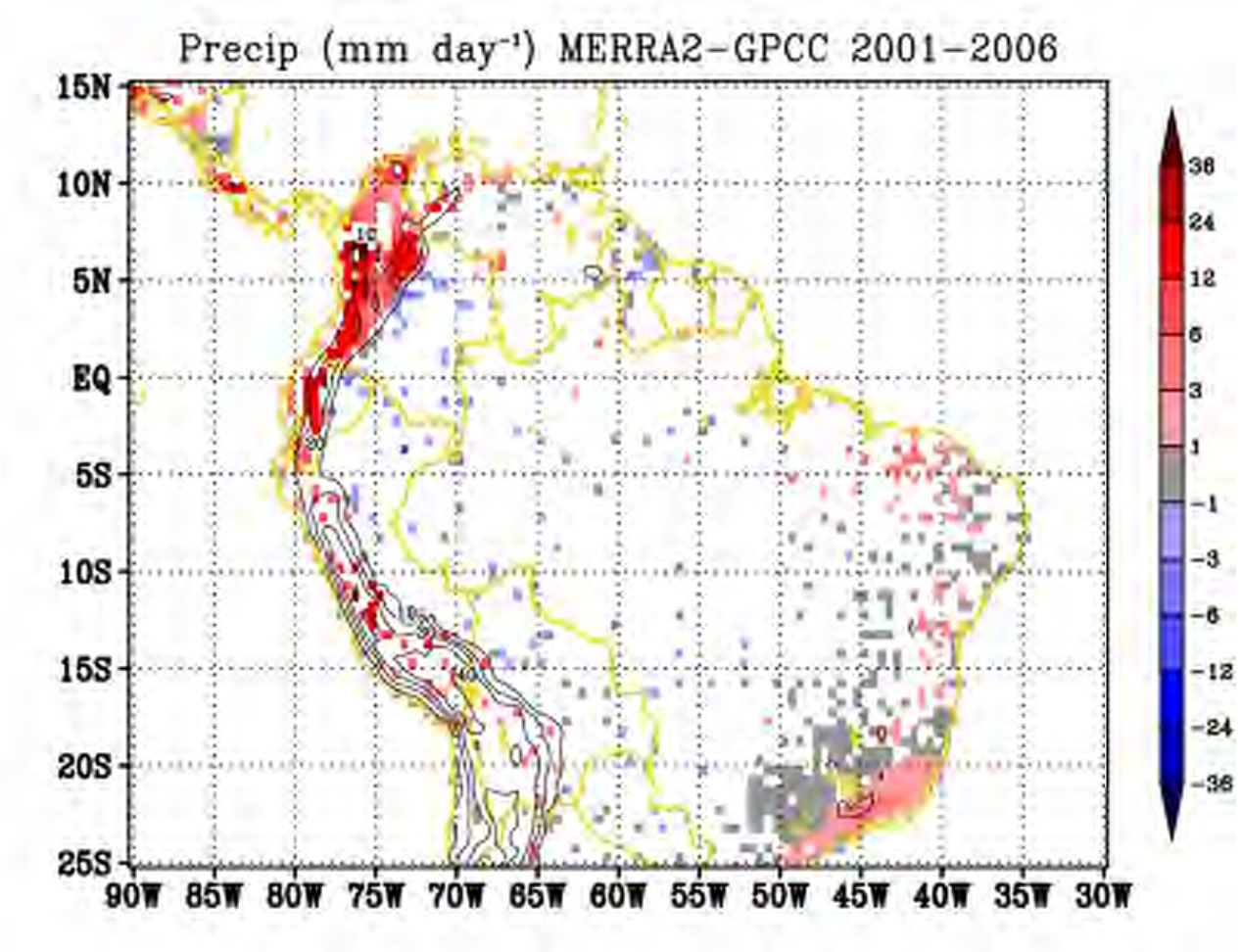

Figure 6-2 Differences between MERRA-2 modeled precipitation and GPCC gridded gauge data product (Schneider et al. 2011) filtered to the locations in space and time where gauges are present. Surface altitude is contoured in meters/100.

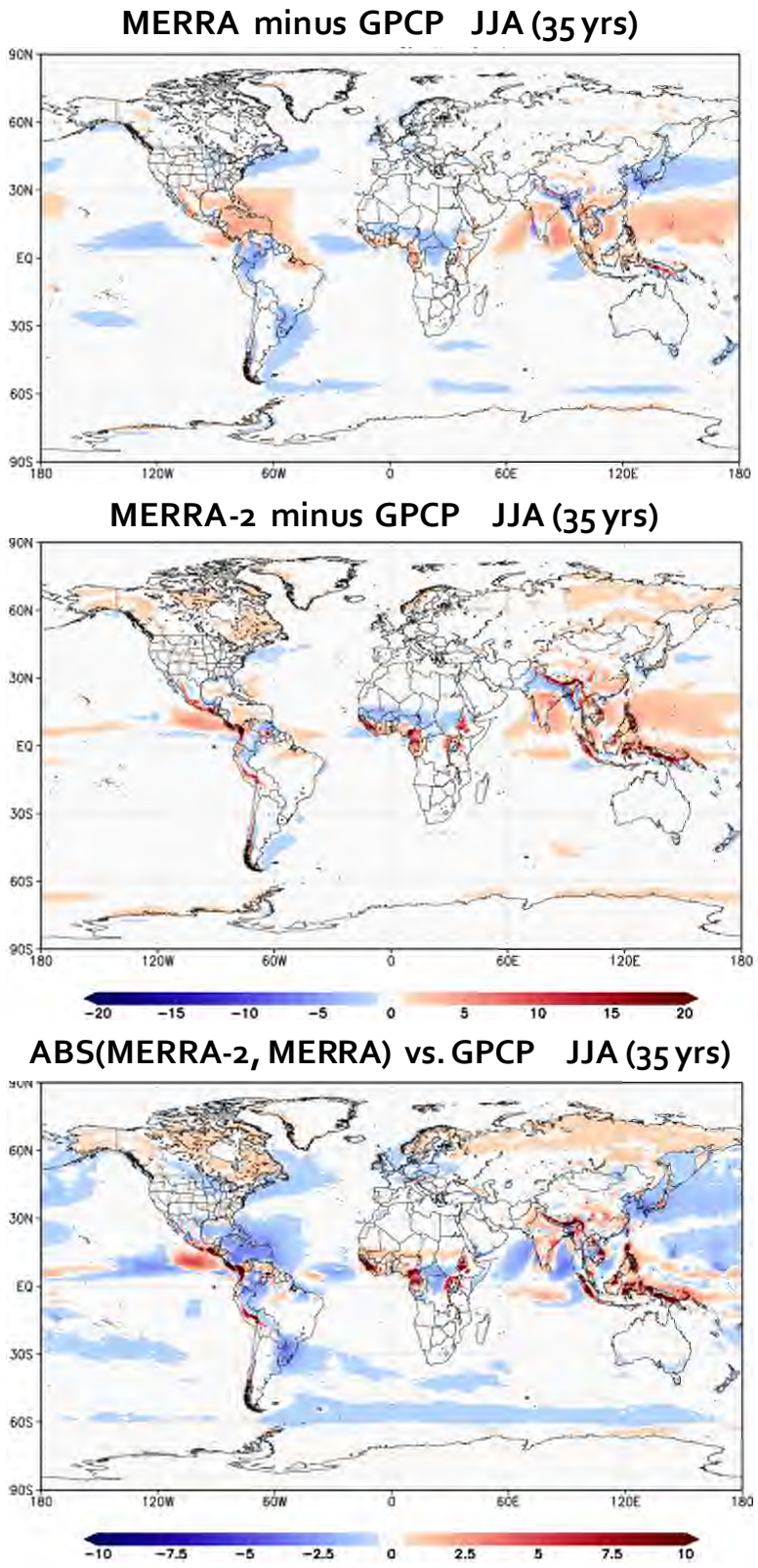

Figure 6-3 Precipitation differences from GPCP for MERRA (top), MERRA-2 (middle) and the closeness map of the biases (bottom). The bottom panel shows |MERRA-2-GPCP|-|MERRA-GPCP|, so blue values indicate that MERRA-2 is closer to GPCP than is MERRA.

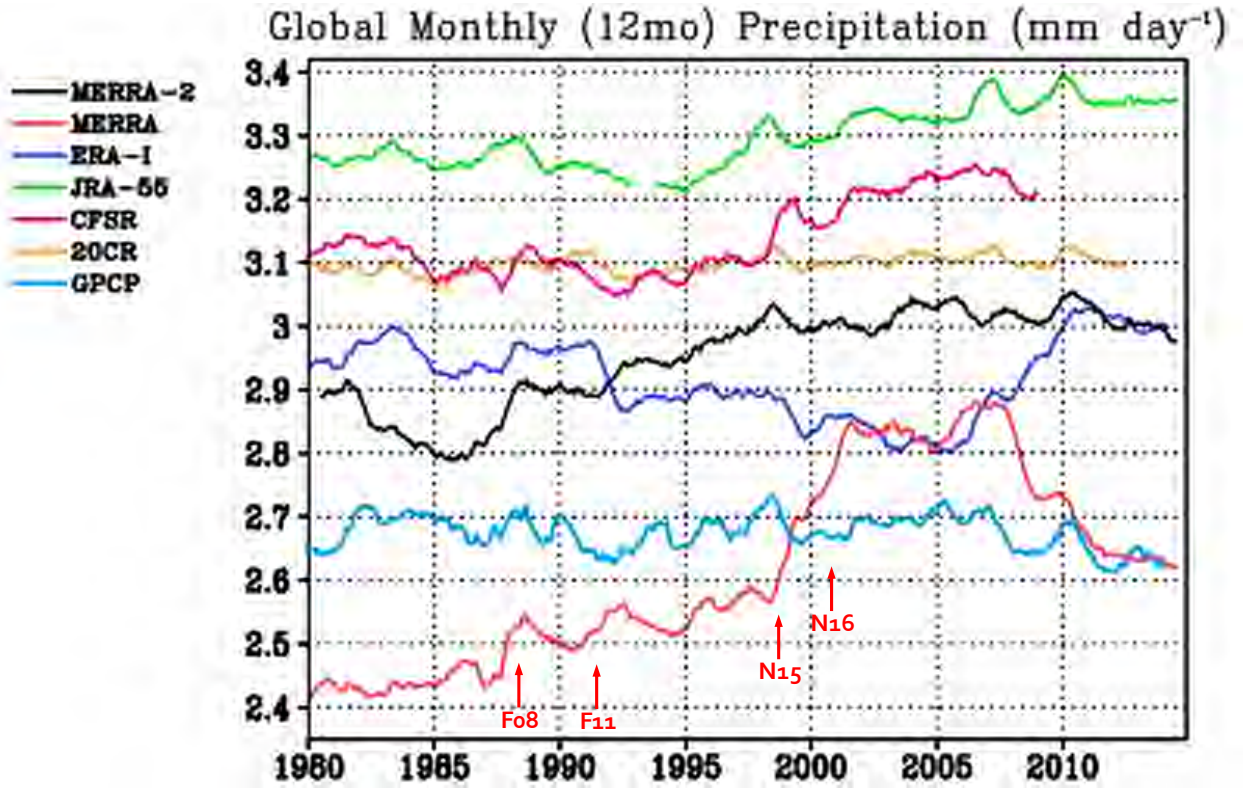

Figure 6-4 Time series of globally averaged precipitation (12 month running mean) for several reanalyses and GPCP merged gauge satellite data. SSM/I instruments (from F08 and F11 satellites) and AMSU-A instruments (from NOAA-15 and NOAA-16) are assimilated starting near the markers on the figure.

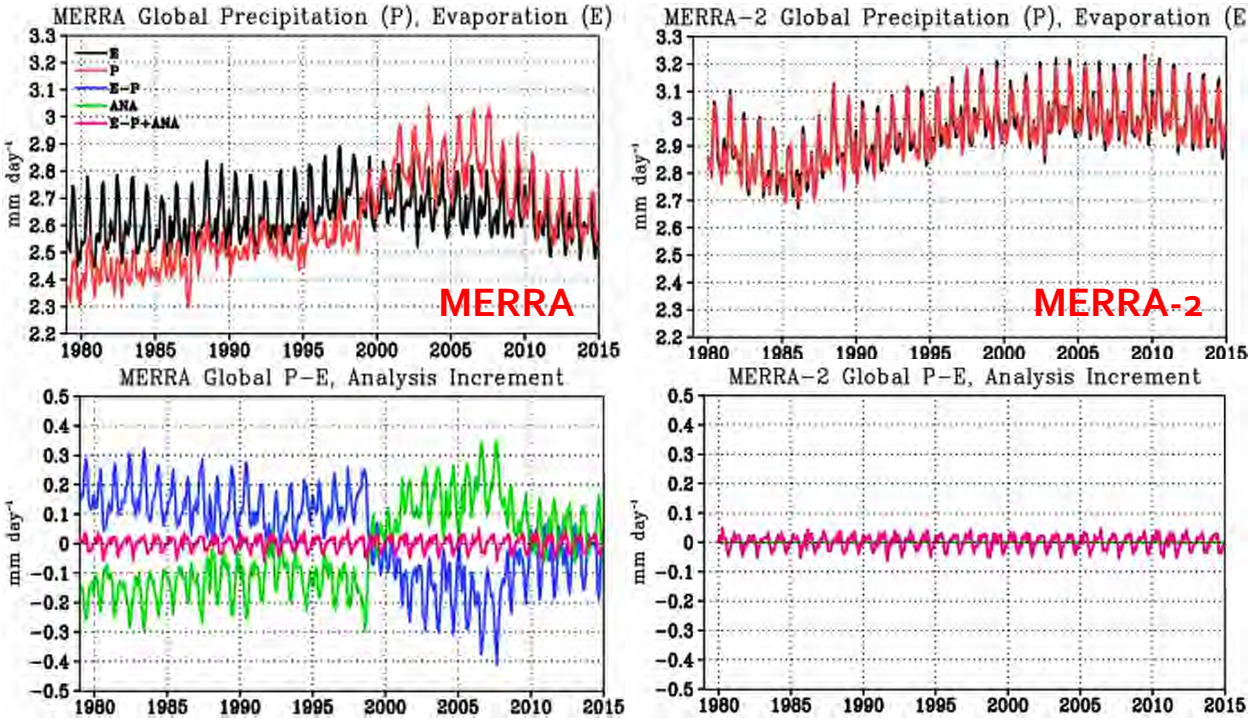

Figure 6-5 Global time series of monthly mean water cycle terms for MERRA (left) and MERRA-2 (right). Here, precipitation is modeled output. Units are mm day^{-1}.

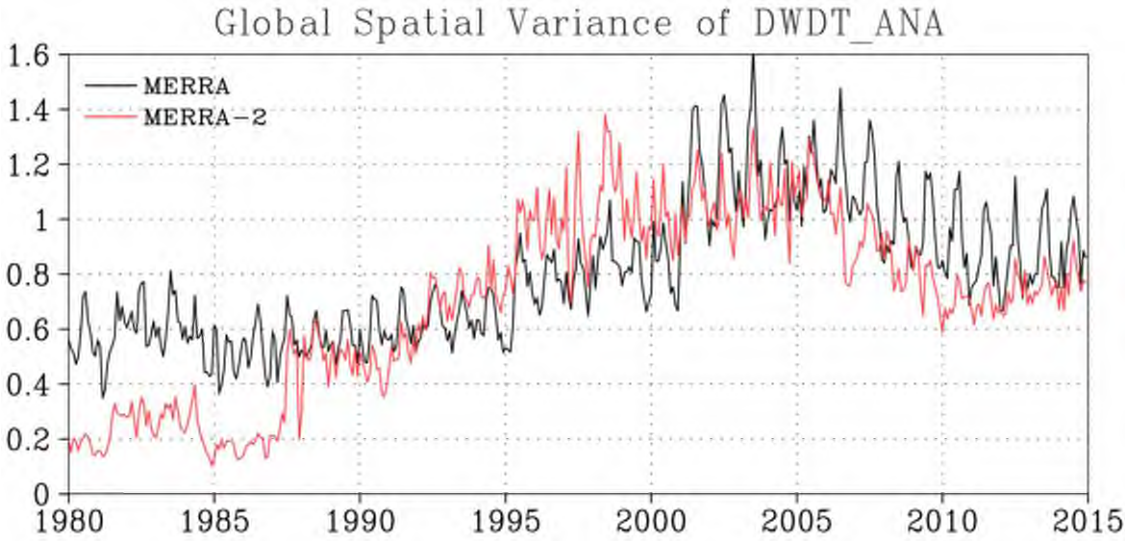

Figure 6-6 Global spatial variance of the analysis tendency of vertically integrated total water mass in the atmosphere for MERRA and MERRA-2. This figure indicates that the global spatial variations of water increment in MERRA-2 are similar to those in MERRA, even though the global mean of the increment is constrained in the former.

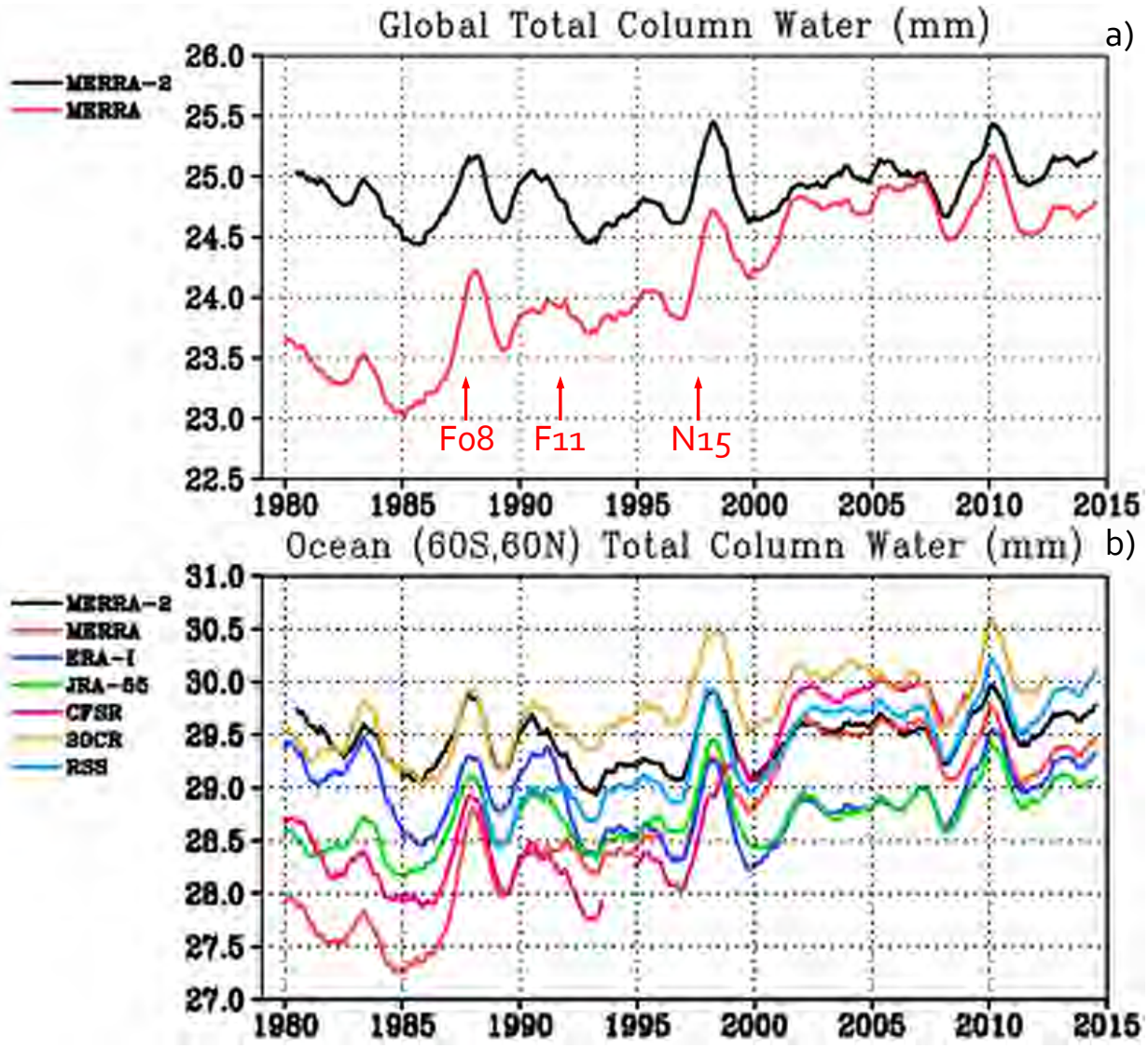

Figure 6-7 Time series of total column water in (a) the global average (comparing MERRA with MERRA-2 and identifying some key changes to the input data systems) and (b) for the ocean domain between 60N and 60S (comparing contemporary reanalyses with RSS total column water based on SSMI data). In (a) the start of some instruments are noted by their satellite platform identifiers, specifically, SSM/I (on board F01 and F11) and AMSU-A (on board NOAA-15).

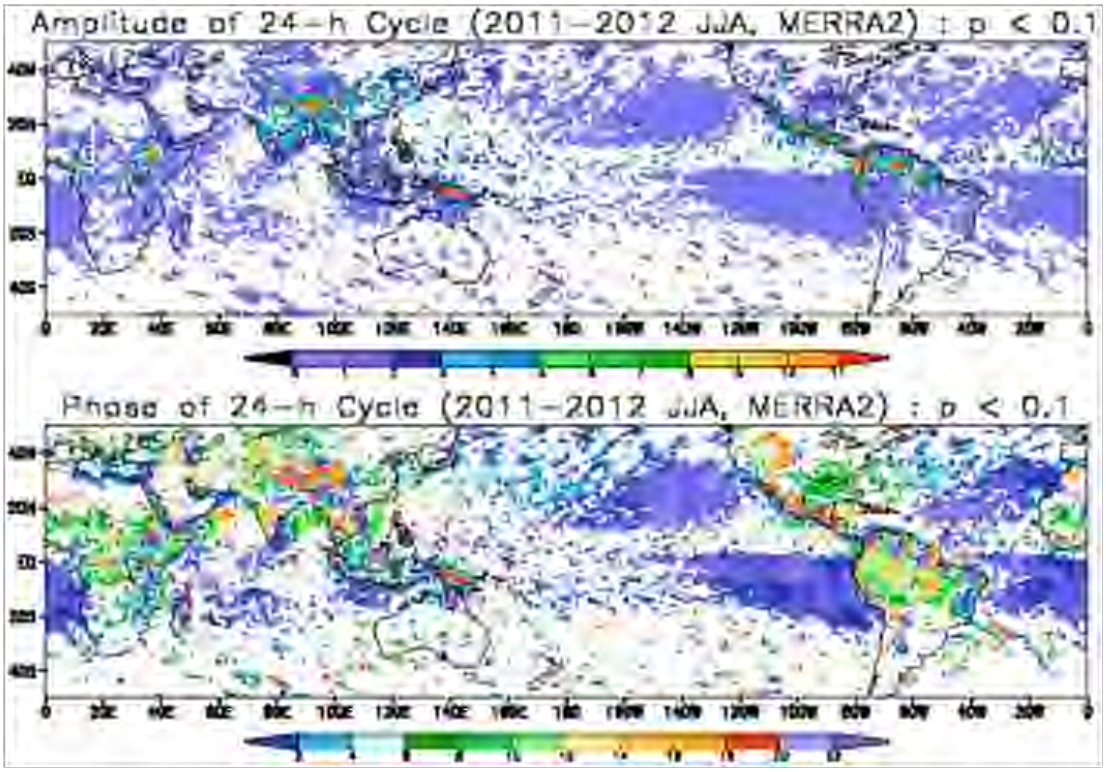

Figure 6-8 Amplitude (top, mm day^{-1}) and phase (bottom, hour of the day) of the modeled precipitation diurnal cycle in MERRA-2.

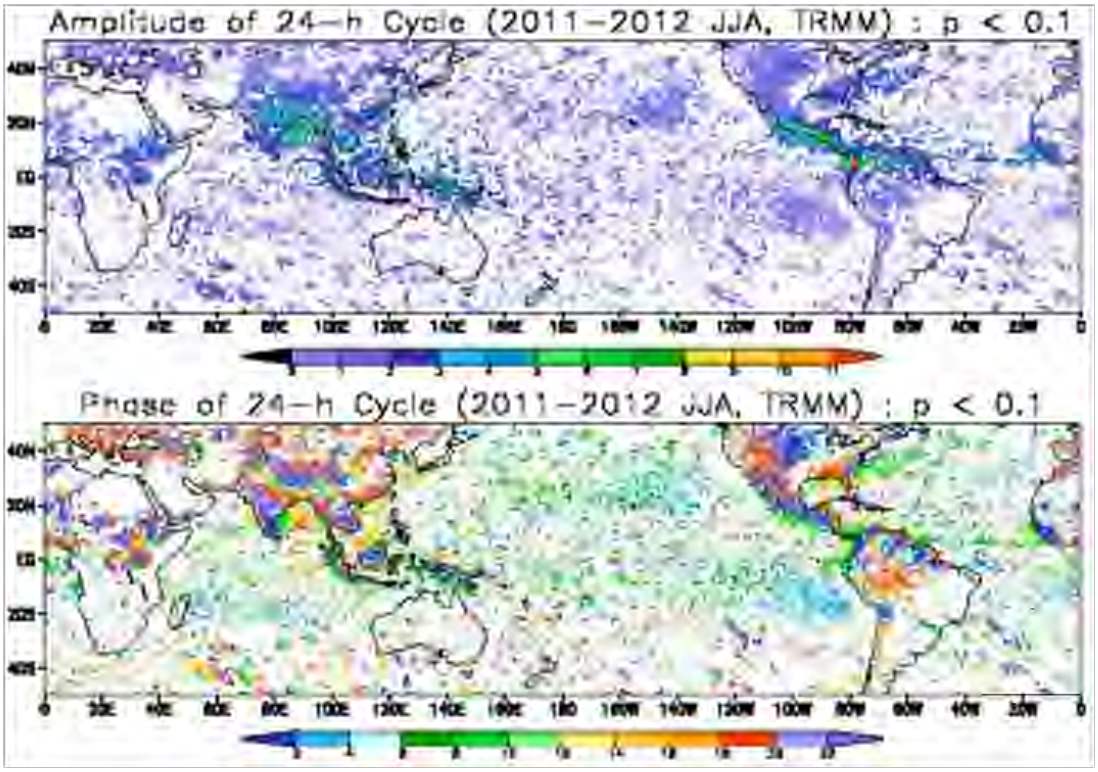

Figure 6-9 As in Figure 6-8 except for TRMM 3 hourly merged gauge-satellite data.

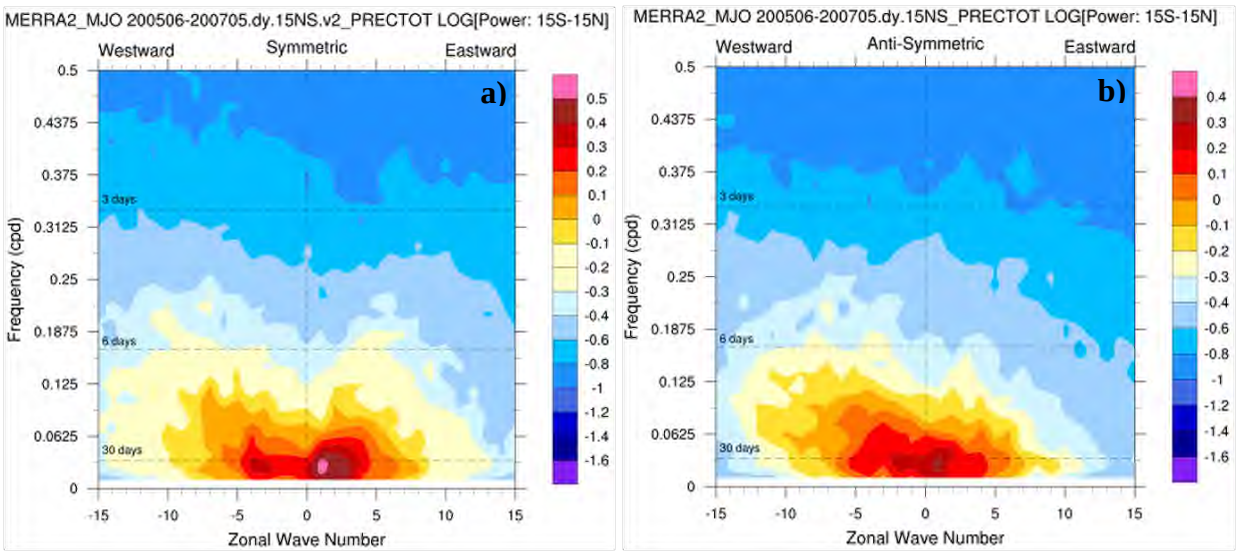

Figure 6-10 Spatio-temporal spectral power (after taking base-10 logarithm) of the MERRA-2 modeled precipitation data (mm/day) from June 2005 to May 2007 for the (a) symmetric component and (b) anti-symmetric component.

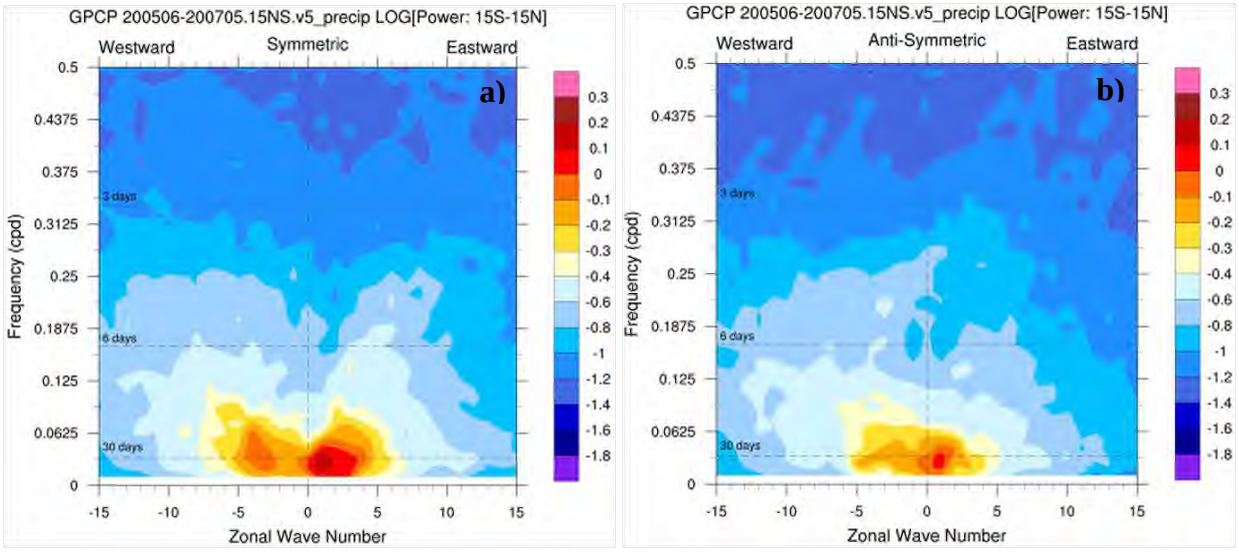

Figure 6-11 As in Figure 6-10, except for GPCP merged gauge-satellite data product.

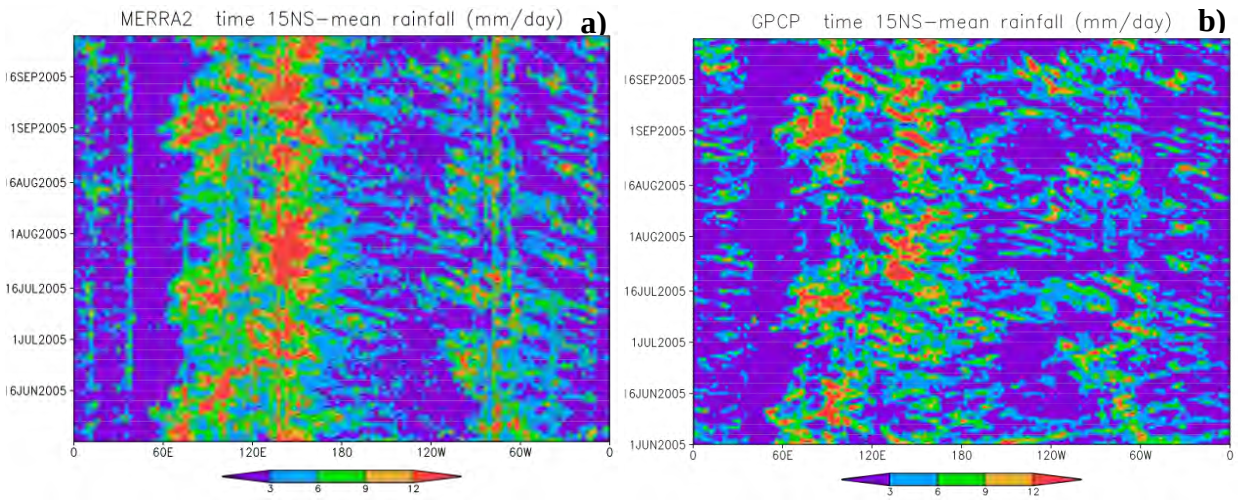

Figure 6-12 Time-longitude plot of (a) MERRA-2 modeled precipitation and (b) GPCP gauge-satellite merged precipitation, in mm/day and averaged between 15N and 15S.

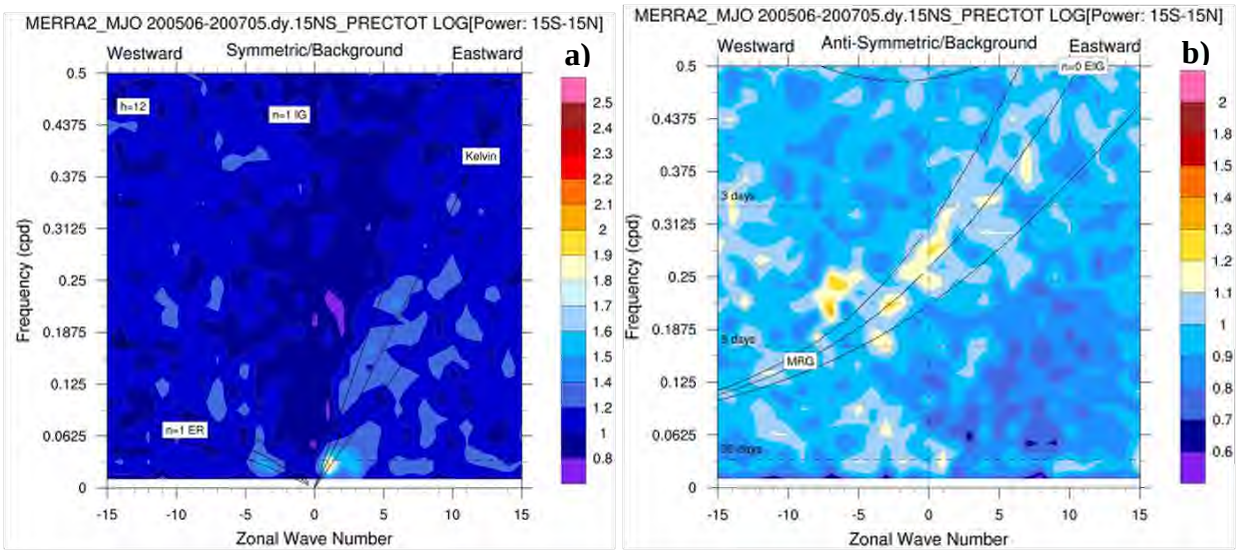

Figure 6-13 The MERRA-2 ratio between Figure 6-10a and the smoothed version of the average of Figure 6-10a and b, for the (a) symmetric component and (b) the anti-symmetric component.

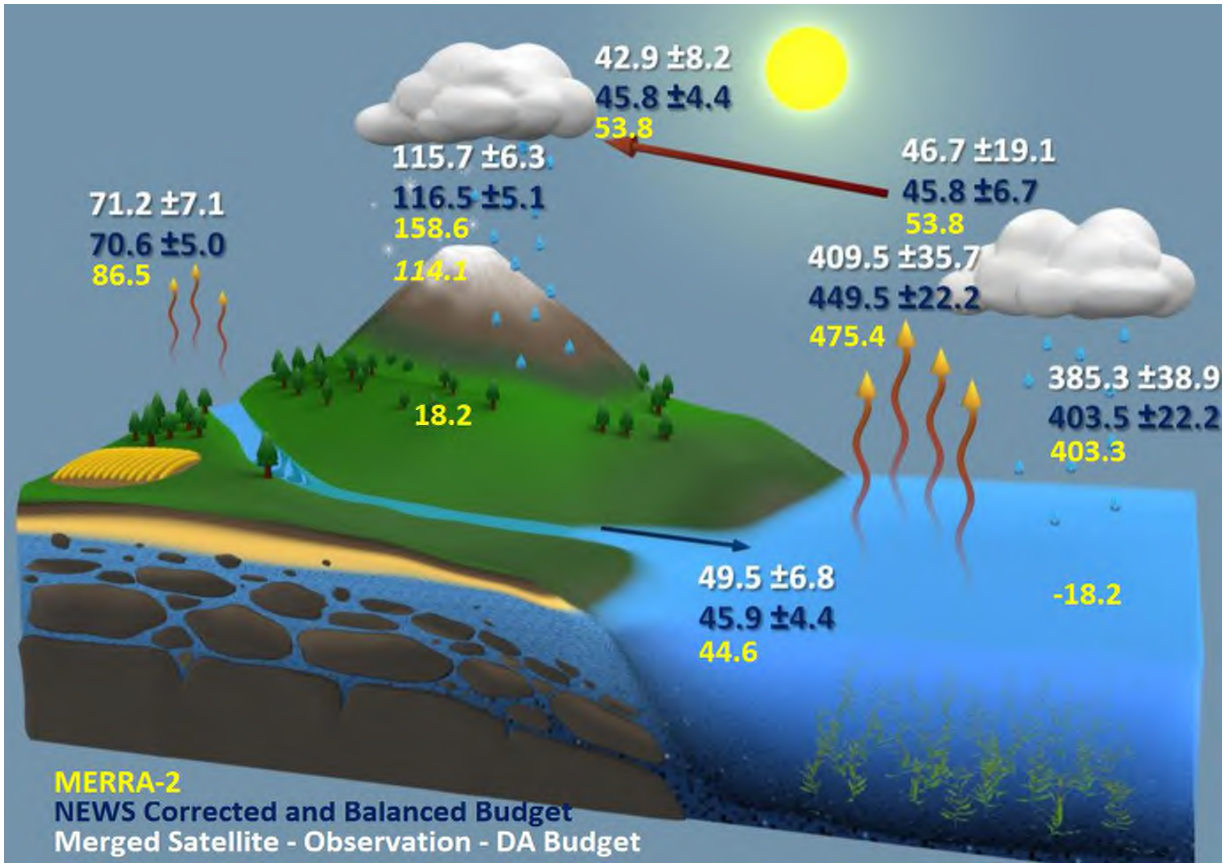

Figure 6-14 Depiction of the global water cycle developed by NEWS (Rodell et al. 2015) from NASA observing systems for 2000-2010, including the collected data (white) and a balance corrected budget (blue). MERRA-2 data are in yellow. The 18.2×1000km^{3}yr^{-1}value for ocean and land indicates the MERRA-2 water vapor analysis increment. The italicized yellow value of precipitation is the observation-corrected land forcing precipitation. Uncertainty estimates were given by data providers and refined in the balanced budget. Units are ×1000km^{3}yr^{-1}.

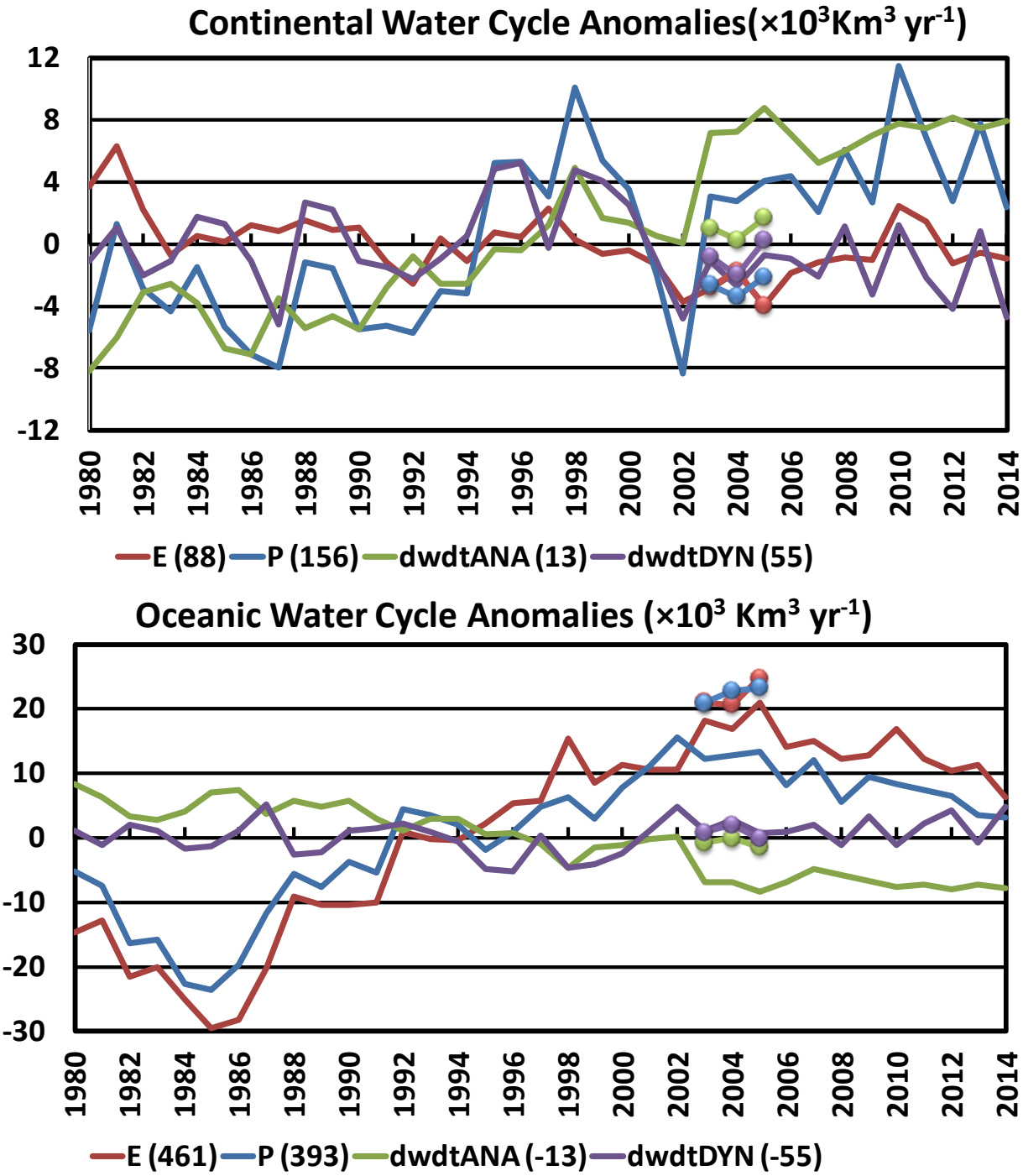

Figure 6-15 Time series of MERRA-2's annual water cycle anomalies (relative to the 1980-2014 mean), areally averaged over land (top) and ocean (bottom). The water cycle components depicted are evaporation (E), modeled precipitation (P), analysis increment (dwdtANA) and transport from ocean to land (dwdtDYN, derived from the moisture flux convergence). An experiment withholding AIRS radiances was executed to test its sensitivity and is depicted here by the 3 dotted years from 2003-2005.

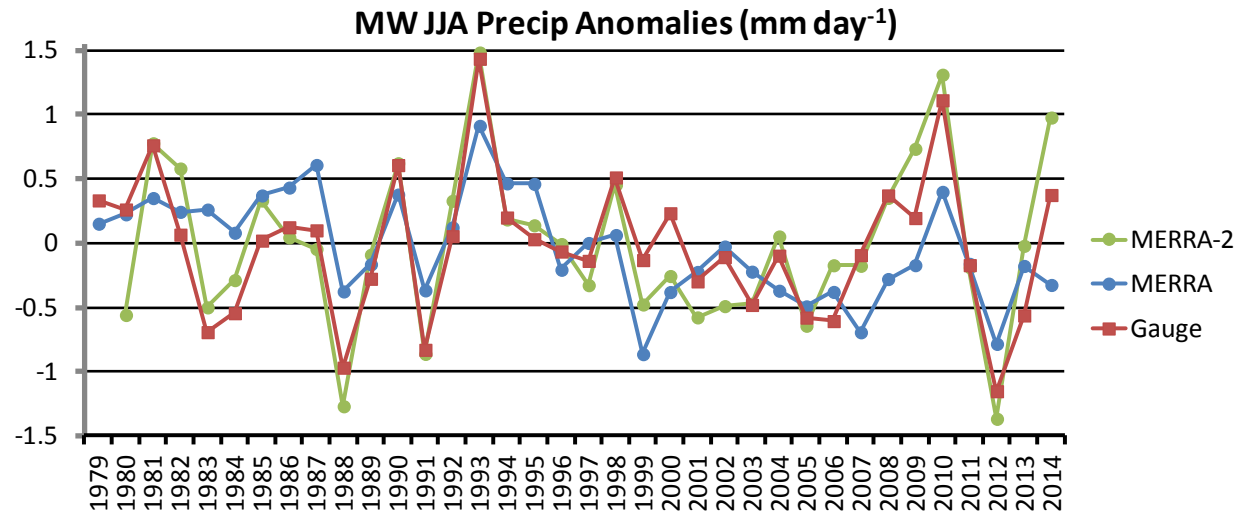

Figure 6-16 Time series of Midwestern US summer seasonal precipitation anomalies, following Bosilovich (2013). The anomalies are from the 1980-2011 JJA mean. The gauge data are from CPC gridded daily data for the US (Chen et al. 2008; Xie et al.2007). MERRA-2 precipitation is from the model-generated fields.

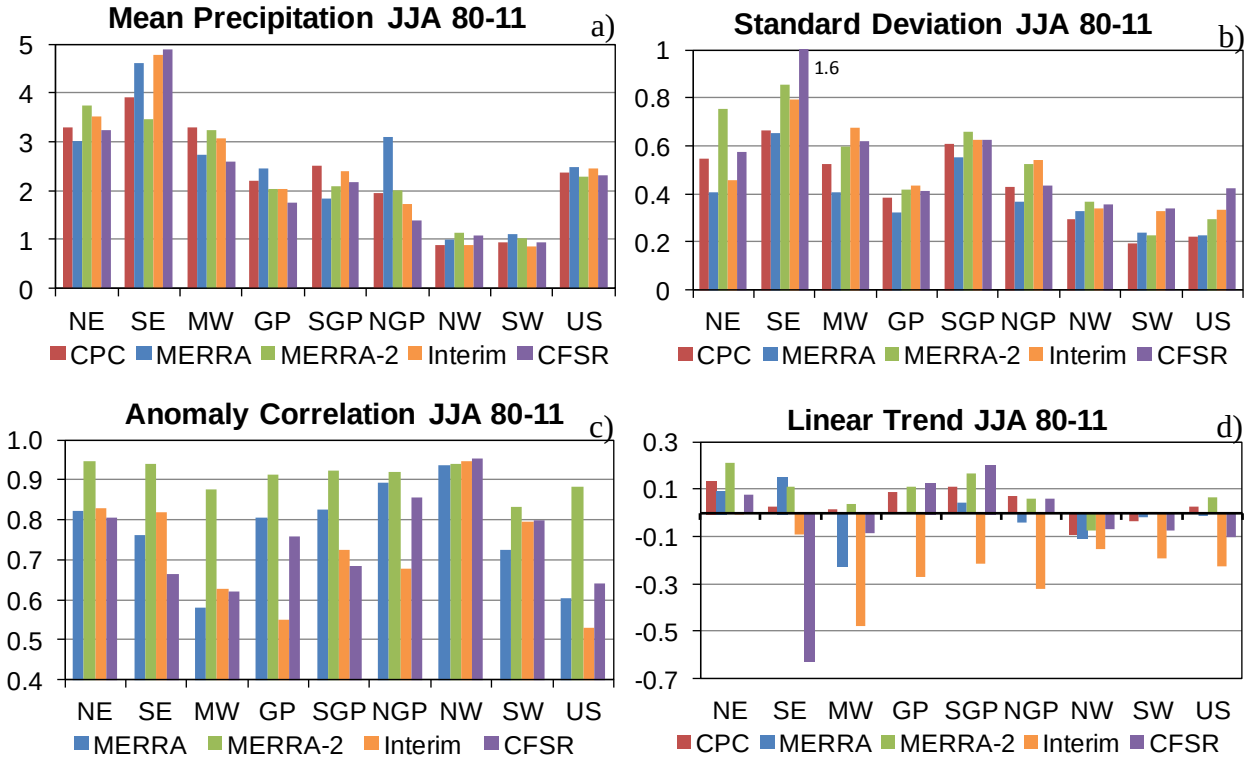

Figure 6-17 Summary statistics for the JJA seasonal anomaly time series of precipitation: (a) mean (mm day^{-1}), (b) standard deviation (mm day^{-1}), (c) anomaly correlation to CPC gauge observations (-), and (d) linear trend (mm day^{-1} per decade). The time series examined covers 1980-2011. The regions listed lie within the continental US and are as defined by Bosilovich (2013). The MERRA-2 precipitation is generated by the model; it is not the observation-corrected data used to force the land.

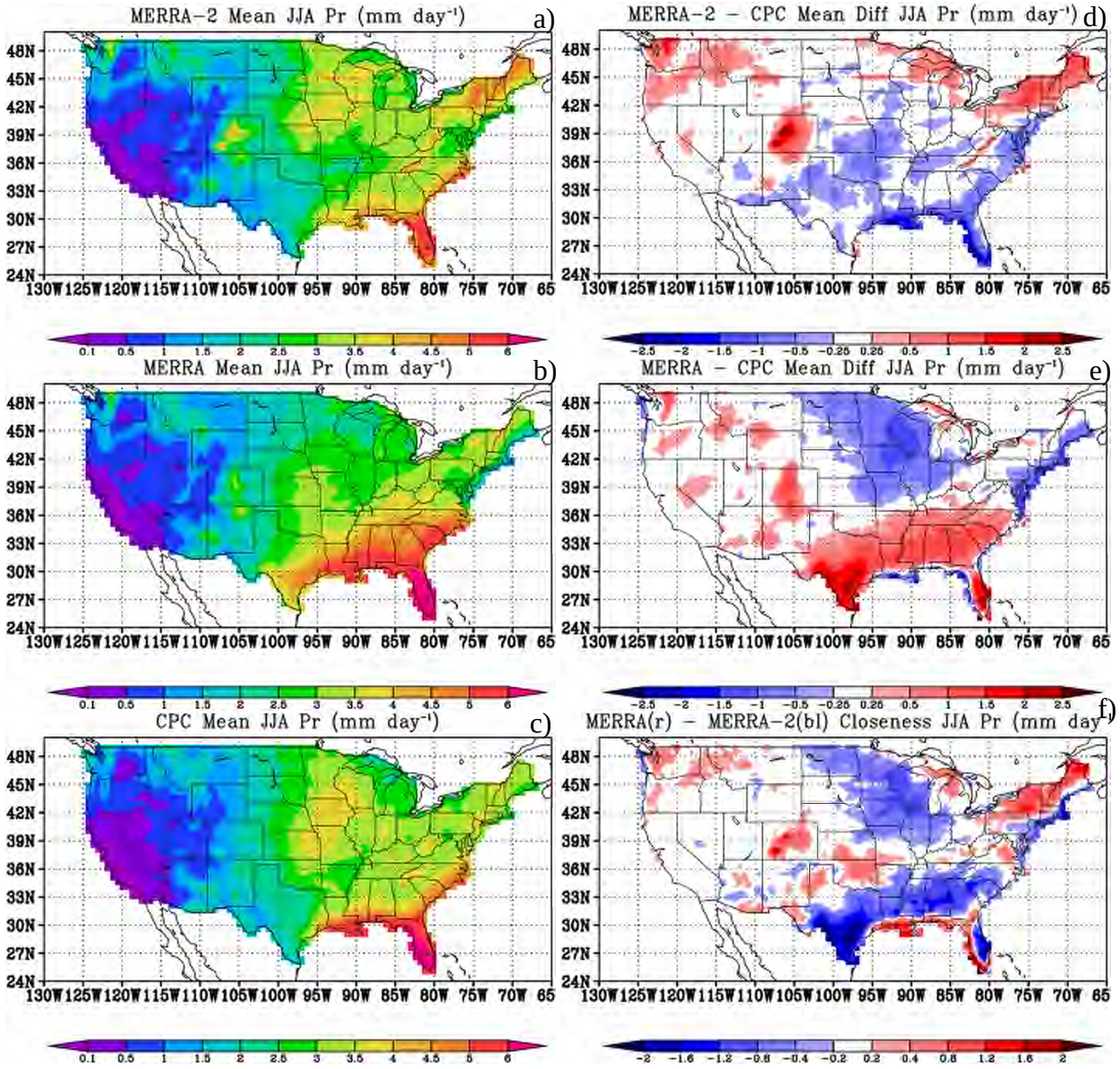

Figure 6-18 Comparison of modeled precipitation from MERRA-2 and MERRA with CPC gauge precipitation for JJA. (a) Mean for MERRA-2. (b) Mean for MERRA. (c) Mean for CPC. (d) Differences: MERRA-2 minus CPC. (e) Differences: MERRA minus CPC. (f) Closeness (|MERRA-2-CPC|-|MERRA-CPC|) shows which system has a mean value closer to CPC, either MERRA-2 (blue) or MERRA (red).

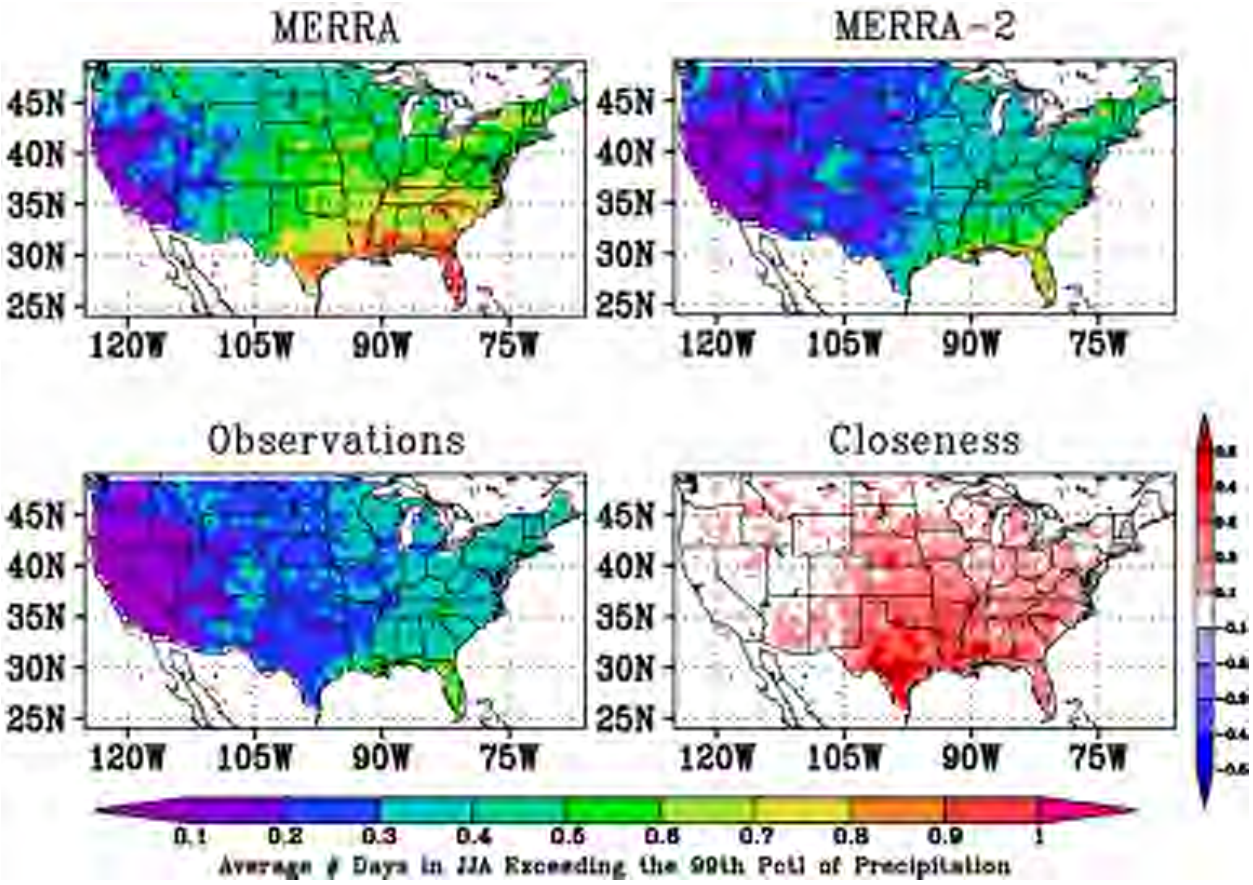

Figure 6-19 Average number of wet days per season of daily precipitation that exceeds the 99th percentile during JJA for MERRA, MERRA-2, and CPC Gauge observations. The lower right panel (closeness |MERRA-CPC|-|MERRA-2-CPC|) shows which reanalysis is closer to the observations – red indicates that MERRA-2 is closer, while blue indicates that MERRA is closer.

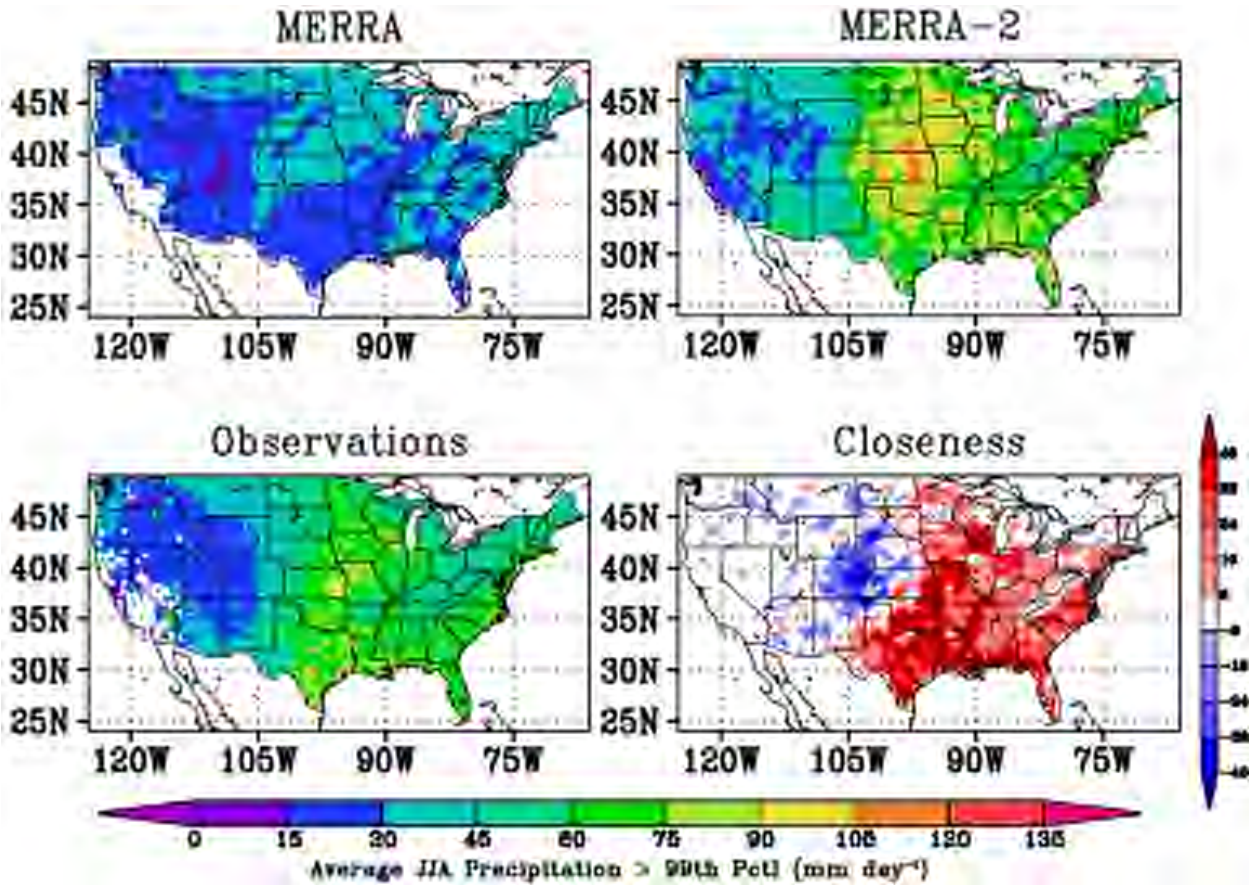

Figure 6-20 The average of the amount of precipitation that exceeds the 99th percentile during JJA for MERRA, MERRA-2, and CPC Gauge observations. The lower right panel (closeness |MERRA-CPC|-|MERRA-2-CPC|) shows which reanalysis is closer to the observations – red indicates that MERRA-2 is closer, while blue indicates that MERRA is closer.

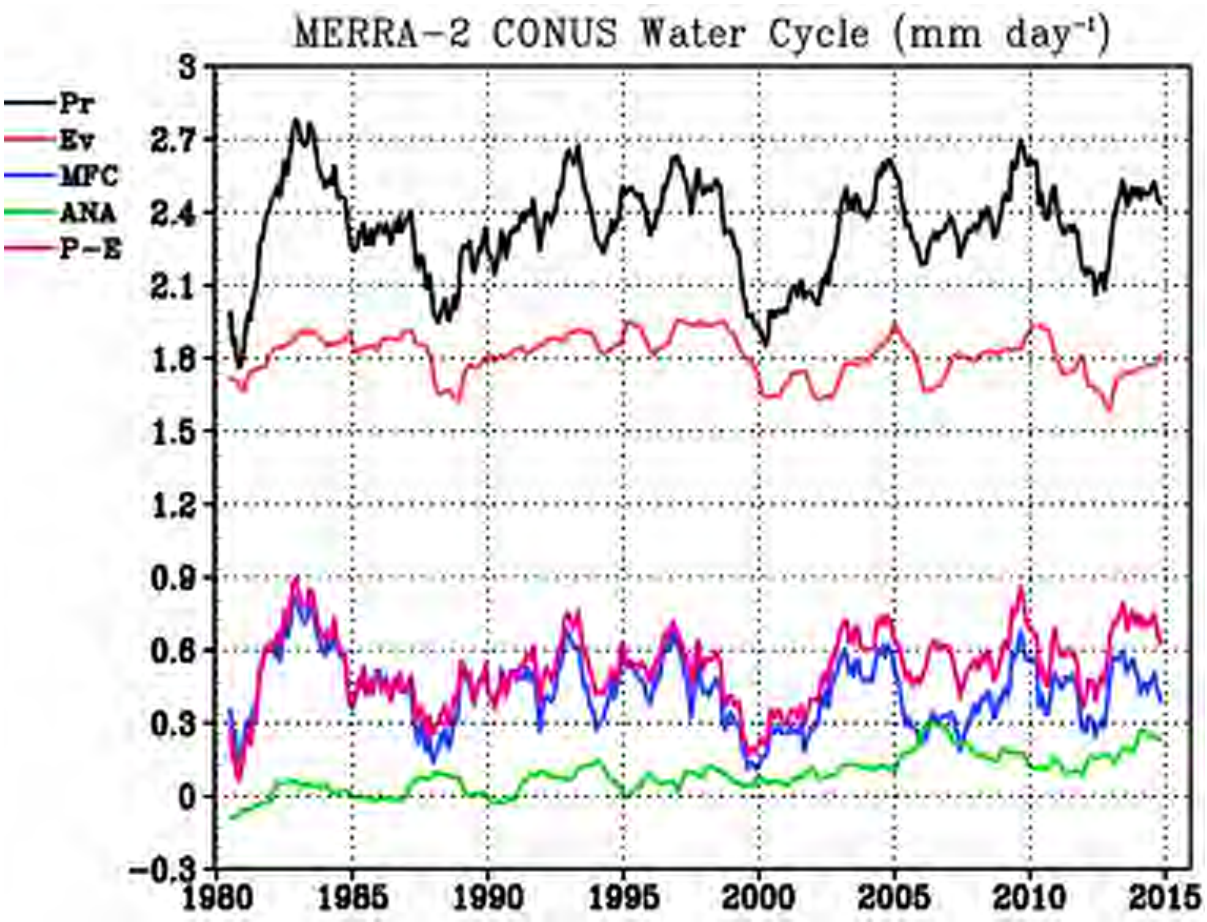

Figure 6-21 Time series of monthly atmospheric water budget terms spatially averaged over the continental US and filtered with a 12 month running average. The terms are precipitation (Pr, model generated), evaporation (Ev), moisture flux convergence (MFC) and analysis increment (ANA).

7. Land Surface

a. Precipitation Corrections at the Surface

A major advance between MERRA and MERRA-2 is the latter's use of observed precipitation to drive the surface water budget. The method used to introduce observed precipitation into the MERRA-2 system is briefly reviewed here; for more details refer to Reichle and Liu (2014). Recall that Section 6a provided a brief discussion of the climatological differences between the corrected precipitation and that which the model generates.

The precipitation seen by the surface of most reanalysis systems, including MERRA, is generated by the atmospheric modeling component of the system following the assimilation of atmospheric temperature and humidity observations. In contrast, the MERRA-2 model-generated precipitation is corrected with merged satellite/gauge-based precipitation observations before it reaches the surface (Reichle and Liu, 2014). Observation-corrected precipitation was used in NCEP's CFSR (Saha et al, 2010) and also in the offline (land surface model only) MERRA-Land data product, where it resulted in significantly better land surface moisture storage dynamics compared with MERRA (Reichle et al, 2011). In Section 7c, evaluation of the MERRA-2 soil moisture suggests that MERRA-2 also has significantly better surface moisture dynamics than MERRA.

Table 7-1 Precipitation correction regimes used in MERRA-2.

Region	**Observations (temporal/spatial resolution)**	**Correction Method**
Oceans and Africa	CMAP/GPCP2.1[a] satellite and gauge data (pentad / 2.5°)	Full correction to observations
Low and mid-latitude land (|lat|<42.5), except Africa	CPCU[b] gauge data (daily /0.5°)	Full correction to observations
Mid- to high latitude land (42.5° < |lat| < 62.5°)		Linear tapering between full observation correction at 42.5° and no correction (full use of MERRA-2 model-generated precipitation) at 62.5°
High latitude land (|lat| > 62.5°)	None	No correction.

[a]NOAA Climate Prediction Center (CPC) Merged Analysis of Precipitation / Global Precipitation Climatology Project, version 2.1 (Xie et al. 2007; Adler et al. 2003)

[b]CPC Unified Gauge-Based Analysis of Global Daily Precipitation (Chen and Xie, 2008).

Globally, there are four precipitation correction regimes in MERRA-2 (Table 7-1), including high-latitude land areas, where corrections are not applied; experience with MERRA-Land suggested that the sparse coverage of precipitation gauges in high latitudes may lead to significant biases there. The observed precipitation data sets in Table 7-1 have coarser temporal resolution and different spatial resolution than MERRA-2. Consequently, the observed precipitation is pre-processed onto the MERRA-2 grid at hourly resolution using precipitation from GEOS-5 systems (MERRA or GEOS-5 FP/IT) to provide the required spatial and temporal detail (Reichle and Liu, 2014).

The precipitation corrections are then calculated and applied separately for each day at each MERRA-2 grid cell, with the result that in regions with full corrections, the precipitation at the MERRA-2 surface for a given grid cell matches the observations at the daily scale. (Over Africa and the oceans, it matches the observations at the 2.5° pentad scale of the CMAP data.) Figure 7-1 shows the annual average corrected precipitation as well as the annual average adjustment made to the model-generated precipitation from MERRA-2. In the annual average sense, the greatest adjustments were made in the tropics, where precipitation is greatest, and over South America.

b. Land Surface Spin up: Discontinuities Over High Latitudes

MERRA-2 was produced using four streams, initialized in 1979, 1991, 2000, and 2010, with the first year of each stream designated as spin-up (Bosilovich et al. 2015). In high latitude land areas there are discontinuities in the land surface moisture storage between the consecutive MERRA-2 streams of which users should be aware. The land surface restart files for each MERRA-2 stream were themselves spun-up for at least 20 years using the offline MERRA-2 land model forced with MERRA surface meteorological fields, and with the precipitation replaced with the disaggregated precipitation observations described in Section 7a. In contrast to the MERRA-2 system, the offline land surface spin up did not taper back the precipitation forcing to the model-generated precipitation over high-latitude land (since the MERRA-2 model precipitation was not yet available). Consequently, over high latitude land, the difference between the observed precipitation used in the land surface spin-up and the MERRA-2 model-generated precipitation being used (at least in part) in the MERRA-2 system resulted in land surface moisture discontinuities at the introduction of each new stream. In other regions, where the MERRA-2 precipitation was fully corrected to the observations, the same precipitation was used in the off-line land spin up and in the MERRA-2 system, resulting in good continuity in the land surface states across consecutive MERRA-2 streams. The use of observation-corrected precipitation in MERRA-2 made this continuity possible.

Figure 7-2a demonstrates these high latitude discontinuities, showing the MERRA, MERRA-Land, and MERRA-2 precipitation over a high latitude land area in Siberia. MERRA-Land is plotted as a proxy for the MERRA-2 off-line land spin-up, since both used the full CPCU precipitation observations north of 42.5N. The peak summer precipitation in MERRA-2 was consistently 1-1.5 mm d^{-1} higher than in MERRA-Land, so that in Figure 7-2b the root-zone soil wetness fraction in MERRA-2 is ~0.2 higher than in MERRA-Land. Consequently, the MERRA-2 soil wetness is substantially lower than its long-term average at the beginning of each new stream, when the soil wetness reflects the drier MERRA-Land precipitation forcing used in the

off-line land spin up. As noted above, the precipitation corrections were not applied over high latitude land due to concerns over the quality of the observations there. However, MERRA-2 precipitation turned out to be much higher than MERRA over high latitude land, and a detailed comparison to observed data sets in Section 9b suggests that this difference can be attributed to a high bias in the MERRA-2 high latitude precipitation.

Figure 7-3 shows the root-zone soil wetness from each of the MERRA-2 streams, with values for the one year spin-up periods plotted alongside the officially released product. It is difficult to isolate the effect of the comparatively dry land surface restarts used to initialize each stream from the inter-annual variability, but Figure 7-2 and Figure 7-3 suggest that at least 2-3 years are required for the soil wetness to recover from each low initialization. Since the land surface turbulent fluxes in high latitudes are mostly energy limited, the consequences of this soil wetness spin up effect are less serious than they would be in other regions. For example, during the overlapping periods between streams in Figure 7-3, the inconsistency in soil wetness caused differences of only ~10 Wm^{-2} (10%) in the daily maximum latent heat flux and ~5 Wm^{-2} (25%) in the daily maximum sensible heat flux, which then resulted in differences of ~0.5 K in the 2m air temperature. The impact on the peak summer run-off is (relatively) larger, at ~1-2 mm d^{-1} (>50%). These values are an upper limit for the consequences of the soil wetness discontinuity in the MERRA-2 product, since in Figure 7-3 roughly half of the soil wetness discontinuity and spin-up effect is removed during the one year of spin-up allowed for each stream.

c. Evaluation of Selected Land Surface Variables

In this section, several land surface and associated low level atmospheric fields from MERRA-2 are evaluated, demonstrating consistent improvements from the MERRA system. Most land surface fields are not confidently observed at global scales, and so model estimates are typically evaluated against ground-based observations at a limited number of locations. Here, the MERRA-2 soil moisture and surface turbulent flux forecasts are evaluated using ground-based observations from within the US. However, the MERRA-2 screen-level (2m) air temperature and specific humidity are evaluated globally, using gridded data sets produced from global networks of weather station observations.

1) **Soil Moisture**

Figure 7-4 shows the average anomaly correlation (R_{anom}) and unbiased RMSE (ubRMSE) obtained with the MERRA, MERRA-Land, and MERRA-2 products when evaluated against in situ soil moisture observations from 140 SCAN network sites (Schaefer et al, 2007) distributed throughout the US. R_{anom} is calculated using anomalies from the mean seasonal cycle to give a measure of the synoptic time scale soil moisture dynamics, while the ubRMSE is defined as the root mean square error calculated after removing the mean difference between the modeled and observed soil moisture. (ubRMSE is thus also sensitive to seasonal-scale variability.) For both metrics, the MERRA-2 (and also MERRA-Land) surface and root-zone soil moisture is significantly better than the MERRA soil moisture. For example, the average root-zone R_{anom} increased from 0.43 for MERRA to 0.56 for MERRA-2, and the average ubRMSE was reduced from 0.06 m^3m^{-3} to 0.05 m^3m^{-3}.

Thus, at the locations tested, and in terms of the temporal variability targeted by the metrics in Figure 7-4, the soil moisture in MERRA-2 is significantly better than that in MERRA. This suggests MERRA-2 has achieved the improved soil moisture dynamics of the offline MERRA-Land system, but in the context of a coupled atmosphere-land system. The MERRA-2 improvements are due largely to the use of observation-corrected precipitation and to updates to the treatment of canopy interception in MERRA-Land and MERRA-2 (Reichle, et al 2011).

2) **Latent and Sensible Heating**

Figure 7-5 compares the surface monthly sensible and latent heat fluxes from MERRA and MERRA-2 to that from CEOP flux tower observations (CEOP/EOP-4, from the CEOP Reference Site Data Archive) over the Southern Great Plains region of Kansas and Oklahoma. The monthly estimates were obtained by averaging hourly estimates from 23 CEOP flux towers (and from the encompassing model grid cell for the corresponding model estimates). Both MERRA and MERRA-2 are quite close to the sensible and latent heat flux observations, with time averaged absolute errors in the monthly fluxes of <10 Wm^{-2}. For both latent and sensible heat, the mean absolute error for MERRA-2 was slightly (~ 1 Wm^{-2}) smaller than for MERRA, but this result is likely not significant given the uncertainty in the observations. There are however, some periods of divergence from the observations. For example, MERRA-2 consistently overestimates the summer latent heat flux (by ~ 20 Wm^{-2} initially, then by ~ 40 Wm^{-2} after 2006), while also overestimating the summertime sensible heat flux after 2006 (by ~ 10-20 Wm^{-2}).

3) **Screen-level (2m) Air Temperature**

Figure 7-6 shows time series of T2m, averaged over land and over each year independently, for MERRA, MERRA-2, and CRU 0.25° gridded station observations (CRU TS v. 3.22; Harris et al, 2014). Results are shown for daily mean, daily minimum, and daily maximum temperatures. Figure 7-7 shows the spatial distributions of the daily minimum and daily maximum mean 1980-2013 T2m biases. In Figure 7-7 the large differences between the reanalyses and CRU data over Greenland and Yemen / Oman are suspected to be due to issues with the CRU data and are not considered further here.

For the time series in Figure 7-6, the annual biases in both MERRA and MERRA-2 remain reasonably consistent through time. While the daily mean MERRA-2 bias is very small (net bias of 0.1 K over the plotted time period), this is due to the offset between the cool daytime bias (Figure 7-6b; net bias of 0.8 K) and the warm nighttime bias (Figure 7-6c; net bias of -0.6K). In contrast, the MERRA daily mean temperature has a warm bias (net bias of 1.0 K), due to warm biases during both day (0.3 K) and night (1.6 K).

The right hand panels of Figure 7-7 show why the magnitude of the spatially averaged daily maximum bias in Figure 7-6b is larger for MERRA-2 than for MERRA: MERRA-2 has corrected MERRA's positive biases in the low and mid latitudes but has not corrected the cool biases north of 45N. Consequently, MERRA-2 is on average still closer to the observations, as indicated by

the prevalence of blue colors in Figure 7-7f. (The spatial average of the absolute daily maximum T2m bias is reduced from 2.0 K for MERRA to 1.5 K for MERRA-2.) Note that in Figure 7-7 the very large warm daily maximum T2m bias over southern South America in MERRA (>5 K) has been largely removed in MERRA-2. For both reanalyses, the cool bias in daily maximum T2m in the high northern latitudes is strongest in the Boreal summer, although it does persist through most of the year (not shown).

For the daily minimum biases, Figure 7-7 shows that MERRA is consistently biased warm across global land areas and that MERRA-2 reduces this bias (with some overshoot to small negative biases), except in a region spanning western China through eastern Russia. The MERRA and MERRA-2 daily minimum T2m biases in this region are greatest in the Boreal winter, although MERRA (but not MERRA-2) is also biased here in other seasons (not shown).

In summary, the T2m biases in MERRA-2 are generally less than in MERRA, particularly in the Southern Hemisphere, where MERRA-2 has corrected large (3-5 K) biases in many areas. In general, the MERRA-2 annual daily maximum biases are typically less than 1 K, except over the Amazon and north of 45N, where MERRA-2 has cool biases of 2-5 K. The latter biases, which peak in Boreal summer, are retained from MERRA, while over the Amazon the MERRA-2 cool bias still represents a substantial improvement from MERRA. The MERRA-2 daily minimum biases are also generally less than 1 K globally, except for an arc from western China through eastern Russia, where warm biases of up to 5 K have been retained from MERRA. This warm bias occurs principally in the Boreal winter.

4) **Screen-level (2m) Specific Humidity**

Figure 7-8 shows, for both MERRA and MERRA-2, maps of the biases in average annual q2m relative to HadISDH 5° gridded observations (HadISH vn 2.0.0.2013p; Willet et al, 2014). The biases are largely unchanged from MERRA to MERRA-2, with the exception of the dramatic reduction in the large dry biases (exceeding 5 g/kg in places) in MERRA over southern South America. Even with the incomplete HadISDH spatial coverage, there is a reasonably clear pattern of MERRA-2 being drier (typically by 1-2 g/kg) than the observations everywhere except in Eurasia north of about 55N, where it is approximately 0.5 g/kg wetter. Specific humidity estimates derived from 6-hourly ERA-Interim output (c/o K. Willet) show good agreement to the HadISDH data, including in northern Eurasia. This suggests that the large differences in northern Eurasia in Figure 7-8 are due to MERRA-2 (and MERRA) biases rather than to artifacts in the HadISDH data. The MERRA-2 dry biases south of 55N occur throughout the year, although they are reduced in the winter hemisphere, and the wet bias in northern Eurasia occurs in Boreal spring and summer only (not shown).

Comparison of Figure 7-6 and Figure 7-7 show some consistency between the biases in q2m and daily maximum T2m. In particular, both show dramatic improvements in MERRA-2 over South America, where MERRA has large warm (>5 K) and dry (<-0.5 g/kg) biases south of -15N. (MERRA's large warm bias over the Amazon is also removed, but the q2m data have insufficient coverage to evaluate the humidity there.) Likewise, MERRA-2 has a larger daily maximum T2m

cool bias north of 45N than does MERRA, which is somewhat consistent with MERRA-2 also having a larger wet bias than MERRA in the same area. These high latitude cool and wet biases both peak in Boreal summer, consistent with the overestimated summer precipitation in Figure 7-2.

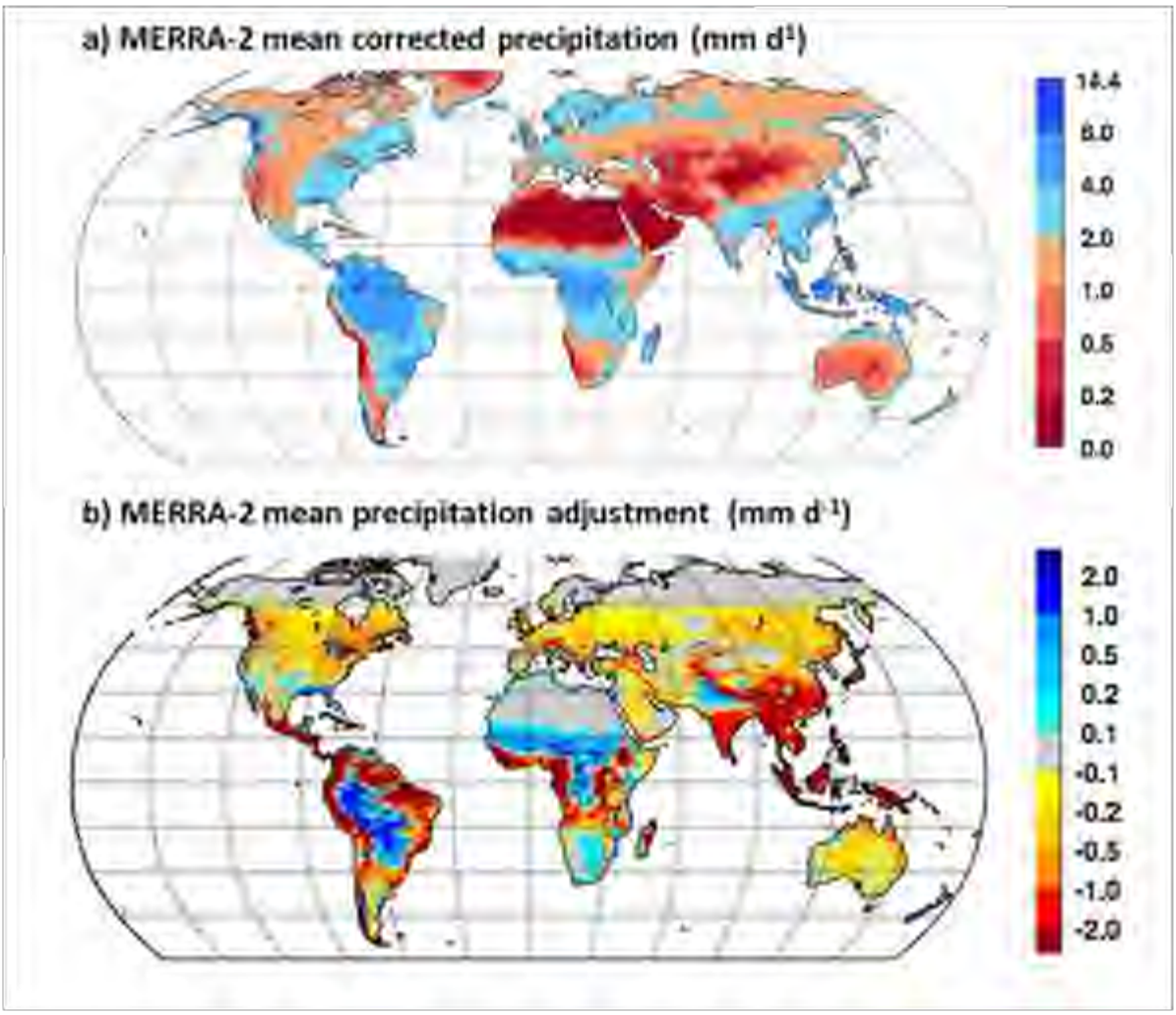

Figure 7-1 (a) Mean (over 1980-2014) observation-corrected precipitation. (b) Associated precipitation adjustments applied in MERRA-2 (observation-corrected precipitation minus model-generated precipitation).

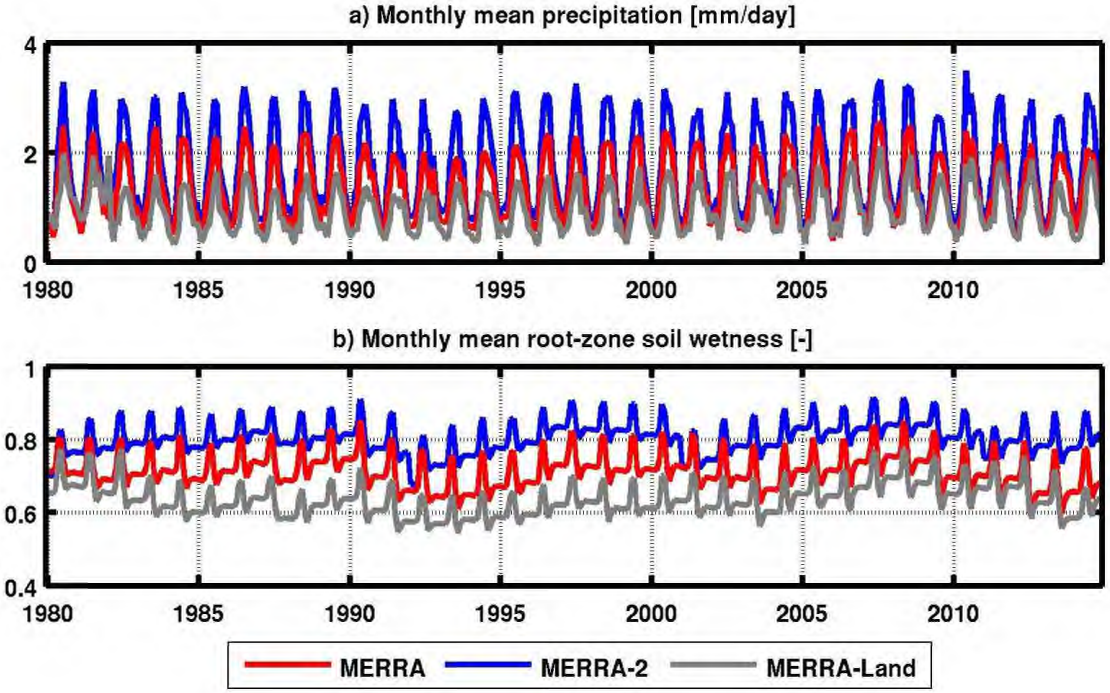

Figure 7-2 Monthly mean (a) precipitation, and (b) root-zone soil wetness, from MERRA, MERRA-2, and MERRA-Land, averaged over a Siberian region [from (60N, 40E) to (75°N,180°E)]. The MERRA-2 product streams begin in January of 1980, 1991, 2000, and 2010 after a full year of spin up.

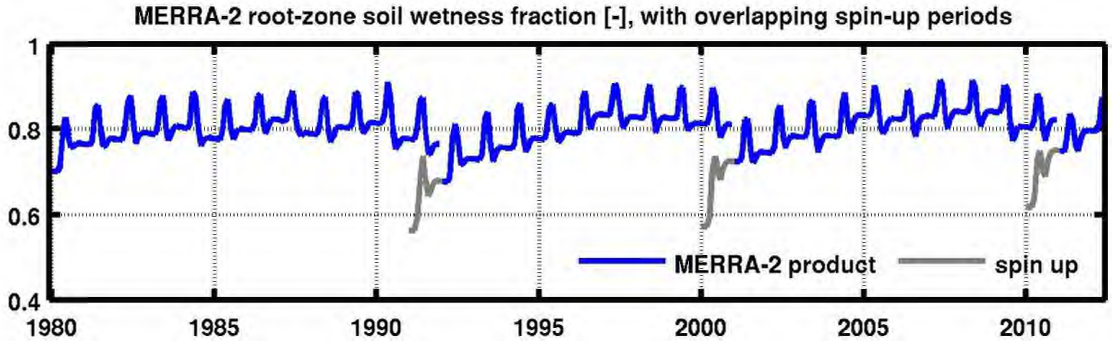

Figure 7-3 Monthly mean root-zone soil wetness for the official MERRA-2 product (blue) and each one year spin up period (grey), for the same Siberian region plotted in Figure 7-2

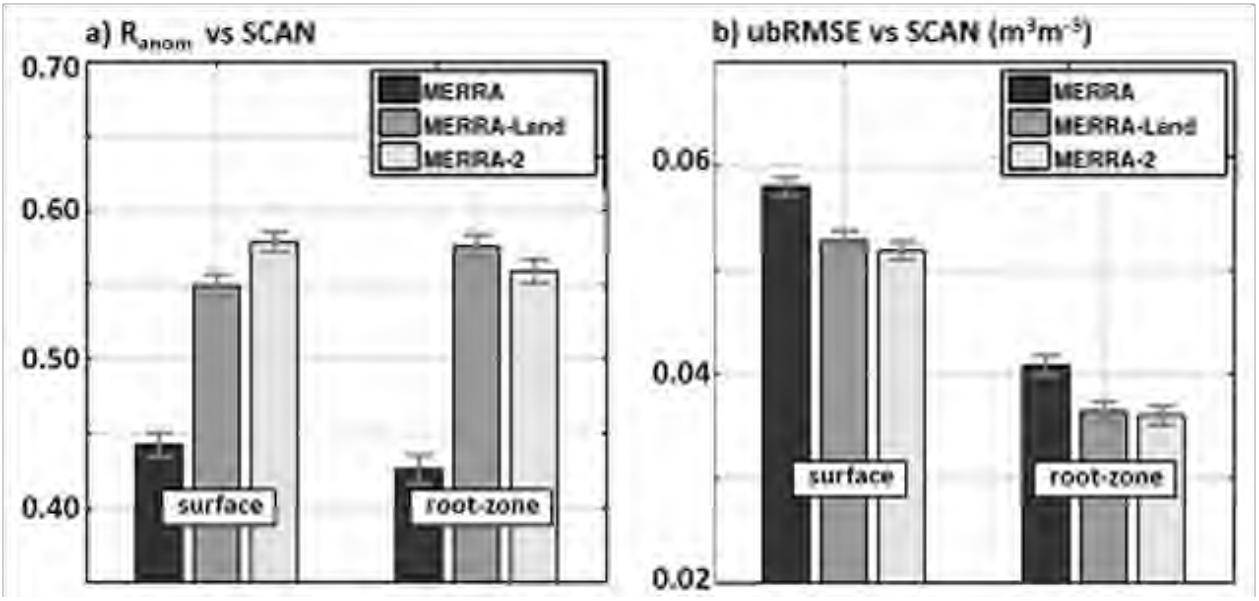

Figure 7-4 Network-averaged (a) R_{anom} and (b) ubRMSE for near-surface and root-zone soil moisture for MERRA, MERRA-Land, and MERRA-2 evaluated against in situ observations from the SCAN network in the US covering 2002-2014. Error bars show 95% confidence intervals.

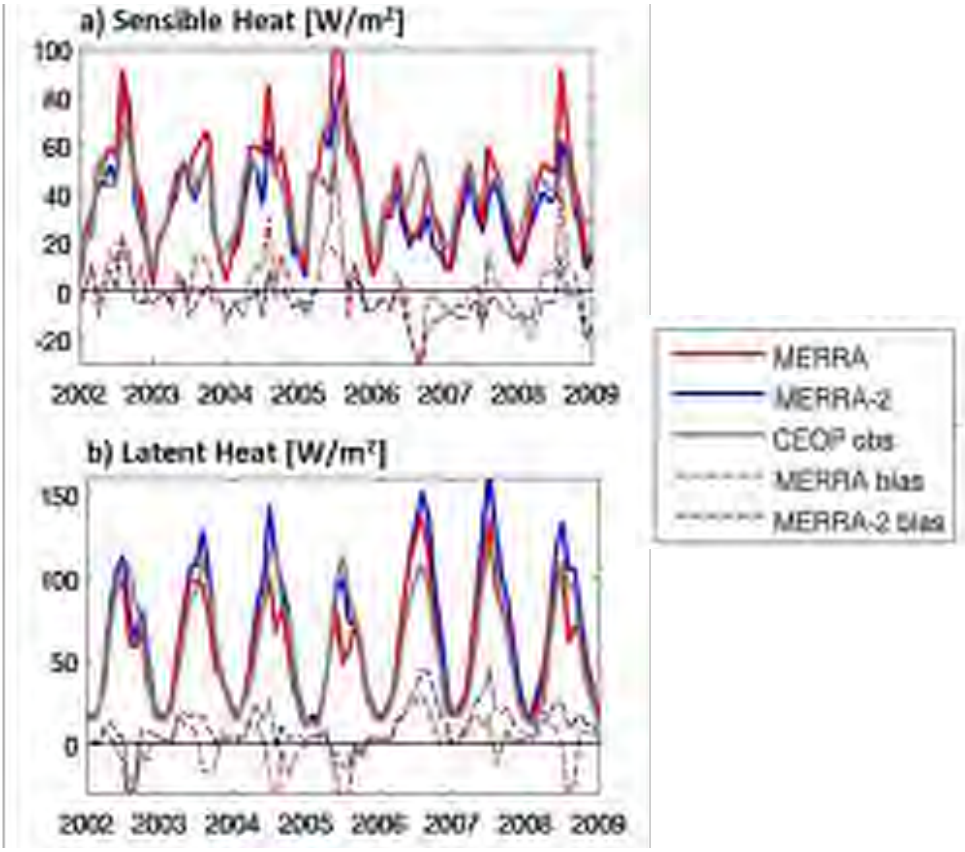

Figure 7-5 Time series of the mean monthly (a) sensible heat, and (b) latent heat over the Southern Great Plains CEOP flux towers sites [bounded by (-99.7E, 34.7N) and (-95.3E, 38.7N)] for MERRA, MERRA-2 and CEOP observations.

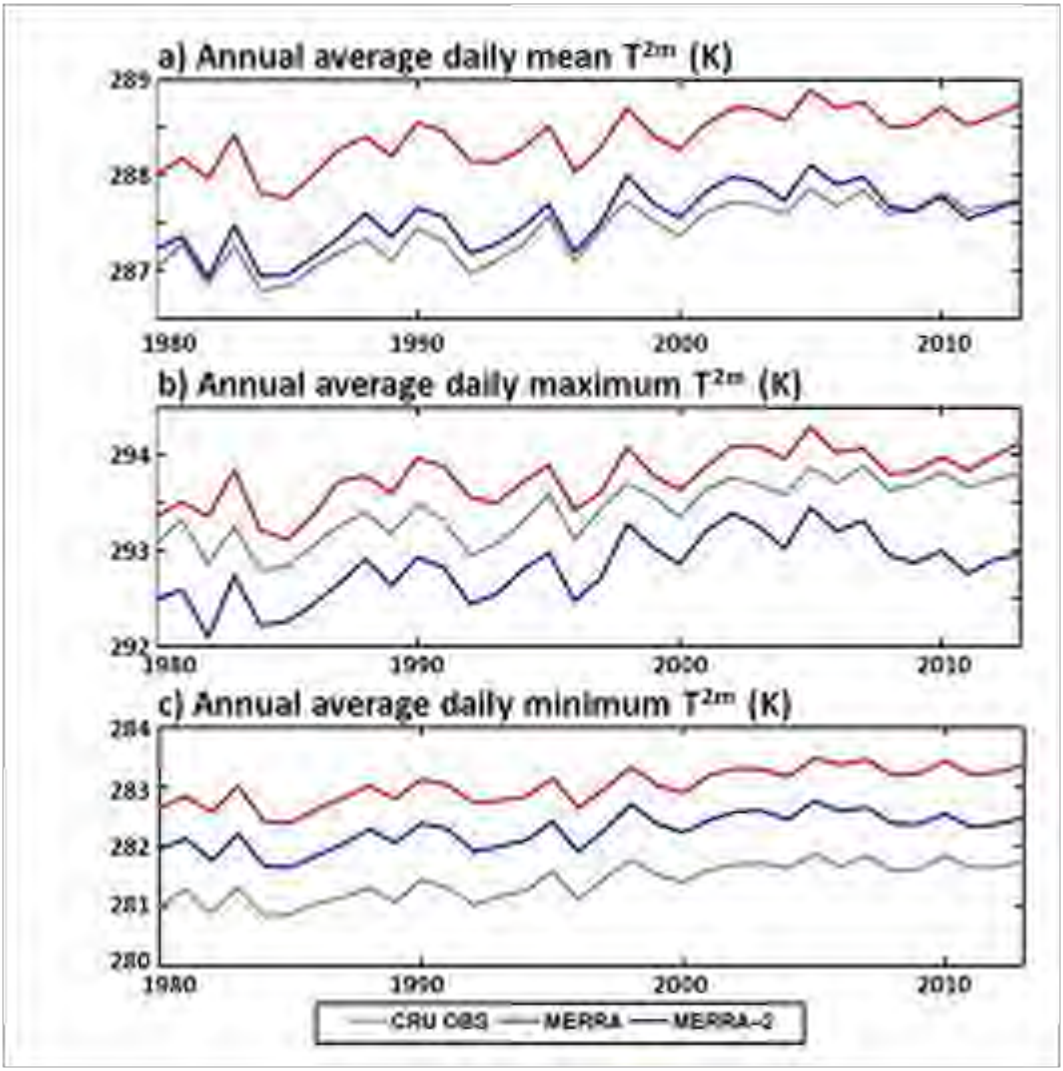

Figure 7-6 Time series of the annual average (a) daily mean, (b) daily maximum, and (c) daily minimum T2m over land from MERRA, MERRA-2, and CRU TS observations.

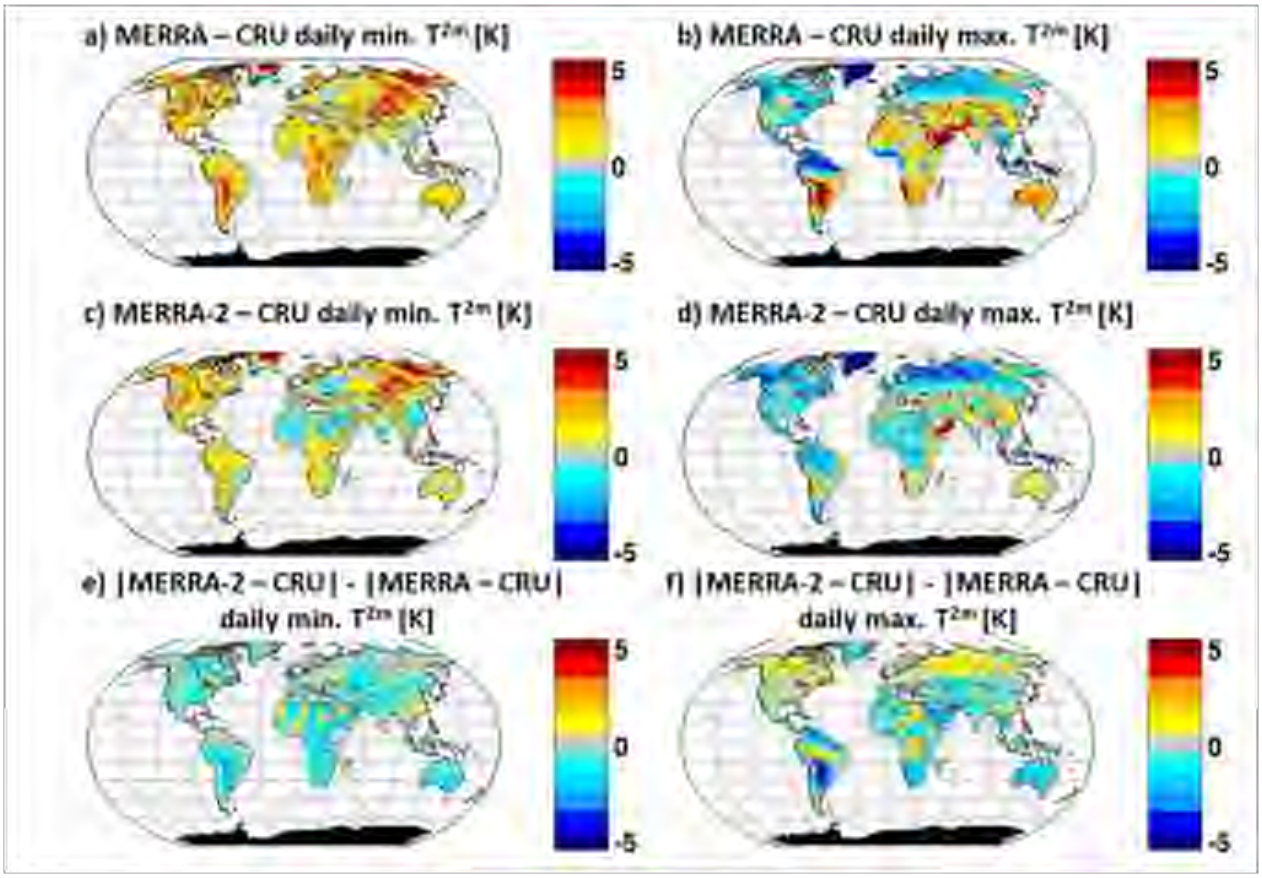

Figure 7-7 The mean 1980-2013 T2m biases (relative to CRU gridded observations) for the (left) daily minimum, and (right) daily maximum temperatures, for MERRA (top row) and MERRA-2 (middle row). The bottom row shows the difference between the absolute biases for MERRA and MERRA-2.

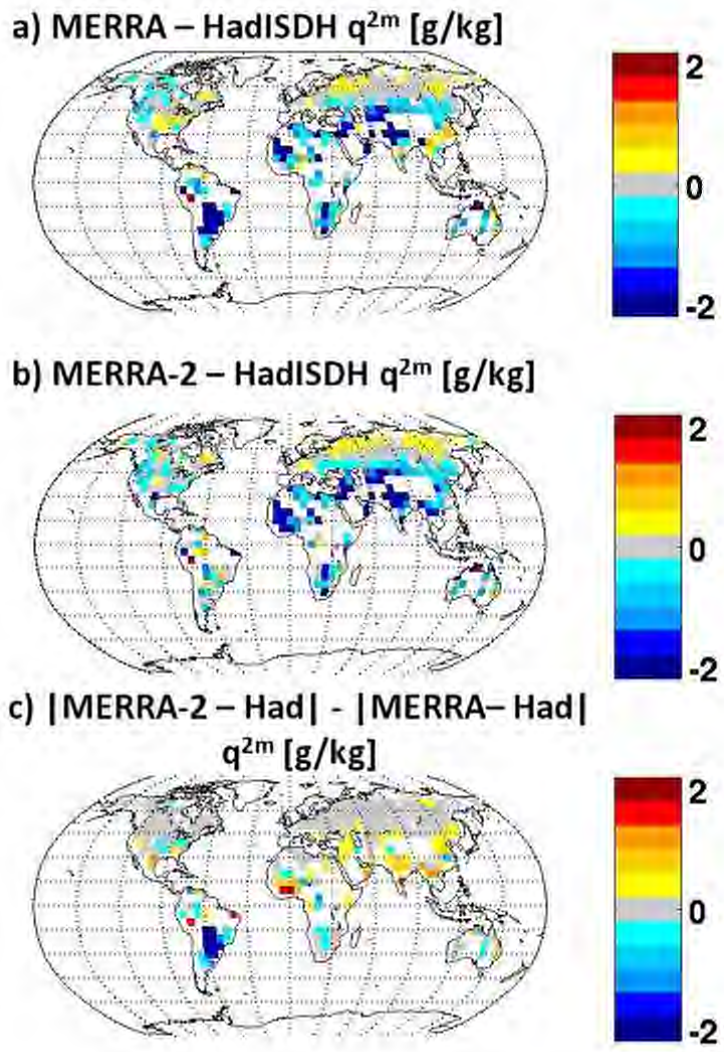

Figure 7-8 The mean 1980-2013 q2m biases (relative to HadISDH gridded observations) for (a) MERRA, and (b) MERRA-2, along with (c) the difference between the absolute biases for MERRA and MERRA-2.

8. Ocean Surface

a. Sea Surface Temperature

The sea surface temperature (SST) and sea ice concentration (SIC) in MERRA were based on 1° product of Reynolds et al. (2002) that is available on a weekly basis since 29 Oct 1981. (Prior to this date, it is a monthly product.) In preparing MERRA-2 boundary conditions we used currently available high resolution (finer than 1°) daily data products. The purpose of this section is to detail the sources from which these boundary conditions were prepared and the steps taken to process and prepare the dataset for MERRA-2. Knowledge of these details will perhaps help users of MERRA-2 do intercomparisons with other reanalyses and to attribute any biases or jumps found to the data sources or to the processing methodology.

Sub-section 1 below lists the different data sources and their period of usage. Processing steps are detailed in sub-section 2 along with associated caveats. Some known issues with the data are listed in sub-section 3. Sub-section 4 provides a comparison of the MERRA-2 SST fields with those in other reanalyses.

1) Data Sources

To the best of our knowledge, there is no continuous, global, gridded, high resolution SST and SIC data product currently available on a daily basis from 1980 onwards that can be used as a source for MERRA-2 boundary conditions. Therefore, we used the following combination of products as our data sources:

1. Daily, 1/20° Donlon et al. (2012) product (hereafter referred to as OSTIA), available from 1 April 2006 (http://podaac.jpl.nasa.gov/dataset/UKMO-L4HRfnd-GLOB-OSTIA)
2. Daily, 1/4° Reynolds et al. (2007) product (hereafter referred to as Reynolds) available since 1 September 1981 (ftp://eclipse.ncdc.noaa.gov/pub/OI-daily-v2/NetCDF/1981/AVHRR/)
3. Monthly, 1° Taylor et al. (2000) product (hereafter referred to as CMIP RAW), which starts in 1870 (http://www-pcmdi.llnl.gov/projects/amip/AMIP2EXPDSN/BCS/amipbcdwnld.php)

We note that all of these datasets are distributed with both SST and SIC information. We took care to take both SST and SIC from the same data source. If we were to use, for example, SIC from the National Snow and Ice Data Center (NSIDC) and SST from somewhere else, potential mismatches in the marginal ice zones could induce inconsistencies that would be non-trivial to correct (see, for example, Reynolds et al. 2007, section 2.c).

Because the OSTIA data are available starting 1 April 2006, we use the Reynolds product prior to this date. However, the Reynolds product only extends back to 1981, so for convenience, we use CMIP RAW before 1 January 1982. The timelines are summarized in Table 8-2.

2) **Processing Steps**

1980-1982

The CMIP RAW dataset provides monthly SST and SIC at the middle of each month and on a 1° degree regular lat/lon grid. We followed recommendations given by Taylor et al. (2000) to obtain daily, 0.25° data from this coarser information, preserving the CMIP RAW values at the coarser scales. In essence, we first interpolated the mid-month 1° values from CMIP RAW to 0.25° grid, and then temporally interpolated to generate daily data.

As discussed in Hurrell et al. (2008), hereafter H2008, it is important to merge climatologies to avoid the creation of spurious jumps. We followed the merging procedure of H2008 by adding the anomaly of daily CMIP RAW (relative to its own climatology) to the Reynolds climatology to obtain daily CMIP MODIFIED data,

$$\hat{\boldsymbol{x}}^{\boldsymbol{CMIP}} = (\boldsymbol{x}^{\boldsymbol{CMIP}} - \overline{\boldsymbol{x}}^{\boldsymbol{CMIP}}) + \overline{\boldsymbol{x}}^{\boldsymbol{Reynolds}} \qquad (8\text{-}1)$$

where the CMIP raw and modified daily data are denoted by $\boldsymbol{x}^{\boldsymbol{CMIP}}$ and $\hat{\boldsymbol{x}}^{\boldsymbol{CMIP}}$, respectively, and where $\overline{\boldsymbol{x}}^{\boldsymbol{CMIP}}$ and $\overline{\boldsymbol{x}}^{\boldsymbol{Reynolds}}$ denote daily climatologies of CMIP RAW and Reynolds data, respectively. (CMIP climatology was computed based on data from 1977- 1982, whereas Reynolds climatology was based on data from 1982- 2006). By construction, then, the climatology of CMIP MODIFIED data is the same as that of Reynolds, as shown in the right panels of Figure 8-1 and Figure 8-2. Also because of this merging procedure, the transition from the CMIP period to the Reynolds period is smoothed out, as shown by the time-series of the anomalies in SIC (Figure 8-2). CMIP MODIFIED data is used for MERRA-2 SST and SIC before 1 January 1982.

1982-2006

The Reynolds dataset is daily and at 0.25° resolution. The AMSR-E and AVHRR version of the data (ftp://eclipse.ncdc.noaa.gov/pub/OI-daily-v2/NetCDF/) is available for 1 Jun 2002 - 4 Oct 2011, but for the sake of convenience we used these data only over 1 Jan 2003- 31 Mar 2006. Prior to 2003, we used the AVHRR-only version of the product.

In the Reynolds data, SIC was missing during 6 December 1987- 10 January 1988. This absence, which was documented by the NSIDC (https://support.nsidc.org/entries/20257046-Why-are-sea-ice-extent-and-area-not-available-for-Dec-1987-and-Jan-1988-), may have resulted from satellite instrument error (Berg and Chase, 1992). Data for these dates were simply filled in by linearly interpolating in time between the data for the days before and after the snag.

2006 Onwards

The daily and 1/20° OSTIA data also required minimal processing; they were conservatively areally averaged (using lats4d, http://opengrads.org/doc/scripts/lats4d/) to a regular 1/4° grid. As for the transition between the Reynolds and OSTIA periods on 1 April 2006, we simply switch

from one dataset to the other without merging the climatologies. (This approach is akin to that used for ERA-Interim; see Dee et al. (2011), Table I.) The anomalies, plotted in Figure 8-1 and Figure 8-2, show a jump on 1 April 2006 that is mostly due to the differences in the Reynolds and OSTIA climatologies. Notice that the SST seasonal cycles (northern hemisphere summer and annual cycle in tropics) are different in MERRA-2 (which mostly reflects Reynolds) and OSTIA (Figure 8-1). In the tropics, OSTIA is cooler than Reynolds, probably due to the fact that OSTIA is an estimate of the foundation SST (Donlon and coauthors, 2007; Donlon et al., 2012), for which measurements during local daytime are excluded, which is not the case with the Reynolds product. There is also an important distinction between skin and sub-skin SSTs, with the skin SST typically being warmer than the sub-skin SST due to diurnal warming (see Donlon and coauthors (2007) for details). As for the SIC (Figure 8-2) we see differences in northern hemisphere summer and throughout the year in the southern hemisphere.

For the SIC, the discontinuity in the anomaly is within 5% concentration for either hemisphere, and for the SST, it is within 0.2°C. Indeed a merger (as for 1980-1982) of CMIP MODIFIED and Reynolds with OSTIA climatology was explored but was not implemented in the production of MERRA-2 boundary conditions. This is because such an approach would mean modifying the SST and SIC from 1980-2006 using OSTIA climatology covering only six years (2006- 2012). We opted not to shift such a long time period using statistics from such a short data period. We would like to caution the users of MERRA- 2 to be mindful in their studies of the 1 April 2006 break point.

Great Lakes and Caspian Sea

In MERRA-2, the inland water masses such as the Great Lakes and the Caspian Sea are also treated as an ocean surface type. Therefore, we need to provide a value for SST and Ice Concentration (IC) in these regions. Because the Reynolds product provides SST and IC over the Great Lakes during the OSTIA period, we use, if OSTIA has no values, data at those grid points from the Reynolds data set.

For the Caspian Sea, both Reynolds and OSTIA have values for SST but not for IC (Reynolds et al., 2007), as shown in Figure 8-3. However, the OI.v2 (Reynolds et al., 2002) has both SST and IC defined over the Caspian Sea. Using this dataset in winter months (November- March) of 1982-2000, we obtained an empirical linear relation between SST and IC. This function was able to fit the winter IC data in OI.v2 from 2001 - 2013 within 1.257 as measured in the Euclidean (l2) norm (not shown). The IC values obtained using this fit are plotted in the bottom panel of Figure 8-3. Because the IC corresponds to the low SST values in the north Caspian Sea, we use such fitted values in MERRA-2.

3) **Known Issues**

Currently we are aware of the following issues with the MERRA-2 boundary conditions.

1. The CMIP MODIFIED data on 29 February 1980 (a leap day) used the leap day climatology from Reynolds (1984-2004) through the merging process described in section 3.1. The 1980

leap day shows a ~-1K anomaly compared to the day before and after (Figure 8-4). Time series of the SST in the eastern Pacific (Figure 8-5) shows that this feature has a minor impact on the MERRA-2 air temperature at 2 meters (T2M), the humidity, and the sea level pressure (not shown), perhaps due to the interpolation of daily boundary conditions to hourly frequency by the atmospheric GCM.

2. During summer, the ice concentration in the Reynolds data set can be greater than zero even when the SST is far above freezing. Figure 8-6 depicts the SST and ice concentration on 1 August 2003. This issue, which might result from noisy events along the coasts as noted by Reynolds et al. (2007), may affect analysis near the Great Lakes.
3. With the introduction of OSTIA, several apparently artificial short duration variations in sea ice cover have been noted. Because the presence of sea ice significantly inhibits the air-sea exchange of energy and moisture and radically alters surface albedo, these variations are expected to detrimentally affect the local surface fluxes as well as temperature and moisture variables in the lower troposphere. Table 8-1 provides a list of affected geographical areas along with a subjective characterization of the severity.

Table 8-1 List of known sea ice issues passed through from OSTIA data.

Date	Location(s)	Severity
7,9-Mar-07	Greenland Sea, Sea of Okhotsk, southern Bering Sea, Ross Sea, and Amundsen Sea	substantial
4-Oct-09	Somov Sea	moderate
23-Apr-12	Rapid advance in the Southern Ocean	slight
19-Jan-13	Bering Sea	substantial
13-Aug-13	Amundsen Sea	substantial
20-Feb-14	Gulf of St. Lawrence and southern Labrador Sea	substantial
10,11-May-14	Greenland Sea/Fram Strait and Weddell Sea	substantial
30-Jun-15	Canadian Archipelago, Baffin Bay, Hudson Bay, and Davis Sea	substantial

4) Reanalyses Intercomparisons

Figure 8-7 compares time-series of MERRA-2 SST (12 month running averages, and spatially averaged between 60S and 60N) to corresponding time series from other reanalyses, including MERRA (Rienecker et al., 2011). Note that at the time of the plotting, the MERRA-2 output was not fully available within the 2010- 2011 period. After 1982, the MERRA-2 SST closely follows that used in CFSR (Saha et al., 2010), perhaps due to the fact that after October 1981 the CFSR used an early version of the Reynolds et al. (2007) SST (see pp.1031 of Saha et al. (2010) for further details). The ERA-Interim (Dee et al., 2011) switched to the OSTIA product on 1 February 2009, which perhaps explains why MERRA-2 is closest to ERA-Interim since 2011. The 20th Century Reanalysis (20CR, Compo et al. (2011)) used the HadISST1 (Rayner et al., 2003) product. The HadISST1 and OI.V2 (Reynolds et al., 2002) products are similar to each other (see Rayner et al. (2003) for details), and perhaps this explains the similarity in the trends of MERRA (which used OI.v2) and 20CR (which used HadISST1). The JRA-55 (Ebita et al., 2011) used Cobe SST, whose differences from OI.v2 are described by Ishii et al. (2005).

Overall, the running means of all the reanalyses are within 1°C for the 30 years spanning 1980-2010, and the anomalies are separated by less than 0.2°C. Regarding the averaged temperatures and anomalies, prior to the availability of the Advanced Very High Resolution Radiometer

(AVHRR) satellite instrument around 1982, most SST retrieval products relied on sparse in situ observations of the SST. A close look at 1982 shows that all reanalyses data almost collapse to a single value of about 293.3*K,* perhaps due to the availability of AVHRR data; however, thereafter, due to the specifics of the retrieval methodology and preparation of the data products, there remains about 0.2K variability between the running means of different reanalyses. The gradual ramping of the temperature and anomalies between 1985- 2006 could be due to the usage of Pathfinder data (see Reynolds et al. (2007) for further details).

Table 8-2 Time period of usage of different data products for MERRA-2 boundary conditions. Notice the switch or break points on 1 January 1982 and 1 April 2006, when the data sources were changed.

Data product	Start Date	End Date	Frequency, spatial resolution
CMIP RAW	1 Jan 1980	31 Dec 1981	mid-Monthly, 1°
Reynolds	1 Jan 1982	31 Mar 2006	Daily, 1/4°
OSTIA	1 Apr 2006	current day	Daily, 1/20°

5) **SST Summary**

The MERRA reanalysis used a coarse resolution (weekly, 1°) SST and SIC data product for ocean boundary conditions. MERRA-2 uses higher resolution (daily, 1/4°) data. Here we describe the steps taken to put together the SST and SIC boundary conditions for 1980 onwards. Before 1 January 1982, we started with the mid-monthly, 1° Taylor et al. (2000) data set and then interpolated it to a daily, 1/4° dataset; the underlying climatology was then modified to match that of the Reynolds et al. (2007) product. The Reynolds product was used from 1982 to 1 April 2006, and after that, the OSTIA product (Donlon et al., 2012) was used without any climatological merger. During the OSTIA period, if the OSTIA dataset held no data for SST and SIC in the Great Lakes, we extracted this information from the Reynolds data. The ice concentration in the Caspian Sea was computed using a linear, empirical fit between the SST and ice concentrations in the OI.v2 (Reynolds et al., 2002) product.

A known problem with the MERRA-2 boundary conditions occurs on 29 February 1980 (a leap day), when the fields are not consistent with those on 28 February and 1 March. However, the anomaly of the 29th from the average of the other two days is within 2°C and is therefore within the range of daily SST variability; hence caution must be used when performing diagnostics, for example, of the net surface heat flux over this period. Another issue we are aware of is the presence of ice in the Great Lakes during summer, when the SST is far above the freezing point.

A comparison of MERRA-2 with other reanalyses shows that the average of the SSTs used by MERRA-2 is within 0.2°C of the average of those used by the other reanalyses, with a negative bias during 1982-2005 and a positive bias thereafter.

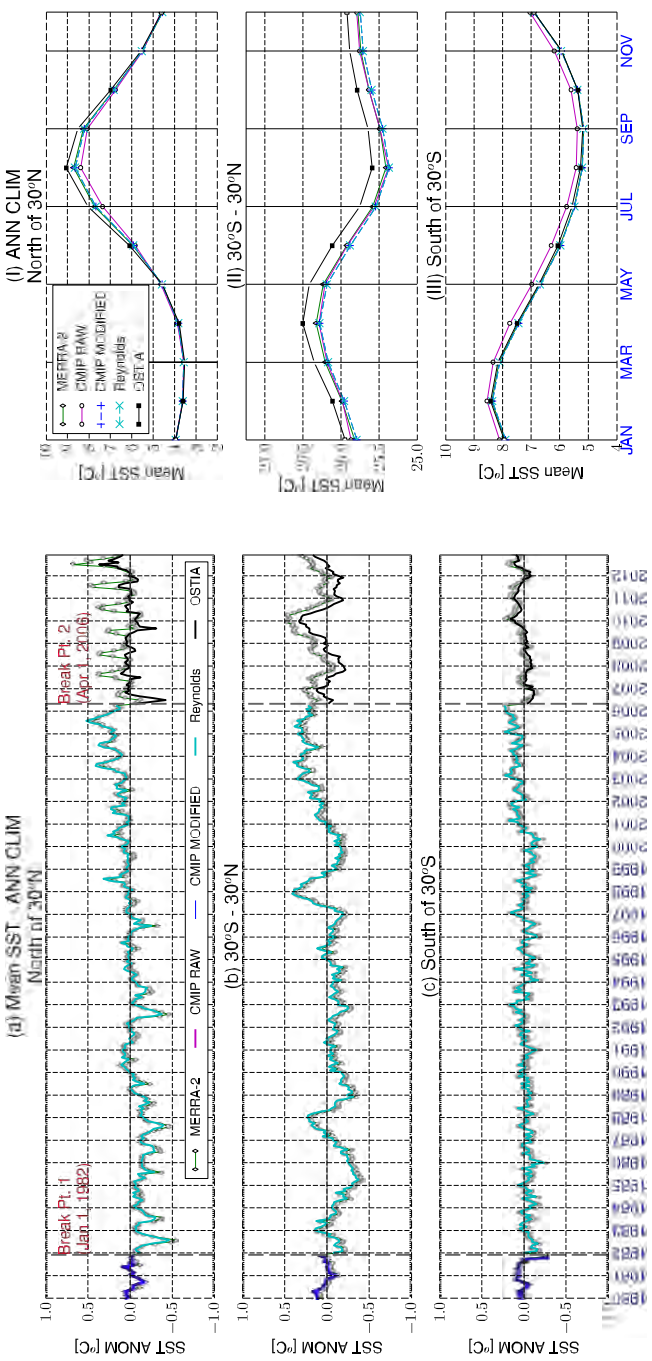

Figure 8-1 (left) Time-series of monthly anomalies in sea surface temperature (SST): (a) northern hemisphere, (b) tropics, and (c) southern hemisphere, for MERRA-2, CMIP RAW, CMIP MODIFIED, Reynolds and OSTIA from 1980-2012. The switch from CMIP MODIFIED to Reynolds occurs on 1 January 1982 (marked as break point 1), and that from Reynolds to OSTIA occurs on 1 April 2006 (break point 2). (right) Monthly mean SST climatologies for these same data in: (I) northern hemisphere, (II) tropics, and (III) southern hemisphere. Note that the OSTIA climatology is different from the MERRA-2 climatology during northern hemisphere summer and in the tropics, which produces the differences seen in the corresponding anomaly time-series in (a) and (b). The climatologies in Reynolds and OSTIA were not made consistent, which explains the jump in the southern hemisphere anomaly on 1 April 2006.

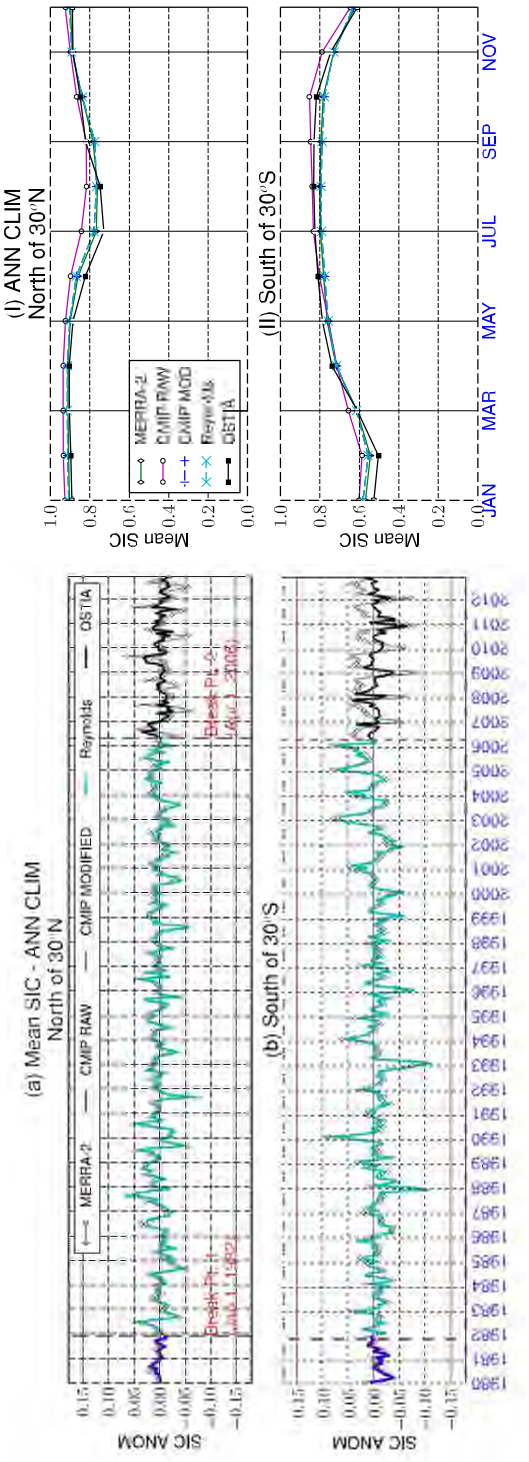

Figure 8-2: Same as in Figure 8-1, but for the sea ice concentration (SIC) and for the northern and southern hemispheres only. The disagreement in the seasonal cycles of MERRA-2 and OSTIA is clearly seen in the anomalies beyond 1 April 2006.

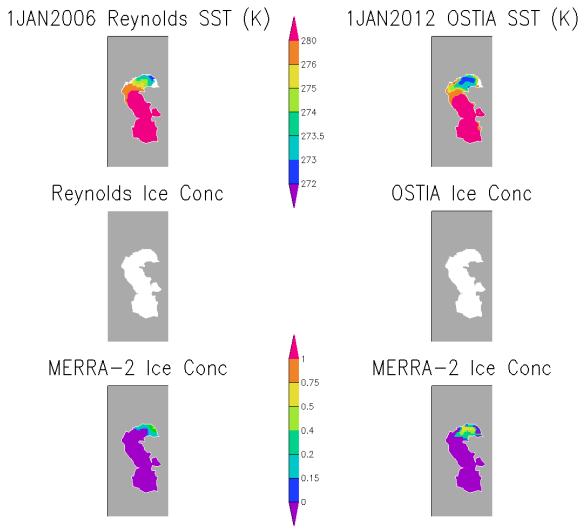

Figure 8-3 Caspian Sea SST (K) and ice concentration (IC) on 1 January 2006 (left) and 2012 (right). The top and middle panels show SST and IC, respectively, from Reynolds (left) and OSTIA (right); the IC in Reynolds over the Caspian Sea is undefined, whereas it is zero in OSTIA. Bottom panel depicts the IC in MERRA-2 obtained using the SST in top panel.

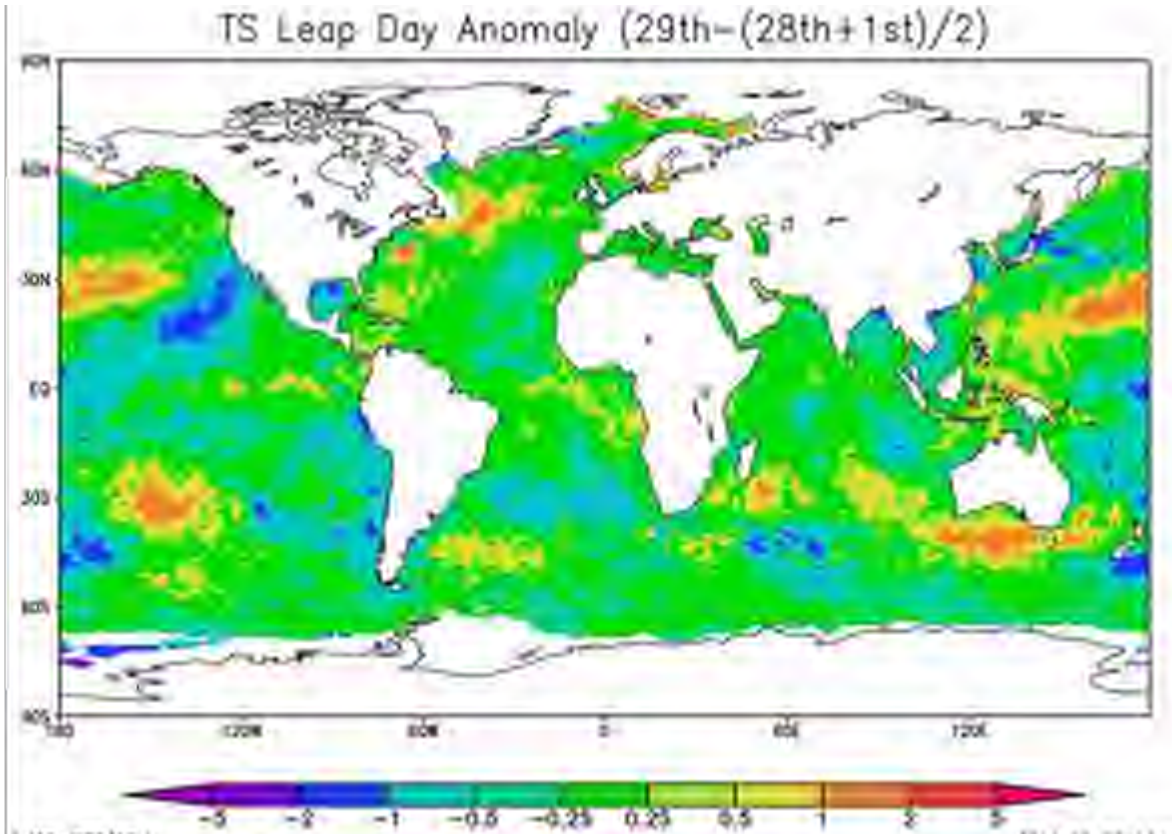

Figure 8-4 SST anomaly (K) on 29 February 1980 compared to the average of the previous and next days.

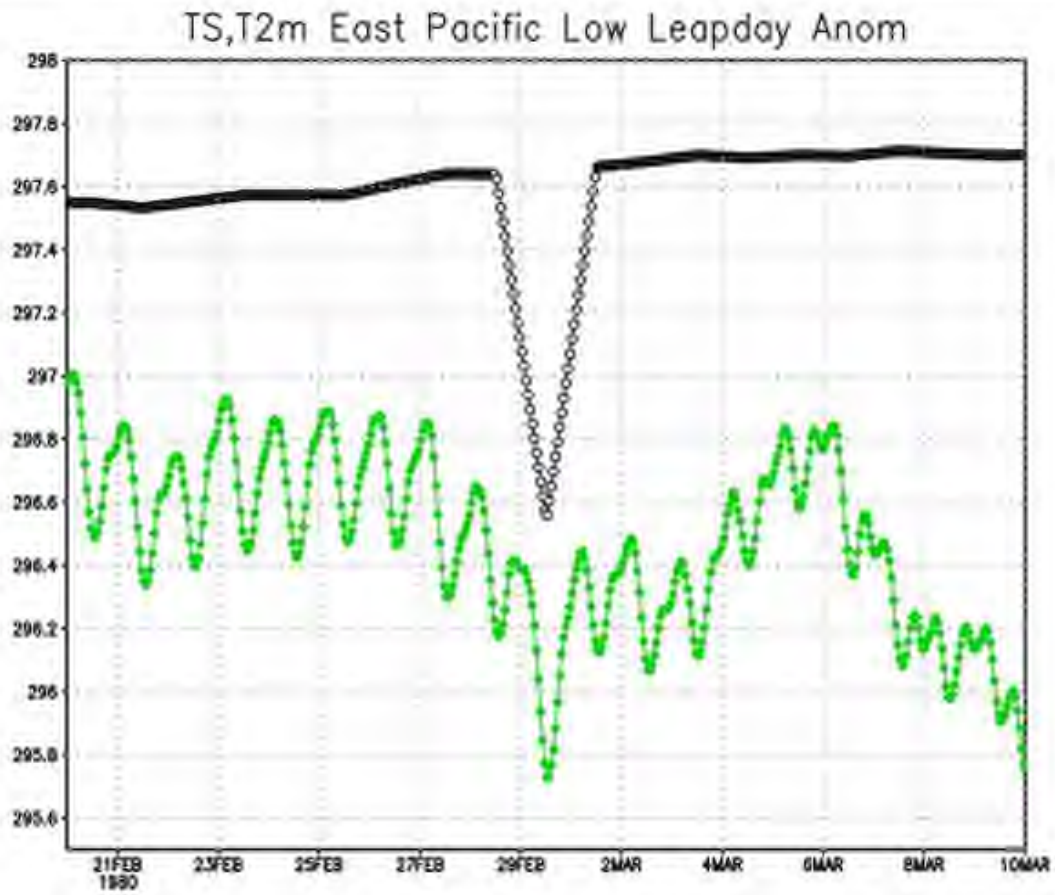

Figure 8-5 Time series of averaged SST (black) and 2m air temperature (green) in the eastern Pacific (144W-125W, 13S-21N) from 21 February- 10 March 1980. Units are in Kelvin.

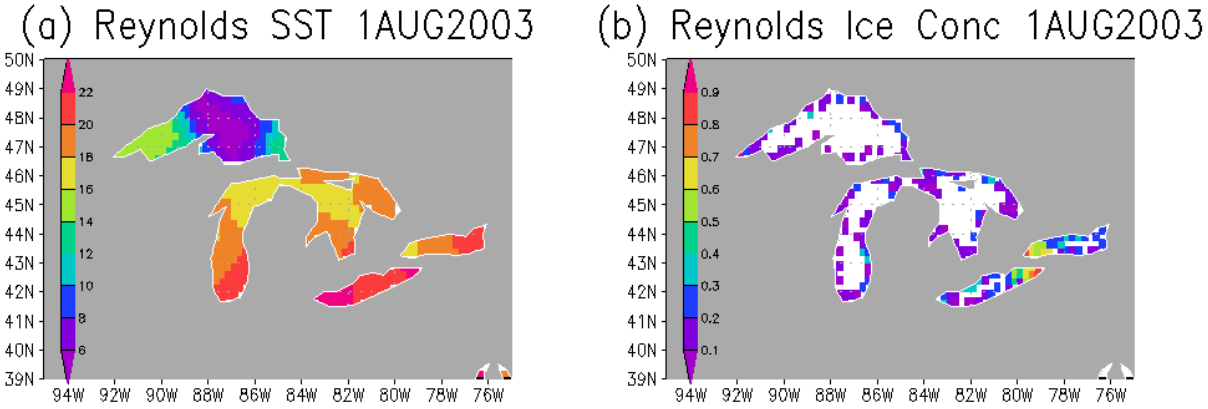

Figure 8-6 SST (℃) and ice concentration in the Great Lakes from the Reynolds product on 1 August 2003. Note the presence of ice, even when SST > 6℃.

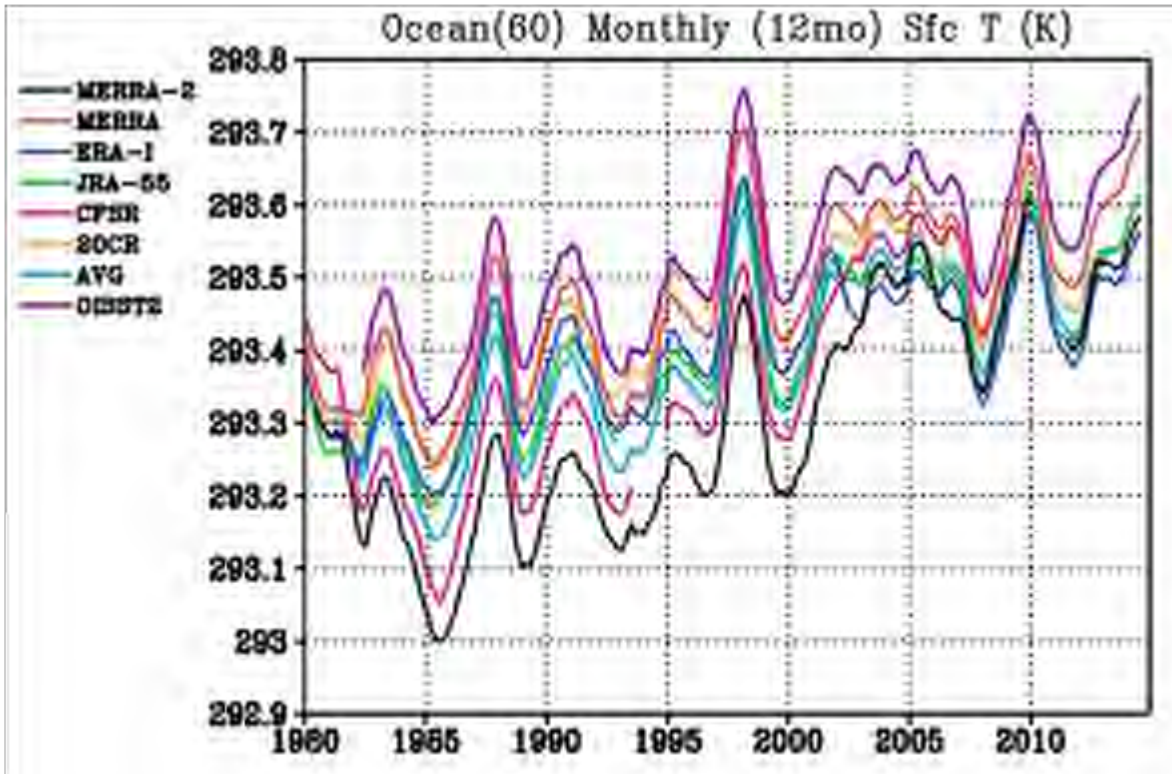

Figure 8-7 Running mean (over 12 months) of SST (K) between 60S-60N since 1980 for satellite reanalyses (MERRA, MERRA-2, ERA-Interim, JRA-55, and CFSR) and the 20th Century reanalysis (in which surface pressure is assimilated). AVG indicates the average of the satellite reanalyses and OI.v2. These SSTs are prescribed input to the reanalyses, though CFSR includes some weakly coupled ocean data assimilation.

b. Surface Wind Speed

This section focuses on the monthly ocean wind fields from MERRA-2, comparing them to available observations at meteorological stations as well as to other analyses, including reanalyses, operational analyses and a synthesis product generated for the ocean modeling community. The data sources for the comparisons discussed in this section are as follows:

MERRA-2: Global monthly mean surface fields are produced from U10M and V10M from the daily tavg1_2d_slv_Nx collection. Time-series data at the WHOI stations are produced from U2M and V2M from the daily tavg1_2d_slv_Nx collection. Time-series data at the ESRL stations are produced from U10M and V10M from the daily tavg1_2d_slv_Nx collection.

1) Comparison Datasets

Reanalyses

MERRA: Global monthly mean surface fields and monthly time-series at the ESRL stations are produced from U10M and V10M from the monthly mean tavgM_2d_slv_Nx collection. Time-series data at the WHOI stations are produced from U2M and V2M from the daily tavg1_2d_slv_Nx collection.

ERA-I: ERA-Interim monthly averages of daily mean surface winds are provided by the European Centre for Medium-Range Weather Forecasts (ECMWF) at http://www.ecmwf.int/en/research/climate-reanalysis/era-interim.

NCEP-R2: The NCEP/DOE AMIP-II Reanalysis is provided by the National Weather Service, Climate Prediction Center, at http://www.cpc.ncep.noaa.gov/products/wesley/reanalysis2/.

Retrievals

SCOW: The Scatterometer Climatology of Ocean Winds (SCOW) is obtained from Oregon State University (http://cioss.coas.oregonstate.edu/scow/). SCOW winds are based on 122 months of QuikSCAT scatterometer data from 1999-2009. For this reason, a climatology from 1999-2009 is used for the global wind fields.

CCMP: Cross-Calibrated Multi-Platform (CCMP) Ocean Surface Wind Vector L2.5A Monthly Analyses are obtained from the Jet Propulsion Laboratory (JPL) via ftp://podaac-ftp.jpl.nasa.gov/OceanWinds/ccmp/L3.5a/monthly/flk/.

Meteorological Stations **ESRL:** Earth System Research Laboratory (ESRL) 10-meter wind speeds are obtained from NOAA/ESRL/GMD at ftp://aftp.cmdl.noaa.gov/data/meteorology/in-situ/. Two of the ocean locations are examined here.

Moored Ocean Buoys

WHOI: Surface wind speeds at 3-3.5 meters are obtained from Woods Hole Oceanographic Institution (WHOI), Upper Ocean Processes Group, at http://uop.whoi.edu/archives/. Data is available for 22 stations around the globe.

TAO: Surface wind speeds at 4 meters are obtained from PMEL TAO at http://www.pmel.noaa.gov/tao/disdel/frames/main.html.

2) Wind Rose Diagram

Figure 8-8 shows the frequency and speed of the 10-meter winds for each product. As you move outward on the radial scale, the frequency of the wind associated with that direction increases. Each spoke is divided by color into wind speed ranges. The radial length of each spoke around the circle is the percentage of time that the wind blows from that direction. The pre-dominant wind for all six products are the Westerly winds (between 35^{o}-65^{o} latitude), followed by the NE Trades (0-30N), and the SE Trades (0-30S). With the exception of CCMP, the Westerly winds are skewed slightly, blowing more from the WNW instead of from due west. The winds in MERRA-2 are stronger than those in MERRA but not as strong as those in NCEP-R2.

3) Global Surface Maps of Wind Speed

Figure 8-9 shows the mean fields of 10-meter wind speeds, averaged over 1999-2009, from six data products. The main features of the minimum and maximum wind speeds are similar in all products, but the intensity of the NCEP-R2 winds are higher than all the others especially south of 30N, with a maximum of 10.8 ms^{-1}. MERRA-2 is generally stronger than MERRA in most regions.

The difference plots in Figure 8-10 show that MERRA-2 winds are stronger than those in MERRA, SCOW, and ERA-Interim, particularly in the western Equatorial Pacific and the temperate regions (30S-60S and 30N-60N). MERRA-2 winds compare best with CCMP, having the smallest mean bias of -0.05ms^{-1}; the RMS difference for MERRA-2 vs. CCMp is 0.630 ms^{-1}. MERRA-2 is stronger than CCMP in the Western Equatorial Pacific but weaker in the Eastern Equatorial Pacific.

4) Time-Series at ESRL Stations

There are 7 available stations, but only the two ocean stations are shown here. Statistics tables show that for 5 of the 7 stations, MERRA-2 is closer to observations than MERRA but that both are weaker than observations.

Figure 8-11 shows the time-series of the 10-meter wind speeds from MERRA, MERRA-2, and station observations (OBS) at Tutuila, Samoa in the South Pacific as well as the differences of both MERRA and MERRA-2 from OBS. Both MERRA and MERRA-2 are weaker than the observations for most of the time-series, with a maximum difference of 5 ms^{-1}. During 1992, both

MERRA and MERRA-2 are stronger than the observations by 2-3 ms^{-1}. By examining this region (14S, 170W) in the wind speed difference maps in Figure 8-10, one can see that MERRA-2 is weaker there than SCOW, ERA-Interim, and CCMP from 1999-2009 but is stronger there than MERRA. After August 1999, both MERRA and MERRA-2 wind speeds have a negative bias. This coincides with the assimilation of QSCAT winds in July 1999.

Figure 8-12 is the same as Figure 8-11, but for the Mauna Loa, Hawaii, station in the South Pacific. Both MERRA and MERRA-2 are weaker than the observations for most of the time-series, with a maximum difference of over 7 ms^{-1}. MERRA is stronger than MERRA-2 for the entire time-series and is slightly stronger than the observations for intermittent months from 1998-2009.

The period when the reanalyses are much weaker than the observations is during the Indian Southwest Monsoon (Figure 8-13), for which both MERRA products are not capturing the strong winds seen in the observations. Figure 8-14 shows the monthly means during the peak of the summer monsoon in July 1995, when MERRA and MERRA-2 underestimate the winds. All data products agree on the regional distribution, though their magnitudes differ. MERRA-2 is weaker than MERRA, SCOW, ERA-Interim, and NCEP-R2 but is stronger than CCMP. MERRA and MERRA-2 are able to capture the pattern and timing of the Arabian Sea monsoon but not the intensity.

The station shown in Figure 8-15 is in the Tropical Pacific Warm Pool, from the TOGA COARE experiment. There is also a PMEL TAO mooring at this location, so there are two observations for comparison (WHOI and TAO). The mean differences between MERRA-2 and the observations are smaller, but the correlations between MERRA and the observations are higher. In general, both MERRA and MERRA-2 underestimate the winds.

Five stations in the subtropical North Atlantic were part of the Subduction Experiment from 1991 to 1993. Both MERRA and MERRA-2 correlate highly with these stations (from 0.79 to 0.95) but underestimate the winds slightly. MERRA-2 has the smallest mean and RMS difference with observations for all five stations. Figure 8-16 shows the time-series for the central station of the array.

Figure 8-17 shows the monthly means of the 10-meter winds from 1991-1993 near the five stations. MERRA-2 is stronger than MERRA for all five stations. For the North West station, where the winds are lowest, MERRA-2 is stronger than SCOW, ERA-Interim, and NCEP-R2. For the South West station, where the winds are strongest, MERRA-2 is weaker than SCOW, ERA-Interim, NCEP-R2, and CCMP.

5) **Ocean Surface Winds Summary**

The patterns of the global wind fields are similar between MERRA-2 and the other five datasets. MERRA-2 compares best with CCMP with a mean difference of 0.05 ms^{-1}. MERRA-2 is stronger

than MERRA, SCOW, and ERA-Interim in most regions but is weaker than NCEP-R2 and CCMP. Although MERRA-2 winds are weaker than 93% of the observations considered, their mean difference from observations is less than that of MERRA for 86% of the stations. Thus, though MERRA-2 winds are weaker than observations, they are an improvement over MERRA winds. MERRA-2 does not capture the intensity of the strong wind events shown in this analysis.

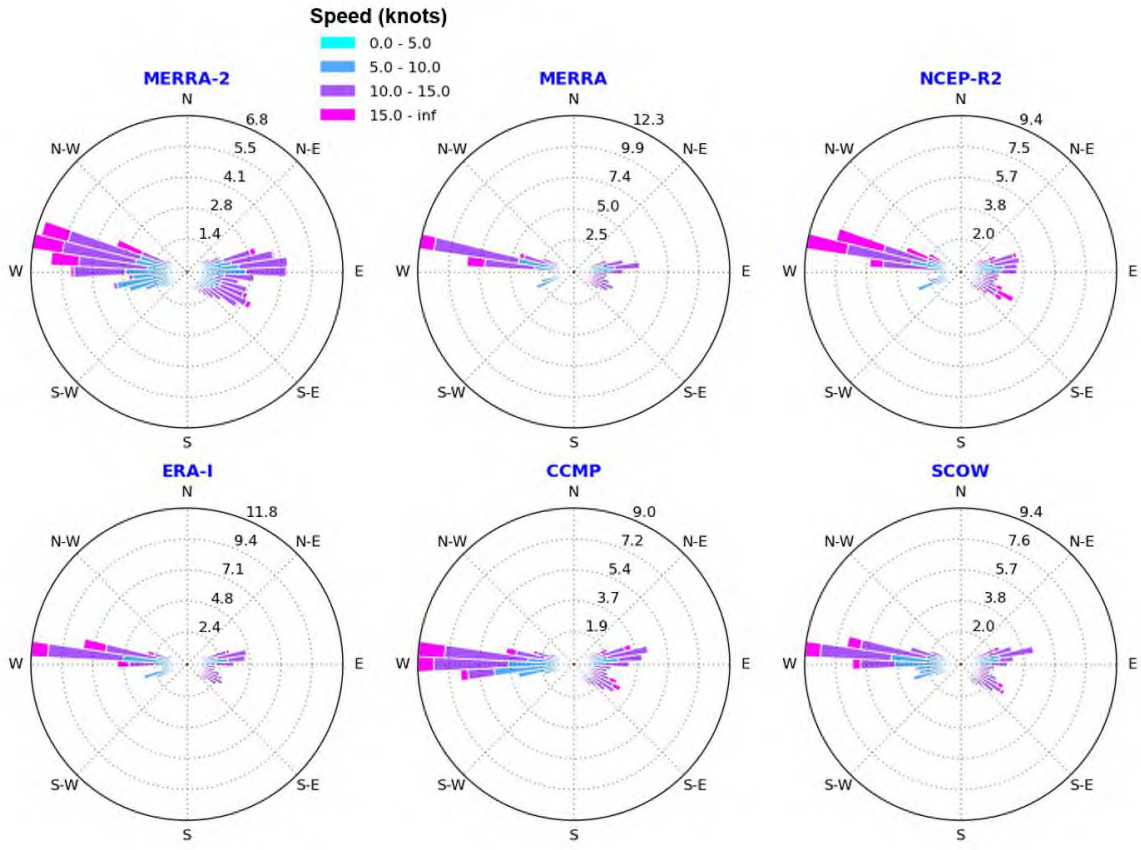

Figure 8-8 Frequency and speed of 10-meter winds, 1999-2009.

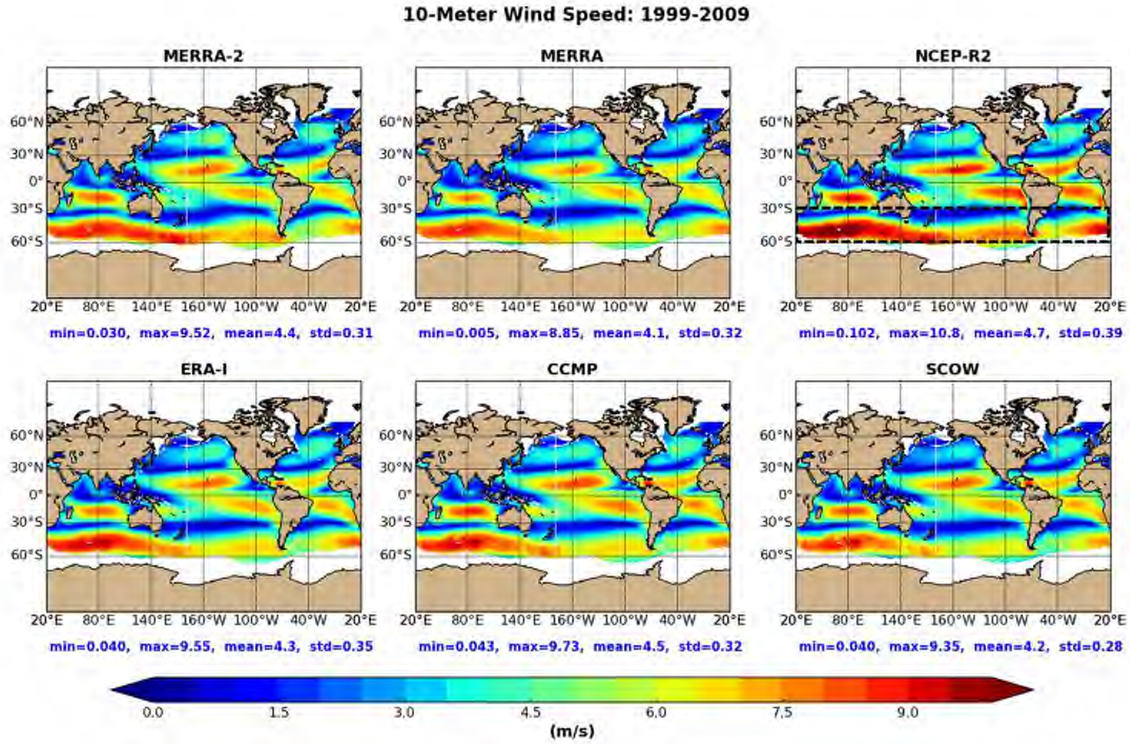

Figure 8-9 Mean 10-meter wind speed (m s^{-1}), 1999-2009.

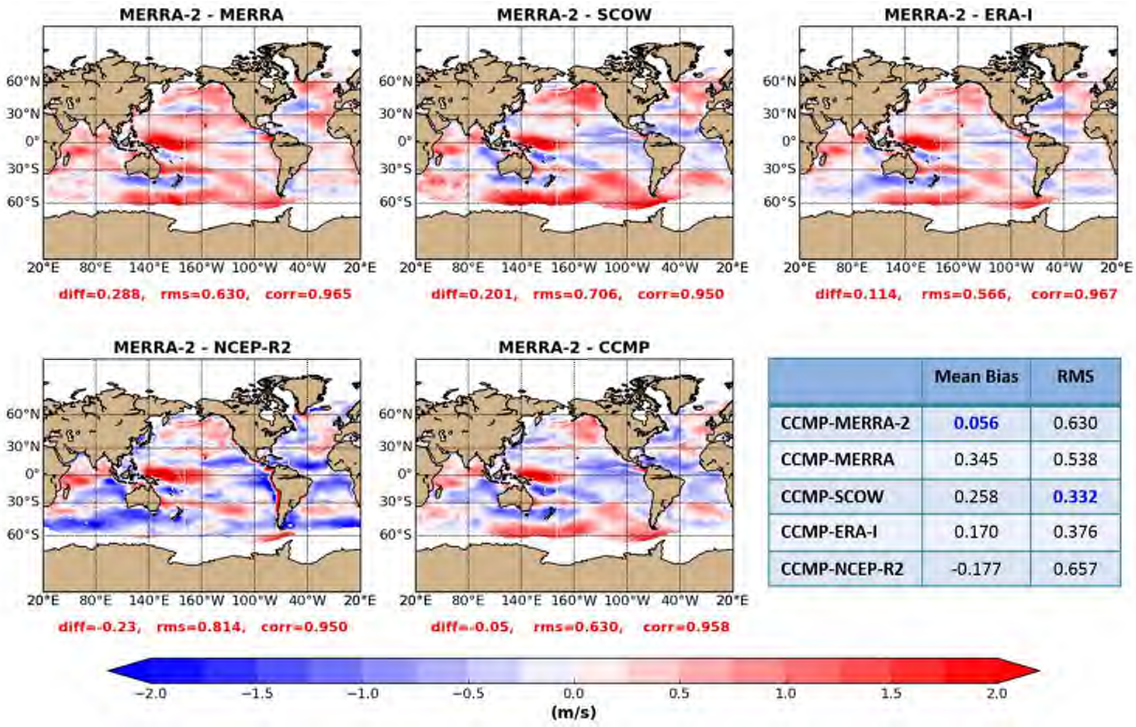

	Mean Bias	RMS
CCMP-MERRA-2	0.056	0.630
CCMP-MERRA	0.345	0.538
CCMP-SCOW	0.258	0.332
CCMP-ERA-I	0.170	0.376
CCMP-NCEP-R2	-0.177	0.657

Figure 8-10 Mean difference of 10-meter wind speeds (ms^{-1}) 1999-2009. The table presents comparison statistics between CCMP data and each of the other reanalyses and data sources.

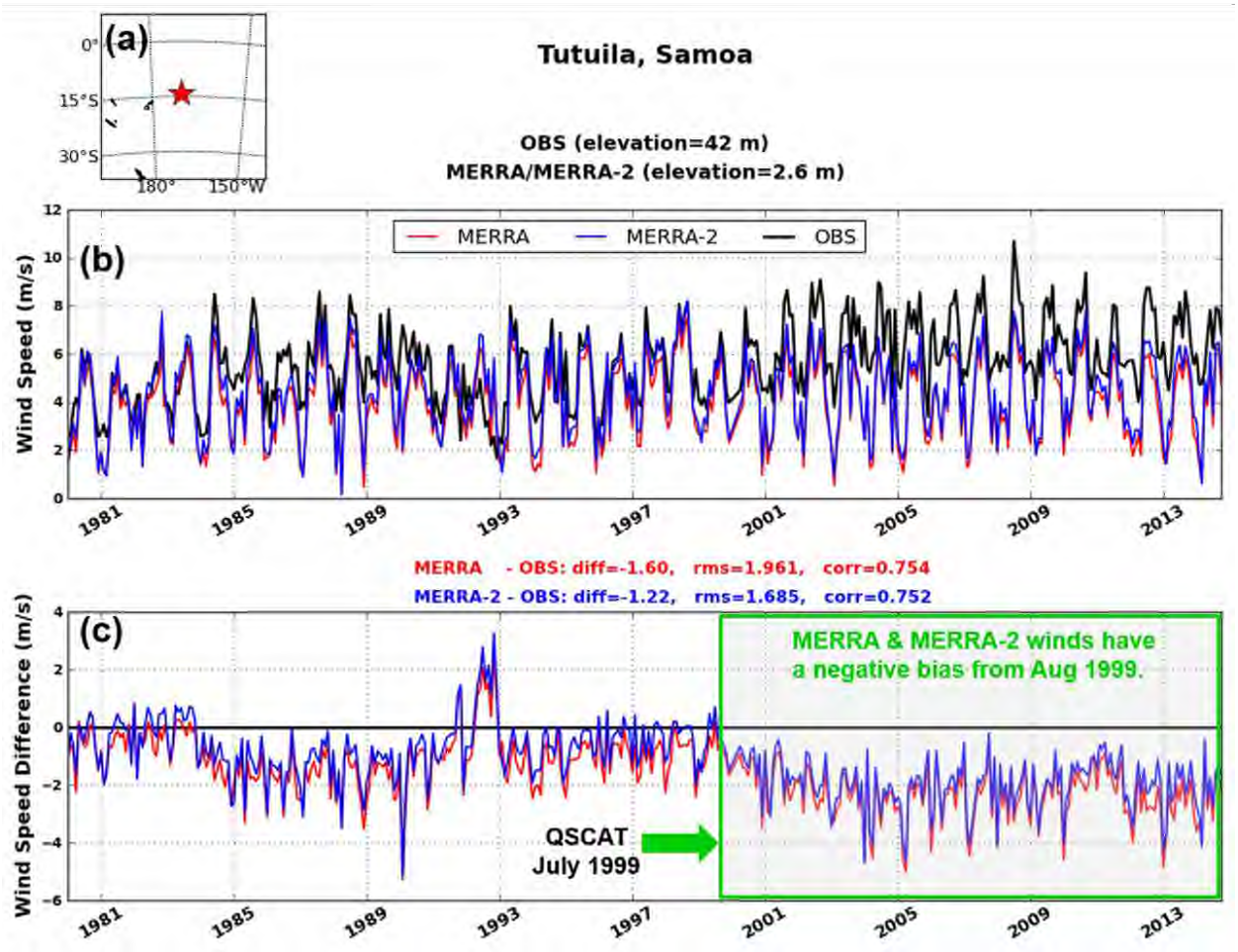

Figure 8-11 Time-series of 10-meter wind speed at Tutuila, Samoa. Panel (a) is the station location, panel (b) is wind speed, and panel (c) is wind speed difference (MERRA minus OBS and MERRA-2 minus OBS). Below the legend are the mean differences, root mean square differences, and correlations between the reanalyses and the observations.

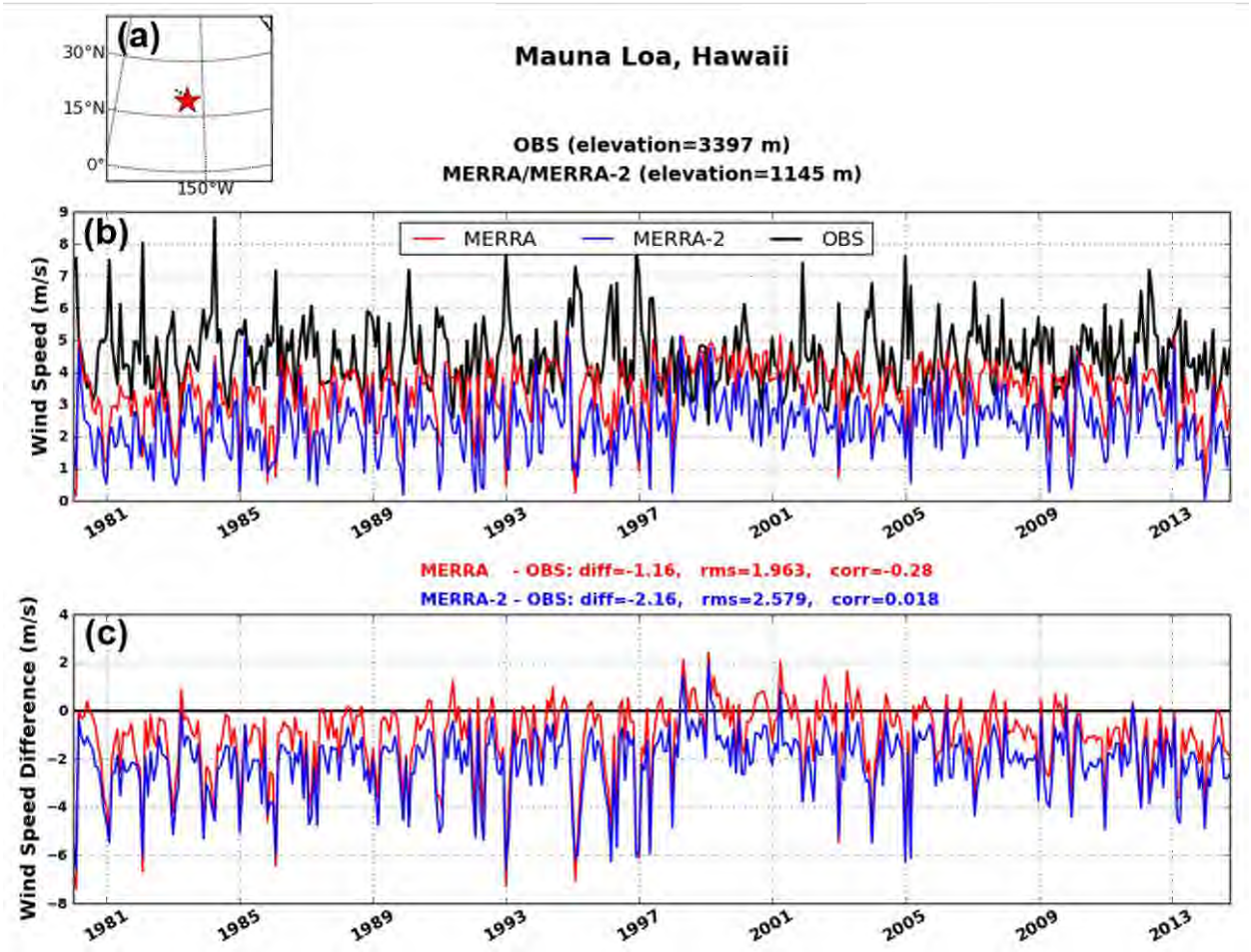

Figure 8-12 Time-series of 10-meter wind speed at Mauna Loa, Hawaii. Panel (a) is the station location, panel (b) is wind speed, and panel (c) is wind speed difference (MERRA minus OBS and MERRA-2 minus OBS). Below the legend are the mean differences, root mean square differences, and correlations between the reanalyses and the observations.

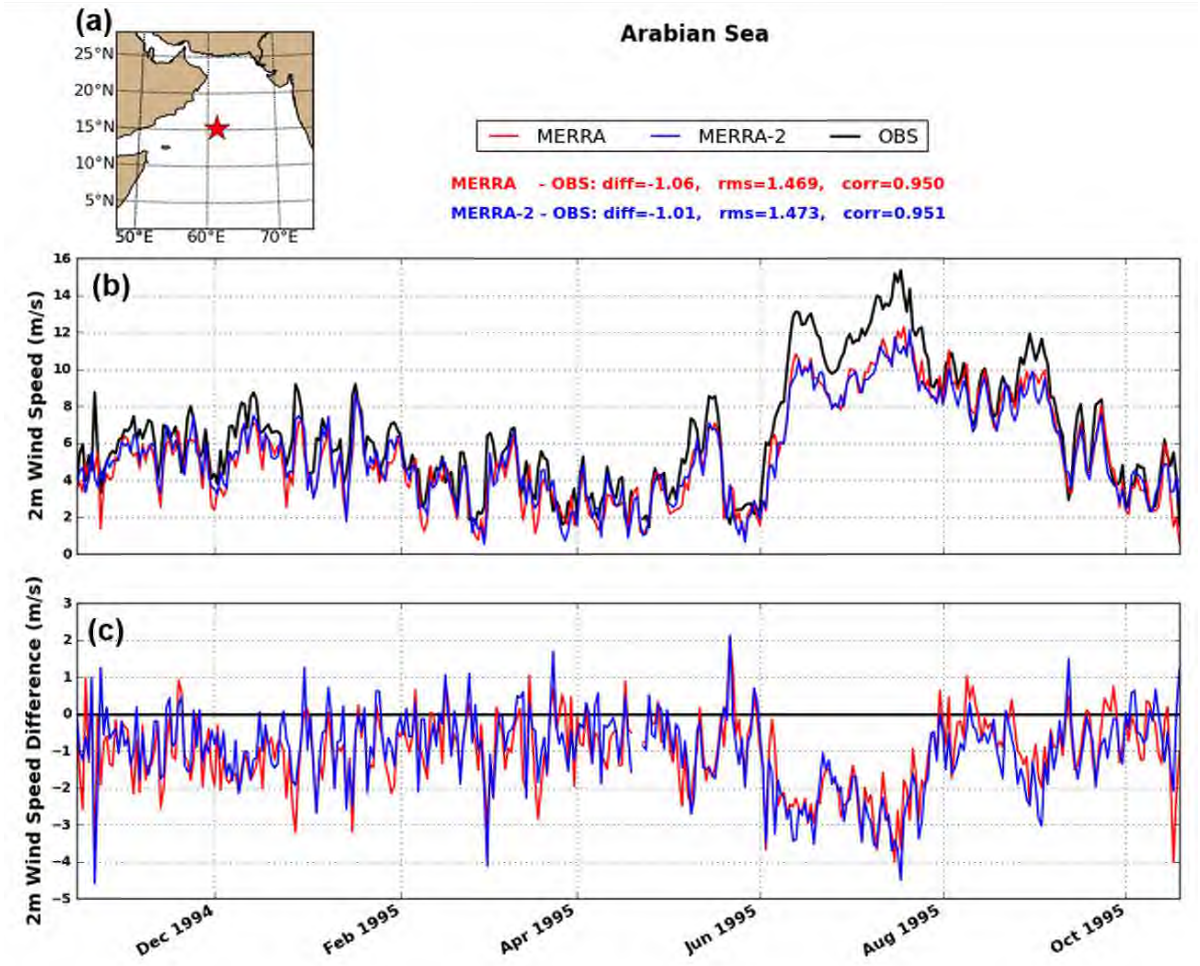

Figure 8-13 Time-series of wind speed in the Arabian Sea. Panel (a) is the station location, panel (b) is wind speed, and panel (c) is wind speed difference (MERRA minus OBS and MERRA-2 minus OBS). Below the legend are the mean differences, root mean square differences, and correlations between the reanalyses and the observations.

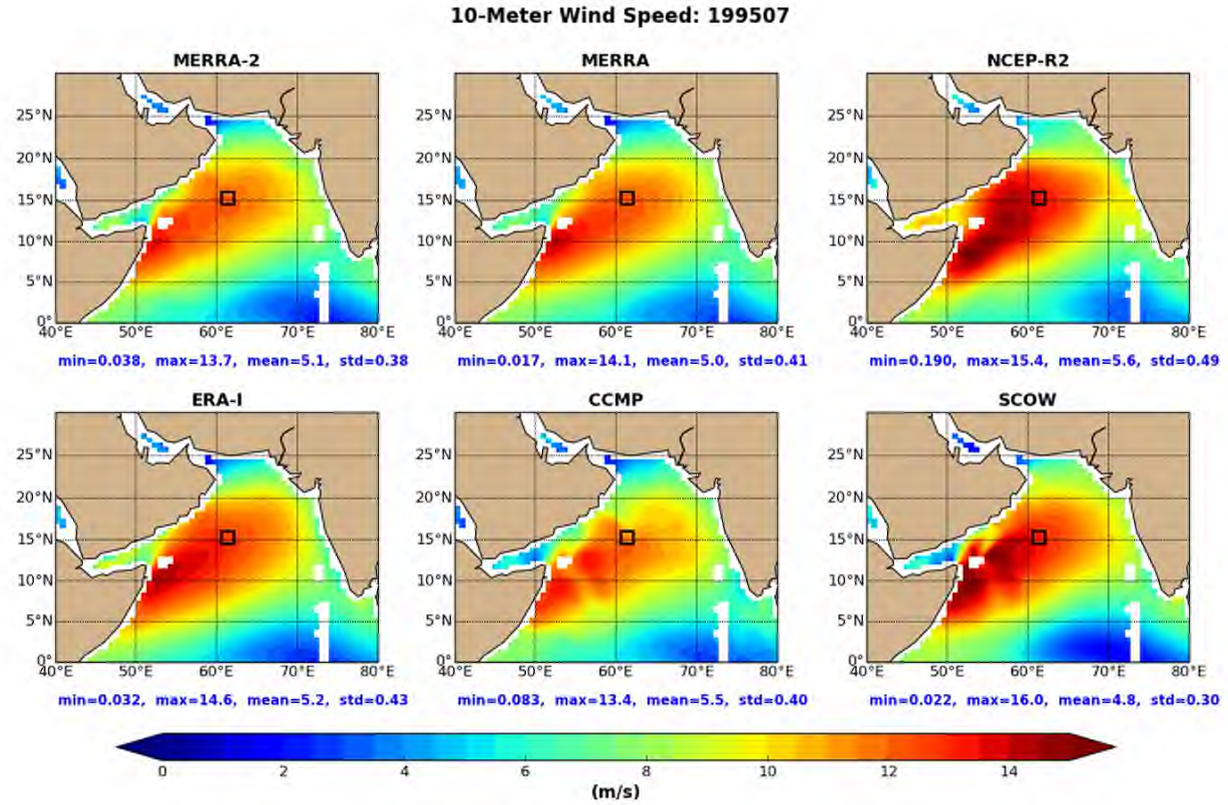

Figure 8-14 Monthly mean of 10-meter wind speed in the Arabian Sea for July 1995. Black square shows the location of the time-series in Figure 8-13.

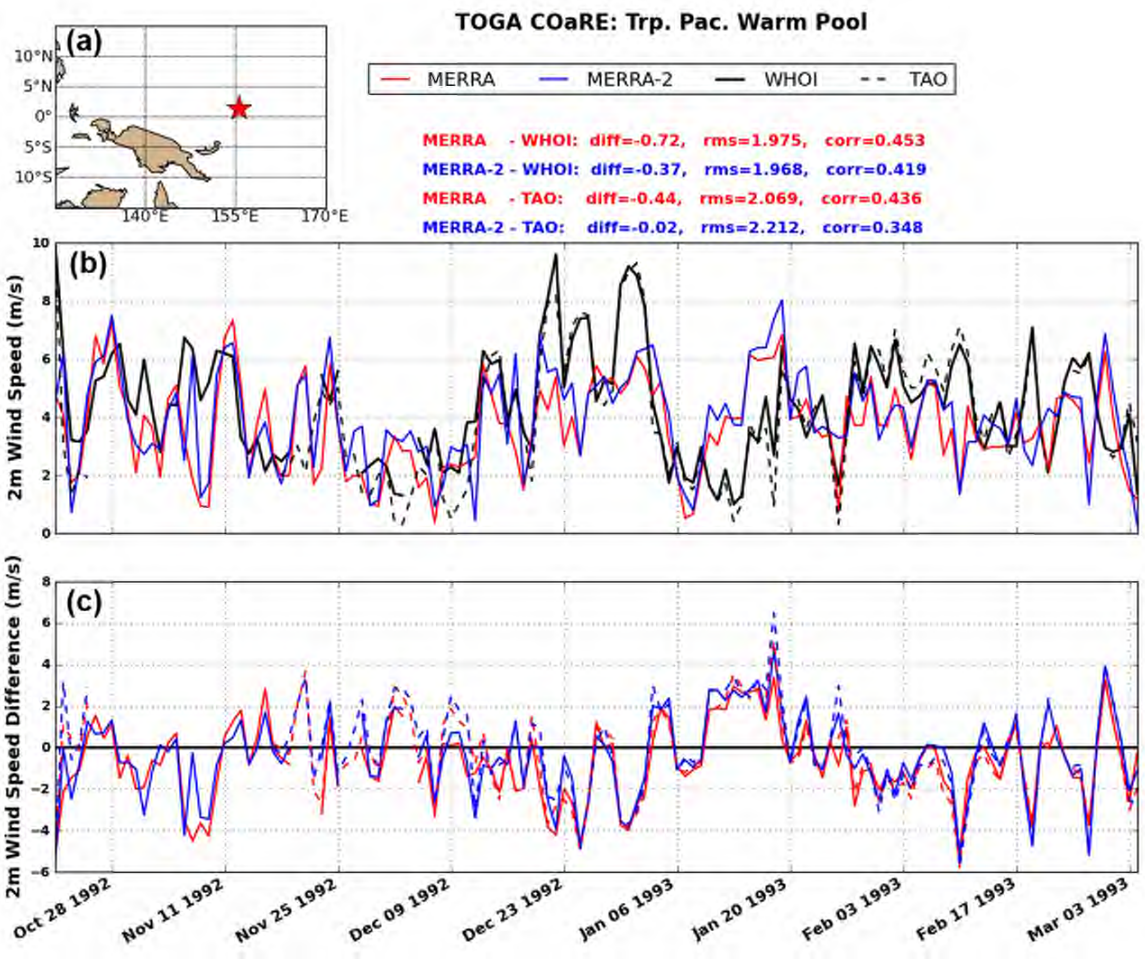

Figure 8-15 Time-series of wind speed in the Tropical Pacific warm pool. Panel (a) is the station location, panel (b) is wind speed, and panel (c) is wind speed difference (MERRA minus OBS and MERRA-2 minus OBS). Below the legend are the mean differences, root mean square differences, and correlations between the reanalyses and the observations. In panel (b), solid lines are differences with WHOI, dashed lines are differences with TAO.

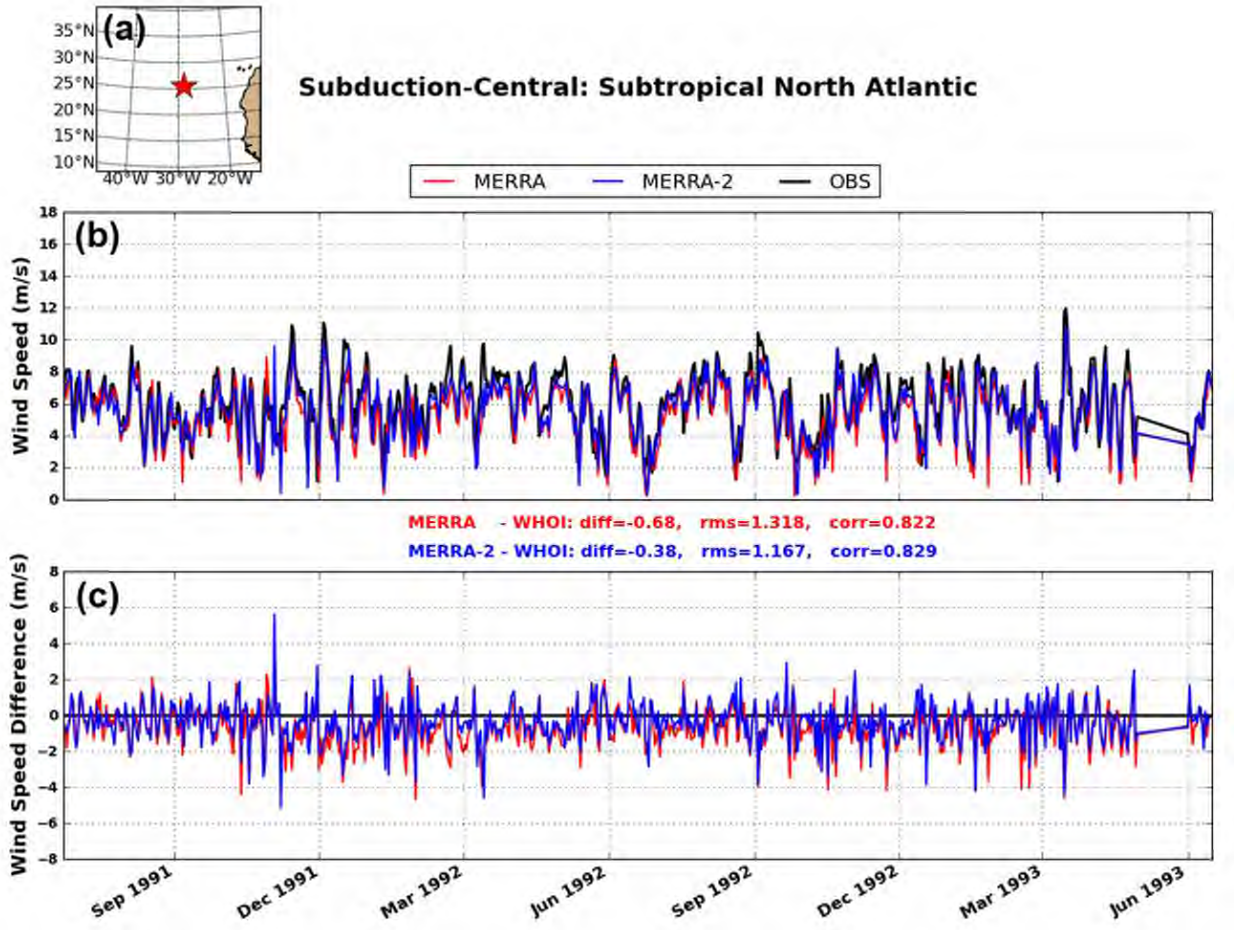

Figure 8-16 Time-series of wind speed in the North Atlantic. Panel (a) is the station location, panel (b) is wind speed, and panel (c) is wind speed difference (MERRA minus OBS and MERRA-2 minus OBS). Below the legend are the mean differences, root mean square differences, and correlations between the reanalyses and the observations.

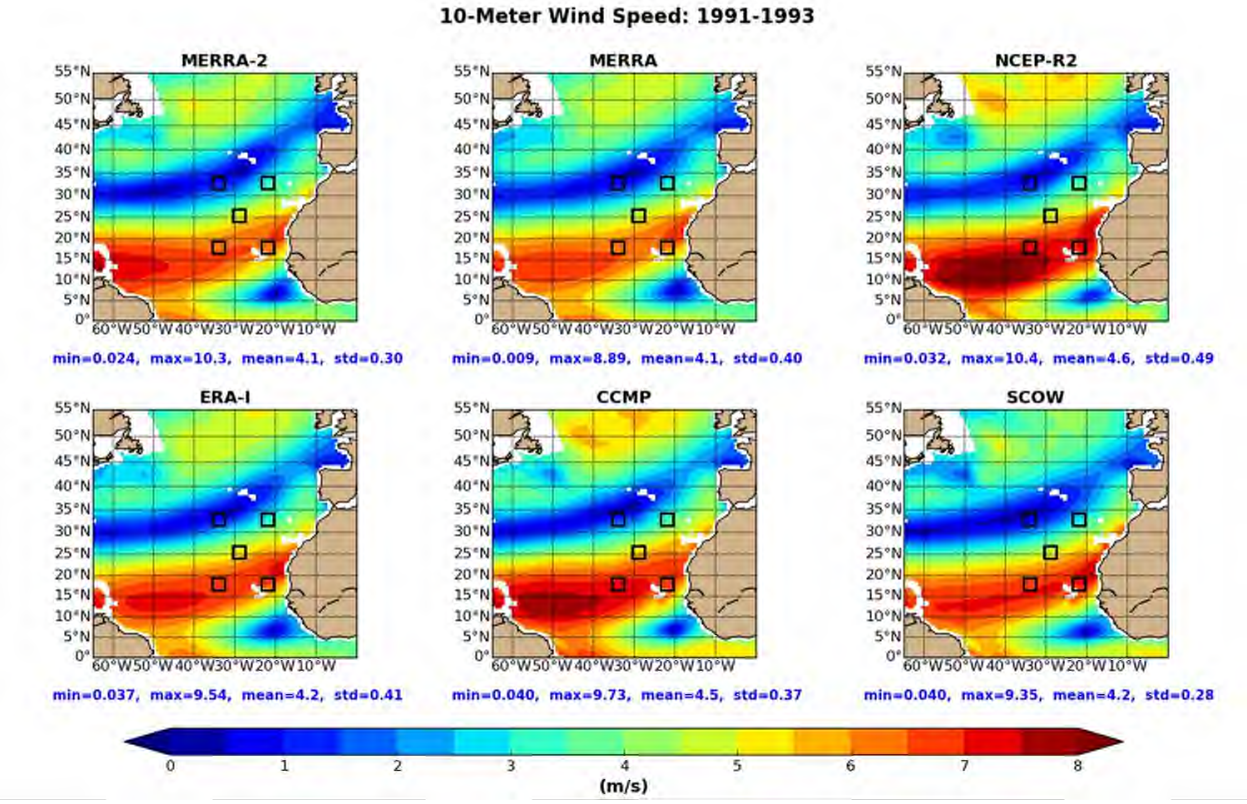

Figure 8-17 Monthly mean of 10-meter wind speed in the North Atlantic from 1991-1993. Black squares show the 5 station locations of the Subduction Experiment array.

9. Polar Regions

a. Glaciated Land Surface

Quasi-permanent, grounded ice surfaces are identified in the MERRA-2 data by the fractional variable **FRLANDICE** in the Constant Model Parameters collection (**const_2d_asm_Nx**). Outside of the Greenland and Antarctic ice sheets, significant land ice cover is found in the eastern Canadian Archipelago (particularly Ellesmere, Devon, and Baffin Islands), as well as Iceland, Svalbard, Franz Josef Land, Novaya Zemlya, Severnaya Zemlya and the New Siberian Islands, southeastern Alaska, the Himalayas, the southern Andes, and Tierra del Fuego. Smaller fractional values are also found on the Aleutian Islands, South Shetlands and Orcadas, Banff, and the central Rockies.

The representation of glaciated land in MERRA-2 differs considerably from that in the original MERRA system. In MERRA, the surface was represented by a prognostic 7 cm water-equivalent surface ice layer. The subsurface energy flux was determined from the prognostic surface layer temperature and a fixed temperature of 230 K (−43°C) at 2 m depth. The land-ice surface albedo was fixed at 0.775. There was no representation of surface hydrologic processes such as snow depth or runoff.

The representation of glaciated land surfaces in MERRA-2, as described in Cullather et al. (2014), allows for fractional snow cover, runoff, and a prognostic surface albedo. The surface represents energy conduction properties of the upper 15m of glacial ice as well as energy and hydrologic properties of an overlying, variable snow cover. Firn of density greater than 500 kg m^{-2} is not explicitly represented. Glaciated land surface variables are maintained separately from non-glaciated land variables (**tavg3_2d_glc_Nx**), and the glaciated variables include variables for surface albedo, snow cover fraction, runoff, snow mass, snow depth, and evaporation (**WESNSC**). Snow cover that persists is allowed to densify to a maximum value of 500 kg m^{-2} before being removed from the surface column. This is tabulated in the **WESNEXT** variable and may be considered a poor man's representation of an iceberg calving flux.

The surface configuration was initialized with output from a prescribed SST atmospheric model integration in addition to the one-year spin-up period for each reanalysis stream. An important consideration is the total depth of the surface representation – composed of glacial ice plus any snow cover – which can potentially range from 15m up to 23m. The interannual temperature wave does not touch this depth over the duration of the stream initialization period, resulting in discontinuities during stream transitions. These discontinuities may be readily found in integrated quantities such as snow mass for locations of persisting snow cover (e.g. between streams 2 and 3 in Figure 9-1). The discontinuities provide a measure of uncertainty in conditions for the surface representation, but the impact at the surface/atmosphere interface is considered small. Given these discontinuities and the lack of constraint in initial conditions, vertical profile information is not

included MERRA-2 glaciated surface output.

Figure 9-2 shows the impact of the new surface configuration on near-surface air temperatures over ice sheets. It may be seen that MERRA is biased when the observed surface temperature differs markedly from the MERRA-prescribed ice temperature of -43°C, and that MERRA-2 closely matches the observed values. Differences between MERRA and MERRA-2 land ice variables at other locations may be associated with other changes to the system between MERRA and MERRA-2. One notable change for Greenland is the difference in topography. The MERRA system used the GTOPO30 topography (Gesch, 1994), which has biases over Greenland of 600m (e.g., Box and Rinke, 2003). These errors have been corrected in MERRA-2.

In addition to improved thermodynamic properties, the MERRA-2 surface representation allows for the computation of surface mass balance (SMB) over the ice sheets, which may be defined as the net of precipitation minus evaporation minus runoff. Other wastage terms such as the divergence and/or sublimation of blowing snow are not considered. Figure 9-3 compares the MERRA-2 SMB for the period 2000-2012 with the corresponding field from the Modèle Atmosphérique Régional (MAR, obtained from the ACADIS Arctic data repository; Fettweis et al., 2011) at 25km grid spacing and a 1958-2007 climatology of the Regional Atmosphere Climate Model (RACMO2, obtained from Sea-level Response to Ice Sheet Evolution project: SeaRISE; Ettema et al., 2009) at 11km grid spacing. Overall, the spatial patterns of accumulation in southeastern Greenland and along higher elevations of the western periphery are very similar among the 3 fields, and there is reasonable agreement between MERRA-2 and the concurrent MAR regional climate model field in the elevation of the zero-contour line along the western coast. The MAR model indicates ablation in southwestern Greenland of greater than (-)2000 mm yr^{-1} over significant areas while MERRA-2 suggests annual ablation of between 700 and 1000 mm in the same region. These differences may be due to differences in resolution, configuration of the surface, differences in atmospheric forcing, or some combination. In general, Greenland SMB is not well constrained, and differences among models and reanalyses serve as a basis for further investigation.

b. Atmospheric Moisture Budget in Polar Regions

For the Arctic and Antarctic, atmospheric reanalyses are important tools for evaluating large-scale weather phenomena and for investigating recent climate variability. Variations in the surface moisture flux may occur as the result of changing temperature patterns in high latitudes and the selective insulation of the atmosphere from oceanic heat and moisture fluxes by sea ice. Variations in the surface moisture flux are noteworthy over grounded polar ice sheets as they have an immediate bearing on eustatic change. Previously, Cullather and Bosilovich (2011) evaluated the polar atmospheric moisture budget in the original MERRA system. A large imbalance was found between the mean atmospheric moisture convergence and the net of precipitation and evaporation for the Arctic. This was attributed in part to the prescribed sea ice albedo, which resulted in incorrect springtime surface flux values. The MERRA system was also found to be overly sensitive to changes in the satellite observing system.

Updates in model physics between the MERRA and MERRA-2 systems are outlined in Molod et al. (2015). Additionally, section 9a describes the glaciated land surface representation changes in the system that are relevant to polar regions. Two other significant changes in the MERRA-2 system are worth mentioning. The first involves the representation of sea ice. Similar to the MERRA system, sea ice in MERRA-2 is represented by a 7-cm skin layer for purposes of heat capacity. The layer is used in the surface energy budget computation and provides a prognostic surface temperature, which is weakly relaxed to 0°C on a 24-hour time scale. Sea ice has no further representation beyond this skin layer. In MERRA, sea ice albedo is a fixed value of 0.6. In MERRA-2, Northern Hemisphere sea ice albedo varies seasonally based on values obtained from the flux tower of the Surface Heat Budget of the Arctic field experiment (SHEBA) (Duynkerke and de Roode, 2001). Monthly values were computed and then linearly interpolated to produce instantaneous values. The sea ice concentration in MERRA-2 is prescribed from various data sets detailed in the ocean and sea ice section of this document. A second significant change is the application of global constraints on dry air mass and moisture analysis increments, with the intended effect of ameliorating abrupt time series jumps due to changes in the observing system (Takacs et al., 2015a and b). Following Cullather and Bosilovich (2011), the atmospheric moisture budget may be written as

$$\frac{\partial\left(W_v + W_l + W_i\right)}{\partial t} + \nabla \cdot \left[\int_{p_{top}}^{p_{sfc}} \left(q_v + q_l + q_i\right) \tilde{\mathbf{V}} \frac{dp}{g} \right] = E - P + ANA_{(MOIST)} + SPUR \quad . \qquad (9\text{-}1)$$

In this form, the moisture storage term plus the divergence of vertically-integrated moisture transport is balanced by the net of evaporation, precipitation, the analysis increment (Bloom et al., 1996), and mostly negligible spurious terms. The budget constraint on moisture that is applied in MERRA-2 locally scales the analysis increment term in equation (9-1) such that its global average is zero, effectively insuring that the global average of precipitation balances evaporation on annual time scales.

From equation 9-1 it may be seen that the surface moisture flux – the net of precipitation minus evaporation – may be computed either as the difference of the model-output fields precipitation and evaporation shown on the right-hand side, or as the difference of atmospheric moisture convergence minus the storage term as shown on the left-hand side. The latter is sometimes referred to as the aerological method (e.g., Serreze et al., 2006). In MERRA and MERRA-2, the aerological and the model-output estimates effectively differ by the analysis increment. In other reanalyses, there is usually a temporal averaging of the prognostic precipitation and evaporation fields so that equation 9-1 is not similarly applicable. The difference between output fields and the aerological method in other reanalyses is referred to here as the quasi analysis increment (which includes the total tendency, roundoff or computational errors in addition to the water vapor analysis increment).

Figure 9-4 shows a comparison (MERRA vs. MERRA-2) of the mean annual cycles of the budget components of equation 9-1 for the north polar cap, defined as poleward of 70°N. In the MERRA system, the analysis increment over the Arctic is sizeable and averages (−)10 mm month^{-1} (water-equivalent) from May through August. In MERRA-2, the analysis increment is of a different sign and averages less than 3 mm month^{-1} over the same period. The magnitude of the analysis

increment in MERRA-2 is greatly reduced throughout the year as compared with MERRA, with a maximum of 5 mm month^{-1} in August.

Changes in the seasonal cycle of various budget components are implied by the reduction of the analysis increment in the newer system. In particular, a springtime maximum in evaporation in MERRA is essentially eliminated in the time series shown for MERRA-2. The difference in evaporation in the two systems for May is 6 mm month^{-1}. These differences are greater over oceanic regions of the Arctic and are consistent with the notion that the use of a fixed sea-ice albedo in MERRA produces unrealistic springtime turbulent fluxes (Cullather and Bosilovich, 2011). A May-June maximum is not found in the observed surface vapor flux over sea ice (e.g., Boisvert et al., 2013).

Another variable in Figure 9-4 that differs substantially between the systems is precipitation. Precipitation in MERRA-2 is greater than that in MERRA over the north polar cap throughout the annual cycle, with the largest differences occurring in summer. The annual mean precipitation for the north polar cap is 304 mm yr^{-1} in MERRA and 401 mm yr^{-1} in MERRA-2. The precipitation field is examined in more detail below. While precipitation, evaporation, and their difference have changed appreciably between MERRA and MERRA-2, terms of the aerological method have not. For the period 1980-2014, atmospheric moisture convergence is 204 mm yr^{-1} for MERRA and 207 mm yr^{-1} for MERRA-2. This compares with aerological estimates computed from two other reanalyses (Trenberth et al., 2011): 195 mm yr^{-1} for the ECMWF-Interim reanalysis (ERA-Interim) for the period 1980-2012, and 190 mm yr^{-1} for the NOAA CFSR reanalysis for the period 1980-2009. A time series of annual surface moisture flux values from the aerological and model-output methods is shown in Figure 9-5. Similar to the conclusion of earlier studies, it may be seen that time series based on the aerological method from various reanalyses are in relatively close agreement, while the model-output curves have a greater spread. From Figure 9-5, the MERRA model-output curve of P − E may be seen as a low-estimate outlier, while the model-output values for MERRA-2 and CFSR are quantitatively similar. Using the mean of the available overlapping time period 1980-2009, the range of north polar cap values from the four reanalyses is about 8 percent of the multi-reanalysis average.

A similar story is shown in Figure 9-6 for the south polar cap bounded by 70S – in going from MERRA to MERRA-2, the analysis increment is reduced, precipitation increases, and atmospheric moisture convergence is largely unchanged. As seen in Figure 9-6, the magnitude of the difference between the model-output and aerological curves is reduced in MERRA-2 as compared with MERRA. The analysis increment for the south polar cap averages (−)32 mm yr^{-1} in MERRA and (+)10 mm yr^{-1} in MERRA-2 for the period 1980-2014. Precipitation changes substantially in the new system, from an average of 206 mm yr^{-1} in MERRA to 253 mm yr^{-1} in MERRA-2. Evaporation is also increased from 44 mm yr^{-1} in MERRA to 54 mm yr^{-1} in MERRA-2. But the aerological estimate of P − E differs only slightly between MERRA and MERRA-2, going from 194 mm yr^{-1} to 189 mm yr^{-1}. These values compare with 172 mm yr^{-1} for ERA-Interim for 1980-2012 and 176 mm yr^{-1} for CFSR for 1980-2009. The larger atmospheric moisture convergence in MERRA and MERRA-2 as compared with other contemporary atmospheric reanalyses for the south polar cap extends to the Antarctic ice sheet. The average surface moisture flux from the

aerological method over Antarctica is 176 mm yr^{-1} for MERRA, 179 mm yr^{-1} for MERRA-2, 139 mm yr^{-1} for ERA-Interim, and 117 mm yr^{-1} for CFSR. Differences with other reanalyses have previously been examined in Cullather and Bosilovich (2011), which found better agreement between MERRA and larger values produced in regional climate models (e.g., Monaghan et al., 2006; van de Berg et al., 2006).

The time series of the surface moisture flux for the south polar cap shown in Figure 9-7 again shows better agreement among the dashed curves denoting the aerological method. It may be seen that the MERRA and MERRA-2 dashed curves are in close agreement over certain periods but diverge for the years 1983-1986 and 1998-2001. It may also be seen that the difference between the aerological and model-output curves varies in time. For example, the difference between the two MERRA curves is markedly reduced after 1998, while the two MERRA-2 curves are in relatively good agreement for the years 1982-1991 but begin to diverge thereafter. While the Arctic is bordered by a relatively dense in situ observational network for observing poleward transport, the south polar cap has known gaps, particularly in the South Pacific Ocean. Thus, south polar regions may be more susceptible to changes in the observing system, which may be reflected by changes in the analysis increments.

Cullather and Bosilovich (2011) further defined a Southern Ocean domain bounded by the Antarctic coastline and the northernmost extent of sea ice since 1980. For this domain, the northern boundary fronting poleward transport is relatively devoid of in situ observations. The time series of precipitation and the difference of model-output minus aerological surface moisture flux for the Southern Ocean are shown in Figure 9-8. The figure clearly shows the abrupt change in the MERRA system associated with the introduction of data from the Advanced Microwave Sounding Unit (AMSU) in 1998, and changes associated with the introduction of other observing systems in the early 2000s. Southern Ocean precipitation in the MERRA system increased by 19 percent over the transition, and the model-output surface flux ($P - E$) increased by 43 percent. Corresponding changes are also seen in the MERRA analysis increment.

Other systems have difficulties in the data-sparse Southern Ocean. ERA-Interim precipitation decreased by 3 percent after the introduction of AMSU in 1998, although the corresponding quasi analysis increment shown in Figure 9-8b is mostly unchanged. Figure 9-8b also shows an abrupt increase in the quasi analysis increment for the CFSR that corresponds to the introduction of AMSU. The CFSR-computed evaporation for the Southern Ocean decreased by 14 percent over this jump. A change in CFSR precipitation associated with AMSU is difficult to discern from Figure 9-8a, although a precipitation decrease from the period prior to 1994 is apparent.

In spite of the application of a global constraint on the moisture budget analysis increment in MERRA-2, changes in the local value for the Southern Ocean are discernible, though they are not as large as in MERRA. The MERRA-2 analysis increment increases from about 40 mm yr^{-1} in the mid-1990s to an average of 56 mm yr^{-1} in 2000-2002. More interestingly, the analysis increment increases from -19 mm yr^{-1} in 1989 to 39 mm yr^{-1} in 1992. While the observing system was significantly altered with the introduction of SSM/I passive microwave data in the late 1980s, the

introduction of ERS scatterometer wind data in 1991 likely aided in quantifying evaporation over the global ocean and may have influenced precipitation and the analysis increment in MERRA-2 via the global moisture budget constraint. While the MERRA-2 analysis increment increases with time with stair-stepped changes, the Southern Ocean precipitation presented in Figure 9-8a shows an intriguing and mostly uniform trend of +30 ± 3 mm per decade. While such trends have been suggested to coincide with changes in climate indices (e.g., Liu and Curry, 2010; Yin et al., 2005; Boer et al., 2001), definitive observational evidence over the recent satellite era remains elusive (Bromwich et al., 2011). There is no trend in MERRA-2 precipitation over the grounded Antarctic ice sheet.

As seen above, reanalyses may be evaluated for soundness through the intercomparison of moisture budget components including the analysis increment. Quantitative comparisons with observations in high latitudes present a challenge due to the scarcity of observations and their representativeness over significant areas. Precipitation measurements in polar regions have special difficulty due to the presence of blowing snow. Figure 9-9 shows a comparison between MERRA-2 precipitation and wind-corrected gauge values from the Surface Heat Budget of the Arctic Ocean (SHEBA) field site for October 1997 to September 1998 (Sturm et al., 2002). MERRA-2 values were obtained using the nearest grid point to the camp location on each day. Consistent with the evaluation against MERRA, the comparison with SHEBA suggests that MERRA-2 precipitation is too large over the central Arctic Ocean, and that this is particularly true during summer months. The annual average for the gauge observation is 177 mm as compared with 267 mm for MERRA-2, and the average for the months of July, August, and September is 76 mm for the gauge as compared with 118 mm for MERRA-2. The differences with this field study are similar to those seen in comparisons with available climatologies. For example, Yang (1999) determined a mean annual precipitation for the Arctic Ocean of 260 mm using wind-corrected gauge values from Russian drifting ice stations over the period 1957-1990. For a comparable domain of the central Arctic Ocean as defined in Cullather and Bosilovich (2011), the mean annual precipitation for 1980-2014 is 287 mm for MERRA and 375 mm for MERRA-2.

Comparisons with regional climate models (RCMs) for the Greenland Ice Sheet (GrIS) are also useful because they have been evaluated against glaciological estimates of accumulation. For the GrIS, 1980-2014 estimates of mean accumulation (P − E) for the period 1980-2014 for MERRA are 415 mm yr^{-1} from model output and 435 mm yr^{-1} from the aerological method. For MERRA-2 the values are 447 mm yr^{-1} from model output and 420 mm yr^{-1} from the aerological method. These may be compared to accumulation values of 360 mm yr^{-1} from Fettweis (2007) and 419 mm yr^{-1} from Ettema et al. (2009). High-resolution simulations with RCMs such as the 11km grid spacing used in Ettema et al. (2009) have yielded larger accumulation values and so the MERRA and MERRA-2 values are not implausible. A comparison of the surface mass balance of the GrIS is given in the glaciated land surface section.

The differences in model output precipitation for MERRA and MERRA-2 for the GrIS are on the order of 10 percent. Spatial differences in MERRA-2 precipitation with other reanalyses are shown in Figure 9-10. The differences between MERRA-2 and MERRA precipitation are associated with the central Arctic and subarctic land surfaces; differences are smaller equatorward of Iceland and

the Norwegian Sea in the North Atlantic. An analysis of wind-corrected gauge data compiled by the University of Delaware (Figure 9-10b) (Willmott and Rawlins, 1999) indicates very large precipitation differences with MERRA-2 over the Arctic boreal zone in Eurasia. In summer months, MERRA-2 precipitation in these areas is more than twice the amount estimated in the Delaware climatology. The difference between MERRA-2 precipitation and MERRA abruptly decreases equatorward of about 60N over Eurasia. MERRA-2 utilizes (at least partially) observation-corrected precipitation for land model forcing equatorward of about 62N (see Section 7a). It could be assumed that the use of corrected precipitation may play a role in the differences shown in Figure 9-10, or that the lack of a correction of soil moisture plays a role in the biases shown for polar regions. These latitudes are co-located with the summertime polar front, however, so that the bias patterns are associated with the spatial distribution of mean values produced by the general circulation. In any event, high latitude precipitation biases in MERRA-2 are certainly not limited to terrestrial zones. Differences with other reanalyses such as ERA-Interim suggest that MERRA-2 may have high biased precipitation extending over most of the perennial sea ice zone. The difference plots of MERRA-2 with MERRA (Figure 9-10a) and ERA-Interim (Figure 9-10c) highlight the close agreement between MERRA and ERA-Interim over the Arctic. The agreement in larger values of precipitation for the north polar cap in MERRA-2 and CFSR (Figure 9-10d) only extends to the Arctic ice pack.

For the grounded Antarctic ice sheet (AIS), 1980-2014 mean accumulation values for the period 1980-2014 for MERRA-2 are 184 mm yr^{-1} from model output and 179 mm yr^{-1} from the aerological method. These numbers compare with MERRA values of 159 mm yr^{-1} from model output and 176 mm yr^{-1} from the aerological method, and they compare with RCM values of 180 mm yr^{-1} from Monaghan et al. (2006) and 171 mm yr^{-1} from van de Berg et al. (2006). More recently, Palerme et al. (2015) estimated precipitation from CloudSat data for the AIS equatorward of 82S as 171 mm yr^{-1} for the period 2006 to 2011. Over this period the MERRA-2 precipitation averages 203 mm yr^{-1} with a standard deviation of 5 mm yr^{-1}.

These comparisons support general conclusions for the polar regions. As compared with MERRA, the analysis increment in MERRA-2 has become smaller, and the time series are generally more stable, with the possible exception of the challenging Southern Ocean sea ice zone. Atmospheric moisture convergence has not changed appreciably between MERRA and MERRA-2, and these values appear to be plausible, particularly in the evaluation of accumulation over polar ice sheets. In the closure of the moisture budget, however, precipitation has increased significantly as compared with MERRA, and this appears to be undesirable. Available metrics suggest that MERRA-2 precipitation is too large over the sea ice zone and is especially too large over the Arctic boreal zone. Significant progress has been made in reducing biases through the application of improved model physics, such as improvements in the annual cycle of evaporation over the Arctic Ocean. Nevertheless, precipitation biases in the Arctic boreal zone are substantial and represent one of the most significant – if not the most significant – challenges associated with reanalyses in the high latitudes.

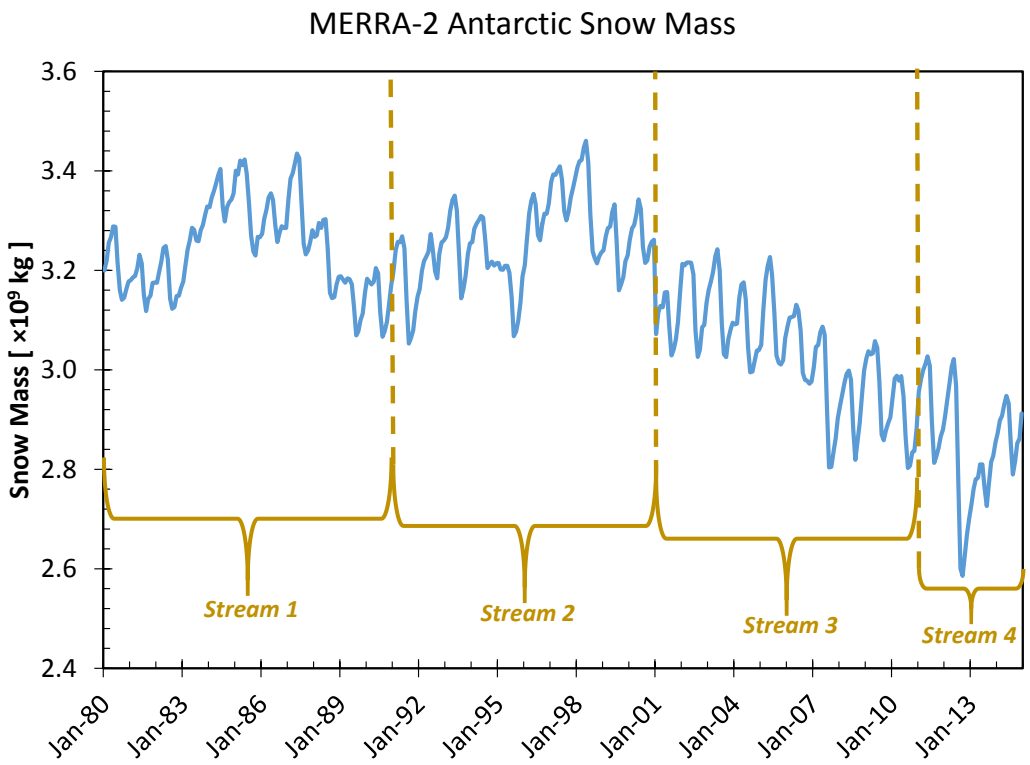

Figure 9-1 The sum of snow mass over the Antarctic Ice Sheet from MERRA-2, in kg. Demarcations of the different streams are indicated.

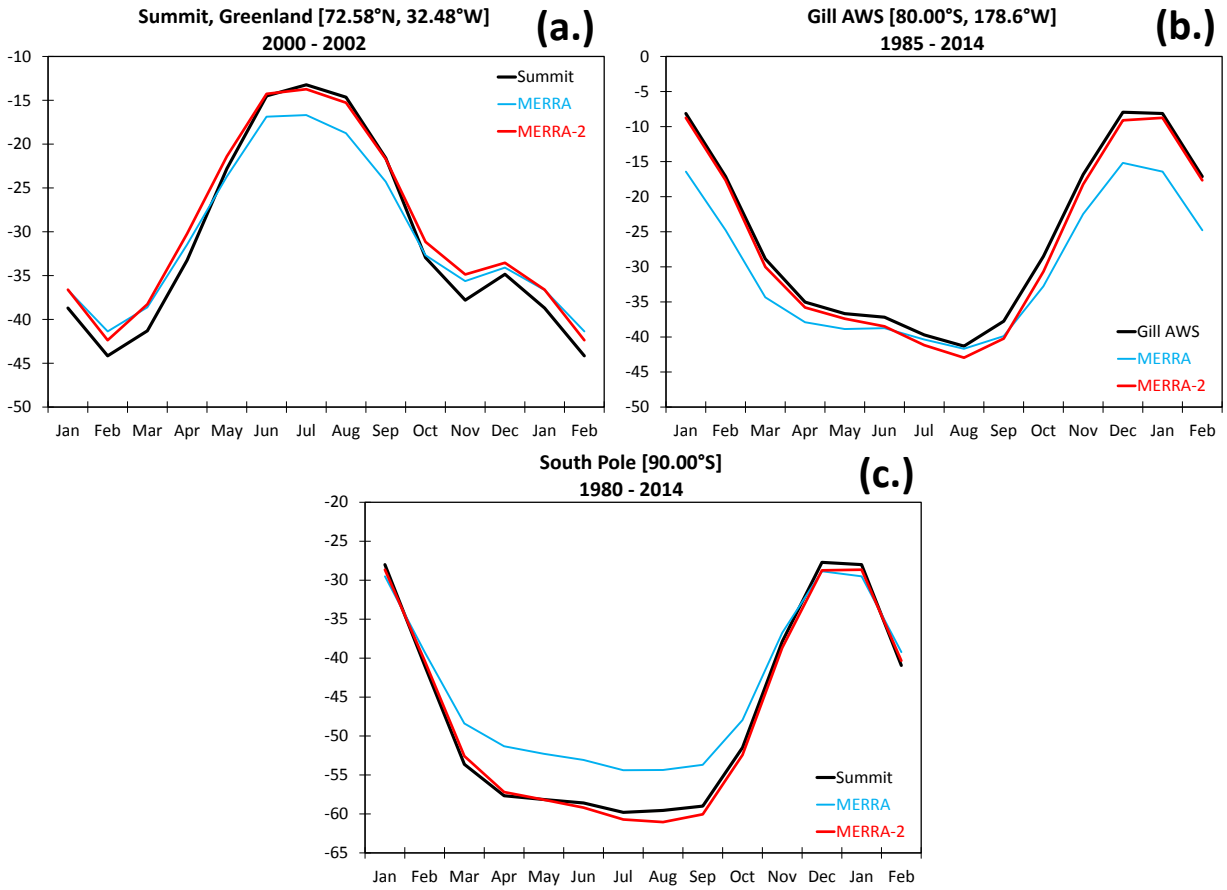

Figure 9-2 Average annual cycle of 2m air temperature for available years for MERRA-2, MERRA and in situ observations at (a) Summit, Greenland (Hoch, 2005), (b) automatic weather station Gill centered on the Ross Ice Shelf, Antarctica, and (c) South Pole. Temperatures are in ℃.

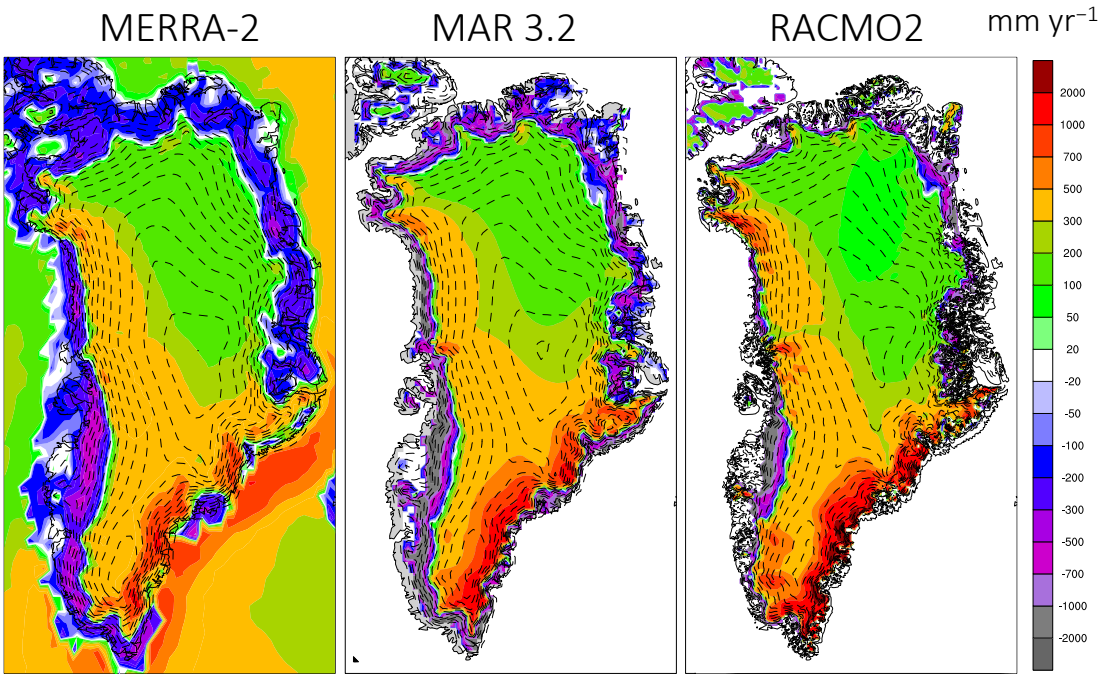

Figure 9-3 The 2000-2012 average surface mass balance for MERRA-2 in comparison to that for regional climate models MAR 3.2 and RACMO2 (long-term average), in water-equivalent mm yr^{-1}*. Topographies are contoured in dashed black lines at every 200m.*

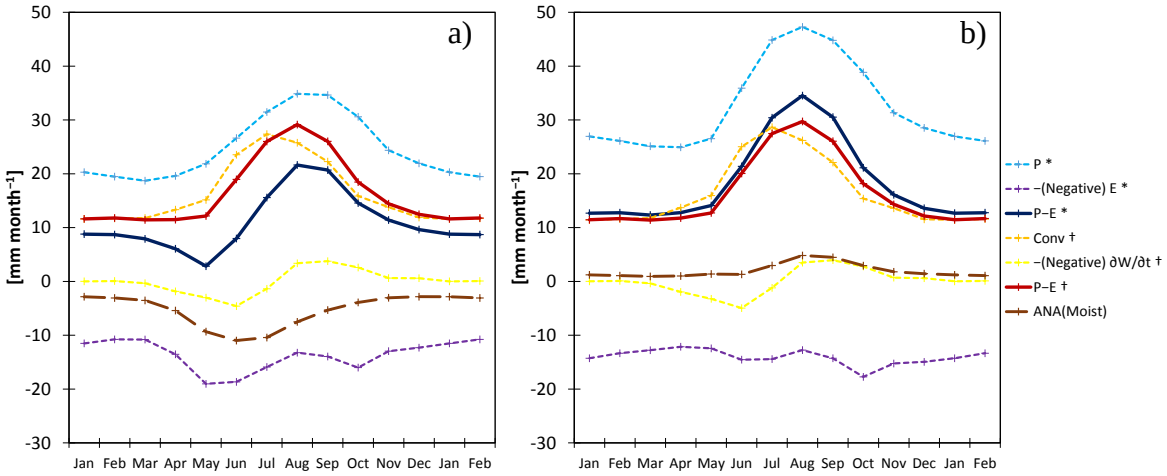

Figure 9-4 Mean annual cycle of atmospheric moisture budget components in (a) MERRA and (b) MERRA-2 for the region poleward of 70N for the period 1980-2014, in mm month^{-1}. Curves denoted with an asterisk are model-derived values indicated on the right-hand side of eq. (9-1) while a dagger indicates terms on the left-hand side. The negative of evaporation is plotted to indicate that the summation with the precipitation curve results in P−E.*

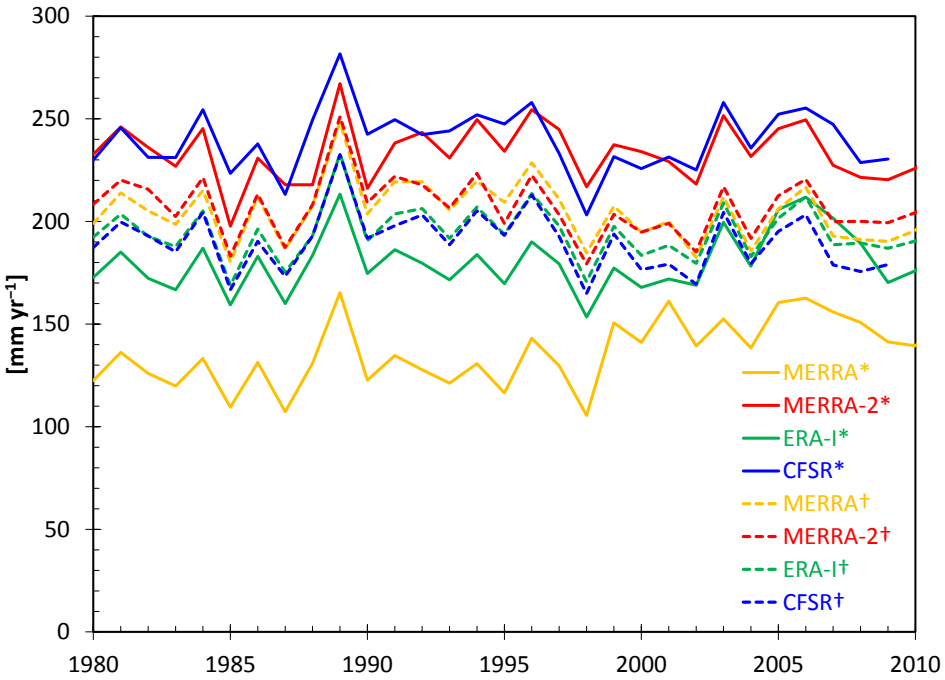

Figure 9-5 Time series of annual mean surface moisture flux (P − E) for the region 70N to 90N in mm yr^{-1} from four reanalyses using output fields (, solid curves) and the aerological method (†, dashed).*

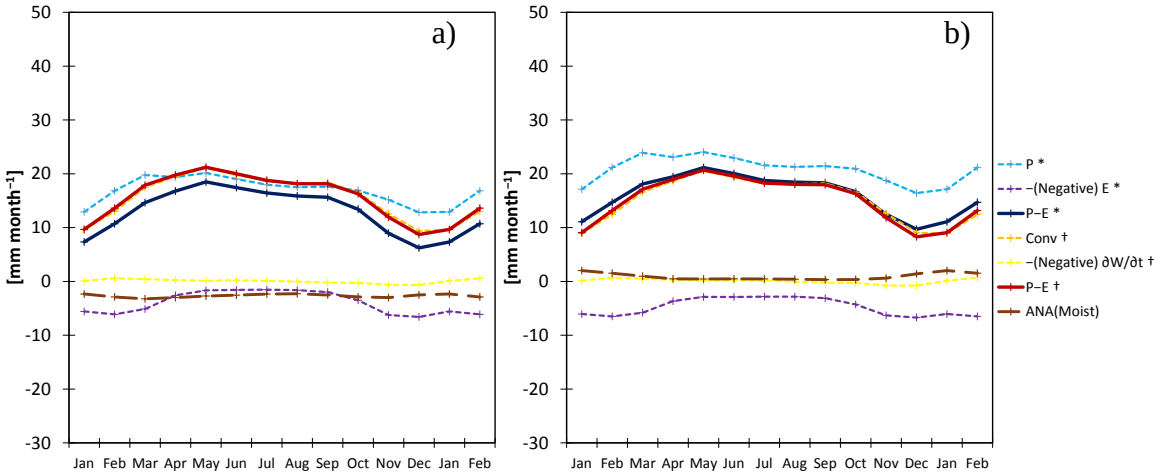

Figure 9-6 As in Figure 9-4 but for the region bounded by 70S and 90S in (a) MERRA and (b) MERRA-2 for the period 1980-2014, in mm month^{-1}.

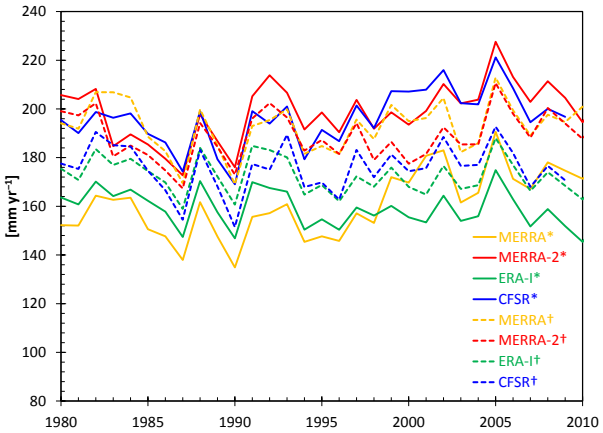

Figure 9-7 As in Figure 9-5 but for the region 70S to 90S, in mm yr^{-1}.

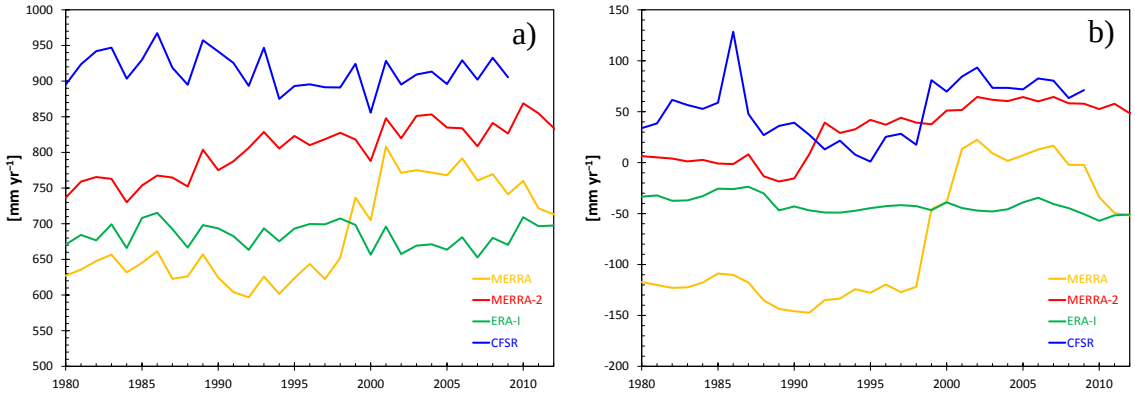

Figure 9-8 Time series of (a) annual precipitation and (b) the difference of model-output minus aerological surface moisture flux (equal to the analysis increment for GMAO systems and the quasi analysis increment for CFSR and ERA-Interim) over the Southern Ocean from four reanalyses, in mm yr^{-1}.

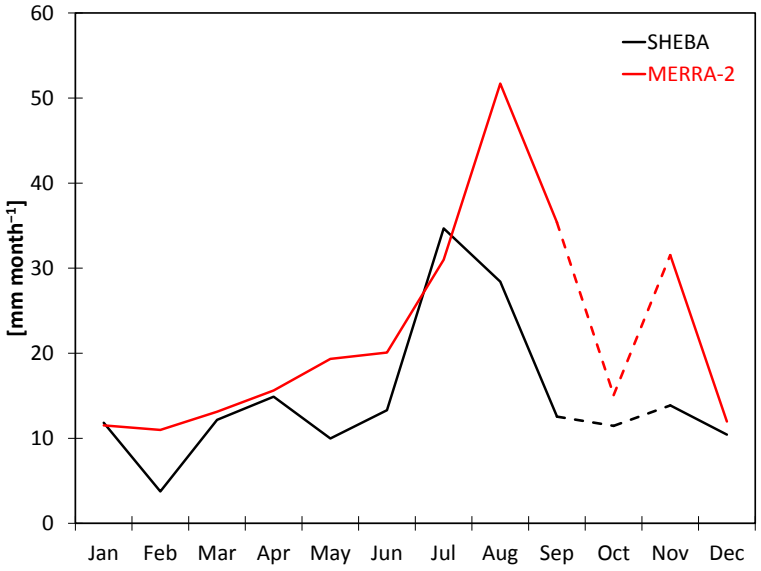

Figure 9-9 Monthly-averaged time series of wind-corrected precipitation from gauge measurements at the Surface Heat Budget of the Arctic Ocean (SHEBA) field site for October 1997 to September 1998 (Sturm et al., 2002), and corresponding values from MERRA-2, in mm month^{-1}. The October value is the precipitation rate computed from only three days and is dashed.

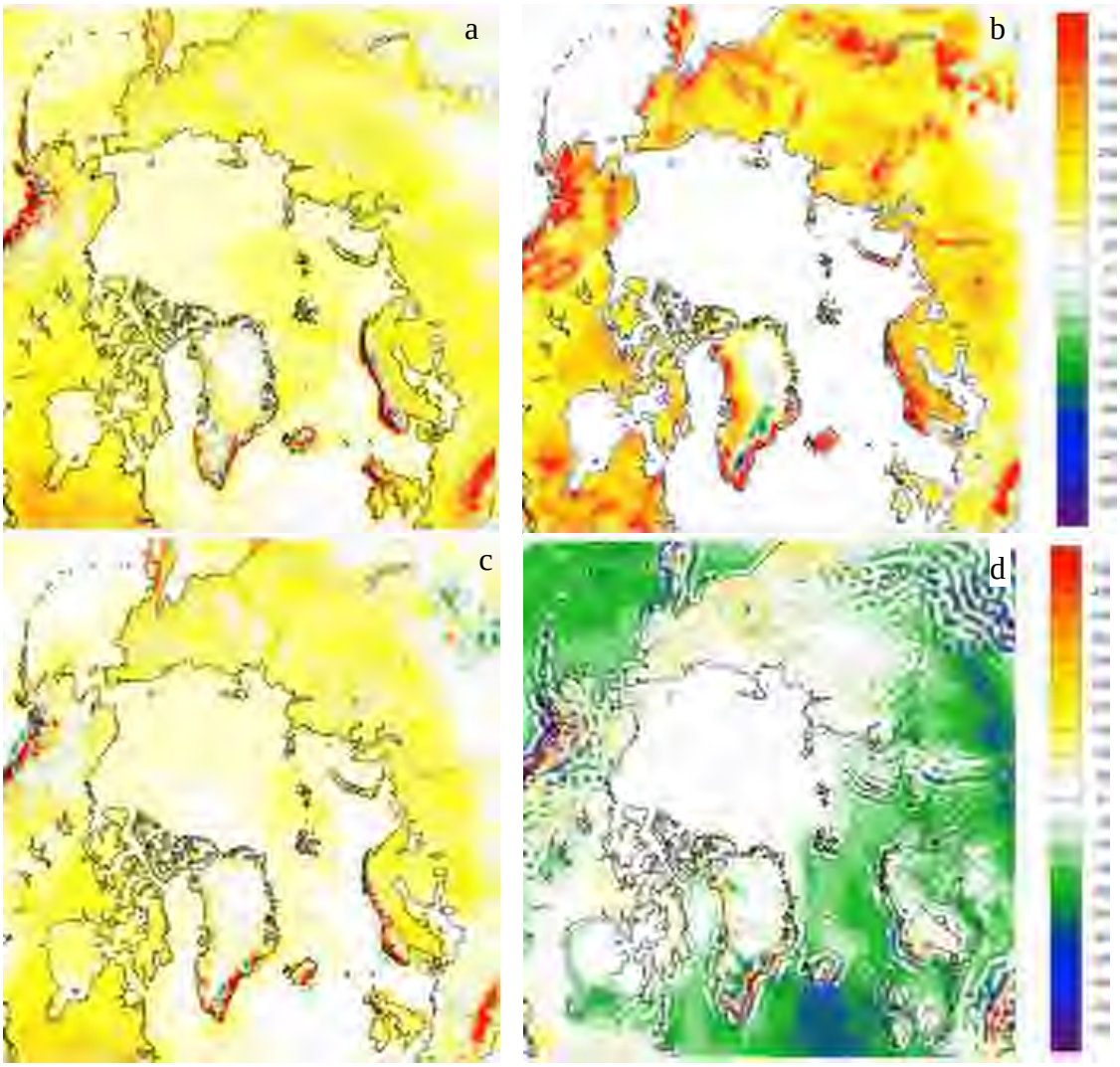

Figure 9-10 The difference of mean annual precipitation minus that for MERRA-2, for: (a) MERRA, 1980-2014; (b) University of Delaware Arctic land-surface, 1980-2004 [Willmott and Rawlins, 1999]; (c) ERA-I, 1980-2012; and (d) CFSR for 1980-2009, in mm yr^{-1}.

10. Stratosphere

The MERRA-2 stratosphere has benefited from improvements to the GSI data assimilation system and GEOS atmospheric model, as well as from the addition of observations that were not used in the original MERRA. Here we highlight some of these changes.

a. Assimilation System Improvements: Use of the CRTM

MERRA-2 takes advantage of the Community Radiative Transfer Model (CRTM) in the assimilation of the Stratospheric Sounder Unit (SSU) radiances (Chen et al., 2011). These three SSU radiance channels are a major source of stratospheric information during the 1980s and 1990s; however, the SSU instruments during this time span several satellite platforms, each with different bias characteristics, making their use somewhat problematic (Zou et al., 2014). The CRTM has been designed for SSU data assimilation and accounts for many of the biasing factors.

Figure 10-1 shows the monthly and globally averaged temperature anomalies for MERRA-2 (blue curve) and MERRA (green curve) as a function of time at 1, 5, 10, 100, 200, 500, and 850 hPa. The 10-year (2000 through 2009) annual cycle and mean have been removed. This figure has been designed for comparison with the corresponding figure in Rienecker et al. (2011; their figure 16). At 1 hPa, for the 1980-1995 time period, MERRA-2 global temperatures are seen to be closer to the current 2005-2015 temperatures than was found in MERRA. Another improved feature of MERRA-2 at 1 hPa is that the anomalous annual cycle (late 1980s to early 1990s) seen in MERRA is lacking in MERRA-2. MERRA-2 is also missing the two largest temperature spikes in the MERRA record. MERRA-2 is low in the late 1990s until the introduction in 1999 of stratospheric AMSU-A channels. This 1999 increase in 1 hPa global averaged temperature is also seen in ERA-Interim (Rienecker et al., 2011).

At 5 hPa (Figure 10-1, second panel) MERRA had a strong anomalous annual cycle throughout the 1980s and 1990s. This 5 hPa annual signal is much reduced in MERRA-2, though both systems have more variability during the 1980s-1990s than in the later record. At 10 hPa and below the two systems agree well, as seen in the lower panels of Figure 10-1. Temperature increases can be seen at 100 hPa due to the two large volcanic eruptions, El Chichón (1982) and Pinatubo (1991).

b. Model Improvements

1) Cubed Sphere Grid

The General Circulation Model component of MERRA-2 uses a cubed sphere grid, thus eliminating computational instability issues near the poles. This can be especially important in the stratosphere, where strong cross polar flows frequently occur, particularly during major sudden warming events. Such features from the cubed sphere grid are then interpolated to a latitude-longitude grid as part of the generation of MERRA-2 final products. Figure 10-2 presents an

example of the cross polar Ertel Potential Vorticity (EPV) field near the North Pole during a strong cross polar flow event showing the stronger and more continuous EPV gradients seen in MERRA-2 (Figure 10-2b) relative to those seen in MERRA (Figure 10-2a).

Note that, while scalar fields such as EPV and temperature are well-behaved near the poles in MERRA-2, the vector wind from the cubed sphere is not saved at all longitudes as a uniquely defined direction and speed at the poles. Therefore, users of MERRA-2 will have to choose how to handle winds near the poles. One possible approach is to simply not use the winds at neither the pole point nor the two nearest to the pole latitudes, setting the pole wind instead to the average wavenumber one component at the third latitude from the pole and then interpolating the winds in between the new pole wind and the third latitude from the pole. Other methods are possible as well.

2) Improved Residual Circulation

The tropical tropopause is the region where most air enters the stratosphere, and wind fields used for tracer transport studies rely on realistic winds in this region. The MERRA-2 GEOS atmospheric model development has led to a retuning of the parameterized gravity wave (GW) drag for improvements in the tropics (and mesosphere as well, Molod et al., 2015). The improvements in the tropics now allow for a model-generated quasi-biennial oscillation (QBO) resulting in smaller MERRA-2 wind analysis increments in the QBO region so that the meridional circulations should be less perturbed by the analysis. Figure 10-3 compares the residual annual mean meridional circulation (see Andrews et al., 1987, page 128) for MERRA-2 and MERRA. In particular the equatorial region near 70 hPa shows a more consistent upward motion in MERRA-2 (Figure 10-3c) than in MERRA (Figure 10-3d). While it is difficult to determine the exact cause of the changes between the MERRA and MERRA-2 circulations, the generation of a model QBO is a significant change, and the new MERRA-2 tropical circulations may provide improvements to off-line transport applications.

c. New Data Types

1) MLS Temperature Profiles

The Earth Observing System (EOS) Microwave Limb Sounder (MLS) on the Aura satellite provides middle atmosphere temperature profiles from August 2004 to the present (Schwartz et al., 2008). These temperature profiles are being assimilated in MERRA-2 at altitudes above 5 hPa, providing a strong constraint on the dynamics of the stratopause and lower mesosphere. While several GEOS-5 data assimilation products are used as a background for the MLS retrieval algorithm, the retrieved MLS temperature profiles still provide significant independent and useful information about middle atmosphere temperatures. There is a discontinuity in the MERRA-2 high-altitude temperatures when the assimilation of MSL temperature begins (August 2004) that is important to note; however the use of MLS temperature profiles is in keeping with the MERRA-2 goal of providing the best possible atmospheric analysis at each time.

An example of the high altitude improvements can be seen in Figure 10-4, which shows the time-

height evolution of polar temperatures during the 2005-2006 northern hemisphere winter – a time during which a major stratospheric sudden warming occurred. In a comprehensive study of this winter, Manney et al. (2008) showed the breakdown of the warm polar stratosphere during the warming and its later high-altitude re-formation as seen in the MLS observations. This high-altitude reformation (in early February 2006) is well captured in MERRA-2 (Figure 10-4a) compared to MERRA (Figure 10-4b), thus showing the direct effect of the MLS temperature assimilation on MERRA-2. The assimilation of the MLS temperatures will directly benefit studies of the stratopause and lower mesosphere dynamics when MERRA-2 is used during the EOS Aura MLS time period.

2) **GPS Radio Occultation**

MERRA-2 assimilated GPS (Global Positioning System) radio occultation bending angle observations up to 30 km. Details of the GPS platforms assimilated by MERRA-2 can be found in McCarty et al. (2015). The GPS observations should aid in bias correction in the lower stratosphere by providing a stable source of temperature and moisture measurements. Here we examine an example of the GPS effects on the assimilation system on 31 January 2010, 18 UTC (Figure 10-5). Figure 10-5a shows two GPS bending angle profiles at different locations showing the typical vertical extent and variability of the observations. Panel b shows the difference between the profiles and the background bending angle forecast (O-F) at the two locations, expressed as a percent to account for the reduction in bending angle with altitude. Figure 10-5c and Figure 10-5d focus on a single profile only (25.4E, 44N). Figure 10-5c repeats the O-F curve from b, focusing on the stratosphere and also shows how the analysis (O-A, blue curve) adjusts by reducing the differences with the observations in this example. In Figure 10-5d, the differences in temperature profile (A-F) produced by the analysis, while influenced to some extent by all nearby observations, are anti-correlated (since temperature is inversely proportional to density/bending angle) with the O-F curve in c from about 21-28 km, suggesting a significant impact of the GPS observations in the MERRA-2 analysis.

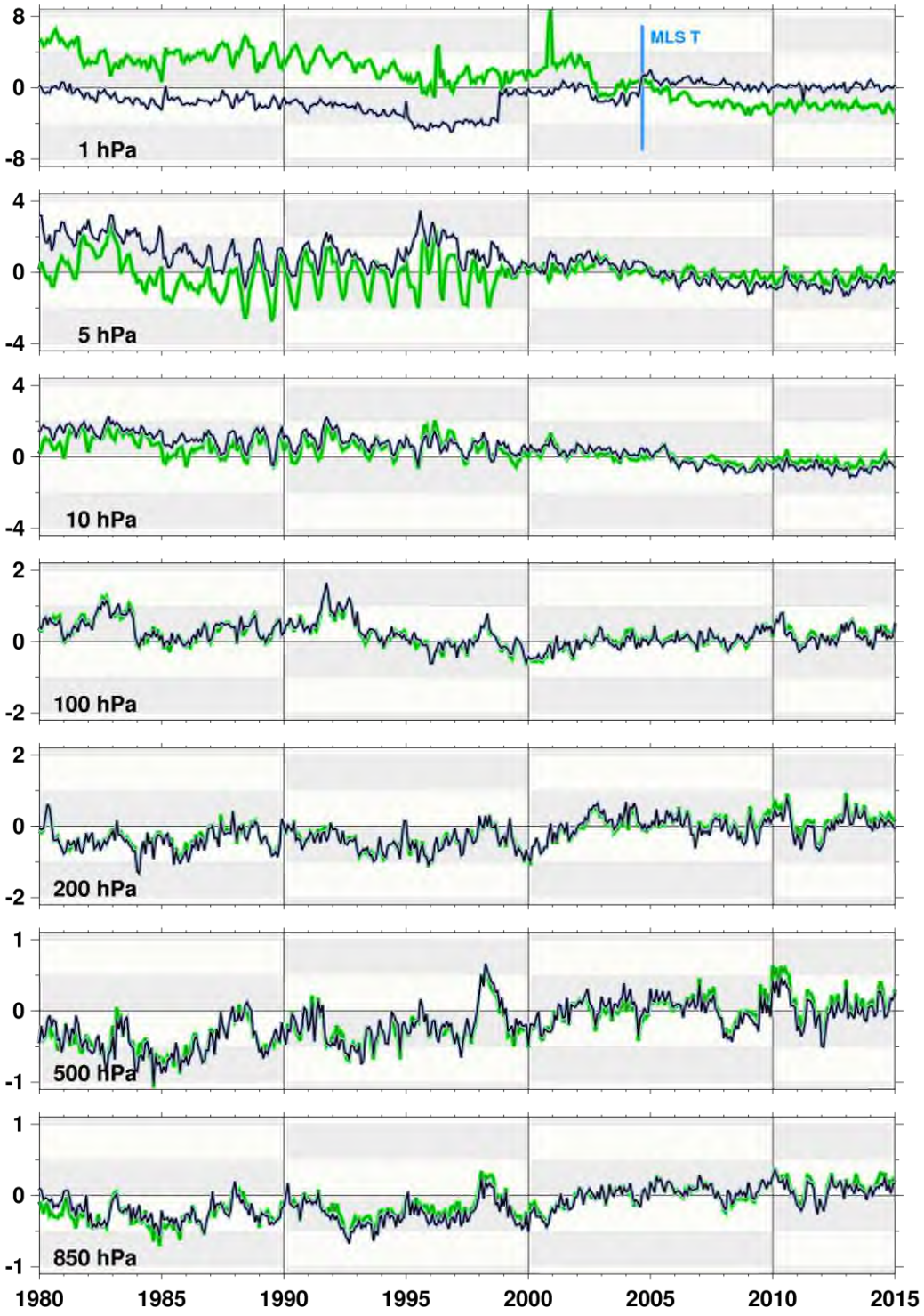

Figure 10-1 The monthly and globally averaged temperature for MERRA-2 (blue curve) and MERRA (green curve) as a function of time at 1, 5, 10, 100, 200, 500, and 850 hPa. The 10-year (2000 through 2009) annual cycle and mean have been removed. The MLS temperatures were introduced above 5 hPa beginning in August 2004 (top panel, blue vertical line).

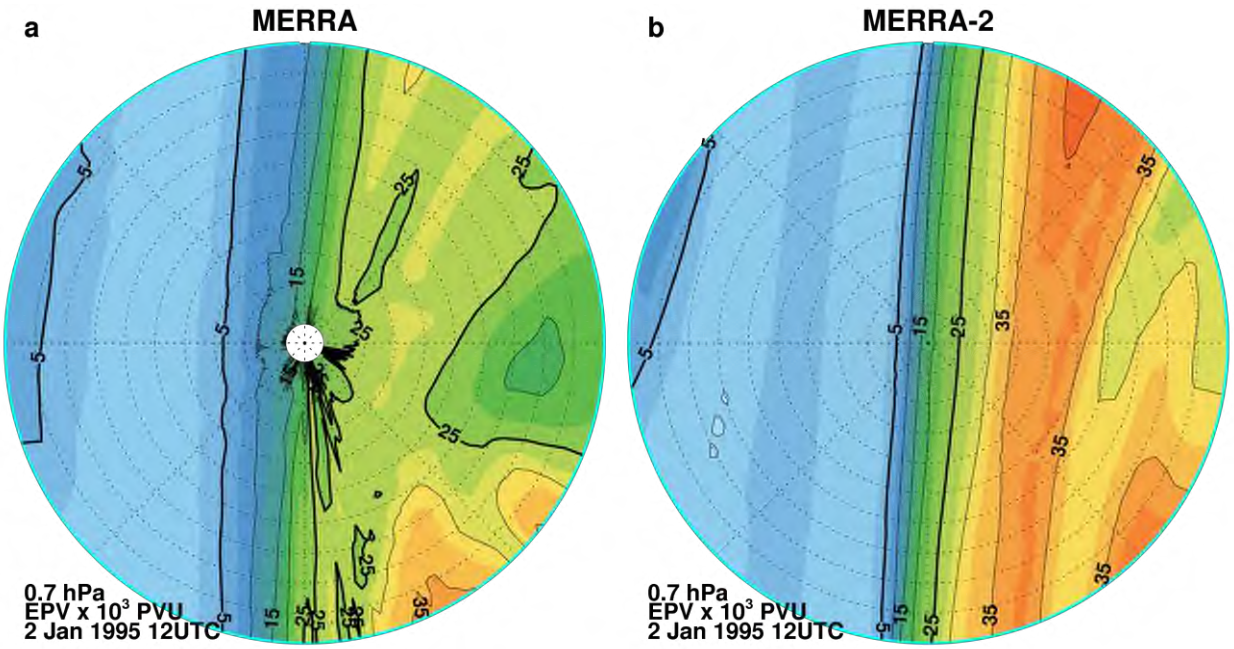

Figure 10-2 Ertel Potential Vorticity (x10^3 PVU) at 0.7 hPa on 2 January 1995, 12 UTC for (a) MERRA and (b) MERRA-2. The polar map projection covers from 80N to the North Pole.

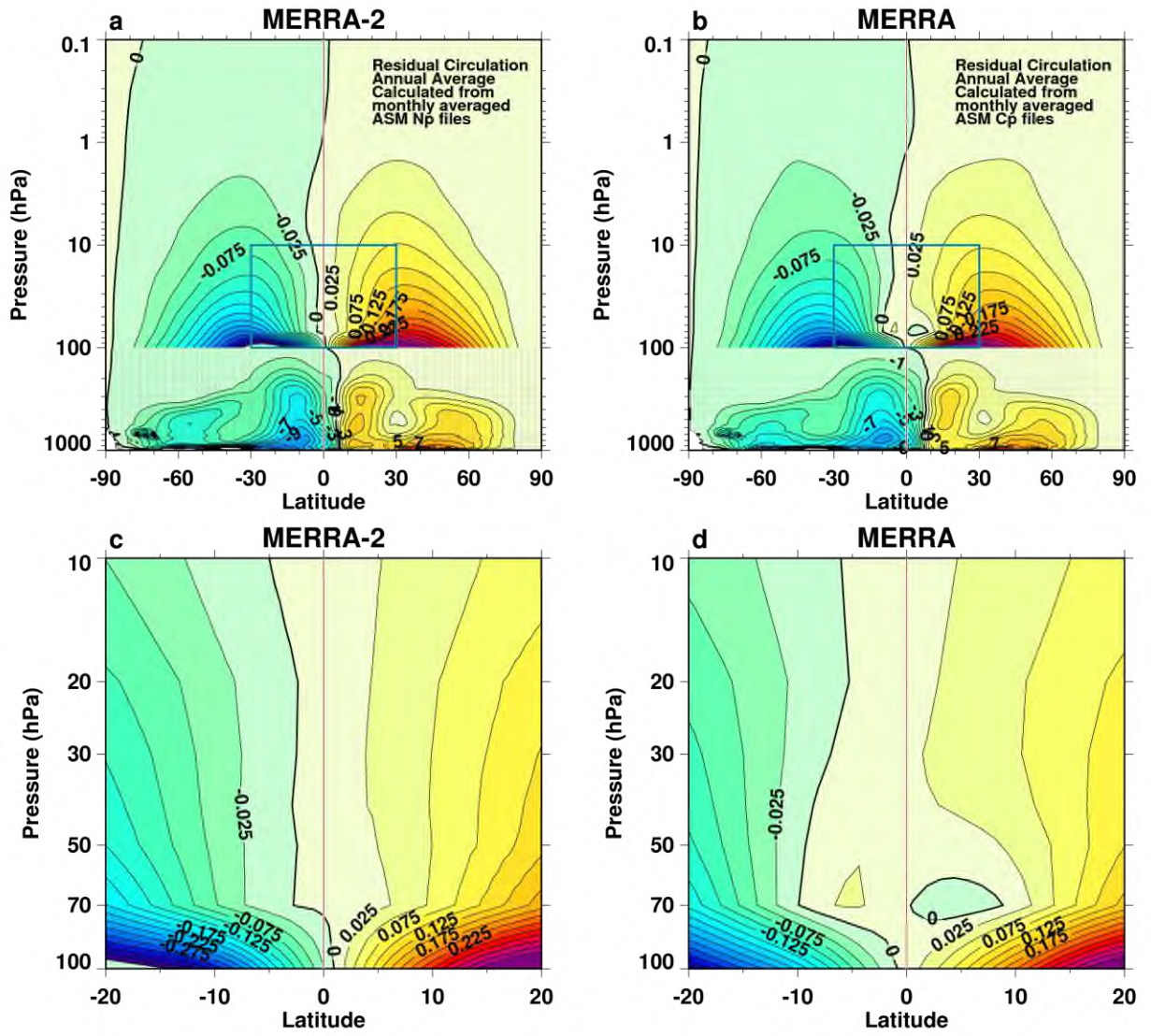

Figure 10-3 Residual mean meridional circulation for MERRA-2 (a and c) and MERRA (b and d) based on monthly averaged output files. Units are 10^{10} kg s^{-1}. The contour interval is 0.025 in the stratosphere and 1 in the troposphere. Panels b and d highlight the tropical lower stratosphere.

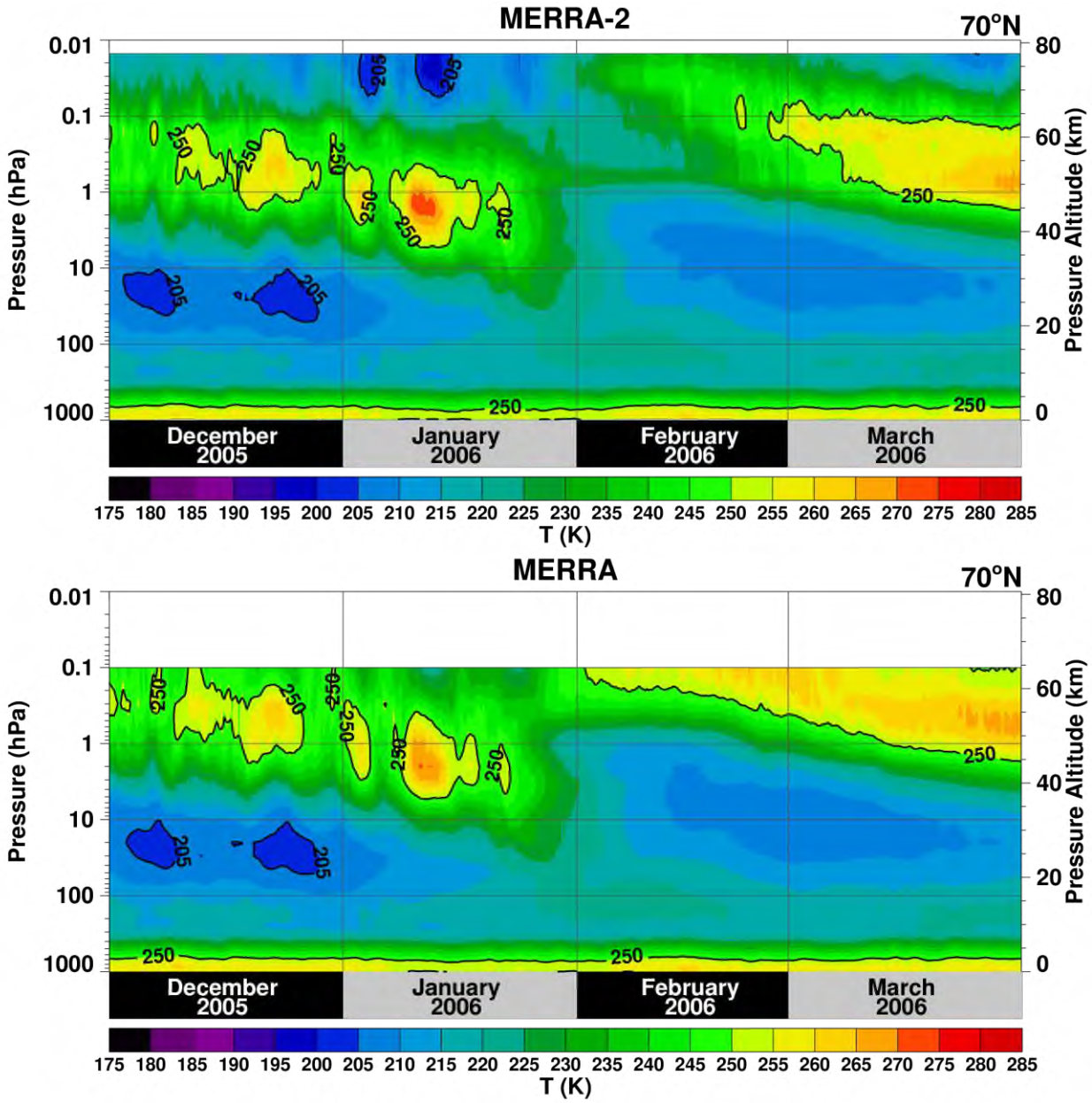

Figure 10-4 Time-Altitude section of zonally averaged temperature at 70N for (a) MERRA-2 and (b) MERRA. Time resolution is twice daily (00 and 12 UTC) for December 2005—March 2006. MERRA-2 is plotted using model levels and MERRA is plotted using constant pressure levels. The contour interval is 5 K.

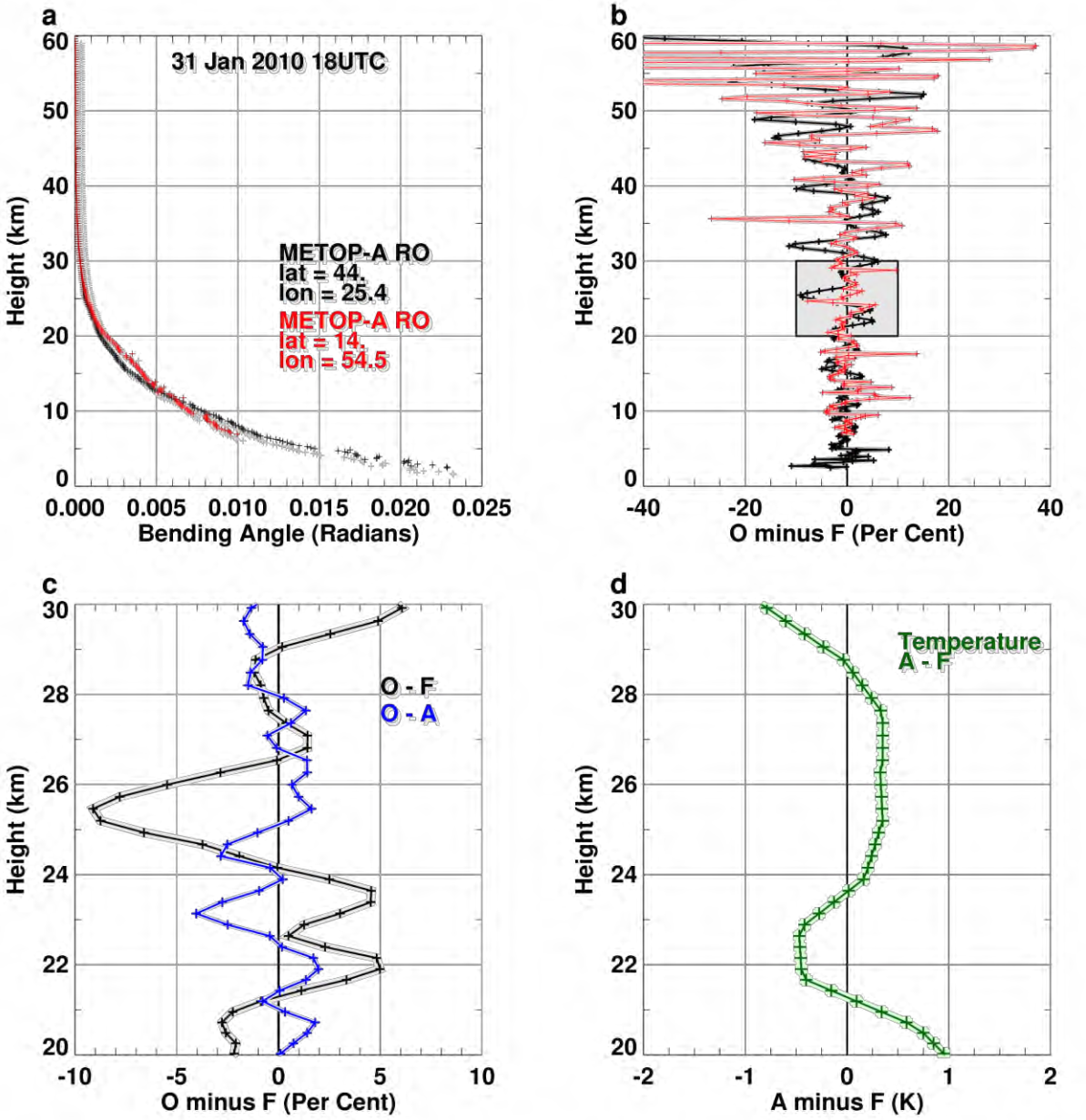

Figure 10-5 GPS assimilation example from 31 January 2010 at 18 UTC as a function of altitude: (a) Observations (bending angles) from two locations (red and black curves, locations as labeled); (b) GPS bending angle observation minus the background bending angle forecast (O-F) at the two locations expressed as a percent; (c) 25.4E, 44N location O-F close-up (black curve) and bending observation minus the analysis (blue curve), expressed as a percent; and (d) 25.4E, 44N location analysis minus background forecast temperature.

11. Ozone

Prior to October 2004, MERRA-2 assimilated ozone fields are based on measurements from the series of Solar Backscatter Ultraviolet (SBUV) radiometers flown on NASA and NOAA platforms beginning in 1970 (Frith et al., 2014; McPeters et al., 2013). SBUV ozone (Version 8.6) is retrieved in 21 partial columns, each approximately 3 km deep; partial and total column data, obtained by summing the partial columns, are assimilated. On 1 October 2004, the SBUV data are replaced by retrieved total ozone column from the Ozone Monitoring Instrument (OMI collection 3, version 8.5) and stratospheric profiles from the Microwave Limb Sounder (MLS version 2.2; version 4.2 starting June 2015) on NASA's EOS Aura satellite. Details of the ozone observing systems and the treatment of observation errors are given in McCarty et al. (2015). The background errors for ozone follow Wargan et al. (2015), except that they are inflated by a factor of 2. The scaling was applied in order to decrease the values of the analysis cost function. The model uses a simple month-dependent ozone chemistry parameterization derived from a 2-dimensional chemistry model (e.g. Stajner et al., 2008).

a. Total Column Ozone

Figure 11-1 shows the time series of 30N-60N total ozone column from MERRA-2, OMI, and the Merged Ozone Dataset (MOD, Frith et al., 2014). The MOD product uses SBUV version 8.6 data from a selection of SBUV instruments that is similar but not identical to that implemented in MERRA-2. Therefore this comparison represents a self-consistency check for the reanalysis. Overall, the agreement between the data sets is very close. MERRA-2 is biased low with respect to MOD by 1 - 6 Dobson units (DU; ~1 - 2 % of the average global ozone) and the bias does not exhibit any significant trends. Larger differences at the end of 1994 and in 2001 are due to limited coverage of the NOAA-11 and NOAA-14 SBUV instruments, respectively. The large number of assimilated OMI observations (~10 times that of SBUV) draws the analysis closer to the data, resulting in no bias between MERRA-2 and OMI. Overall, MERRA-2 faithfully reproduces the observed total ozone column except for a very small negative bias (less than 2 %) with respect to MOD.

Figure 11-2 shows the instantaneous longitudinal distribution of hourly total ozone from MERRA-2 at 40N on 25 October 1998. Also shown are the (assimilated) SBUV observations and data retrieved from the Total Ozone Mapping Spectrometer (TOMS, not assimilated) for the same day. Here the TOMS data serve as an independent validation of MERRA-2. Dynamically driven spatial variability with total ozone amplitudes up to 100 DU is seen in both MERRA-2 and TOMS. All synoptic and planetary-scale features are in a very good agreement between the two data sets. In particular, the maxima at 100E and 150E and the minimum between them seen in the TOMS data are very well captured by MERRA-2 despite the fact that no SBUV observations exist near those locations. This example is typical of comparisons made over a range of times and latitudes and points to the value of the MERRA-2 reanalysis as an efficient data interpolator.

We note that the quality of MERRA-2 total ozone is degraded in polar night, particularly during the SBUV era as no wintertime observations of the polar regions are available. However,

comparisons against the South Pole ozonesondes (not shown) indicate that representation of ozone depletion during Antarctic spring improves from 2004 onward when MLS data are used.

b. Ozone Profiles

Comparisons of the MERRA-2 ozone profiles against available ozonesondes between 30N and 90N in 2003 (SBUV period) and 2005 (OMI and MLS period) are shown in Figure 11-3. The comparisons are done as follows: for each sounding the MERRA-2 profile closest to the sonde time and location is interpolated to a set of constant pressure levels, the sonde data are integrated within the layers centered at the same pressure levels, and the statistics are calculated. Ozonesonde data are from the Network for the Detection for Atmospheric Composition Change (NDACC) (http://www.ndsc.ncep.noaa.gov/) and the Southern Hemisphere Additional Ozonesondes (SHADOZ) (Thompson et al., 2003). There is generally good agreement between MERRA-2 and the sondes in both years given the large variability of ozone in the extratropics, but the standard deviation of the differences is smaller in 2005, especially in the upper troposphere and lower stratosphere as expected given the high vertical resolution of MLS data. The MERRA-2 sonde correlations are also slightly improved in that layer. The upper-tropospheric portion of the mean ozone profile (pressures higher than ~200 hPa) is biased low by up to 0.5 mPa in 2005. This is likely a result of the lack of accurate ozone sources in the parameterized chemistry and limited sensitivity of OMI measurements to tropospheric ozone (note that neither MLS nor OMI provide ozone profile information in the troposphere). In the lowermost troposphere the correlations drop to ~0.4 in both years as a consequence of very limited information content provided by UV measurements and, again, simplified chemistry in that layer of the atmosphere. Overall, we expect the MERRA-2 ozone profile product to be useful for scientific studies that focus on the upper troposphere and the stratosphere given the high correlations with independent sonde data at these altitudes; however, the differences in quality between the SBUV and MLS periods require further evaluation.

c. Comparison to MERRA's Ozone

Figure 11-4 shows a comparison of the area-weighted global mean total ozone column from MERRA and MERRA-2 and the difference between the two. Both reanalyses display similar features: the seasonal cycle, a decline of the global ozone in the 1980s and 1990s, deep minima in years following the eruption of Mt. Pinatubo in 1991, and the solar cycle signal. The largest differences are seen in the early 1990s and after 2005. The latter is a result of the OMI and MLS assimilation in MERRA-2. A preliminary analysis reveals that the largest differences between the two reanalysis occur in the polar region. We note that the total ozone over the South Pole in MERRA-2 exhibits a much better agreement with that derived from ozonesondes during the OMI and MLS period than before 2005 (not shown).

Improvements in MERRA-2 ozone analysis relative to MERRA include:

- Improved representation of polar ozone loss in austral spring starting in October 2004 with the use of MLS.
- Expected improved representation of vertical structures in the upper tropospheric and lower stratospheric ozone with the use of MLS data and ozone-dependent background error correlations. Previous studies suggest this result but more detailed validation is required to

confirm this in MERRA-2.

- More realistic total ozone trends in the SBUV period with the use of version 8.6 retrievals. MERRA assimilated version 8 of SBUV data degraded from 21 to 12 layers.
- Diminished negative impacts of data gaps. Globally averaged total ozone in MERRA was unrealistically high in 1994 and 2012 due to reduced data coverage. The 1994 peak still exists in MERRA-2 but the bias is significantly reduced. In 2012 MERRA-2 is in excellent agreement with the assimilated OMI data.

A comprehensive evaluation of MERRA-2 ozone will be provided in a future publication. Preliminary results presented here show an overall good performance of the MERRA-2 ozone analysis in both the SBUV and Aura (OMI and MLS) periods. The total ozone columns are in very good agreement with the MOD product and independent TOMS data. A small negative bias of 1-6 DU exists throughout the reanalysis period. Comparisons with ozonesondes yield better agreement of upper-tropospheric and lower-stratospheric profiles when MLS is assimilated (from October 2004 onward). While more comprehensive validation continues, we expect MERRA-2 to provide a useful ozone data set for scientific research.

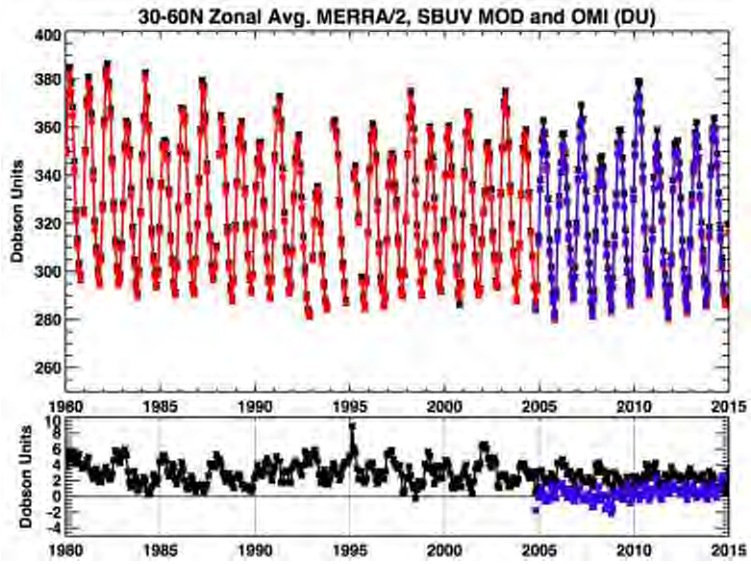

Figure 11-1 Top: time series of monthly total ozone column averaged between 30N and 60N from MERRA-2 (black), the SBUV MOD product (red) and OMI (blue). Bottom: the differences: MOD minus MERRA-2 (black) and OMI minus MERRA-2 (blue).

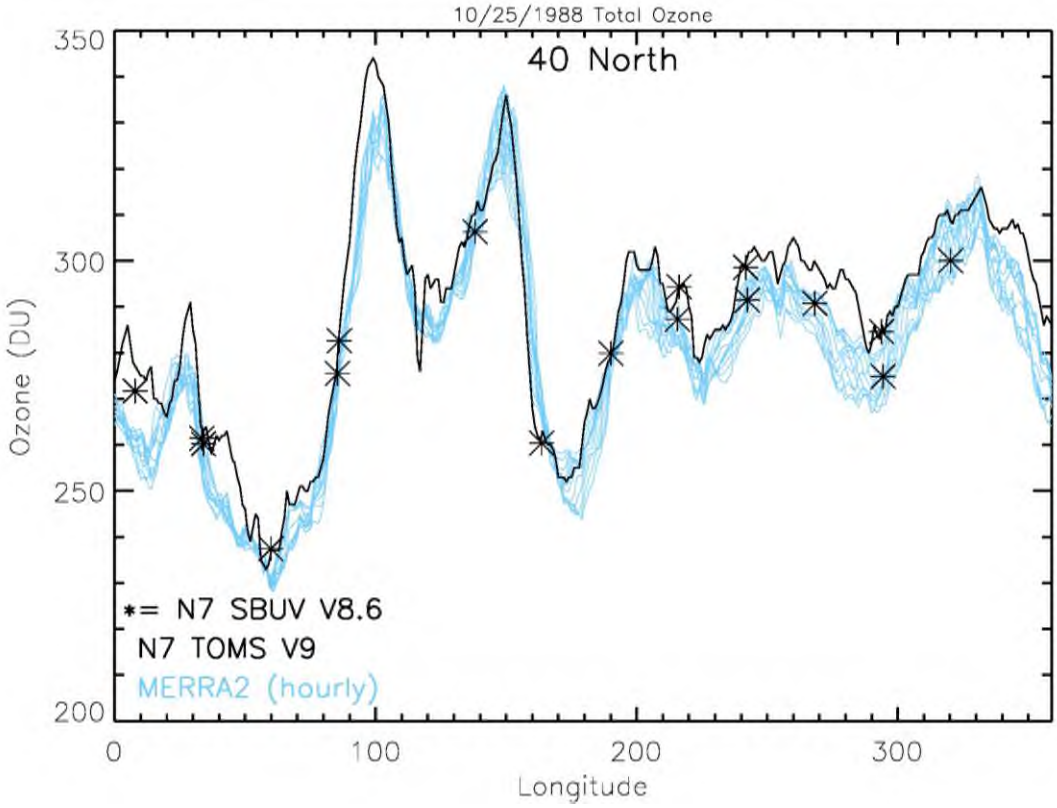

Figure 11-2 Total ozone column at 40N on 25 October 1998 from SBUV (asterisk), TOMS (black line), and MERRA-2 (cyan). Hourly data are shown for MERRA-2, one line for each of 24 hourly averages.

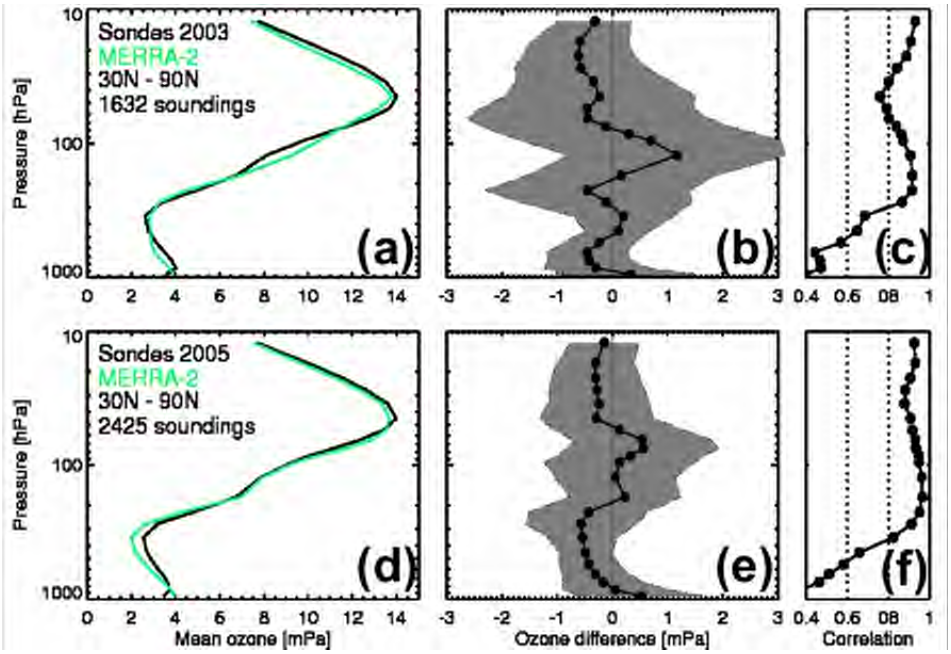

Figure 11-3 Comparisons of MERRA-2 ozone profiles with vertically-interpolated ozonesonde observations between 30N-90N in 2003 (a-c) and 2005 (d-f). Shown are the mean partial pressure profiles (a and d), the mean differences (b and e), and correlations (c and f). All data are interpolated to a set of constant pressure levels shown as black dots (b, c, e, and f). One standard deviation around the mean difference is shown in gray in (b) and (e).

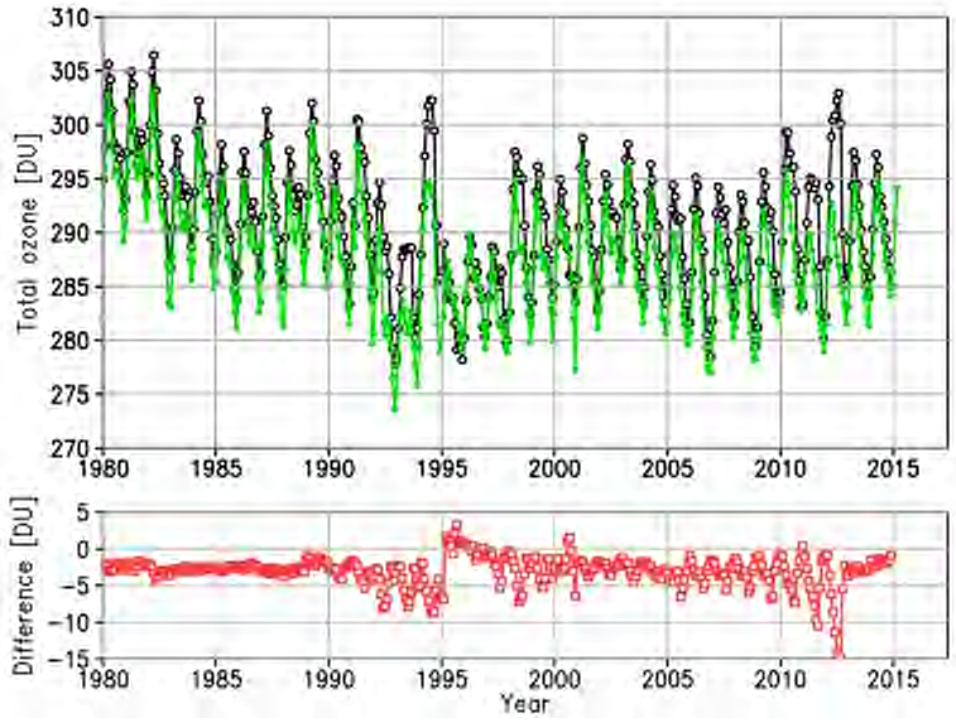

Figure 11-4 Top: time series of monthly total ozone column area-averaged over the entire globe from MERRA (black) and MERRA-2 (green). Bottom: MERRA-2 minus MERRA difference.

12. Summary

While MERRA-2 clearly provides a very good quality reanalysis data set with improvements over MERRA, there are also areas where challenges remain. Here, we summarize some of the strengths and weaknesses uncovered in MERRA-2's representation of climate. The noted sections should be consulted for further details.

- In the state fields, some systematic differences with previous reanalyses are present (e.g. an overly moist upper tropospheric bias, a stronger Hadley cell than MERRA), but there are also many similarities in the state fields owing to the observational analysis. (Section 3)
- Globally, reflected shortwave radiation at the TOA is too large while OLR matches observations, and this contributes to a net radiation imbalance at the top of the atmosphere. The surface downwelling longwave radiation is too large, while other terms are within the range of observational estimates. Some of the radiation components show trends that do not match observations (Section 4).
- While some regions in MERRA-2 exhibit improved shortwave cloud radiative forcing compared to MERRA, MERRA-2's excessive shortwave cloud forcing in the southern oceans and in the tropical oceans contributes to the global energy imbalance at the TOA. (Section 5)
- In the global sense, the MERRA-2 water cycle is stronger than that in MERRA and in the NEWS merged observation data; ocean evaporation is overestimated in MERRA-2, leading to high moisture transport and eventually high model-generated precipitation over land (though there are some regional variations). (Section 6e)
- When using MERRA-2 precipitation, it is important to differentiate between the observation-corrected precipitation (which is used to force the land and to determine aerosol wet deposition) and the model-generated precipitation (which relates to the simulated atmospheric latent heating and the net condensation of water from the atmosphere). (Section 7a)
- MERRA-2 model-generated precipitation in the tropical warm pool remains biased high against GPCP and only slightly improved from MERRA. However, precipitation in the tropical land regions, especially near topography, is biased high and is worse than in MERRA. The diurnal cycle of precipitation has not improved from MERRA. The interannual variability and extreme precipitation over the US is improved in MERRA-2. (Section 6a-c,f)
- MERRA-2 soil moisture is consistently improved over that in MERRA when evaluated against independent observational data. However, the somewhat limited sensible and latent heat flux observations indicate mixed results for MERRA-2. 2m air temperature biases in certain regions have been improved in MERRA-2. (Section 7c)
- The SST boundary conditions used in MERRA-2 were derived from more recent observational datasets, compared to MERRA. Some issues have been identified with the

merging of the different data sources, which should be considered when evaluating the SSTs used and comparing them with those used in other reanalyses. (Section 8a)

- MERRA-2 ocean surface winds are, in general, weaker than observations but are an improvement over MERRA winds. MERRA-2 does not capture the intensity of strong ocean surface wind events. (Section 8b)
- Enhancements to the model parameterizations of glaciated land and sea ice have led to improvements in MERRA-2 near surface temperature at high latitudes (related to surface albedo). However, MERRA-2 precipitation is biased high at high latitudes. (Section 9 and 6a)
- Aspects of the new system underlying MERRA-2, specifically the cube-sphere grid, updates to CRTM, and the assimilation of new data, have led to a substantial improvement in the representation of the stratosphere. (Section 10)
- Evaluation with available independent measurements shows that MERRA-2 ozone is improved over that in MERRA. The MERRA-2 ozone profile product will be useful for scientific studies that focus on the upper troposphere and the stratosphere. (Section 11)

These brief points only summarize the more detailed results presented in this report. In time, further analysis and evaluation will sharpen the picture of the strengths and weaknesses of MERRA-2's representation of the Earth's climate. Note that the assimilation of aerosols is a major new feature in the MERRA-2 representation of the Earth system, and is discussed in a separate technical memorandum (Randles et al. 2015). While much of this work continues within the GMAO, the scientific community will undoubtedly have to perform their own evaluations to demonstrate MERRA-2's fit to their specific needs. We invite the community of users to forward their results and experiences with MERRA-2 to the GMAO (via merra-questions@lists.nasa.gov) to promote communication and feedback into the development of the next reanalysis.

13. References

Adler, R., and Coauthors, 2003: The Version 2 Global Precipitation Climatology Project (GPCP) Monthly Precipitation Analysis (1979-Present), *J. Hydrometeor*., 4, 1147-1167.

Allan, R.P., C.Liu, N.G.Loeb, M. D. Palmer, M. Roberts, D. Smith, and P.-L. Vidale, 2014: Changes in global net radiative imbalance 1985–2012, Geophys. Res. Lett., 41, 5588–5597, doi:10.1002/2014GL060962.

Andrews, D. G. , J. R. Holton, and C. B. Leovy, Middle Atmosphere Dynamics, Academic Press, 1987.

Atlas, R., R. N. Hoffman, J. Ardizzone, S. M. Leidner, J. C. Jusem, D. K. Smith, D. Gombos, 2011: A cross-calibrated, multiplatform ocean surface wind velocity product for meteorological and oceanographic applications. Bull. Amer. Meteor. Soc., 92, 157-174. doi: 10.1175/2010BAMS2946.1

Bacmeister, J. T. and Stephens, G., 2011: Spatial statistics of likely convective clouds in CloudSat data, *J. Geophys. Res*., 116, D04104, doi:10.1029/2010JD014444.

Berg, W., and R. Chase, 1992: Determination of mean rainfall from the Special Sensor Microwave/Imager (SSM/I) using mixed lognormal distribution. J. Atmos. Ocean. Tech., 9, 129– 141.

Berrisford, P., P. Kallberg, S. Kobayashi, D. Dee, S. Uppala, A. J. Simmons, P. Poli, and H. Sato, 2011: Atmospheric conservation properties in ERA-Interim. *Quart. J. Roy. Meteor. Soc*., **137**, 1381–1399.

Bloom, S., L. Takacs, A. DaSilva, and D. Ledvina, 1996: Data assimilation using incremental analysis updates. *Mon. Wea. Rev.*, **124**, 1256-1271.

Boer, G.J., S. Fourest, and B. Yu, 2001. The signature of the annular modes in the moisture budget. *J. Climate*, **14**(17), 3655-3665,

doi:10.1175/1520-0442(2001)014<3655:TSOTAM>2.0.CO;2

Boisvert, L. N., T. Markus, and T. Vihma, 2013. Moisture flux changes and trends for the entire Arctic in 2003–2011 derived from EOS Aqua data, *J. Geophys. Res.*, **118**(C10), 5829-5843, doi:10.1002/jgrc.20414.

Bosilovich, M. G., 2013: Regional Climate and Variability In NASA MERRA and Recent Reanalyses: US Summertime Precipitation and Temperature, J. Appl. Meteor. Climatol., 52, 1939–1951. doi: http://dx.doi.org/10.1175/JAMC-D-12-0291.1

Bosilovich, M. G., J-D. Chern, D. Mocko, F. R. Robertson and A. M. da Silva, 2015a: Evaluating observation influence on regional water budgets in reanalyses. *Journal of Climate*, 28, 3631-3649. doi: http://dx.doi.org/10.1175/JCLI-D-14-00623.1

Bosilovich, M. G., R. Lucchesi, and M. Suarez, 2015b: *MERRA-2: File Specification*, GMAO Office Note No. 8 (Version 1.3), PP 73, available from

http://gmao.gsfc.nasa.gov/pubs/office_notes.

Bosilovich, M.G., F.R. Robertson, and J Chen, 2011: Global energy and water budgets in MERRA.

J. Climate, **24**, 282–300.

Bosilovich, M.G., J. Chen, S. D. Schubert, F. R. Robsertson, P. Pegion and H. C. Liu, 2008: Evaluation of the late 80s observing system and the impacts on the GEOS-5 data assimilation system. 3rd WCRP International Conference on Reanalysis, Tokyo Japan, Jan. 28-Feb 1, 2008. http://gmao.gsfc.nasa.gov/pubs/docs/Bosilovich353.pdf

Box, J.E. and A. Rinke, 2003: Evaluation of Greenland Ice Sheet surface climate in the HIRHAM Regional Climate Model using automatic weather station data. *J. Climate*, **16**, 1302-1319, doi: http://dx.doi.org/10.1175/1520-0442-16.9.1302

Bromwich, D.H., J.P. Nicolas, and A.J. Monaghan, 2011: An assessment of precipitation changes over Antarctica and the Southern Ocean since 1989 in contemporary global reanalyses. *J. Climate*, **24**(16), 4189-4209, doi:10.1175/2011JCLI4074.1.

Buchard, V., A. M. da Silva, P. R. Colarco, A. Darmenov, C. A. Randles, R. Govindaraju, O. Torres, J. Campbell, and R. Spurr, 2015: Using the OMI aerosol index and absorption aerosol optical depth to evaluate the NASA MERRA Aerosol Reanalysis. *Atmos. Chem. Phys*., **15**, 5743–5760, doi:10.5194/acp-15-5743–2015.

Cardinali, C., L. Isaksen, and E. Anderson, 2003: Use and impact of automated aircraft data in a global 4DVAR data assimilation system. *Mon. Wea. Rev.*, **131**, 1865–1877.

Chao, W. C. 2012: Correction of Excessive Precipitation over Steep and High Mountains in a GCM. J Atmos Sci, 69 (5): 1547-1561 [10.1175/JAS-D-11-0216.1]

Chao, W. C., 2013: Catastrophe concept-based cumulus parameterization: Correction of systematic errors in the precipitation diurnal cycle over land in a GCM. J. Atmos. Sci.. 70, 3599-3614. doi: 10.1175/JAS-D-13-022.1

Chen, M., and P. Xie, 2008: CPC Unified Gauge-based Analysis of Global Daily Precipitation, Western Pacific Geophysics Meeting, 29 July – 1 August 2008, Cairns, Australia.

Chen Y, F. Weng, Y. Han, and Q. Liu, 2008: Validation of the community radiative transfer model (CRTM) by using CloudSat Data. *J. Geophys.Res*., **113(D8)**, 2156–2202.

Chin, M., P. Ginoux, S. Kinne, B. N. Holben, B. N. Duncan, R. V. Martin, J. A. Logan, A. Higurashi, and T. Nakajima, 2002: Tropospheric aerosol optical thickness from the GOCART model and comparisons with satellite and sunphotometer measurements, *J. Atmos. Sci.* **59**, 461–483.

Collins, N., G. Theurich, C. DeLuca, M. Suarez, A. Trayanov, V. Balaji, P. Li, W. Yang, C. Hill, and A. da Silva, 2005: Design and implementation of components in the Earth System Modeling Framework. *Int. J. High Perf. Comput. Appl*., **19**, 341-350, DOI: 10.1177/1094342005056120.

Compo, G. P., and Coauthors, 2011: The Twentieth Century Reanalysis Project. Q. J. R. Meteorol. Soc., 137, 1– 28, doi:10.1002/qj.776.

Cullather, R.I., and M.G. Bosilovich, 2011. The moisture budget of the polar atmosphere in MERRA. *J. Climate*, **24**(11), 2861-2879, doi:10.1175/2010JCLI4090.1.

Cullather, R.I., S.M.J. Nowicki, B. Zhao, and M.J. Suarez, 2014: Evaluation of the surface representation of the Greenland Ice Sheet in a general circulation model. *J. Climate*, **27**,

4835-4856. doi: 10.1175/JCLI-D-13-00635.1

Dee, D. P., and Coauthors, 2011: The ERA-Interim reanalysis: configuration and performance of the data assimilation system. Q. J. R. Meteorol. Soc., 137, 553– 597, doi:10.1002/qj.828.

Dee, D. P., and S. Uppala, 2009: Variational bias correction of satellite radiance data in the ERA-Interim reanalysis. *Quart. J. Roy. Meteor. Soc*., **135**, 1830–1841.

Derber, J. C., R. J. Purser, W.-S. Wu, R. Treadon, M. Pondeca, D. Parrish, and D. Kleist, 2003: Flow-dependent Jb in a global grid-point 3D-Var. *Proc. ECMWF annual seminar on recent developments in data assimilation for atmosphere and ocean.* Reading, UK, $8^{-1}2$ Sept. 2003.

Donlon, C., and coauthors, 2007: The global ocean data assimilation experiment high- resolution sea surface temperature pilot project. Bull. Amer. Meteor. Soc, 88, 1197– 1213, doi:http://dx.doi.org/10.1175/BAMS-88-8-1197.

Donlon, C. J., M. Martin, J. Stark, J. Roberts-Jones, E. Fiedler, and W. Wimmer, 2012: The Operational Sea Surface Temperature and Sea Ice Analysis (OSTIA) system. Remote Sens. Environ., 116, 140–158, doi:10.1016/j.rse.2010.10.017.

Ducharne, A., R. D. Koster, M. J. Suarez, M. Stieglitz, and P. Kumar, 2000: A catchment-based approach to modeling land surface processes in a general circulation model 2. Parameter estimation and model demonstration. *J. Geophys. Res.*, **105**, 24823–24838, doi:10.1029/2000JD900328.

Duynkerke, P., and S. de Roode, 2001. Surface energy balance and turbulence characteristics observed at the SHEBA Ice Camp during FIRE III. *J. Geophys. Res.*, **106**(D14), 15313-15322, doi:10.1029/2000JD900537.

Ebita, A., and Coauthors, 2011: The Japanese 55-year reanalysis JRA-55: An interim report. SOLA Scientific Online Letters on the Atmosphere, 7, 149– 152, doi:http://doi. org/10.2151/sola.2011-038.

Ettema, J., M.R. van den Broeke, E. van Meijgaard, W.J. van de Berg, J.L. Bamber, J.E. Box, and R.C. Bales, 2009. Higher surface mass balance of the Greenland ice sheet revealed by high-resolution climate modeling. *Geophys. Res. Lett.*, **36**, L12501, doi:10.1029/2009GL038110.

Fettweis, X., M. Tedesco, M. van den Broeke, and J. Ettema, 2011. Melting trends over the Greenland ice sheet (1958–2009) from spaceborne microwave data and regional climate models. *The Cryosphere*, **5**, 359-375, doi:10.5194/tc-5-359-2011.

Fettweis, X., 2007. Reconstruction of the 1979-2006 Greenland ice sheet surface mass balance using the regional climate model MAR. *The Cryosphere*, **1**, 21-40, doi:10.5194/tc-1-21-2007.

Frith, S. M., N. A. Kramarova, R. S. Stolarski, R. D. McPeters, P. K. Bhartia, and G. J. Labow, 2014: Recent changes in total column ozone based on the SBUV Version 8.6 Merged Ozone Data Set, *J. Geophys. Res. Atmos*., **119**, 9735-9751, doi:10.1002/2014JD021889.

Ganachaud, A., and C. Wunsch, 2000: Improved estimates of global ocean circulation, heat transport and mixing from hydrological data. Nature 408 453457.

Gesch, D.B., 1994. *Topographic data requirements for EOS global change research.* Open-File Report No. 94-626, U.S. Geological Survey, 60 pp.

Ham, Y.-G., S. Schubert, Y. Vikhliaev, and M. J. Suarez, 2014: An assessment of the ENSO forecast skill of GEOS-5 system, *Climate Dynamics*, doi:10.1007/s00382-014-2063-2.

Harris, I., Jones, P., Osborn, T and Lister, D. (2014), Updated high-resolution grids of monthly climatic observations – the CRU TS3.10 Dataset. *Int. J. Climatol*., 34, 623–642.

Hoch, S.W., 2005. *Radiative flux divergence in the surface boundary layer. A study based on observations at Summit, Greenland.* Ph.D. dissertation, Swiss Federal Institute of Technology (ETH), Zurich, 164 pp.

Hurrell, J. W., J. J. Hack, D. Shea, J. M. Caron, and J. Rosinski, 2008: A new sea surface temperature and sea ice boundary dataset for the community atmosphere model. *J. Climate*, **21**, 5145?5153, doi:http://dx.doi.org/10.1175/2008JCLI2292.1.

Ishii, M., A. Shouji, S. Sugimoto, and T. Matsumoto, 2005: Objective analyses of sea- surface temperature and marine meteorological variables for the 20th century using ICOADS and the KOBE collection. *Int. J. Climatol.*, **25**, 865– 879, doi:10.1002/joc. 1169.

Kanamitsu, M., W. Ebisuzaki, J Woollen, S.-K. Yang, J. J. Hnilo, M. Fiorino, and G. L. Potter, 2002: NCEP-DOE AMIP-II Reanalysis (R-2), Bull. Amer. Meteor. Soc., 83, 1631-1643.

Kleist, D. T., D. F. Parrish, J. C. Derber, R. Treadon, R. M. Errico, and R. Yang, 2009: Improving incremental balance in the GSI 3DVAR analysis system. *Mon. Wea. Rev.*, **137**, 1046–1060.

Kleist D. T., D. F. Parrish, J. C. Derber, R. Treadon, W.-S. Wu, and S. Lord, 2009: Introduction of the GSI into the NCEPs Global Data Assimilation System. *Wea. Forecasting*, **24**, 1691-1705.

Koster, R. D., M. J. Suárez, A. Ducharne, M. Stieglitz, and P. Kumar, 2000: A catchment-based approach to modeling land surface processes in a GCM, Part 1, Model Structure. *J. Geophys. Res.*, **105**, 24809-24822.

L'Ecuyer, T., H. Beaudoing, M. Rodell, W. Olson, B. Lin, S. Kato, C. Clayson, E. Wood, J. Sheffield, R. Adler, G. Huffman, M. Bosilovich, G. Gu, F. Roberston, P. Houser, D. Chambers, J. Famiglietti, E. Fetzer, W. Liu, X. Gao, C. Schlosser, E. Clark, D. Lettenmaier, and K. Hilburn, 2015: The Observed State of the Energy Budget in the Early 21st Century. J. Climate, doi:10.1175/JCLI-D-14-00556.1

Lee, M.-I., and Coauthors, 2007: Sensitivity to horizontal resolution in the AGCM simulations of warm season diurnal cycle of precipitation over the United States and northern Mexico. J. Climate, 20, 1862–1881.

Lin J.-L.. and coauthors, 2006: Tropical Intraseasonal Variability in 14 IPCC AR4 Climate Models. Part I: Convective Signals. *J Clim*, *19*, 2665-2690.

Lin, S. J., 2004: A vertically Lagrangian finite-volume dynamical core for global models. *Mon. Wea. Rev*., **132**, 2293–2307.

Liu, J., and J.A. Curry, 2010. Accelerated warming of the Southern ocean and its impacts on the hydrological cycle and sea ice. *Proc. Natl. Acad. Sci.*, **107**(34), 14987-14992, doi:10.1073/pnas.1003336107.

Liu, Q. and S. Boukabara, 2014: Community Radiative Transfer Model (CRTM) applications in supporting the Suomi National Polar-orbiting Partnership (SNPP) mission validation and verification. *Remote Sens. Environ.*, **140**, 744–754.

Loeb, N. G., B. A. Wielicki, D. R. Doelling, G. L. Smith, D. F. Keyes, S. Kato, N. Manalo-Smith, and T. Wong, 2009: Toward Optimal Closure of the Earth's Top-of-Atmosphere Radiation Budget. *J. Climate*, **22**, 748–766.

doi: http://dx.doi.org/10.1175/2008JCLI2637.1

Manney, G.L., K. Kruger, S. Pawson, K. Minschwaner, M.J. Schwartz, W.H. Daffer, N.J. Livesey, M.G. Mlynczak, E.E. Remsberg, J.M. Russell, J.W. Waters, 2008: The evolution of the stratopause during the 2006 major warming: Satellite Data and Assimilated Meteorological Analyses, Journal of Geophysical Research 113, D11115, doi:10.1029/2007JD00909.

Matsuura, K., and C.J. Willmott, 2005. Arctic land-surface precipitation. 1930-2004 gridded monthly time series (V. 1.03).

McCarty, W., L. Coy, R. Gelaro, D. Merkova, E. B. Smith, M. Sienkiewicz, and K. Wargan, 2015: MERRA-2 Input Observations: Summary and Initial Assessment. *NASA/TM*, in preparation.

McPeters, R. D., P. K. Bhartia, D. Haffner, G. J. Labow, and L. Flynn, 2013: The version 8.6 SBUV ozone data record: An overview, *J. Geophys. Res. Atmos*., **118**, 8032-8039, doi:10.1002/jgrd.50597

Mefford, T.K., M. Bieniulis, B. Halter, and J. Peterson, Meteorological Measurements, in CMDL Summary Report 1994 - 1995, No. 23, 1996, pg. 17

Molod, A., Takacs, L., Suarez, M., and Bacmeister, J., 2015: Development of the GEOS-5 atmospheric general circulation model: evolution from MERRA to MERRA2, *Geosci. Model Dev*., **8**, 1339-1356, doi:10.5194/gmd-8-1339-2015.

Molod, A., L. Takacs, M. Suarez, J. Bacmeister, I.-S. Song, and A. Eichmann, 2012. The GEOS-5 Atmospheric General Circulation Model: Mean Climate and Development from MERRA to Fortuna. *NASA Technical Report Series on Global Modeling and Data Assimilation, NASA TM—2012-104606*, Vol. **28**, 117 pp

Monaghan, A.J., D.H. Bromwich, and S.-H. Wang, 2006. Recent trends in Antarctic snow accumulation from Polar MM5 simulations. *Phil. Trans. Roy. Soc. A*, **364**(1844), 1683-1708, doi:10.1098/rsta.2006.1795.

Moorthi, S. and M. J. Suarez, 1992: Relaxed Arakawa Schubert: A parameterization of moist convection for general circulation models, *Mon. Weather Rev*., **120**, 978–1002.

Palerme, C., J.E. Kay, C. Genthon, R. L'Ecuyer, N.B. Wood, and C. Claud, 2014. How much snow falls on the Antarctic ice sheet? *The Cryosphere*, **8**, 1577-1587, doi:10.5194/tc-8-1577-2014.

Pfaendtner, J., S. Bloom, D. Lamich, M. Seablom, M. Sienkiewicz, J. Stobie, A. da Silva, 1995. Documentation of the Goddard Earth Observing System (GEOS) Data Assimilation System: Version 1. *NASA Technical Memorandum 104606*, Vol. 4.

Putman, W. and S.-J. Lin, 2007: Finite Volume Transport on Various Cubed Sphere Grids. *J.*

Comput. Phys., **227**, 55–78. doi:10.1016/j.jcp.2007.07.022.

Randles, C. A., A. da Silva, V. Buchard, A. Darmenov, P. R. Colarco, V. Aquila, H. Bian, E. P. Nowottnick, X. Pan, S. Smirnov, H. Yu, and R. Govindaraju, 2015: Evaluation of the MERRA-2 Aerosol Assimilation. *NASA/TM,* in preparation.

Rayner, N. A., D. E. Parker, E. B. Horton, C. K. Folland, L. V. Alexander, and D. P. Rowell, 2003: Global analyses of sea surface temperature, sea ice, and night marine air temperature since the late nineteenth century. *J. Geophys. Res.*, **108 (4407)**, doi: 10.1029/2002JD002670.

Reichle, R. H., and Q. Liu, 2014. Observation-Corrected Precipitation Estimates in GEOS-5. *NASA/TM–2014-104606*, Vol. **35**.

http://gmao.gsfc.nasa.gov/pubs/tm/docs/Reichle734.pdf

Reichle, R. H., 2012: The MERRA-Land Data Product, version 1.1. GMAO Technical Report, NASA Global Modeling and Assimilation Office, Goddard Space Flight Center, Greenbelt, MD, USA. Available at:

http://gmao.gsfc.nasa.gov/research/merra/file_specifications.php

Reichle, R. H., R. D. Koster, G. J. M. De Lannoy, B. A. Forman, Q. Liu, S. P. P. Mahanama, and A. Toure, 2011: Assessment and enhancement of MERRA land surface hydrology estimates. *J. Climate,* **24**, 6322-6338, doi:10.1175/JCLI-D^{-1}0-05033.1.

Reynolds, R. W., and T. M. Smith, 1994: Improved global sea surface temperature analysis using optimal interpolation. *J. Climate,* **7,** 929–948.

Reynolds, R. W., N. A. Rayner, T. M. Smith, D. C. Stokes, and Q. Wang, 2002: An improved in situ and satellite SST analysis for climate. *J. Climate,* **15**, 1609–1625.

Reynolds, R. W., T. M. Smith, C. Liu, D. B. Chelton, K. S. Casey, and M. G. Schlax, 2007: Daily high-resolution-blended analyses for Sea Surface Temperature. *J. Climate,* **20**, 5473–5496, doi:10.1175/2007JCLI1824.1.

Rienecker and Coauthors, 2011: MERRA - NASA's Modern-Era Retrospective Analysis for Research and Applications. *J. Climate,* **24**, 3624-3648, doi:10.1175/JCLI-D^{-1}1-00015.1.

Rienecker, M.M., M.J. Suarez, R. Todling, J. Bacmeister, L. Takacs, H.-C. Liu, W. Gu, M. Sienkiewicz, R.D. Koster, R. Gelaro, I. Stajner, and E. Nielsen, 2008: The GEOS-5 Data Assimilation System - Documentation of Versions 5.0.1, 5.1.0, and 5.2.0. *Technical Report Series on Global Modeling and Data Assimilation 104606*, **Vol. 27**.

Risien, C.M., and D.B. Chelton, 2008: A Global Climatology of Surface Wind and Wind Stress Fields from Eight Years of QuikSCAT Scatterometer Data. J. Phys. Oceanogr., 38, 2379-2413.

Robertson, F. R., M. G. Bosilovich, J. Chen, and T. L. Miller, 2011: The Effect of Satellite Observing System Changes on MERRA Water and Energy Fluxes. *J. Climate*, **24**, 5197–5217. doi: http://dx.doi.org/10.1175/2011JCLI4227.1

Robertson, F. R., M. G. Bosilovich, J. B. Roberts, R. H. Reichle, R. Adler, L. Ricciardulli, W. Berg, and G. J. Huffman, 2014: Consistency of Estimated Global Water Cycle Variations over the Satellite Era. J. Climate, 27, 6135–6154.

Rodell, M., H. Beaudoing, T. L'Ecuyer, W. Olson, J. Famiglietti, P. Houser, R. Adler, M.

Bosilovich, C. Clayson, D. Chambers, E. Clark, E. Fetzer, X. Gao, G. Gu, K. Hilburn, G. Huffman, D. Lettenmaier, W. Liu, F. Robertson, C. Schlosser, J. Sheffield, and E. Wood, 2015: The Observed State of the Water Cycle in the Early 21st Century. *J. Climate*, **28**, 8289–8318. doi:10.1175/JCLI-D-14-00555.1.

Saha, S., and Coauthors, 2010: The NCEP climate forecast system reanalysis. Bull. Amer. Meteor. Soc., 91, 1015– 1057, doi:http://dx.doi.org/10.1175/2010BAMS3001.1.

Schubert, S. D., R. B. Rood, and J. Pfaendtner, 1993: An Assimilated Dataset for Earth Science Applications. *Bull. Amer. Meteor. Soc.*, **74**, 2331–2342. doi: http://dx.doi.org/10.1175/1520-0477(1993)074<2331:AADFES>2.0.CO;2

Schaefer, G.., M. Cosh, and T. Jackson, 2007: The USDA Natural Resources Conservation Service Soil Climate Analysis Network (SCAN), *J. Atmos. Oceanic Technol.*, 24, 2073–2077.

Schneider, U., A. Becker, P. Finger, A. Meyer-Christoffer, B. Rudolf, and M. Ziese (2011): GPCC Full Data Reanalysis Version 6.0 at 0.5°: Monthly Land-Surface Precipitation from Rain-Gauges built on GTS-based and Historic Data. DOI: 10.5676/DWD_GPCC/FD_M_V6_050

Schwartz, M.J., A. Lambert, G.L. Manney, W.G. Read, N.J. Livesey, L. Froidevaux, C.O. Ao, P.F. Bernath, C.D. Boone, R.E. Cofield, W.H. Daffer, B.J. Drouin, E.J. Fetzer, R.A. Fuller, R.F. Jarnot, J.H. Jiang, Y.B. Jiang, B.W. Knosp, K. Kruger, J.L.F. Li, M.G. Mlynczak, S. Pawson, J.M. Russell, M.L. Santee, W.V. Snyder, P.C. Stek, R.P. Thurstans, A.M. Tompkins, P.A. Wagner, K.A. Walker, J.W. Waters, D.L. Wu, 2008: Validation of the Aura Microwave Limb Sounder Temperature and Geopotential Height Measurements. Journal of Geophysical Research 113, D15S11 doi:10.1029/2007JD008783.

Serreze, M.C., A.P. Barrett, A.G. Slater, R.A. Woodgate, K. Aagaard, R.B. Lammers, M. Steele, R. Moritz, M. Meredith, and C.M. Lee, 2006. The large-scale freshwater cycle of the Arctic. *J. Geophys. Res.*, **111**, C11010, doi:10.1029/2005JC003424.

Stajner, I., et al. (2008), Assimilated ozone from EOS-Aura: Evaluation of the tropopause region and tropospheric columns, *J. Geophys. Res*., **113**, D16S32, doi:10.1029/2007JD008863.

Sturm, M., J. Holmgren, and D.K. Perovich, 2002. Winter snow cover on the sea ice of the Arctic Ocean. Winter snow cover on the sea ice of the Arctic Ocean at the Surface Heat Budget of the Arctic Ocean (SHEBA). Temporal evolution and spatial variability. *J. Geophys. Res.*, **107**(C10), 8047, doi:10.1029/2000JC000400.

Susskind, J., J. Rosenfield, and D. Reuter, 1983: An accurate radiative transfer model for use in the direct physical inversion of HIRS and MSU temperature sounding data. *J. Geophys. Res*., **88**, 8550–8568.

Takacs, L. L., M. Suarez, and R. Todling, 2015. Maintaining Atmospheric Mass and Water Balance Within Reanalysis. *NASA/TM–2014-104606*, Vol. **37.**

http://gmao.gsfc.nasa.gov/pubs/docs/Takacs737.pdf

Taylor, K. E., D. Williamson, and F. Zwiers, 2000: The sea surface temperature and sea ice concentration boundary conditions for AMIP II simulations. Program for Climate Model Diagnosis and Intercomparison (PCMDI). Report 60, Lawrence Livermore National Laboratory.

Thompson, A. M., and co-authors, 2003: Southern Hemisphere Additional Ozonesondes (SHADOZ) 1998–2000 tropical ozone climatology 1. Comparison with Total Ozone Mapping Spectrometer (TOMS) and ground-based measurements, *J. Geophys. Res*., **108**, 8238, doi:10.1029/2001JD000967, D2.

Trenberth, K.E. and J. Caron, 2001: Estimates of Meridional Atmosphere and Ocean Heat Transports. J. Climate, 14, 3433-3443.

Trenberth, K. E., J. T. Fasullo, and J. Mackaro, 2011: Atmospheric moisture transports from ocean to land and global energy flows in reanalyses. J. Climate, 24, 4907–4924, doi:10.1175/2011JCLI4171.1.

Trenberth, K.E., and L. Smith, 2005: The mass of the atmosphere: A constraint on global analysis. *J. Climate*, **18**, 864–875.

Trenberth, K. E., Y. Zhang, J. T. Fasullo, and S. Taguchi, 2015: Climate variability and relationships between top-of-atmosphere radiation and temperatures on Earth. J. Geophys. Res. Atmos., 120, 3642–3659. doi: 10.1002/2014JD022887.

van de Berg, W.J., M.R. van den Broeke, C.H. Reijmer, and E. van Meijgaard, 2006. Reassessment of the Antarctic surface mass balance using calibrated output of a regional atmospheric climate model. *J. Geophys. Res.*, **111**, D11104, doi:10.1029/2005JD006495.

Wargan, K., S. Pawson, M. A. Olsen, J. C. Witte, A. R. Douglass, J. R. Ziemke, S. E. Strahan and J. E. Nielsen, 2015: The global structure of upper troposphere-lower stratosphere ozone in GEOS-5: A multiyear assimilation of EOS Aura data. *J. Geophys. Res. Atmos*., **120**: 2013–2036. doi: 10.1002/2014JD022493.

Wentz, FJ, and MC Schabel, 2000: Precise climate monitoring using complementary satellite data sets, *Nature*, **403**, 414-416.

Wheeler, M. and G. N. Kiladis, 1999: Convectively Coupled Equatorial Waves: Analysis of Clouds and Temperature in the Wavenumber–Frequency Domain. *J. Atmos. Sci.*, **56**, 374–399.

Willett, K., R. Dunn, P. Thorne, S. Bell, M. de Podesta, D. Parker, P. Jones, and C. Williams Jr., 2013: HadISDH land surface multi-variable humidity and temperature record for climate monitoring, *Clim. Past*, 10, 1983-2006. doi:10.5194/cp-9-657-2013

Wu, W.-S., R.J. Purser and D.F. Parrish, 2002: Three-dimensional variational analysis with spatially inhomogeneous covariances. *Mon. Wea. Rev.*, **130**, 2905-2916.

Verdin, K.L. and J.P. Verdin, 1999: A topological system for delineation and codification of the Earth's river basins. *J. Hydrology*, **218**, nos. 1-2, pp. $1^{-1}2$

http://gis.esri.com/library/userconf/proc01/professional/papers/pap1008/p1008.htm.

Xie, P., A. Yatagai, M. Chen, T. Hayasaka, Y. Fukushima, C. Liu, and S. Yang, 2007: A gauge-based analysis of daily precipitation over East Asia, *J. Hydrometeorol*., 8, 607-626.

Yang, D., 1999. An improved precipitation climatology for the Arctic Ocean. *Geophys. Res. Lett.*, **26**(11), 1625-1628, doi:10.1029/1999GL900311.

Yin, J.H., 2005. A consistent poleward shift of the storm tracks in simulations of 21st century climate. *Geophys. Res. Lett.*, **32**, L18701, doi:10.1029/2005GL023684.

Yong Chen, Yong Han, Quanhua Liu, Paul Van Delst, and Fuzhong Weng, 2011: Community Radiative Transfer Model for Stratospheric Sounding Unit. J. Atmos. Oceanic Technol., 28, 767–778, doi: http://dx.doi.org/10.1175/2010JTECHA1509.1

Zou, C.-Z., H. Qian, W. Wang, L. Wang, and C. Long, 2014: Recalibration and merging of SSU observations for stratospheric temperature trend studies, J. Geophys. Res. Atmos., 119, 13,180–13,205, doi:10.1002/2014JD021603.

14. Web Resources

GMAO web site: http://gmao.gsfc.nasa.gov/ (take note of the Technical Memo and Office Notes, under Publications)

GMAO Operations page: http://gmao.gsfc.nasa.gov/products/

Reanalysis.org – a community resource for understanding all types of reanalyses

Previous Volumes in This Series

Volume 1 *September 1994*	Documentation of the Goddard Earth Observing System (GEOS) general circulation model - Version 1 **L.L. Takacs, A. Molod, and T. Wang**
Volume 2 *October 1994*	Direct solution of the implicit formulation of fourth order horizontal diffusion for gridpoint models on the sphere **Y. Li, S. Moorthi, and J.R. Bates**
Volume 3 *December 1994*	An efficient thermal infrared radiation parameterization for use in general circulation models **M.-D. Chou and M.J. Suarez**
Volume 4 *January 1995*	Documentation of the Goddard Earth Observing System (GEOS) Data Assimilation System - Version 1 **James Pfaendtner, Stephen Bloom, David Lamich, Michael Seablom, Meta Sienkiewicz, James Stobie, and Arlindo da Silva**
Volume 5 *April 1995*	Documentation of the Aries-GEOS dynamical core: Version 2 **Max J. Suarez and Lawrence L. Takacs**
Volume 6 *April 1995*	A Multiyear Assimilation with the GEOS-1 System: Overview and Results **Siegfried Schubert, Chung-Kyu Park, Chung-Yu Wu, Wayne Higgins, Yelena Kondratyeva, Andrea Molod, Lawrence Takacs, Michael Seablom, and Richard Rood**
Volume 7 *September 1995*	Proceedings of the Workshop on the GEOS-1 Five-Year Assimilation **Siegfried D. Schubert and Richard B. Rood**
Volume 8 *March 1996*	Documentation of the Tangent Linear Model and Its Adjoint of the Adiabatic Version of the NASA GEOS-1 C-Grid GCM: Version 5.2 **Weiyu Yang and I. Michael Navon**
Volume 9 *March 1996*	Energy and Water Balance Calculations in the Mosaic LSM **Randal D. Koster and Max J. Suarez**
Volume 10 *April 1996*	Dynamical Aspects of Climate Simulations Using the GEOS General Circulation Model **Lawrence L. Takacs and Max J. Suarez**

Volume 11 *May 1997*	Documentation of the Tangent Linear and its Adjoint Models of the Relaxed Arakawa-Schubert Moisture Parameterization Package of the NASA GEOS-1 GCM (Version 5.2) **Weiyu Yang, I. Michael Navon, and Ricardo Todling**
Volume 12 *August 1997*	Comparison of Satellite Global Rainfall Algorithms **Alfred T.C. Chang and Long S. Chiu**
Volume 13 *December 1997*	Interannual Variability and Potential Predictability in Reanalysis Products **Wie Ming and Siegfried D. Schubert**
Volume 14 *August 1998*	A Comparison of GEOS Assimilated Data with FIFE Observations **Michael G. Bosilovich and Siegfried D. Schubert**
Volume 15 *June 1999*	A Solar Radiation Parameterization for Atmospheric Studies **Ming-Dah Chou and Max J. Suarez**
Volume 16 *November 1999*	Filtering Techniques on a Stretched Grid General Circulation Model **Lawrence Takacs, William Sawyer, Max J. Suarez, and Michael S. Fox-Rabinowitz**
Volume 17 *July 2000*	Atlas of Seasonal Means Simulated by the NSIPP-1 Atmospheric GCM **Julio T. Bacmeister, Philip J. Pegion, Siegfried D. Schubert, and Max J. Suarez**
Volume 18 *December 2000*	An Assessment of the Predictability of Northern Winter Seasonal Means with the NSIPP1 AGCM **Philip J. Pegion, Siegfried D. Schubert, and Max J. Suarez**
Volume 19 *July 2001*	A Thermal Infrared Radiation Parameterization for Atmospheric Studies **Ming-Dah Chou, Max J. Suarez, Xin-Zhong, and Michael M.-H. Yan**
Volume 20 *August 2001*	The Climate of the FVCCM-3 Model **Yehui Chang, Siegfried D. Schubert, Shian-Jiann Lin, Sharon Nebuda, and Bo-Wen Shen**
Volume 21 *September 2001*	Design and Implementation of a Parallel Multivariate Ensemble Kalman Filter for the Poseidon Ocean General Circulation Model **Christian L. Keppenne and Michele M. Rienecker**
Volume 22 *August 2002*	Coupled Ocean-Atmosphere Radiative Model for Global Ocean Biogeochemical Models **Watson W. Gregg**

Volume 23
November 2002

Prospects for Improved Forecasts of Weather and Short-term Climate Variability on Subseasonal (2-Week to 2-Month) Time Scales

Siegfried D. Schubert, Randall Dole, Huang van den Dool, Max J. Suarez, and Duane Waliser

Volume 24
July 2003

Temperature Data Assimilation with Salinity Corrections: Validation for the NSIPP Ocean Data Assimilation System in the Tropical Pacific Ocean, 1993–1998

Alberto Troccoli, Michele M. Rienecker, Christian L. Keppenne, and Gregory C. Johnson

Volume 25
December 2003

Modeling, Simulation, and Forecasting of Subseasonal Variability

Duane Waliser, Siegfried D. Schubert, Arun Kumar, Klaus Weickmann, and Randall Dole

Volume 26
April 2005

Documentation and Validation of the Goddard Earth Observing System (GEOS) Data Assimilation System – Version 4

Senior Authors: S. Bloom, A. da Silva and D. Dee

Contributing Authors: M. Bosilovich, J-D. Chern, S. Pawson, S. Schubert, M. Sienkiewicz, I. Stajner, W-W. Tan, and M-L. Wu

Volume 27
December 2008

The GEOS-5 Data Assimilation System - Documentation of Versions 5.0.1, 5.1.0, and 5.2.0.

M.M. Rienecker, M.J. Suarez, R. Todling, J. Bacmeister, L. Takacs, H.-C. Liu, W. Gu, M. Sienkiewicz, R.D. Koster, R. Gelaro, I. Stajner, and J.E. Nielsen

Volume 28
April 2012

The GEOS-5 Atmospheric General Circulation Model: Mean Climate and Development from MERRA to Fortuna

Andrea Molod, Lawrence Takacs, Max Suarez, Julio Bacmeister, In-Sun Song, and Andrew Eichmann

Volume 29
May 2012

Atmospheric Reanalyses – Recent Progress and Prospects for the Future.

A Report from a Technical Workshop, April 2010

Michele M. Rienecker, Dick Dee, Jack Woollen, Gilbert P. Compo, Kazutoshi Onogi, Ron Gelaro, Michael G. Bosilovich, Arlindo da Silva, Steven Pawson, Siegfried Schubert, Max Suarez, Dale Barker, Hirotaka Kamahori, Robert Kistler, and Suranjana Saha

Volume 30
September 2012

The GEOS-ODAS, description and evaluation

Guillaume Vernieres, Michele M. Rienecker, Robin Kovach and Christian L. Keppenne

Volume 31 *March 2013*	Global Surface Ocean Carbon Estimates in a Model Forced by MERRA **Watson W. Gregg, Nancy W. Casey and Cecile S. Rousseaux**
Volume 32 *March 2014*	Estimates of AOD Trends (2002-2012) over the World's Major Cities based on the MERRA Aerosol Reanalysis **Simon Provencal, Pavel Kishcha, Emily Elhacham, Arlindo M. da Silva, and Pinhas Alpert**
Volume 33 *August 2014*	The Effects of Chlorophyll Assimilation on Carbon Fluxes in a Global Biogeochemical Model **Cécile S. Rousseaux and Watson W. Gregg**
Volume 34 *September 2014*	Background Error Covariance Estimation using Information from a Single Model Trajectory with Application to Ocean Data Assimilation into the GEOS-5 Coupled Model **Christian L. Keppenne, Michele M. Rienecker, Robin M. Kovach, and Guillaume Vernieres**
Volume 35 *December 2014*	Observation-Corrected Precipitation Estimates in GEOS-5 **Rolf H. Reichle and Qing Liu**
Volume 36 *March 2015*	Evaluation of the 7-km GEOS-5 Nature Run **Ronald Gelaro, William M. Putman, Steven Pawson, Clara Draper, Andrea Molod, Peter M. Norris, Lesley Ott, Nikki Prive, Oreste Reale, Deepthi Achuthavarier, Michael Bosilovich, Virginie Buchard, Winston Chao, Lawrence Coy, Richard Cullather, Arlindo da Silva, Anton Darmenov, Ronald M. Errico, Marangelly Fuentes, Min-Jeong Kim, Randal Koster, Will McCarty, Jyothi Nattala, Gary Partyka, Siegfried Schubert, Guillaume Vernieres, Yuri Vikhliaev, and Krzysztof Wargan**
Volume 37 *March 2015*	Maintaining Atmospheric Mass and Water Balance within Reanalysis **Lawrence L. Takacs, Max Suarez, and Ricardo Todling**

Volume 38
September 2015

The Quick Fire Emissions Dataset (QFED) – Documentation of versions 2.1, 2.2 and 2.4

Anton S. Darmenov and Arlindo da Silva

Volume 39
September 2015

Land Boundary Conditions for the Goddard Earth Observing System Model Version 5 (GEOS-5) Climate Modeling System – Recent Updates and Data File Descriptions

Sarith P. Mahanama, Randal D. Koster, Gregory K. Walker, Lawrence L. Takacs, Rolf H. Reichle, Gabrielle De Lannoy, Qing Liu, Bin Zhao, and Max J. Suarez

Volume 40
October 2015

Soil Moisture Active Passive (SMAP) Project Assessment Report for the Beta-Release L4_SM Data Product

Rolf H. Reichle, Gabrielle J. M. De Lannoy, Qing Liu, Andreas Colliander, Austin Conaty, Thomas Jackson, John Kimball, and Randal D. Koster

Volume 41
October 2015

GDIS Workshop Report

Siegfried Schubert, Will Pozzi , Eric F. Wood , Kerstin Stahl , Mike Hayes, Juergen Vogt, Sonia Seneviratne, Ron Stewart, Roger Pulwarty, Robert Stefanski

Volume 42
November 2015

Soil Moisture Active Passive (SMAP) Project Assessment Report for the Beta-Release L4_SM Data Product

John S. Kimball, Lucas A. Jones,Joseph Glassy, E. Natasha Stavros, Nima Madani, Rolf H. Reichle, Thomas Jackson, and Andreas Colliander